



Performance-Based Evaluation and Design of Cold-Formed Steel Lateral Force-Resisting Systems for Multi-Storey Buildings

By:

Ioannis Papargyriou

A thesis submitted in partial fulfilment of the requirements for the degree of
Doctor of Philosophy

The University of Sheffield
Faculty of Engineering
Department of Civil and Structural Engineering

Submission Date

July 9, 2021

To

my beloved

Gina, George and Stratos

Abstract

Cold-formed steel (CFS) is becoming popular in building construction as it is more economical and lightweight compared to conventional hot-rolled steel whilst offering ease and speed of construction and greater flexibility in manufacture. However, due to the low element thickness it is more prone to buckling; hence, the design of elements and structures is more challenging, especially when called to resist lateral loads, like wind and earthquakes. While CFS strap-braced stud walls can be used to provide light steel frames with high lateral strength and stiffness, more research is needed to investigate their seismic performance. Furthermore, secondary moments due to P- Δ effects, amplified by the presence of additional vertical loading, are generally ignored in conventional design and can lead to premature failure of compressive studs and low ductility.

In this research, the non-linear behaviour of CFS strap-braced stud walls is comprehensively examined to improve structural efficiency. By considering P- Δ effects, the key design parameters are identified, and a novel design framework is developed. CFS multi-storey frames are analysed numerically, and the efficiency of the proposed methodology is investigated by using local and global damage indices under seismic loading with different intensity levels. Finally, the work focuses on the development of new types of CFS moment-resisting beam-column joints, transferring bending moments through the flanges or both the webs and flanges, and design considerations are proposed to reach a balanced performance, combining high flexural capacity, deformability, ductility and rotational stiffness.

The results of this study indicate that diagonal strap thickness and vertical loading had the most significant impact on critical seismic performance parameters, such as the lateral load and deformation capacity, ductility and energy dissipation. A case study 6-storey strap-braced frame, designed in accordance with Eurocode 8 specifications, exhibited very low ductility at some storey levels, below the target value of 4, while the design solution following the proposed methodology reached high ductility, preventing premature failure of the chord studs. The efficiency of Eurocode 8 and the proposed design solutions was studied and assessed under artificial and real spectrum-compatible ground motion records using non-linear dynamic analyses. The proposed design solution met all target performance levels and reached low damage index values. By contrast, Eurocode 8 design solution failed to meet the life safety (LS) and collapse prevention (CP) targets while sustaining extensive global damage even under low earthquake intensity levels of 0.20 g.

The newly developed flange and web-flange connected joints proved to be an appropriate and efficient alternative solution to web-connected joints, exhibiting high bending moment capacity, ductility and energy dissipation while facilitating assembly. The results of this research have the potential to contribute to the development of more resilient CFS strap-braced systems in seismic regions.

Research contribution

In the present work, extensive analytical research was performed on the lateral behaviour of CFS lateral force-resisting systems, employing strap-braced stud walls and beam-column moment-resisting connections, and resulted in the following standalone journal and conference papers, either published or submitted and under peer review:

Journal papers

Published

Papargyriou I., Hajirasouliha I., Becque J., Pilakoutas K., Performance-based assessment of CFS strap-braced stud walls under seismic loading, *Journal of Constructional Steel Research*, 183 (2021) 106731.

<https://doi.org/10.1016/j.jcsr.2021.106731>

Papargyriou I., Hajirasouliha I., More efficient design of CFS strap-braced frames under vertical and seismic loading, *Journal of Constructional Steel Research*, 185 (2021) 106886.

<https://doi.org/10.1016/j.jcsr.2021.106886>

Submitted and under peer review

Papargyriou I., Hajirasouliha I., Performance-based seismic design and assessment of multi-storey CFS strap-braced frames. Submitted to: *Engineering Structures*, Date submitted: 8/9/2021.

Papargyriou I., Mojtabaei S., Hajirasouliha I., Becque J., Pilakoutas K., Cold-formed steel beam-to-column bolted connections for seismic applications. Submitted to: *Thin Walled Structures*, Date submitted: 22/8/2021.

Conference papers

Papargyriou I., Mojtabaei S.M., Hajirasouliha I., Becque J. (2021). Cyclic and Monotonic Moment-Rotation Behaviour of CFS Web-Connected Beam-to-Column Joints. 1st Croatian Conference on Earthquake Engineering, 22-24 March, Zagreb, Croatia.

<https://doi.org/10.5592/CO/1CroCEE.2021.122>

Mojtabaei S.M., Papargyriou I., Hajirasouliha I., Becque J. (2019), Optimum seismic design of cold-formed steel moment-resisting frames. 9th International Conference on Steel and Aluminium Structures (ICSAS19), 3-5, July, Bradford, UK.

Mojtabaei S.M., Papargyriou I., Hajirasouliha I., Becque J., Pilakoutas K. (2018), Development of cold-formed steel moment-resisting frames using optimum beams in seismic applications. 16th European conference on earthquake engineering, 18-21 June, Thessaloniki, Greece.

Acknowledgements

This work would not have been possible without the continuous help, support and encouragement of my first supervisor Dr. Iman Hajirasouliha. He has always been there for me as a mentor, offering his expert advice, guidance and knowledge during all stages of my research. I need to express my deepest gratitude and cannot thank him enough for his excellent, exemplary and friendly collaboration.

I would like to express my appreciation and cordially thank my second and third supervisors, Dr. Jurgen Becque and Professor Kypros Pilakoutas, for their always well-intended, supportive and constructive advice and guidance. They have contributed significantly to the completion of this work.

I am deeply grateful to my colleague in the Cold-Formed Steel Group, Dr. Mohammad Mojtabaei. He has always been a very supportive friend and helped me considerably with his knowledge and teamwork. I would also like to thank Dr. Francisco Meza Ortiz for our valuable discussions and his willingness to offer me his advice, whenever needed.

I very much appreciate the support of the Concrete and Earthquake Engineering Research Group at the Department of Civil & Structural Engineering, as well as my room D120 colleagues, Mr. Soheil Khoshkholghi and Mr. Mohammad Moavi. It was a great pleasure to meet all of you. You made my years in Sheffield unforgettable.

Throughout this journey, I had my wife, Gina and our sons George and Stratos by my side. Your love, support and encouragement kept me going. Thank you for your immense patience and sacrifices, I couldn't have made it without you. George, we are graduating together this year, isn't that fantastic?

Finally, I would like to thank my father George, my mother Tassoula and my sister Eleni for their unconditional love and guidance throughout my life.

Table of Contents

Abstract	v
Research contribution	vi
Acknowledgements	viii
Table of Contents	ix
List of Figures	xiv
List of Tables	xix
CHAPTER 1	1
Introduction	
1.1 Research motivation.....	1
1.2 Background review	3
1.2.1 Full-scale tests of CFS strap-braced shear walls under lateral loads.....	3
1.2.2 Numerical modelling of CFS strap-braced walls and building systems.....	5
1.2.3 Performance-based seismic design methodologies of building systems	10
1.2.3.1 Application of performance-based seismic design methodologies in CFS strap-braced structures	12
1.2.4 Full-scale tests and numerical modelling of CFS beam-column connections.....	13
1.2.4.1 CFS beam-column connections of single-storey buildings.....	13
1.2.4.2 CFS beam-column connections of multi-storey buildings	14
1.3 Scope of research	15
1.4 Aims and objectives	15
1.5 Tasks and methodology	15
1.6 Thesis layout	17
1.6.1 Chapter 1	17
1.6.2 Chapter 2	17
1.6.3 Chapter 3	18
1.6.4 Chapter 4	18
1.6.5 Chapter 5	18
1.6.6 Chapter 6	19

CHAPTER 2.....	20
Performance-based assessment of CFS strap-braced stud walls under seismic loading	
2.1 Abstract	20
2.2 Introduction	21
2.3 Description of the reference experimental tests	24
2.4 Description of the ABAQUS models	25
2.4.1 Material properties.....	26
2.4.2 Finite element type and mesh-size.....	26
2.4.3 Connection modelling.....	27
2.4.3.1 Validation of the connection model.....	28
2.4.4 Boundary conditions.....	30
2.4.5 Component interactions	31
2.4.6 Loading.....	32
2.4.7 Initial Geometric Imperfections.....	32
2.5 Model validation	33
2.5.1 Monotonic analysis.....	33
2.5.2 Cyclic analysis.....	34
2.6 Evaluation of the non-linear performance of strap-braced walls	37
2.6.1 Effect of vertical load	38
2.6.2 Number of studs.....	40
2.6.3 Thickness of the studs.....	41
2.6.4 Thickness of the diagonal straps.....	41
2.6.5 Thickness of the wall frame elements	42
2.6.6 Thickness of the chord studs and the tracks	43
2.6.7 Steel grade of the diagonal straps	44
2.7 Efficiency assessment of the design solutions	46
2.8 Summary and conclusions.....	47
2.9 Acknowledgements	48
2.10 Author contribution	49
CHAPTER 3.....	50
More efficient design of CFS strap-braced frames under vertical and seismic loading	
3.1 Abstract	50
3.2 Introduction	51
3.3 Description of the numerical model in ABAQUS.....	52
3.3.1 Geometry – FE type and mesh size	53

3.3.2	Material properties	54
3.3.3	Connections and member interactions	54
3.3.4	Verification of the FE model.....	55
3.4	Non-linear structural performance of single strap-braced walls	56
3.4.1	Effect of the diagonal strap thickness.....	56
3.4.2	Effect of the vertical load	57
3.5	Design of CFS strap-braced frames under simultaneous vertical and seismic loading	60
3.5.1	General design concept	60
3.5.2	Proposed design equations	62
3.5.2.1	Lateral load capacity under zero vertical loading.....	62
3.5.2.2	Ductility under zero vertical loading.....	63
3.5.2.3	Lateral load capacity under a vertical loading ratio	64
3.5.2.4	Ductility under a vertical loading ratio.....	65
3.5.3	Practical design procedure for the preliminary design of multi-storey stud wall frames...67	
3.6	Design of a case study frame	69
3.6.1	Design for gravity loading.....	70
3.6.2	Design for seismic loading.....	71
3.6.2.1	Reference wall properties.....	73
3.6.2.2	Design of straps and chord studs.....	73
3.6.2.3	Lateral load capacity of the wall panels	74
3.6.2.4	Ductility of the wall panels	74
3.6.2.5	Verification of the predicted values	75
3.7	Summary and concluding remarks.....	76
3.8	Acknowledgements.....	77
3.9	Author contribution.....	77
CHAPTER 4		78
Performance-Based Seismic Design and Assessment of Multi-Storey CFS Strap-Braced Frames		
4.1	Abstract.....	78
4.2	Introduction.....	79
4.3	Proposed design methodology	82
4.3.1	Design solutions of a case study frame	84
4.3.2	Design specifications.....	85
4.3.3	Conventional and proposed design solutions	85
4.4	Development of non-linear numerical models.....	86
4.4.1	Detailed non-linear numerical model in ABAQUS.....	86

4.4.1.1	Summary of model features.....	87
4.4.1.2	Model validation.....	88
4.4.2	Non-linear numerical models in OpenSees	90
4.4.3	Hysteretic response.....	91
4.4.4	Multi-storey frame system.....	93
4.5	Non-linear time-history analysis	95
4.5.1	Artificial spectrum-compatible ground motion records.....	95
4.5.2	Performance Assessment Parameters	96
4.6	Performance evaluation of CFS strap-braced wall multi-storey frames.....	97
4.6.1	Seismic Performance Assessment	97
4.6.2	Non-linear Incremental Dynamic Analysis (IDA)	100
4.6.3	Seismic performance under real ground motion records	101
4.7	Summary and Conclusions.....	105
4.8	Author contribution	106

CHAPTER 5..... 107

Cold-formed steel beam-to-column bolted connections for seismic applications

5.1	Abstract	107
5.2	Introduction.....	108
5.3	Description of the ABAQUS numerical models	110
5.3.1	Material properties.....	110
5.3.2	Finite element type and mesh-size.....	111
5.3.3	Bolt modelling.....	112
5.3.4	Boundary conditions and interactions	113
5.3.5	Initial geometric imperfections.....	114
5.3.6	Loading.....	115
5.3.7	Numerical model validation	115
5.4	Flexural behaviour of various connection configurations	117
5.4.1	Connection configurations.....	117
5.4.2	Evaluation of connections under monotonic loading	119
5.4.2.1	Performance criteria	119
5.4.2.2	Moment-rotation results and discussions.....	121
5.4.2.2.1	W-C connections	121
5.4.2.2.2	F-C connections.....	123
5.4.2.2.3	WF-C connections	126
5.4.3	Connection types with the best overall seismic performance.....	128

5.5	Seismic efficiency of the selected connection types	131
5.5.1	Ductility.....	134
5.5.2	Energy dissipation	136
5.5.3	Damping coefficient.....	137
5.6	Summary and Conclusions	138
5.7	Author contribution.....	140
CHAPTER 6.....		141
Conclusions and recommendations for future work		
6.1	Summary and conclusions	141
6.1.1	Performance-based assessment of CFS Strap-braced stud walls under seismic loading..	142
6.1.2	More efficient design of CFS strap-braced frames under vertical and seismic loading...	142
6.1.3	Performance-based seismic design and assessment of multi-storey CFS strap-braced frames	143
6.1.4	Cold-formed steel beam-to-column bolted connections for seismic applications.....	144
6.2	Recommendations for future work	145
References		147

List of Figures

Fig. 1.1 CFS sections: (a) single open, (b) open built-up, (c) closed built-up and (d) panels and decks (Dubina <i>et al.</i> , 2012).....	1
Fig. 1.2 Cold-formed steel buildings.....	2
Fig. 1.3 a) Typical screw connected strap-braced wall configuration, b) Detail D1, of the wall’s anchoring system.....	4
Fig. 1.4 Failure modes and hysteretic behaviour of (a) OSB-sheathed walls, (b) steel-sheathed walls and (c) strap-braced walls (Madsen <i>et al.</i> , 2016)	5
Fig. 1.5 Strap-braced wall modelled in (a) Ansys and (b) in SAP (Zeynalian and Ronagh, 2012)	6
Fig. 1.6 Model of high-aspect ratio shear wall (Mirzaei <i>et al.</i> , 2015)	7
Fig. 1.7 Strap-braced wall model (Gerami <i>et al.</i> , 2015).....	7
Fig. 1.8 Strap-braced wall model (Fiorino <i>et al.</i> , 2017)	8
Fig. 1.9 Modelling of 2D CFS strap-braced frames (Velchev, 2008b)	8
Fig. 1.10 The “bi-linear with slackness” hysteretic model adopted in (Velchev, 2008b).....	9
Fig. 1.11 Modelling of 2D CFS strap-braced frames (Comeau <i>et al.</i> , 2010)	9
Fig. 1.12 A frame, being part of the 3D model (Fiorino <i>et al.</i> , 2017)	10
Fig. 1.13 Performance-based design process (Hamburger, 2004).....	10
Fig. 1.14 Connection configuration proposed by Shahini <i>et al.</i> (Shahini <i>et al.</i> , 2018)	14
Fig. 2.1 Configuration of specimen 25A-M, tested by Velchev (Velchev, 2008b).....	24
Fig. 2.2 Details of the developed Finite Element model	26
Fig. 2.3 Lateral load-displacement curves for different mesh sizes	27
Fig. 2.4 Behaviour of a) No. 8 screws and b) No. 10 screws	28
Fig. 2.5 a) ABAQUS fastener configuration, and b) Discrete fastener in the FE model	28
Fig. 2.6 Configuration of shear-lap tests (adopted from (Meza, 2018)).....	29
Fig. 2.7 Predicted and measured load-deformation curves of a) SL14-14c and b) SL20-14c	30
Fig. 2.8 a) Top track, b) Bottom track and plate and c) Top plate boundary conditions.....	31
Fig. 2.9 Component interactions	32
Fig. 2.10 Effect of a) strap imperfection and b) chord stud imperfection on the lateral response	33

Fig. 2.11 Lateral load-displacement curves of a) 25A-M-1 and b) 31A-M-1 test specimens and corresponding FE analysis results	34
Fig. 2.12 Distribution of von Mises stresses and failure modes of test specimen 25A-M-1	34
Fig. 2.13 Lateral load-displacement curves of a) 26A-C, and b) 32A-C test specimens and corresponding FE analysis results.....	35
Fig. 2.14 Cumulative energy-time curves of a) 26A-C, and b) 32A-C test specimens and corresponding FE analysis results.....	36
Fig. 2.15 Comparison of a) 26A-C backbone curve with 25A-M-1 monotonic curve and b) 32A-C backbone curve with 31A-M-1 monotonic curve.....	36
Fig. 2.16 Lateral load-displacement curves in the presence of vertical loading	38
Fig. 2.17 Failure mode under vertical loading equal to 35% P_w	39
Fig. 2.18 Lateral load-displacement curves, varying the number of studs with 35% P_w vertical load .	40
Fig. 2.19 Lateral load-displacement curves for walls with different diagonal strap thicknesses.....	42
Fig. 2.20 Lateral load-displacement curves for frames with different thicknesses a) bare frame, b) frame with diagonal straps.....	43
Fig. 2.21 Yielding of the chord studs in a bare frame with twice the original thickness	43
Fig. 2.22 Lateral load-displacement curves for wall panels with different thickness of a) the chord studs and b) the tracks	44
Fig. 2.23 Stress-strain curves for steel grades S280, S460 and S690	45
Fig. 2.24 Lateral load-displacement curves for various steel grades of the diagonal straps.....	45
Fig. 2.25 Efficiency Index (R_{ef}) for a) lateral capacity, b) deformation capacity, c) ductility, and d) energy dissipation.....	47
Fig. 3.1 Wall geometry and cross-sectional dimensions.....	53
Fig. 3.2 Numerical model in ABAQUS	54
Fig. 3.3 a) Comparison of the lateral load-displacement curves of a) 25A-M-1 and b) 31A-M-1 test specimens and corresponding FE analyses.	55
Fig. 3.4 Distribution of von Mises stresses and failure modes for walls with a) 1.11 mm straps and b) 2.78 mm straps, under no vertical loading	57
Fig. 3.5 Lateral load-displacement curves for walls with diagonal strap thickness a) $t_s=0.56$ mm, b) $t_s=1.11$ mm, c) $t_s=1.67$ mm, d) $t_s=2.22$ mm, e) $t_s=2.78$ mm and f) $t_s=3.33$ mm under various levels of vertical loading.....	59
Fig. 3.6 Schematic of the proposed design concept.....	61

Fig. 3.7 Effect of strap and chord stud thickness ratio on the lateral load capacity ratio	62
Fig. 3.8 Effect of strap ratio on the ductility ratio	63
Fig. 3.9 Secondary force and moment for the calculation of (t_{so}) strap thickness.....	64
Fig. 3.10 Effect of vertical load ratio on the lateral load capacity	65
Fig. 3.11 Effect of vertical load ratio on the lateral load capacity, a) results of analyses, and b) predicted values using Eq. (9)	66
Fig. 3.12 Proposed design procedure of CFS strap-braced frames under simultaneous vertical and seismic loading	68
Fig. 3.13 Case study frame under a) non-seismic and b) seismic actions	69
Fig. 3.14 Lateral force distribution on a wall panel	72
Fig. 4.1 Geometry of the case-study strap-braced wall frame.....	84
Fig. 4.2 Detailed ABAQUS numerical model.....	87
Fig. 4.3 Reversed cyclic protocol per ASTM E2126 (ASTM, 2019).....	88
Fig. 4.4 Comparison of the experimental and FE analysis predicted cyclic responses of specimens a) 26A-C, and b) 32A-C	89
Fig. 4.5 Single strap-braced wall model in OpenSees.....	91
Fig. 4.6 Definition of OpenSees (Mazzoni <i>et al.</i> , 2007) “Pinching4” hysteretic model	91
Fig. 4.7 Lateral load-displacement relationships for walls SW1 and SW2	92
Fig. 4.8 ABAQUS and OpenSees hysteretic response and cumulative energy of (a & c): SW1 wall and (b & d): SW2 wall	93
Fig. 4.9 The strap-braced wall frame model in OpenSees	94
Fig. 4.10 Comparison between elastic response spectra of artificial records and the selected Eurocode 8 design spectrum	95
Fig. 4.11 Inter-storey drift distribution of a) Eurocode design and b) Proposed design under seven artificial spectrum compatible records	98
Fig. 4.12 Storey ductility demand and capacity distribution of a) Eurocode design and b) proposed design under seven artificial spectrum compatible records, IO performance limit	99
Fig. 4.13 Storey ductility demand and capacity distribution of a) Eurocode design and b) proposed design under seven artificial spectrum compatible records, LS performance limit.....	99
Fig. 4.14 Storey ductility demand and capacity distribution of a) Eurocode design and b) proposed design under seven artificial spectrum compatible records, CP performance limit	99

Fig. 4.15 Global damage index (DI_g) for the Eurocode and proposed design solution frames subjected to artificial spectrum-compatible ground motion records	101
Fig. 4.16 Comparison between the response spectra of the real earthquakes and the elastic design response spectrum of Eurocode.....	102
Fig. 4.17 Inter-storey average drift distribution for (LS) performance limit of a) the Eurocode design and b) the proposed design solutions subjected to real ground motion records	103
Fig. 4.18 Average storey ductility demand and capacity for (LS) performance limit of a) the Eurocode design and b) the proposed design solutions subjected to real ground motion records	104
Fig. 4.19 Global damage index (DI_g) for the Eurocode and proposed design solution frames subjected to a set of real ground motion records.....	105
Fig. 5.1 FE modelling of the tested connections: a) bolt arrangement and b) discrete fastener	113
Fig. 5.2 Bearing behaviour of the beam to gusset plate bolts incorporated into the FE models of tests A1 and B1	113
Fig. 5.3 Boundary conditions of the FE models.....	114
Fig. 5.4 Cyclic loading protocol adopted from AISC 341-16 (AISC, 2016)	115
Fig. 5.5 Comparison between experimental moment-rotation behaviour (Sabbagh, 2011) and FE analysis results for: (a) A1 and (b) B1 specimens.....	116
Fig. 5.6 Comparison between the experimental (Sabbagh, 2011) and predicted failure modes under cyclic loading for: (a) A1 and (b) B1 specimens.....	117
Fig. 5.7 Connection configuration	118
Fig. 5.8 Definition of a) moment-rotation relationship, b) initial stiffness ($S_{j,ini}$), and c) boundaries for the rotational stiffness classification of connections.....	120
Fig. 5.9 Moment-rotation responses of W-C connections with various gusset plate thicknesses (t_g) and shapes (①: T-shape, ②: rounded T-shape and ③: chamfered shape), and beam thicknesses (t_b) of a) 1 mm, b) 2 mm, c) 4 mm and d) 6 mm	122
Fig. 5.10 Failure modes of W-C connections with: a) T shape, b) rounded T-shape and c) chamfered gusset plate, for $t_b=4$ mm and $t_g=1.5t_b$	123
Fig. 5.11 Moment-rotation responses of F-C connections with various gusset plate thicknesses (t_g) and shapes (①: unstiffened angles and ②: stiffened angles), and beam thicknesses (t_b) of a) 1 mm, b) 2 mm, c) 4 mm and d) 6 mm.....	124
Fig. 5.12 Failure modes of connections with a) unstiffened angles and b) stiffened angles, when $t_b=2$ mm and $t_g=3t_b$	125

Fig. 5.13 Moment-rotation responses of WF-C connections with various gusset plate thicknesses (t_g), and beam thicknesses (t_b) of a) 1 mm, b) 2 mm, c) 4 mm and d) 6 mm.....	126
Fig. 5.14 Failure modes of WF-C connections for $t_b=1$ and a) $t_g=t_b$ and b) $t_b=3t_b$	127
Fig. 5.15 FE model of CFS beam with back-to-back channel sections used to determine the cross-sectional flexural capacity ($M_{u,b}$).....	128
Fig. 5.16 $M_{max}/M_{u,b}$ ratios for W-C connections with beam thicknesses t_b of a) 1 mm, b) 2 mm, c) 4 mm and d) 6 mm.....	129
Fig. 5.17 $M_{max}/M_{u,b}$ ratios for F-C connections with beam thicknesses t_b of a) 1 mm, b) 2 mm, c) 4 mm and d) 6 mm.....	130
Fig. 5.18 M_{max}/M_{ub} ratios for WF-C connections with beam thicknesses t_b of a) 1 mm, b) 2 mm, c) 4 mm and d) 6 mm.....	130
Fig. 5.19 Hysteretic moment-rotation curves for balanced W-C connections with gusset plate thickness $t_g=2t_b$ and beam thickness (t_b) of a) 1 mm, b) 2 mm, c) 4 mm and d) 6 mm	132
Fig. 5.20 Hysteretic moment-rotation curves for balanced F-C connections with beam and gusset plate thicknesses of a) $t_b=1$ mm, $t_g=4t_b$, b) $t_b=2$ mm, $t_g=4t_b$, c) $t_b=4$ mm, $t_g=3t_b$ and d) $t_b=6$ mm, $t_g=2t_b$	133
Fig. 5.21 Hysteretic moment-rotation curves for balanced WF-C connections with gusset plate thickness $t_g=2t_b$ and beam thickness (t_b) of a) 1 mm, b) 2 mm, c) 4 mm and d) 6 mm	134
Fig. 5.22 Equivalent (EEEP) analysis model per ASTM E2126.....	135
Fig. 5.23 Ductility (μ_ϕ) of different connection configurations with balanced performance	135
Fig. 5.24 Yield rotation (ϕ_y) of different connection configurations with balanced performance.....	136
Fig. 5.25 Energy dissipation (E) of connections with balanced performance.....	136
Fig. 5.26 Definition of equivalent viscous damping coefficient (ζ_{eq}).....	137
Fig. 5.27 Equivalent viscous damping coefficient (ζ_{eq}) at M_{max} for connections with balanced performance.....	138
Fig. 5.28 Equivalent viscous damping coefficient (ζ_{eq}) at M_u for connections with balanced performance	138

List of Tables

Table 2.1 Element thicknesses and material properties.....	25
Table 2.2 Plate thicknesses and steel properties of the shear lap tests (Meza, 2018).....	29
Table 3.1 Material properties.....	54
Table 3.2 Cross-sections of wall elements for Eurocode and Proposed Design solutions	70
Table 3.3 Design for gravity loading.....	71
Table 3.4 Strap and chord stud axial capacity	73
Table 3.5 Lateral load capacities and adequacy ratios of storey wall panels	74
Table 3.6 Storey wall ductility values	75
Table 3.7 Verification of the predicted values.....	75
Table 4.1 Functions f_1 , f_2 , f_3 and f_4 used to obtain lateral load capacity and ductility per Eqs. (15), (16), (17) and (18).....	83
Table 4.2 The plate thickness of the members in the Eurocode and the proposed design solutions (sizes are shown in Fig. 4.1).....	85
Table 4.3 Material properties of ABAQUS model.....	87
Table 4.4 Lateral load and ductility capacities of the Eurocode and the proposed design solutions....	90
Table 4.5 Real ground motion records	102
Table 5.1 Material properties of the tests A1 and B1	111
Table 5.2 Connection configurations and selected design variables	119
Table 5.3 Ultimate rotation (ϕ_{max}), flexural rigidity per EC3 (CEN, 2005), rotational category per AISC provisions (AISC, 2016) and failure modes of W-C connections.....	122
Table 5.4 Ultimate rotation (ϕ_{max}), flexural rigidity per EC3 (CEN, 2005), rotational category per AISC provisions (AISC, 2016) and failure modes of F-C connections	125
Table 5.5 Ultimate rotation (ϕ_{max}), flexural rigidity as per EC3 (CEN, 2005), rotational category as per AISC provisions (AISC, 2016) and failure modes for WF-C connections	127
Table 5.6 Connections with balanced performance.....	131

CHAPTER 1

Introduction

1.1 Research motivation

The use of “cold-formed” or “light-gauge” steel (CFS) in construction has gained increased popularity over the recent years, offering the ability to form efficient, alternative structural systems to conventional hot-rolled steel framing solutions. A whole industry has been developed in the field, offering a wide range of cross-sections used as primary structural members or secondary elements. CFS cross-sections are manufactured by roll forming or folding and press-braking steel flat strips or coils. Their thickness ranges between 0.4-6 mm, and they appear in various shapes, such as single open sections, open built-up sections, closed built-up sections, panels and decks (Fig. 1.1) (Dubina *et al.*, 2012).

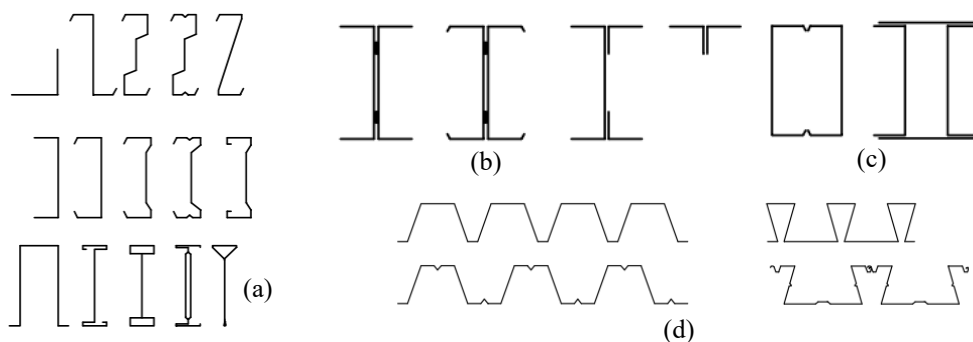


Fig. 1.1 CFS sections: (a) single open, (b) open built-up, (c) closed built-up and (d) panels and decks (Dubina *et al.*, 2012)

Cold-formed steel buildings offer many advantages, which fulfil modern requirements of low embodied energy consumption and provide durability and sustainability. Moreover, they: (a) are lightweight, facilitating easy and speedy transportation and construction, (b) have high strength and stiffness, and (c) are suitable for prefabrication and mass-construction, resulting in a reduced final cost (Dubina *et al.*,

2012). Depending on the application, CFS provides the flexibility to either construct all structural members of a building on-site, using steel coils and a small roll-forming machine, or manufacture complete blocks of a building in the factory and assemble them on-site (Schafer *et al.*, 2016).

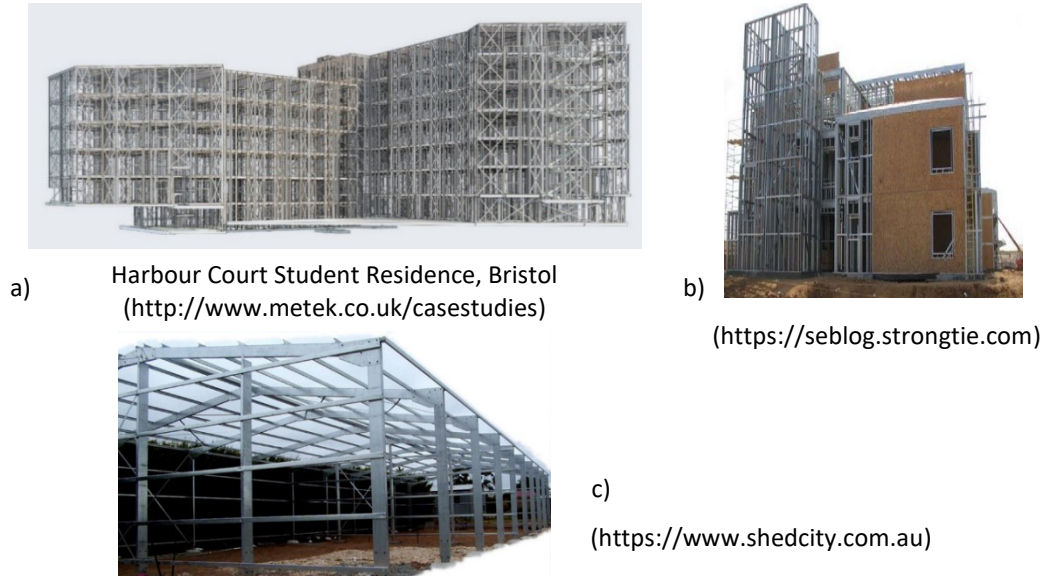


Fig. 1.2 Cold-formed steel buildings

CFS buildings resist lateral loading (e.g. wind or earthquake) through strap-braced stud walls (Fig. 1.2a), sheathed stud walls (Fig. 1.2b) or moment-resisting frames (Fig. 1.2c), with the latter being most commonly employed for single-storey buildings of industrial use. A significant number of studies have been conducted, especially in the experimental field, where different lateral force resisting systems (e.g. sheathed walls and strap-braced walls) were tested under monotonic and cyclic loading, in order to understand and evaluate the performance of members and connections and define the application limits of these systems. The present study will focus on CFS strap-braced wall systems and beam-column moment-resisting connections, as the key elements in multi-storey frame systems. A critical literature review on the performance of these systems indicated several research gaps, which can be summarised as follows:

- The vast majority of experimental tests on CFS strap-braced walls under lateral loading were performed without any additional vertical loading. Only a few tests exist on the combined action of additional vertical and lateral loading. However, they were not systematic in studying its effect on the system's lateral load capacity, ductility, and energy dissipation and involved sheathed and not strap-braced wall systems.
- While previous studies indicated the suitability of strap-braced walls for seismic applications, there is a lack of practical recommendations for seismic design and reliable numerical models

to predict the structural performance of these systems under monotonic and cyclic loading, especially under the presence of vertical loads.

- Eurocode 8 does not provide design specifications to predict the lateral load capacity and ductility of CFS strap-braced wall systems. This is especially important when these systems are subjected to additional vertical loading and secondary moments due to the amplified P- Δ effects. Contrary to designing against wind forces, where strength is critical, ductility is the most significant parameter for seismic applications, ensuring that the structure has the deformation capacity to dissipate energy by maintaining its original strength.
- Performance-based design, i.e. the design that satisfies specific performance objectives, is a new and unexplored field for CFS multi-storey frames. Research studies are minimal and based on specific experimental test results of single-storey strap-braced walls, which do not necessarily represent the behaviour of multi-storey systems under different loading conditions. The performance of CFS strap-braced wall multi-storey frames under dynamic loading has not been adequately studied, and their efficiency and reliability for different performance levels need to be determined and quantified.
- Research on CFS beam-column connections, suitable for multi-storey buildings in seismic regions, is very limited and has not rigorously studied the effect of design parameters, such as the element thicknesses and gusset plate shape, to identify the system's limits and reach the most efficient design solution with balanced characteristics. Currently, the only existing configurations are web-connected joints, and there are no studies on CFS beam-column moment-resisting connections, transferring bending moments through the flanges of the beam and the column or a combination of the two. Moreover, there are no design recommendations for such connections to satisfy different performance levels.

1.2 Background review

1.2.1 Full-scale tests of CFS strap-braced shear walls under lateral loads

The main lateral force-resisting system of cold-formed steel (CFS) buildings under wind and earthquake loading is the stud wall. It consists of top and bottom track members and vertical stud elements. The edge studs are usually built-up sections comprising two stud elements, connected back-to-back, and due to the developed truss-like action are known as “chord studs”. The tracks and intermediate studs are most frequently connected through self-drilling screws (acting as pins), but welded connections are also used. The frame comprising the studs alone has a low lateral load capacity, and two approaches are available for the structural analysis and design of cold-formed steel systems: “all-steel design” and “sheathing-braced design”. According to the first approach, the bearing structure consists only of the

steel elements, without allowing for the stiffness, strength and lateral restraint provided by the sheathing panels. In this case, it is necessary to use bracing members in the form of X-formed strap braces. In the “sheathing-braced design” approach, the sheathing participates, through its high stiffness, in the lateral force-resisting system and increases the axial capacity of the horizontal and vertical steel elements by stabilising them against global, local and distortional buckling (Dubina *et al.*, 2012).

The elements mainly contributing to the lateral performance of the strap-braced walls are the steel tensile braces (Fig. 1.3), which can be a) screw connected (Al-Kharat and Rogers, 2007), b) all-screw connected with gusset plates (Iuorio *et al.*, 2014) and c) all-welded with gusset plates (Al-Kharat and Rogers, 2007). The lateral forces get transferred to the chord studs and then through the hold-downs and the anchor rods to the foundation. The strength and stiffness of straps under compression is considered to be negligible due to their high slenderness (Mirzaei *et al.*, 2015).

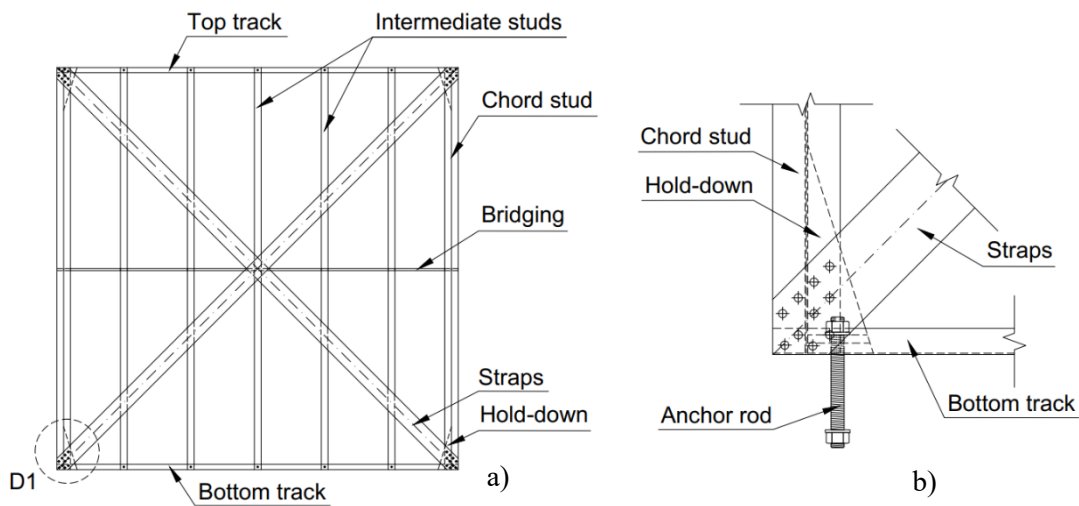


Fig. 1.3 a) Typical screw connected strap-braced wall configuration, b) Detail D1, of the wall's anchoring system

The most desirable and ductile failure of strap-braced shear walls is yielding of the straps, meaning that the non-dissipative elements (e.g. chord studs, connections) have to be designed so that they do not fail before the straps reach their yielding capacity (Al-Kharat and Rogers, 2007). To this end, current seismic design codes, such as AISI S400 (AISI S400, 2015), Eurocode 8 (CEN, 2004) and Eurocode 3 (CEN, 2003), provide capacity-design guidelines, which aim to prevent non-ductile failure modes, including net-section fracture of the straps, premature failure of non-dissipative members, and brittle failure of the fasteners (Iuorio *et al.*, 2014). In this respect, screws perform better than bolts, because they provide a greater net cross-section of the straps (Casafont *et al.*, 2007a), thus allowing for a greater strap energy dissipation capacity. In order to protect the strap-to-chord stud connections, it is beneficial not to have straps of a uniform cross-section along their length but to trim their middle part away, forming a

“dogbone” shape (Velchev, 2008a, 2008b; Kasaeian *et al.*, 2020). This region of reduced cross-section plays the role of a ductile fuse, and experiments showed that they were able to attract all inelastic deformations. Moreover, to achieve a more ductile behaviour, other studies suggested a lower steel grade to be used for the straps than for the rest of the wall’s components (Casafont *et al.*, 2006a, 2007b).

The cyclic behaviour of CFS strap-braced walls is highly non-linear, and although characterised by pinching, if capacity design rules are followed the strength and stiffness degradation is insignificant and the hysteresis loops are more stable. In Fig. 1.4, failure modes and hysteretic behaviour of a) OSB-sheathed walls, b) steel-sheathed walls and c) strap-braced walls (Madsen *et al.*, 2016) are depicted. As it can be observed, the hysteretic behaviour of OSB- and steel-sheathed shear walls is characterised by a reduction in strength and stiffness after the peak load is reached, which is due to the progressive damage of the connections after each loading cycle (Fig. 1.4a) and buckling of the steel plates (Fig. 1.4b). By contrast, the cyclic response of the strap-braced wall (Fig. 1.4c) exhibits a negligible drop in strength and stiffness, providing maximum energy dissipation.

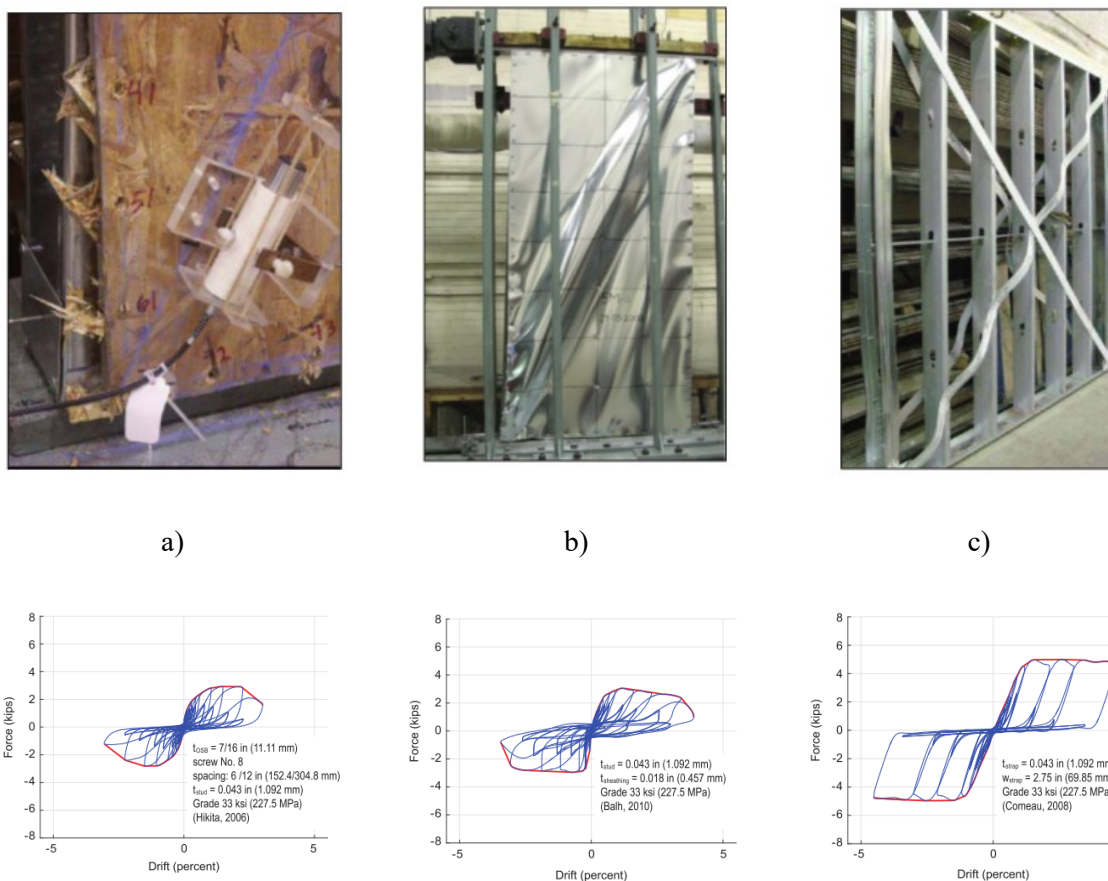


Fig. 1.4 Failure modes and hysteretic behaviour of (a) OSB-sheathed walls, (b) steel-sheathed walls and (c) strap-braced walls (Madsen *et al.*, 2016)

1.2.2 Numerical modelling of CFS strap-braced walls and building systems

Numerical modelling and analysis of strap-braced walls are challenging due to their highly non-linear response and complex failure modes. Therefore, a critical step in developing reliable numerical models is their validation against experimental results before being further used. They are divided into “detailed” or “high-fidelity” and “reduced-order” models (Grant *et al.*, 2011). In the first category, members and local details are simulated with the highest possible accuracy, and their failure modes are precisely captured. These models are suitable for the numerical simulation of single elements and wall panels because of the high computational effort needed for the analysis. On the other side, “reduced order” models are less accurate at a local level but are the most effective solution for the simulation of building systems when their global behaviour is the subject of study.

Zeynalian and Ronagh (Zeynalian and Ronagh, 2012) proposed an alternative configuration of a conventional stud wall system, where the corners were reinforced by brackets, improving the overall performance in lateral loads. This reinforcement led to the capacity increment of chord studs and tracks against buckling by exploiting the bending resistance of the brackets as a subsidiary energy absorption mechanism. Modelling was done in ANSYS using type “SHELL181” finite elements, and the model was validated against experimental results. Moreover, a SAP2000 model was developed to determine the lateral capacity of the walls and derive Ω_0 and R factors.

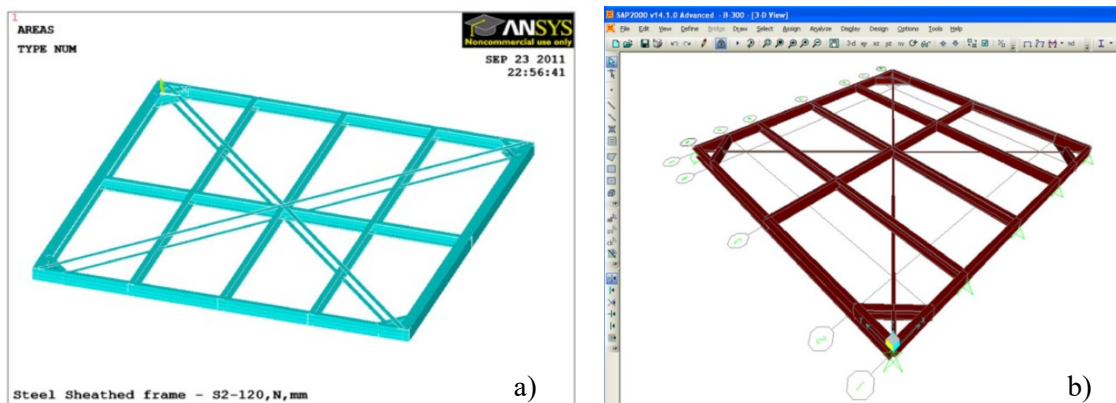


Fig. 1.5 Strap-braced wall modelled in (a) Ansys and (b) in SAP (Zeynalian and Ronagh, 2012)

Mirzaei et al. (Mirzaei *et al.*, 2015) experimentally studied high-aspect-ratio walls with welded connections and gusset plates. Alongside they developed simplified numerical models (Fig. 1.6) to determine the moment demand in the chord studs. The walls were simulated, by adopting simple truss elements, assuming fixed connections everywhere, except for the braces’ ends, where pins were employed. The compressive strap and the intermediate studs were omitted, and the corners of the bottom track were fixed. Since the loading was monotonic, modelling the hysteretic behaviour was not necessary.

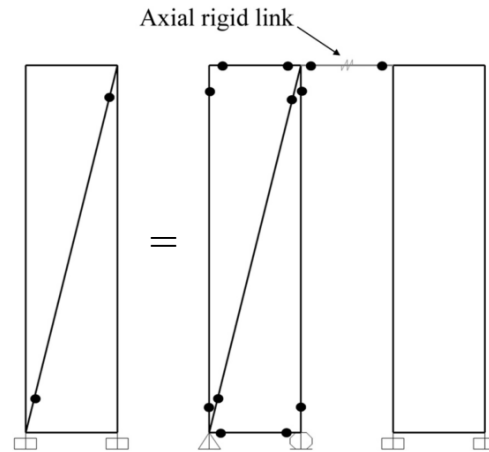


Fig. 1.6 Model of high-aspect ratio shear wall (Mirzaei et al., 2015)

Gerami et al. (Gerami *et al.*, 2015) developed a numerical model in ABAQUS (see Fig. 1.7) to study the nonlinear behaviour of strap braces under monotonic and cyclic loading. After they validated their model against experimental results found in (Al-Kharat and Rogers, 2007) they conducted a parametric study of frames with different arrangements. To achieve this, MSC PATRAN-NASTRAN software was used by employing standard 4-noded (CQUAD 4) elements and a mesh size of 20 mm. For the non-linear material definition, the Von Mises yield surface was adopted.

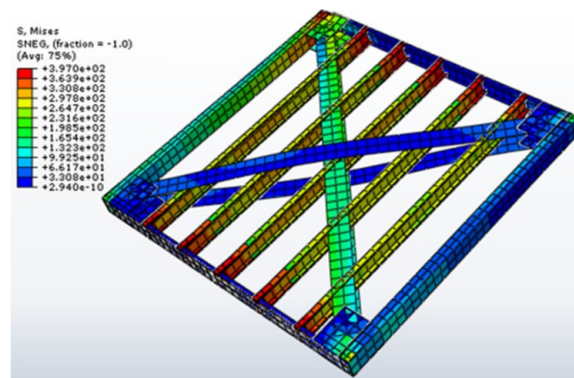


Fig. 1.7 Strap-braced wall model (Gerami *et al.*, 2015)

In their effort to define behaviour factors of CFS strap-braced walls, per FEMA P695 rules (ATC, 2009), Fiorino et al. (Fiorino *et al.*, 2017) developed a single strap-braced wall model in OpenSees (Mazzoni *et al.*, 2007) (Fig. 1.8). For the representation of the diagonal straps, “Truss” elements were used, while for the chord studs, “elastic beam-column” elements were adopted. The “pinching4” material model, able to capture their hysteretic behaviour, was assigned to the straps and a “Uniaxial elastic” material to the chord studs. The parameters of the hysteretic model were defined based on experimental results (Iuorio *et al.*, 2014). The connections to the ground were modelled with “Zero Length” elements, being assigned appropriate stiffness values in tension and compression derived from experiments.

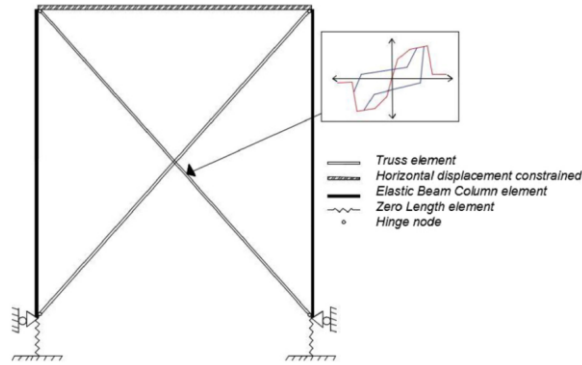


Fig. 1.8 Strap-braced wall model (Fiorino et al., 2017)

Based on the experimental results of strap-braced shear walls, Velchev (Velchev, 2008b) performed nonlinear dynamic analyses of 5, 4 and 2-storey CFS frames, using scaled earthquake time histories. The objective was to derive inter-storey drifts, seismic force modification factors and define building height limits for such systems. The simplified numerical model (Fig. 1.9) assumed lumped masses representing each storey, which were connected with spring elements, allowing for shear deformations only. P- Δ effects were considered by adopting a fictitious column, which was an axially rigid element with no flexural stiffness, connected to each storey through rigid links. The hysteretic behaviour of the walls was expressed through the “bi-linear with slackness” hysteretic model (Fig. 1.10), adopted from (Carr, 2007), which is suitable to diagonally braced systems, considers a slackness of the braces, occurring when they are stretched after yield. Moreover, it considers pinching and strain hardening, but no strength degradation (Velchev, 2008b). Modelling and analyses were performed with the program RUAUMOKO (Carr, 2007).

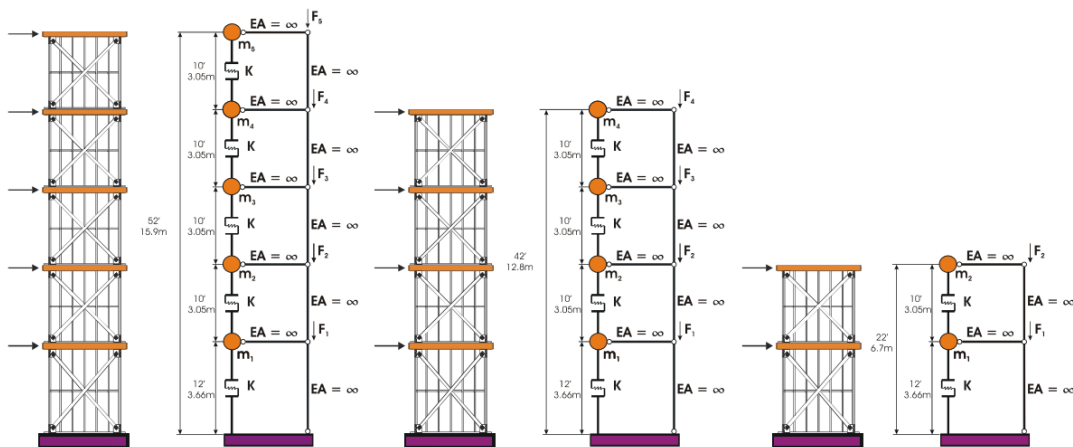


Fig. 1.9 Modelling of 2D CFS strap-braced frames (Velchev, 2008b)

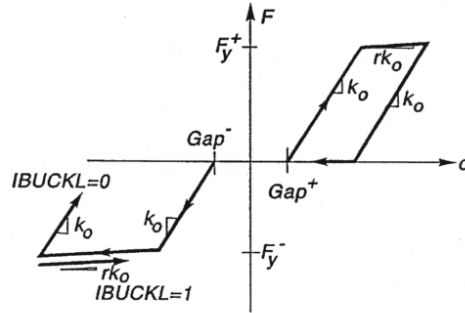


Fig. 1.10 The “bi-linear with slackness” hysteretic model adopted in (Velchev, 2008b)

A further development of the model was made by Comeau et al. (Comeau *et al.*, 2010), who incorporated in the model the chords and the diagonal straps (Fig. 1.11). Their aim was to confirm the soundness of AISI S213 design guidelines for CFS buildings, of Limited Ductility and Conventional Construction.

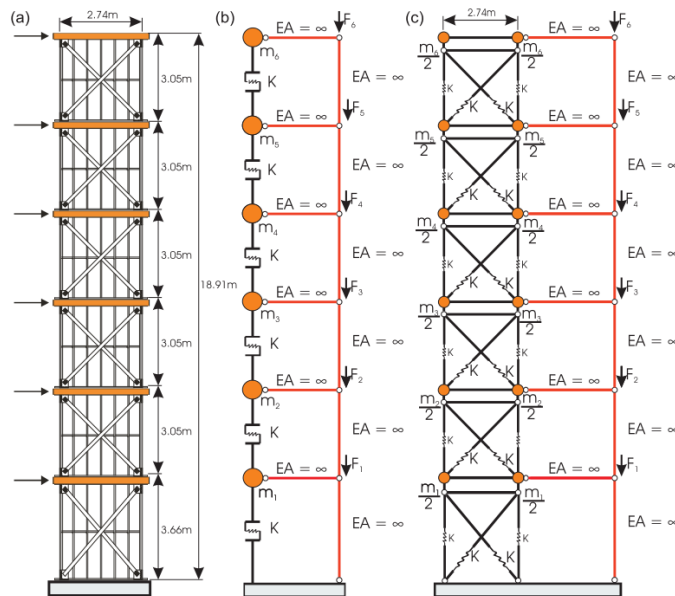


Fig. 1.11 Modelling of 2D CFS strap-braced frames (Comeau *et al.*, 2010)

Using the same concept as for the single strap-braced wall model Fiorino *et al.*, (2017) created 3D models in OpenSees of one to four-storey buildings, being regular in plan and elevation, and performed nonlinear static and nonlinear Incremental Dynamic Analyses, following the FEMA P695 (ATC, 2009) guidelines. The model included all features of the single wall model, with the addition of frame elements added in the direction of the seismic action to incorporate P- Δ effects. These frames comprised axially elastic “beam-column” elements with pins at the top and the bottom, connected with the building through rigid elements (Fig. 1.12).

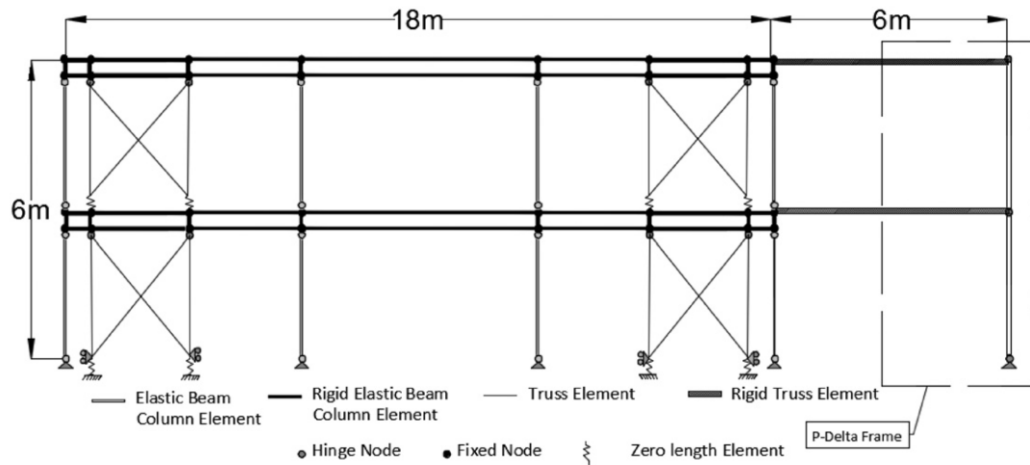


Fig. 1.12 A frame, being part of the 3D model (Fiorino et al., 2017)

1.2.3 Performance-based seismic design methodologies of building systems

In recent years, seismic design methods of structures are shifting to a new approach, the so-called “performance-based seismic design” concept, according to which a structure is designed in such a way as to achieve specific performance objectives (Fajfar and Krawinkler, 2004). Hence, the intended non-linear response and final design of structures are determined by limits imposed to performance criteria, such as element inelastic deformation demands or global parameters, such as drift (PEER, 2010). Modern seismic design codes, e.g. (FEMA 356, 2000; ASCE, 2017), define damage control limits for various performance levels (i.e. operational, immediate occupancy, life safety, and collapse prevention) and different seismic hazard levels (i.e. occasional, rare and maximum), depending on the buildings’

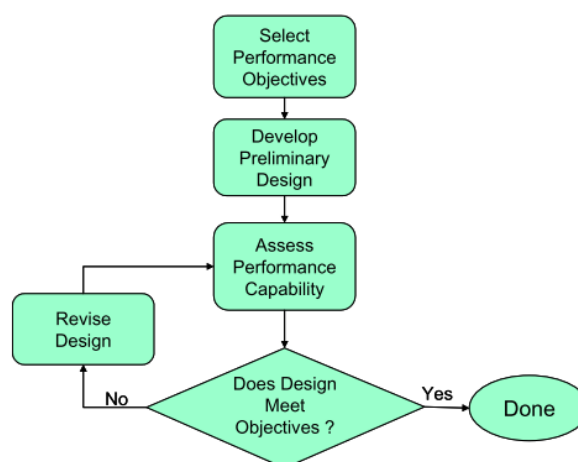


Fig. 1.13 Performance-based design process (Hamburger, 2004)

use and importance class. Hamburger (Hamburger, 2004) summarises the performance-based design process in the flowchart shown in Fig. 1.13.

The process starts with the definition of one or more performance objectives. For example, a residential building could be designed to be operational after an earthquake of low intensity and not collapse after an earthquake of the maximum intensity. At the second stage, a preliminary design is performed to define all the necessary features which could affect the seismic performance of the building (Hamburger, 2004). Such features include the structural system, materials, site characteristics, foundation, and non-structural components, vital to the operation of the building, depending on its use and importance.

The evaluation of the performance of a building is the next step of the process and commences with the definition of the seismic hazard at the site through intensity measures (IM), such as the peak ground acceleration, peak ground velocity or peak ground displacement (Deierlein, 2004; Maio and Tsionis, 2015). The intensity measures should accurately reflect the seismic characteristics of the site, and therefore should be selected very carefully. In this respect, artificial or real accelerograms can be used (Maio and Tsionis, 2015).

Performing static or dynamic non-linear analysis under the seismic excitation, expressed by the intensity measures, results in damage both at the local element- and the global building level; hence there is a need to define appropriate damage thresholds for the damage states, corresponding to different performance limit states (D'Ayala *et al.*, 2015). To evaluate damage, "Engineering Demand Parameters (EDPs)" are used, usually expressed by quantities, such as inter-storey drift, roof displacement, plastic hinge rotation, and peak storey ductility (Vamvatsikos and Cornell, 2002; D'Ayala *et al.*, 2015). The thresholds of these EDPs can be either obtained by current seismic codes, such as ASCE/SEI 41-17 (ASCE, 2017) or can be custom-defined by non-linear modelling (D'Ayala *et al.*, 2015). The performance of the building can be evaluated through fragility curves, which indicate the probability of an EDP exceeding different performance levels for a given seismic hazard level. Fragility curves can be derived using several analytical methodologies, some of which are: (a) Non-linear dynamic analysis, (b) Non-linear static analysis, (c) Non-linear static analysis based on Simplified Mechanism Models (SMM-NLS) and (d) Linear static analysis (D'Ayala *et al.*, 2015; Maio and Tsionis, 2015). Non-linear dynamic analysis is the most complex, but it provides the highest degree of accuracy. The most common method following this approach is the "Incremental Dynamic Analysis" (IDA) (Vamvatsikos and Cornell, 2002), where a structural model is subjected to various ground motion records, which are scaled to represent seismic events of different intensities. Guidelines on the development of fragility functions using Incremental Dynamic Analysis can be found in (ATC, 2009; FEMA, 2012).

1.2.3.1 Application of performance-based seismic design methodologies in CFS strap-braced structures

Performance-based seismic design of cold-formed steel buildings is still an unexplored field. Until recently, seismic codes did not contain explicit guidelines regarding the performance limits of CFS structural systems. FEMA 355F (FEMA, 2000b) contains performance-based design and evaluation guidelines for steel moment frame buildings. FEMA 356 (FEMA, 2000c) also contains performance-based design provisions and performance limits for many structural typologies, including moment-resisting and braced steel frames. These limits, however, are intended for hot-rolled steel structures, and their use for CFS frames is not justified. ASCE/SEI 41-17 (ASCE, 2017), which contains requirements for evaluating and retrofitting existing buildings, provides ductility performance limits for CFS strap-braced frames.

Lee and Foutch (Lee and Foutch, 2010) employed the guidelines of FEMA 355F (FEMA, 2000b) to two, four and six-storey CFS brace-framed buildings, based on the full-scale two-storey test results found in (Kim *et al.*, 2006). The study aimed to evaluate their performance and validate the use of the R factors in the code. By performing a Modified Incremental Dynamic Analysis process, they found that the evaluated collapse drift capacities were too conservative. Hence, they adopted the energy-equivalent elastoplastic analogy (EEEP), as suggested in (Ding and Foutch, 2004), to define a more reasonable value. The numerical models were developed in DRAIN-2DX (Prakash *et al.*, 1993) and included features, such as the hysteretic response of the gypsum walls. The four and six-storey buildings failed to reach the “Collapse Prevention” performance level of 2% in the 50 years hazard level with a confidence level of 90%. The performance target was reached after making the top storey stiffer. Finally, the R factor of 4 was found to be adequate for this structural system.

Davani *et al.* (Davani *et al.*, 2016) applied Incremental Dynamic Analysis to derive fragility curves for strap-braced stud walls. They evaluated the performance of 9 full-scale wall specimens found in (Moghimi and Ronagh, 2009) against different ground motions and performance levels. Performance limits were allocated to each performance level based on damage observations found in the literature. Their conclusions were based on the correlation of the peak ground acceleration (IM) to the maximum inter-storey drift ratio (EDP). They showed that cladding and the use of corner brackets could have a beneficial contribution to the lateral load capacity and stiffness of strap-braced wall systems, diminishing the occurrence of damage.

Fiorino *et al.* (Fiorino *et al.*, 2017) applied FEMA P695 (ATC, 2009) to assess the behaviour factor for CFS strap-braced stud wall building systems. The set of archetypes included residential and office buildings, having a maximum height of 12 m and being regular in plan and elevation. Three seismicity zones were considered, low, medium and high. Using fragility curves and measuring the collapse

fragility, they confirmed the suitability of the system for seismic applications. However, the studied structures exhibited a relatively low behaviour factor (q) around 2.5.

1.2.4 Full-scale tests and numerical modelling of CFS beam-column connections

The lateral performance of CFS moment-resisting frames relies on the beam-column joints, which predominately employ bolted gusset plates, connecting the webs of the connecting parts. However, these systems, especially in seismic-prone regions, are limited to single-storey, portal-frame buildings because of the challenges associated with their resilience and ability to prevent premature local failure of the members.

1.2.4.1 CFS beam-column connections of single-storey buildings

Early experimental tests (Chung and Lau, 1999; Wong and Chung, 2002) demonstrated that these connections could reach a bending moment resistance between 42% and 84% of the moment capacity of the beam and classified as semi-rigid regarding their rotational stiffness. The most ductile failure mode was due to bearing, but it happened at a low load level, which was unfavourable. Dubina *et al.* (Dubina *et al.*, 2009) tested eaves and apex portal frame joints and observed initial hole elongation due to bearing, while failure occurred due to local buckling of the beam web. However, no hole elongation appeared when the flanges were connected alongside the webs, and the failure mode shifted to the local buckling of the compression flange, followed by the beam web. A similar study of web-connected eaves and apex joints (Lim and Nethercot, 2003) showed that premature local buckling of the web reduced the transverse bending stiffness of the cross-section, resulting in buckling of the compression flanges. Full-scale tests of portal frames (Dubina *et al.*, 2009) indicated that local buckling could lead to a rapid strength loss, attributed to the reduced bending moment capacity of the buckled members. Zhang *et al.* (Zhang *et al.*, 2016) tested three full-scale portal frames and reached the conclusion that the stiffness of the apex and eaves connections is associated with the bolt tightness and the gusset plate dimensions. Blum and Rasmussen (Blum and Rasmussen, 2019) quantified the stiffness of the connections based on experimental results, while Bučmys *et al.* (Bučmys *et al.*, 2018) used the component method and experimental results to derive an analytical formula for the stiffness calculation of beam-column connections. Similarly, Rinchen and Rasmussen (Rinchen and Rasmussen, 2019) derived simplified relations for modelling the stiffness of portal frame connections. Finally, in a recent study Mojtabaei *et al.* (Mojtabaei *et al.*, 2021b) established capacity design equations for portal frame connections subject to combined axial and shear forces alongside bending moments.

CFS web-connected beam-column connections have fundamental differences compared to their hot-rolled counterparts. They transfer shear forces and bending moments through the webs without the

flanges' contribution, affecting both their strength and stiffness. Local stress concentration and instabilities arising due to this function further reduce the capacity of the connection (Mojtabaei *et al.*, 2020).

1.2.4.2 CFS beam-column connections of multi-storey buildings

Research on CFS web-connected joints intended for multi-storey buildings goes just a decade back and is still limited. In the experimental study of Sabbagh *et al.* (Sabbagh *et al.*, 2010), a connection for use in CFS multi-storey frames was developed, employing hollow-section columns filled with concrete and a bolted gusset plate connecting the beam. It reached a rotation greater than 0.04 rad and a bending moment capacity of 80% of the plastic moment. Two follow-up research works (Sabbagh *et al.*, 2012, 2013) performed experimental and numerical studies of CFS web-connected joints. Regarding their bending moment capacity and stiffness, per Eurocode 3 (CEN, 2005), the connections were categorised as partial or full-strength and rigid, respectively. Curved-flange beams and stiffeners increased the bending moment capacity by 35%, the ductility by 75% and the energy dissipation by 240%. The numerical model included initial geometric imperfections and slip-bearing action of the bolts. A similar study (Serror *et al.*, 2016) reported an improvement in the connection's performance, while the gusset plate remained elastic with the plastic hinge forming in the beam. Shahini *et al.* (Shahini *et al.*, 2018) proposed a circular arrangement with slotted holes, employing a friction-slip mechanism (Fig. 1.14). It was shown that the system was effective in eliminating local buckling failure modes or delaying them to appear after a 0.02 drift angle value.

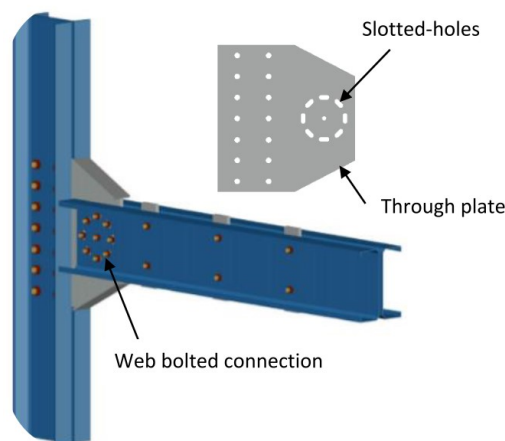


Fig. 1.14 Connection configuration proposed by Shahini *et al.* (Shahini *et al.*, 2018)

Ye *et al.* (Ye, Mojtabaei and Hajirasouliha, 2019) developed CFS web-connected beam-column joints', detailed numerical models, and studied how key design parameters, as the shape and thickness of the beam's cross-section, the plate slenderness and the bolt arrangement, affected the cyclic performance. A friction-slip fuse mechanism was proposed and studied, and the results were compared to similar

connections, where the bolt slippage was prevented. It resulted in the improvement of the ductility, energy dissipation and damping coefficient by 200%.

1.3 Scope of research

This study provides a better understanding of the complex non-linear behaviour of CFS lateral force resisting systems, such as strap-braced stud walls and beam-column moment connections, through detailed experimentally validated numerical simulations. For the strap-braced systems, the key design parameters are identified, and a performance-based design methodology is developed and evaluated at the wall and the structural level, leading to more efficient, ductile and resilient multi-storey frame systems. For the CFS moment-resisting systems, new beam-column connection types are proposed, and practical design considerations for balanced seismic performance are presented.

1.4 Aims and objectives

This research aims to study the response of cold-formed steel (CFS) lateral force-resisting systems, i.e. strap-braced stud walls and beam-column moment-resisting joints under lateral loading, and to develop and propose design considerations to improve their performance, efficiency, and resilience. The work will comprise the following main objectives:

1. Extensively study the non-linear lateral behaviour of cold-formed steel (CFS), strap-braced stud walls, identify the key design parameters and investigate ways to improve the system's efficiency.
2. Develop a practical methodology for the seismic design of CFS strap-braced stud wall frames under vertical loading, accounting for the secondary moments developed due to P- Δ effects.
3. Investigate the efficiency of the proposed design methodology compared to the conventional methods by studying the performance of CFS multi-storey strap-braced frames and quantifying damage at the structural level.
4. Develop new types of CFS beam-column moment-resisting connections capable of transferring the loads through the beam and column flanges or a combination of flanges and webs, and propose practical design considerations to reach the best overall performance and satisfy different seismic performance levels.

1.5 Tasks and methodology

In order to achieve the research objectives, the following methodology was followed:

1. Detailed numerical models of CFS strap-braced stud walls were developed in ABAQUS, accounting for material nonlinearity, initial geometric imperfections, non-linear behaviour of the connections and secondary moments due to P- Δ effects, and validated against previous experimental results on full-scale wall systems. A comprehensive parametric study was performed, using the validated models to study the effect of key design parameters, as the number of studs, the presence and intensity of vertical loading, the thickness of the structural elements and the steel grade of the straps, on the lateral performance of the system. The different design solutions corresponding to each of these variables were rated relative to their ability to improve the performance and the material efficiency, proposing and employing an “Efficiency index”, and performance-based design recommendations were provided (Objective 1).
2. The detailed FE models, which were developed in ABAQUS and validated against experimental results in the literature, were adopted to investigate the lateral-load capacity and ductility under the variation of strap thickness alongside the intensity of the vertical loading. Based on their responses, design formulae were derived, and a preliminary design methodology was proposed for predicting the lateral load capacity and ductility of single strap-braced stud walls under different element thicknesses and vertical loading ratios. The efficiency of the methodology in the design of multi-storey systems was demonstrated through a case study, 6-storey CFS frame, designed in accordance with Eurocode 8 specifications and the proposed methodology (Objective 2).
3. Detailed experimentally validated FE models of CFS wall panels were developed in ABAQUS under different loading conditions and used to obtain equivalent hysteretic models of the CFS strap-braced frames in OpenSees. Subsequently, the seismic performance of CFS 6-storey case study frames was studied under a set of spectrum-compatible artificial and real ground motion records. Finally, the efficiency of the Eurocode 8 and the proposed design methodology was assessed based on ASCE/SEI 41-17 ductility limits, wall ductility capacities derived by ABAQUS analyses and global damage indices (Objective 3).
4. Detailed Finite Element models of beam-column moment-resisting joints were developed in ABAQUS, accounting for material nonlinearities and initial geometric imperfections, and were validated against the results of available experimental tests. The validated FE models were then employed for a comprehensive numerical study of web-connected and newly developed flange and web-flange connected joints. The aim was to investigate the effects of key design parameters, including beam thickness and gusset plate shape and thickness, on the moment-rotation behaviour. The connection types exhibiting the best overall performance in terms of bending moment capacity, ultimate rotation and rotational rigidity were identified for each connection configuration and studied under cyclic loading. Finally, the performance of those

selected connection configurations was compared in terms of ductility, energy dissipation and equivalent damping coefficient and design recommendations were made (Objective 4).

1.6 Thesis layout

The thesis comprises six chapters. Chapters one and six are written in a conventional format, whereas chapters two to five are written in journal format as standalone papers.

1.6.1 Chapter 1

Introduction

This chapter presents an introduction to the research work, with a description of the research problems and motivation, followed by the scope of the research, the aims and objectives, the followed methodology and the thesis layout. Included is also a background review on the following topics:

- Full-scale tests of CFS strap-braced shear walls under lateral loads.
- Numerical modelling of CFS strap-braced walls and building systems.
- Performance-based seismic design methodologies of building systems.
- Full-scale tests and numerical modelling of CFS beam-column connections.

1.6.2 Chapter 2

Performance-based assessment of CFS Strap-braced stud walls under seismic loading

This chapter describes the development of the strap-braced wall numerical model in ABAQUS and the validation process by comparing the results between the FE models and the experimental tests. The non-linear performance of the walls, affected by critical design parameters, is evaluated and thoroughly discussed, and the most important are identified. Finally, the efficiency of each design parameter in terms of combining maximum performance and optimal material use are investigated by the definition of an “Efficiency Index”.

1.6.3 Chapter 3

More efficient design of CFS strap-braced frames under vertical and seismic loading

This chapter describes the adopted numerical model of the strap-braced wall in ABAQUS, the verification against experimental test results and the comprehensive parametric study of the effect the diagonal strap thickness and the vertical loading ratio have on the system's lateral performance. Next, based on the results, design equations to calculate the lateral load and ductility capacities under vertical and lateral loading are derived, and the proposed methodology is described. Finally, the efficiency of the proposed methodology is demonstrated through the design of a case study CFS 6-storey frame compared against the design provisions of Eurocode 8.

1.6.4 Chapter 4

Performance-based seismic design and assessment of multi-storey CFS strap-braced frames

This chapter starts with a description of the proposed design methodology under vertical loading and the 6-storey frame design solutions developed in Chapter 3. Next, the adopted numerical model in ABAQUS and its validation are presented, followed by developing the 6-storey frame model in OpenSees. The modelling parameters and the definition of the hysteretic “Pinching4” material model are thoroughly discussed, alongside the verification of its accuracy. The steps of non-linear time-history analysis are explained, i.e. the selection of spectrum-compatible artificial and real ground motion records, the performance levels and finally, the efficiency and reliability of the design solutions are evaluated through code limits and damage indices.

1.6.5 Chapter 5

Cold-formed steel beam-to-column bolted connections for seismic applications

In this chapter, the development of CFS beam-column moment-resisting joints in ABAQUS is described. First, the modelling assumptions alongside the validation against experimental test results from the literature are provided in detail. Then, the numerical model in ABAQUS is adopted, and the behaviour of web-connected, flange connected, and web-flange connected joint configurations under monotonic loading is presented. Based on the results, design recommendations are proposed for each configuration to identify and select the connections with the most desirable seismic characteristics, combining high moment capacity, ultimate rotation, and rotational rigidity. Finally, the efficiency of

those selected connection configurations is evaluated under cyclic loading based on their ductility, energy dissipation and equivalent damping coefficient.

1.6.6 Chapter 6

Conclusions and recommendations for future work

This chapter summarises the research work, presents general conclusions and provides recommendations for future work.

CHAPTER 2

Performance-based assessment of CFS strap-braced stud walls under seismic loading

This chapter is based on the published paper titled: “I. Papargyriou, I. Hajirasouliha, J. Becque, K. Pilakoutas, Performance-based assessment of CFS strap-braced stud walls under seismic loading”, Journal of Constructional Steel Research, 183 (2021) 106731.

2.1 Abstract

The use of cold-formed steel (CFS) systems has significantly increased in the past few decades, especially in the construction of low to mid-rise buildings. Compared to hot-rolled sections, CFS members are often more economical and efficient due to their low weight, ease and speed of construction and greater flexibility in manufacture. In most conventional CFS buildings, diagonally strap-braced stud walls provide the primary lateral force-resisting system. This study aimed to develop a better understanding of the structural behaviour of CFS strap-braced stud wall systems under seismic loading. To achieve this, a detailed numerical model was developed, accounting for material nonlinearity, initial geometric imperfections, nonlinear behaviour of the connections and secondary moments due to P- Δ effects. This model was validated against previous experimental results on full-scale wall systems. A comprehensive parametric study was then conducted using the validated model to investigate the effect of key design parameters, namely the number of studs, the presence and intensity of vertical loading, the thickness of the structural elements and the steel grade of the straps, on the seismic performance of the system. The lateral load-resisting capacity, deformation capacity, ductility and energy dissipation under lateral loading were investigated and are here discussed. An efficiency index was proposed for each of these variables, allowing design solutions to be rated in terms of their ability to improve the

material efficiency of the system, and design recommendations were derived for performance-based design.

2.2 Introduction

The use of cold-formed steel (CFS) has gained increased popularity in structural applications in recent years, offering an efficient alternative to hot-rolled steel construction. Structures made of CFS have many advantages compared to their hot-rolled counterparts, such as being lightweight, resilient, sustainable and cost-effective.

CFS buildings typically rely on load-bearing stud walls to transfer gravity loads down to the foundation as line loads. These stud walls are invariably clad on both sides with various materials (e.g. gypsum board, OSB, plywood) and their behaviour under lateral loading is summarised in a study by Sharafi et al. (Sharafi *et al.*, 2018). This sheathing participates in resisting in-plane lateral forces through its diaphragm stiffness and also increases the axial capacity of the vertical steel elements by increasing their resistance against global, local and distortional buckling (Dubina *et al.*, 2012). However, current design standards such as Eurocode 3, Part 1-3 (CEN, 2003) do not contain design provisions to account for composite action between the studs and the sheathing, instead necessitating an “all-steel” design approach. In this case, it is necessary to use bracing members to resist lateral forces, for example, in the form of X-shaped strap braces.

Strap-braced stud walls, which are the focus of this study, consist of a steel frame made up of top and bottom tracks, intermediate studs and chord studs, and diagonal straps (Iuorio *et al.*, 2014). Generally, a bridging element is also used at the wall mid-height to reduce the buckling length of the vertical elements. An example is provided in Fig. 1. In this system, the lateral forces are transferred from the straps to the chord studs, and through the hold-down devices to the anchor rods, eventually finding their way into the foundation. The straps experiencing compression are considered to yield no contribution to the lateral resistance, due to their high slenderness and ensuing susceptibility to buckling (Mirzaei *et al.*, 2015).

Over the past two decades, extensive experimental research has been carried out to study the behaviour of CFS strap-braced stud wall systems under monotonic and cyclic loading. In general, the parameters under investigation have included the lateral load capacity, the lateral stiffness, the deformation capacity (ultimate lateral displacement) and the energy dissipation capacity. Al-Kharat and Rogers (Al-Kharat and Rogers, 2007) conducted 16 experiments on three types of wall configurations, where they employed screwed connections which were chosen without applying any capacity design rules. Their results showed significant strength and stiffness degradation in the wall elements under cyclic loading. In a follow-up study, the same programme was repeated (Al-Kharat and Rogers, 2008), this time

following the connection design rules specified by ASCE 7-05 (ASCE, 2005). The design rules proved to be effective in preventing non-ductile modes of failure and significantly improved the lateral performance of the stud walls. This conclusion was independently verified by Velchev (Velchev, 2008b), based on the results of 30 wall specimens under monotonic and cyclic loading. Following a capacity-based design approach, Kasaeian et al. (Kasaeian *et al.*, 2020) experimentally tested and evaluated the lateral behaviour of six strap-braced wall configurations with fused straps. The tested specimens exhibited a ductile response, with yielding of the straps being the dominant failure mode.

Strap-braced walls with welded connections were the subject of a study by Comeau (Comeau, 2008) and Velchev et al. (Velchev *et al.*, 2010). The test specimens, designed following the AISI S213 (AISI S213, 2012) design rules, exhibited ductile behaviour, undergoing large inelastic deformations while maintaining their yield capacity. The dominant mode of failure was strap yielding. In other relevant studies, Mirzaei et al. (Mirzaei *et al.*, 2015), Comeau (Comeau, 2008), and Velchev et al. (Velchev *et al.*, 2010) compared the response of walls with different aspect ratios and showed that walls with aspect ratios of 1:1 and 1:2 generally exhibited a more ductile behaviour compared to those with an aspect ratio of 1:4, in which case the chord studs failed prematurely due to flexure and compression. Tian et al. (Tian *et al.*, 2004) and Moghimi and Ronagh (Moghimi and Ronagh, 2009) studied the capacity and stiffness of single-sided versus two-sided braced walls. Lu and Rogers (Lu and Rogers, 2018) studied the interaction of strap-braced walls with gypsum panel sheathing. They showed that attaching one or two layers of gypsum sheathing significantly increased the lateral capacity of the panels. However, Moghimi and Ronagh (Moghimi and Ronagh, 2009) concluded that due to the brittle behaviour of gypsum panels, they are unreliable in transferring lateral forces and can lead to an abrupt failure of the system. Kim et al. (Kim *et al.*, 2006) and Fiorino et al. (Fiorino *et al.*, 2019) conducted full-scale shaketable tests on two-storey and three-storey CFS strap-braced walls, respectively, aiming to investigate the dynamic response of these systems. The studies confirmed the adequacy and robustness of strap-braced walls as lateral load resisting systems. The tested systems were able to reach high strength and ductility at lateral displacements exceeding 2% drift, without significant damage.

While it is clear from the above that many studies have investigated the response of CFS stud-walls under lateral loads, few studies have been conducted on the response of these systems under additional vertical loading. Lange and Naujoks (Lange and Naujoks, 2007) tested cement-bonded chipboard sheathed walls under horizontal and vertical loading. Similarly, Accorti et al. (Accorti *et al.*, 2016) tested different types of stud walls under lateral and vertical loading and compared their structural response. Ye et al. (Jihong Ye *et al.*, 2016) also tested a series of sheathed stud walls in compression, to study the effect of various relevant parameters, in particular the type of sheathing, the stud cross-section, the stud spacing and the joint details. However, none of the above studies were conducted on CFS strap-braced walls (i.e. the lateral resistance was provided entirely by sheathing). Moreover, the effects of different

levels of vertical loading on the lateral response of the walls were not investigated. In one of the few studies on CFS strap-braced walls subject to vertical loads, Moghimi and Ronagh (Moghimi and Ronagh, 2009) concluded that if the chord studs can withstand the full load capacity of the straps, then a vertical load equal to 80% of the vertical load capacity of the studs does not affect the lateral capacity of the wall.

The highly nonlinear response of individual wall components poses a significant challenge for the numerical study of CFS systems, requiring detailed numerical models that rely on experimental data for their validation and calibration. Several studies have modelled stud walls sheathed with gypsum panels (Fiorino *et al.*, 2018), OSB panels (Buonopane *et al.*, 2015; Henriques *et al.*, 2017), glass panes (Van Lancker *et al.*, 2015), and steel sheets (Niari *et al.*, 2012; Attari *et al.*, 2016). However, detailed numerical studies on the monotonic and cyclic behaviour of unsheathed strap-braced stud walls are limited. Following an experimental programme on CFS walls reinforced with brackets at their corners, Zeynalian and Ronagh (Zeynalian and Ronagh, 2012) developed a numerical model that was validated against the test results. They then carried out a parametric study by varying the bracket length to determine the best arrangement. Gerami *et al.* (Gerami *et al.*, 2015) studied the nonlinear behaviour of strap braces under monotonic and cyclic loading on the basis of a wall specimen with welded connections taken from the experimental work by Al-Kharat and Rogers (Al-Kharat and Rogers, 2007). Whilst previous experimental studies on the lateral behaviour of individual CFS strap-braced walls have generally indicated their suitability for seismic applications, only limited information is available on the influence of different design parameters on this performance. Even less so has any knowledge in this regard been translated into practical recommendations and guidelines for seismic design. In conjunction with this, it is of paramount importance to develop reliable numerical tools to predict the structural performance of these complex systems under both monotonic and cyclic loading conditions.

This study aimed to develop a better understanding of the seismic behaviour of CFS strap-braced walls. To achieve this, detailed FE models of single strap-braced stud walls were developed in ABAQUS (Dassault Systèmes Simulia, 2014), based on full-scale tests from the literature, while taking into account initial geometric imperfections, material nonlinearity and secondary moments due to P- Δ effects. Available results from shear lap tests on screwed connections were used to develop the model for the nonlinear behaviour of the connections. The numerical models were validated against experimental results pertaining to monotonic as well as cyclic loading and were further employed in a comprehensive parametric study. The key design parameters were identified and were discussed in terms of their impact on critical performance criteria, namely the lateral load-bearing capacity, deformation capacity, ductility and energy dissipation of the system. Based on the definition of an Efficiency Index parameter, design recommendations are proposed to obtain the most efficient design solution, achieving maximum performance with minimum material use.

2.3 Description of the reference experimental tests

The numerical models developed in this study were based on wall specimens 25A-M-1 and 31A-M-1, tested under monotonic loading, and specimens 26A-C and 32A-C, tested under cyclic loading, reported by Velchev (Velchev, 2008b). These configurations were selected because they were deemed to be representative of typical wall systems used in practice, featuring simple connections. The wall measured 2744 mm in width by 2440 mm in height. Five intermediate studs were evenly spaced between the chord studs at 407 mm, while two additional studs were placed on the outside of the chords, as shown in Fig. 2.1.

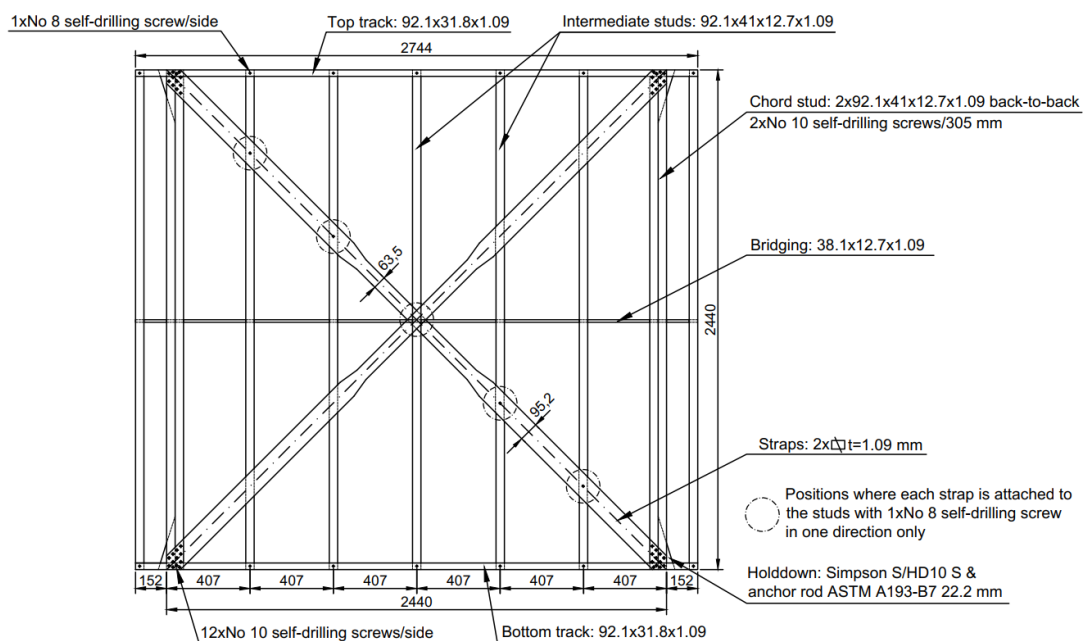


Fig. 2.1 Configuration of specimen 25A-M, tested by Velchev (Velchev, 2008b)

The chord studs consisted of two lipped channel cross-sections, connected back-to-back with 2 No.10-3/4" (19mm) wafer head self-drilling screws, placed every 305 mm along their height. The top and bottom tracks were extended by 152 mm beyond the chord studs to transmit the horizontal component of the diagonal strap force through tension (Velchev, 2008b). The walls belonged to the "Light" wall series, which featured screwed strap-to-chord stud and stud-to-track connections, without any gusset plates at the corners. The straps had a non-uniform cross-section along their length, with the middle part being of reduced width, forming a "fuse" to protect the connections from premature failure. Both walls shared the same geometric and material properties, apart from the fuse length. This length was 762 mm (short fuse) for the 25A-M-1 and 26A-C specimens and 1524 mm (long fuse) for the 31A-M-1 and 32A-C specimens (Velchev, 2008b). At mid-height of the wall, a bridging channel was used to reduce the buckling length of the vertical elements (see Fig. 1).

The hold-downs connecting the wall to the ground (bottom) and to the loading beam (top) were placed on the exterior side of the chords using four ASTM A193-B7 7/8” (22.2 mm) threaded anchor rods. Shear anchors along the top and the bottom tracks were of type ASTM A325 3/4” (19 mm). The straps were connected to the chord studs with 12 No. 10-3/4” (19mm) wafer head self-drilling screws at each end, and the studs were attached to the top and bottom tracks with a total of four No. 8-1/2 (12.7mm) wafer head self-drilling screws, one on each side of each track. One pair of straps, in one direction, was attached to the interior studs with No. 8 self-drilling screws, while the other pair was left unconnected.

The static and dynamic material properties were determined from coupon tests. A cross-head speed of 0.1 mm/min was selected to test the material of the vertical elements and the tracks. The strap material specimens were tested at two different cross-head speeds of 0.1 mm/min and 100 mm/min, representative of the rates in the monotonic and cyclic wall panel tests, respectively.

Table 2.1 summarises the outer cross-section dimensions and the nominal and base metal thicknesses of the straps, studs and tracks, along with their yield stresses and ultimate tensile strengths.

Table 2.1 Element thicknesses and material properties

Element	Cross-section dimensions (mm)	Cross-head rate (mm/min)	Nominal Thickness (mm)	Base metal Thickness (mm)	Yield stress f_y (MPa)	Ultimate stress f_u (MPa)
Straps	95.2	0.1	1.09	1.11	296	366
	(63.5 for fuse)	100			314	377
Studs/Chords	92.1×41×12.7	0.1	1.09	1.16	325	382
Tracks	92.1×31.8	0.1	1.09	1.11	296	366

2.4 Description of the ABAQUS models

In the analysis and design of complex, nonlinear systems, such as CFS lateral-force resisting systems, detailed numerical simulations provide an invaluable tool to assess their structural behaviour and failure modes (Usefi *et al.*, 2019, 2020). Detailed numerical models of the selected strap-braced walls were developed using the ABAQUS software (Dassault Systèmes Simulia, 2014), which has previously proved its effectiveness in accurately simulating the behaviour of CFS elements and structural systems (Jun Ye *et al.*, 2016; Mojtabaei *et al.*, 2018; Ye, Mojtabaei, Hajirasouliha, *et al.*, 2018). The general model, depicted in Fig. 2.2, accounted for material and geometric nonlinearity, nonlinear connection behaviour and initial geometric imperfections. The constituent elements of the wall were the top and bottom tracks, the intermediate studs, the chord studs, the bridging element at mid-height, the

connections of the studs to the tracks, the connections of the straps to the chord studs, the hold-downs and the anchor rods.

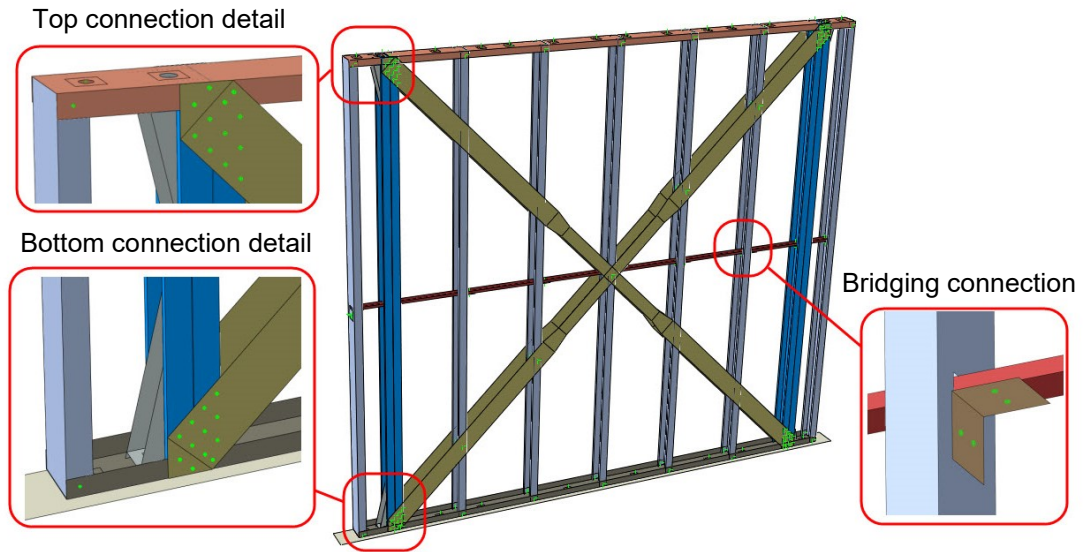


Fig. 2.2 Details of the developed Finite Element model

2.4.1 Material properties

The nominal (engineering) values of the stresses, σ_{nom} , and strains, ϵ_{nom} , obtained from coupon tests (Rogers, 2018) were converted to true stresses and true strains for input into ABAQUS (Dassault Systèmes Simulia, 2014). The modulus of elasticity, E , and the Poisson's ratio, ν , were 203 GPa and 0.3, respectively.

In the monotonic analyses the isotropic hardening rule was implemented, whereas in the cyclic analyses the linear kinematic hardening rule was applied.

2.4.2 Finite element type and mesh-size

The general-purpose, 4-noded "S4R" shell finite element was selected from the ABAQUS element library to model all the structural components of the wall panel. This element with 6 degrees of freedom per node supports reduced integration, hourglass control and finite membrane strains. It has been shown to be suitable for modelling thin-walled components, having yielded accurate results in previous studies (Jun Ye *et al.*, 2016; Kyvelou *et al.*, 2018; Ye, Mojtabaei, Hajirasouliha, *et al.*, 2018). For the anchor rods "standard linear beam" elements were employed. The mesh size for all parts was taken as 15×15 mm, apart from the base plate, which had a 20×20 mm mesh. Based on the results of a mesh

sensitivity analysis, these mesh sizes were found to provide results of satisfactory accuracy with acceptable computational effort. Fig. 2.3 depicts the lateral load-displacement curves for different mesh sizes. The difference in ultimate capacity between the 15×15 mesh and the coarser 20×20 mesh was less than 0.5%, leading to the conclusion that the results had converged. Due to the nevertheless substantial computing requirements, the analyses were performed using the High-Performance Computing (HPC) resource at the University of Sheffield.

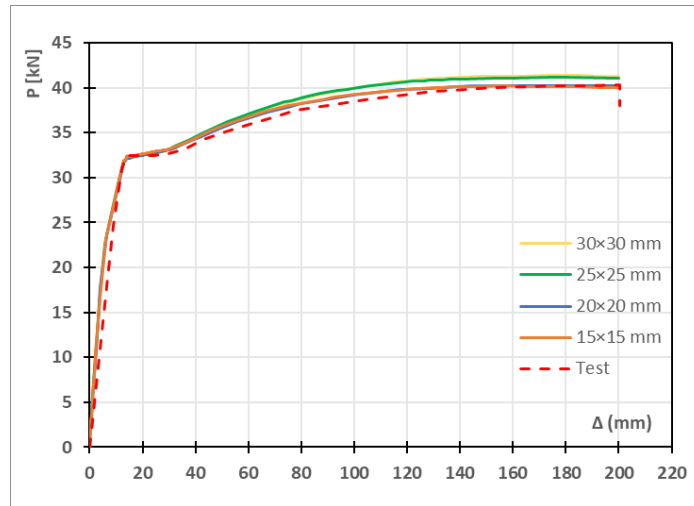


Fig. 2.3 Lateral load-displacement curves for different mesh sizes

2.4.3 Connection modelling

In general, the strength and stiffness of the strap-to-chord stud connections can significantly affect the response of the strap-braced wall system (Al-Kharat and Rogers, 2007). In order to prevent non-ductile premature failure in the strap-to-chord connection, it is necessary to follow the relevant design rules to ensure failure develops in the strap elements (Fiorino, Iuorio, *et al.*, 2016). The importance of this design approach was proven by Al-Kharat and Rogers (Al-Kharat and Rogers, 2008). Several research studies have experimentally investigated the structural behaviour and dominant failure modes of strap-to-chord stud connections in strap-braced wall systems e.g. (Tomà and Stark, 1978; Pekoz, 1990; Casafont *et al.*, 2006b, 2007a; Serrette and Peyton, 2009; Yan and Young, 2012). In this study, the equations proposed by Pham and Moen (Pham and Moen, 2015) were adopted to define the strength and stiffness characteristics of the connection. These relationships are based on the AISI S100-12 (AISI, 2012) equations but were modified using the results of a series of CFS shear-lap tests for a range of plate thicknesses and screw diameters. The equivalent monotonic response of the connections is described by three points, corresponding to 40%, 80% and 100% of the maximum capacity. Fig. 2.4 depicts the calculated force-displacement (P-Δ) curves, up to the peak load, of the connections with No. 8 and No. 10 self-drilling screws used in this study.

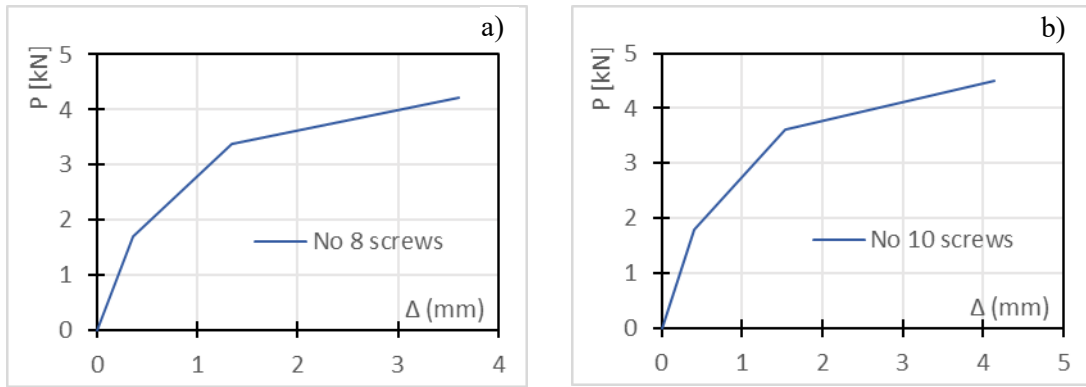


Fig. 2.4 Behaviour of a) No. 8 screws and b) No. 10 screws

To model the screwed connections, the “discrete fastener” capability of ABAQUS was used as a convenient way to connect surfaces (Fig. 2.5a). Each fastener layer uses a connector element, the nodes of which do not depend on the location of the nodes of the meshes on the connected surfaces. A local coordinate system is defined for each connector, with the z-axis being coincident with the connector axis. The connector has three translational and three rotational degrees of freedom. Fig. 2.5b depicts the implementation of such a fastener in the developed numerical model. Regarding the translational degrees of freedom, the movement along the z-axis was constrained while the movements along the x- and the y-axes followed the behaviour shown in Fig. 2.4. Rotations were free about the z-axis, and fully constrained about the x- and y-axes.

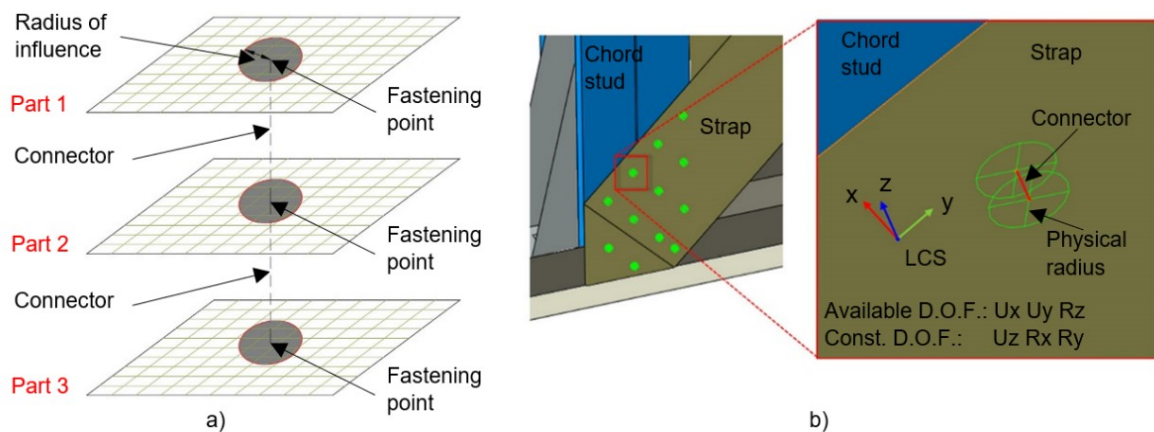


Fig. 2.5 a) ABAQUS fastener configuration, and b) Discrete fastener in the FE model

2.4.3.1 Validation of the connection model

The numerical model of the connections implemented in ABAQUS was validated against experimental results reported by Meza (Meza, 2018) and Meza and Becque (Meza and Becque, 2017). A series of shear lap tests on bolted and screwed connections were conducted, out of which two tests were selected

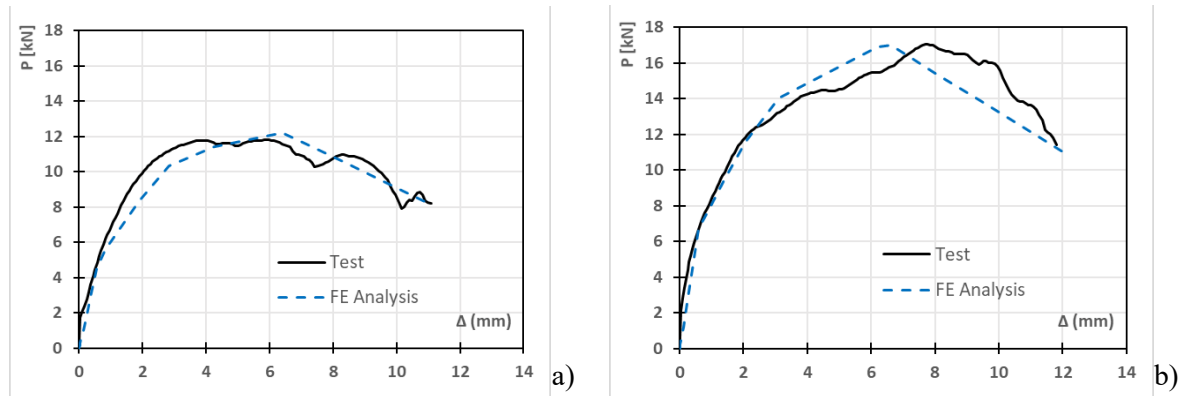


Fig. 2.7 Predicted and measured load-deformation curves of a) SL14-14c and b) SL20-14c

2.4.4 Boundary conditions

Fig. 2.8(a) and (b) depict the top and bottom boundary conditions of the stud wall panel for the case of lateral loading. In the reference experiment the top track was connected through a 25.4 mm thick aluminium plate to the loading beam, using shear anchors and anchor rods. Moreover, additional vertical columns constrained the out-of-plane displacements of the wall. To simulate these conditions the horizontal out-of-plane displacement (UX) and the rotations RY and RZ of the end points of the shear anchors and the anchor rods were restrained ($UX=RY=RZ=0$). Similarly, the connection of the bottom track to the testing frame was provided by shear anchors and anchor rods through an intermediate 25.4 mm thick aluminium plate. A plate consisting of shell elements with a high modulus of elasticity ($E=1 \times 10^6$ MPa) was used to simulate these boundary conditions in the FE models. The end points of the anchor rods and the shear anchors were fully fixed. In addition, the translational degrees of freedom of the bottom surface of the aluminium plate were all constrained ($UX=UY=UZ=0$). For the top plate, all degrees of freedom, apart from the vertical displacement, were constrained during the initial load step when the vertical load was applied ($UX=UZ=RX=RY=RZ=0$). During the next load step, in which the lateral load was applied, both the displacement along the Z-axis and the rotation about the X-axis were released (Fig. 2.8c).

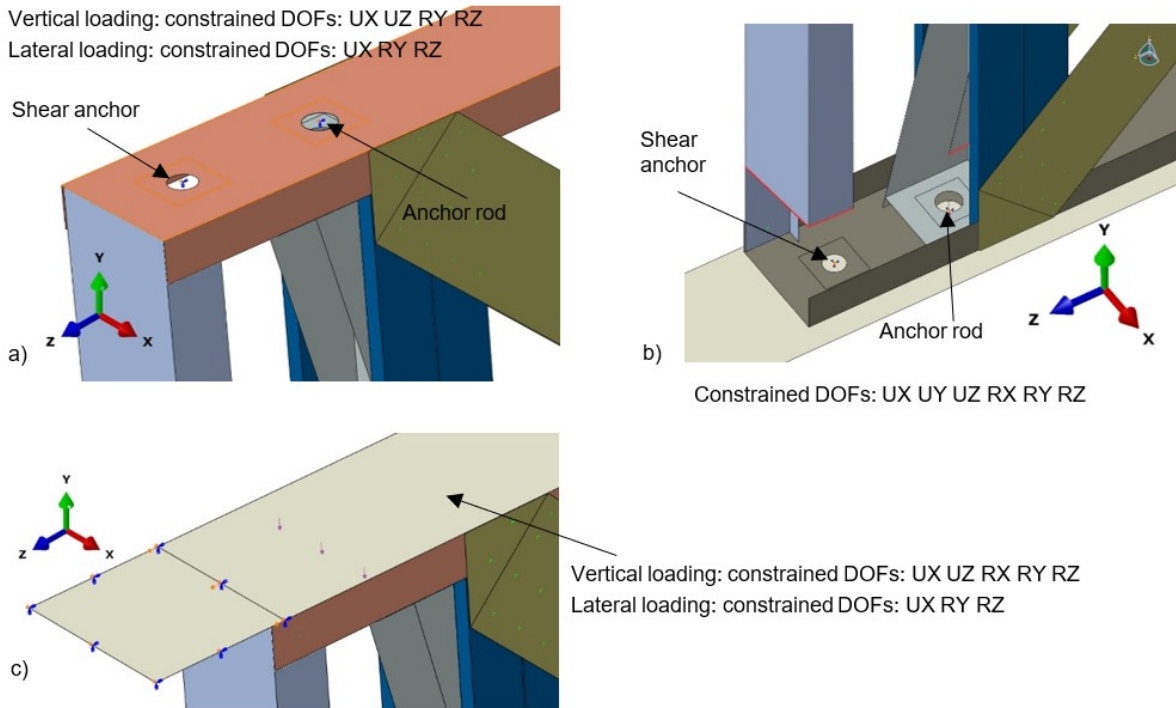


Fig. 2.8 a) Top track, b) Bottom track and plate and c) Top plate boundary conditions

2.4.5 Component interactions

The ABAQUS interaction module enables the definition of constraints, couplings and contact interactions between different regions of an FE model. Contact occurred in the model between the two channels of the built-up chord studs, which were connected back-to-back with No. 10 self-drilling screws, spaced at 305 mm along the height. Instead of simulating these connections explicitly, which would have increased the complexity of the model, tie constraints were used, as shown in Fig. 2.9a and Fig. 2.9b. The same approach was used for the Simpson S/HD10 S hold-down devices, which were connected to the chord studs with screws. It should be noted that these regions did not exhibit any damage in the tests.

The holes in the tracks at the positions of the anchor rods and the shear anchors were modelled explicitly in this study. At their centre, an attachment point was defined, to which boundary conditions and loads were applied. The displacements of this centre point were coupled to those of the surrounding region of the track through ‘continuum distributing’ coupling constraints, as shown in Fig. 2.9d.

Surface-to-surface contact was defined in the interface between a) the stud flanges and the tracks, b) the L-shaped brackets connecting the bridging and the studs (Fig. 2.2), and c) the bottom track and the base plate. In the normal direction, “hard” contact was specified, while in the transverse direction “frictionless” contact was employed.

At the centroids of the end cross-sections of the vertical elements (studs and chord studs), a reference point was defined, which was coupled to all nodes in the cross-section. Subsequently, a node-to-surface contact interaction between the end sections and the track surface was created, to allow for the transfer of vertical loads (see Fig. 2.9c).

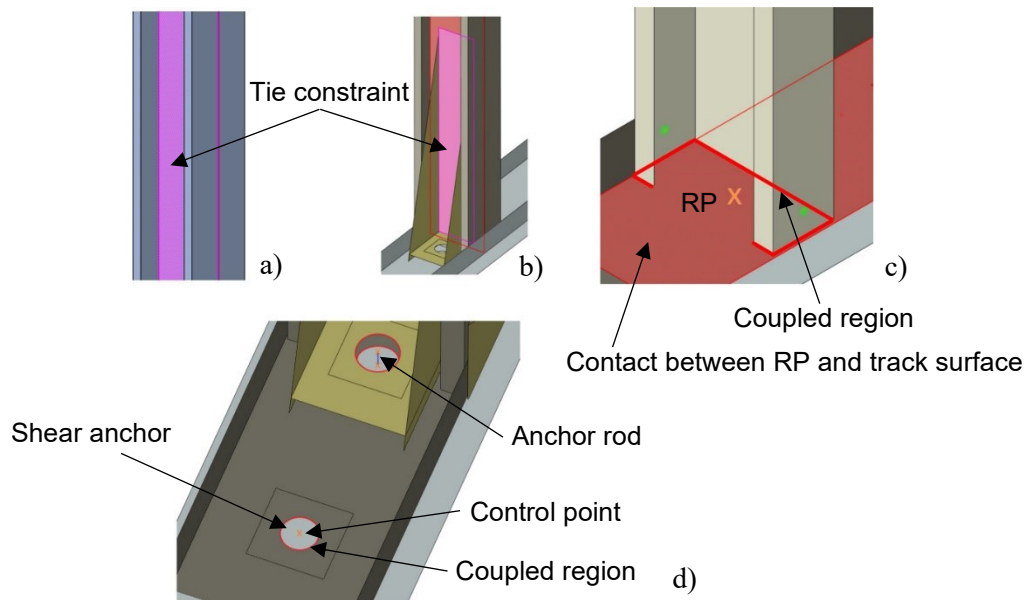


Fig. 2.9 Component interactions

2.4.6 Loading

The lateral load was applied through an imposed displacement at all nodes corresponding to the top anchor rods and shear anchors. Under monotonic loading, a maximum displacement of 300 mm was defined, whereas cyclic loading followed the reversed cyclic CUREE test protocol adopted in the experiments (Velchev, 2008b). The vertical load was applied at the top plate as a surface load, and constituted a certain fraction of the combined axial capacity of all vertical elements P_w , calculated according to Eurocode 3, Part 1-3 (CEN, 2003).

2.4.7 Initial Geometric Imperfections

In order to study the effect of geometric imperfections on the response of the wall panel, an eigenvalue buckling analysis was performed in ABAQUS (Dassault Systèmes Simulia, 2014) and the first mode was scaled to define the initial geometric imperfections, as recommended by Schafer and Peköz (Schafer and Peköz, 1998). In this analysis the nodes corresponding to the top anchor rods and shear anchors were given a unit lateral displacement, so that this induced compression in the pair of diagonal straps which experienced tension under monotonic loading or in the first cycle of the cyclic loading case. The

rationale behind this was to introduce some slackness into the tension straps. The amplitude of this imperfection was taken equal to one, two and three times the strap thickness in a number of preliminary analyses to assess the effects of an imperfection. However, the system under consideration showed itself to be highly insensitively to geometric imperfections, and no noticeable difference was observed in the ultimate capacity or ultimate displacement of the system (Fig. 2.10a). Similarly, introducing an imperfection into the chord stud in the shape of its lowest buckling mode with amplitudes of either $0.34t$ or $0.94t$ (with t_s being the stud thickness) (Schafer and Peköz, 1998) did not noticeably affect the capacity or behaviour of the system in analyses under vertical load levels of $0.3P_w$ and $0.44P_w$ (Fig. 2.10b).

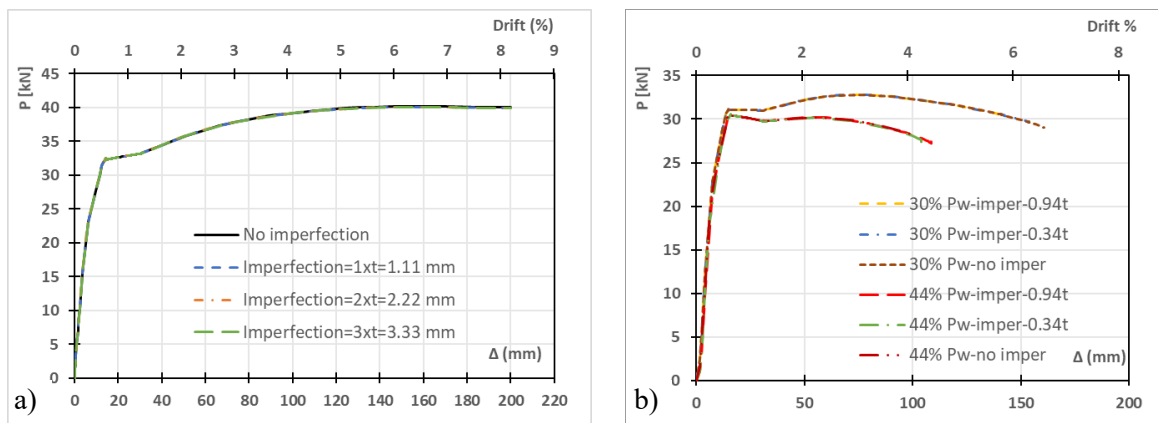


Fig. 2.10 Effect of a) strap imperfection and b) chord stud imperfection on the lateral response

2.5 Model validation

The accuracy of the developed numerical model in predicting the behaviour of the wall panel was first verified against experimental results pertaining to both monotonic and cyclic loading, obtained from (Velchev, 2008b).

2.5.1 Monotonic analysis

The wall panel specimens in (Velchev, 2008b) were designed in accordance with AISI S213 (AISI S213, 2012) and reached a drift of over 8%, ultimately limited by the maximum stroke of the actuator. The main failure mechanisms were yielding of the straps and distortional buckling of the chord flanges (Velchev, 2008b). Fig. 2.11a and Fig. 2.11b illustrate the lateral load-displacement curves of test specimens 25A-M-1 and 31A-M-1, respectively, and compare them to the FE analysis predictions. It is seen that the numerical model was able to accurately capture the overall experimental response of the walls, as well as critical parameters including the initial stiffness, the yield load P_y , and the maximum capacity P_u . The latter was predicted with less than 2.5% error.

Fig. 2.12 depicts the distribution of the von Mises stresses in specimen 25A-M-1 at the ultimate displacement. The numerical model accurately predicted distortional buckling failure at the bottom of the chord studs (circled in red), which is in agreement with the experimental results reported in (Velchev, 2008b).

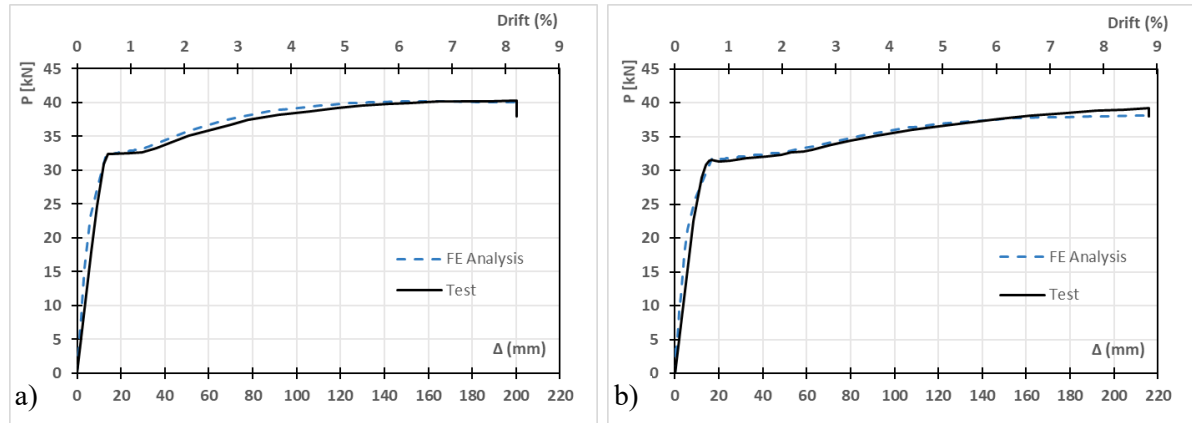


Fig. 2.11 Lateral load-displacement curves of a) 25A-M-1 and b) 31A-M-1 test specimens and corresponding FE analysis results

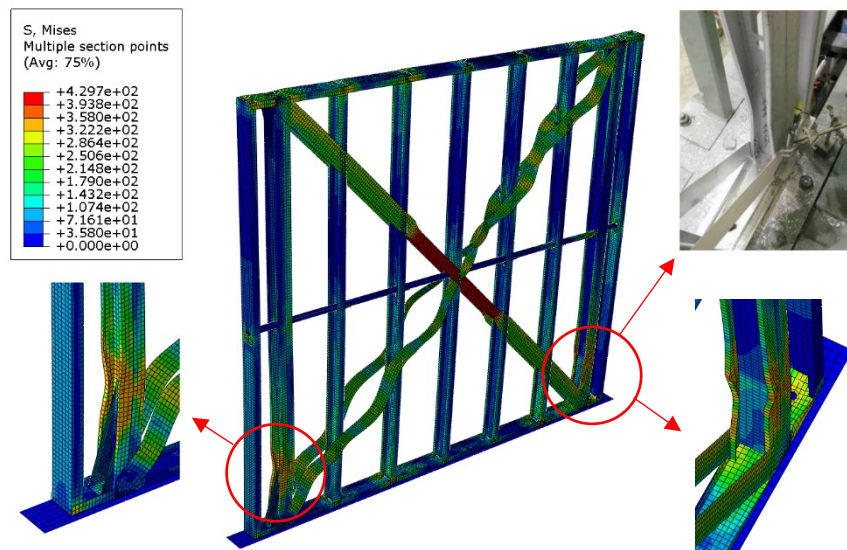


Fig. 2.12 Distribution of von Mises stresses and failure modes of test specimen 25A-M-1

2.5.2 Cyclic analysis

Test specimens 26A-C and 32A-C [8] were used for the validation of the FE model under cyclic loading. The same modelling techniques were employed as used for the corresponding monotonic test specimens, 25A-M and 31A-M. Fig. 2.13a and Fig. 2.13b illustrate the experimentally observed hysteretic behaviour of test specimens 26A-C and 32A-C, alongside the numerical predictions. The hysteretic

responses of the walls show significant pinching, without any noticeable strength or stiffness degradation. It can be seen that the FE model matched the experimental response throughout the whole history of repeated loading and unloading. However, after the load reached a maximum value within each cycle, a small drop in load was experimentally observed before unloading commenced, which the FE model did not capture. This response is likely attributed to the difference between the strain rate exercised in the material coupon tests and the higher strain rate experienced by the wall brace elements during the large displacement cycles in the actual tests, as stated in (Velchev, 2008b). The lower strain rates in the coupon tests resulted in lower values of the yield stress f_y (Yun and Gardner, 2017).

Both test specimens completed all cycles of the CUREE loading protocol. In the case of specimen 26A-C, the pair of diagonal straps connected to the intermediate studs failed due to net-section fracture at their mid-length at the end of the test. In the case of specimen 32A-C, block shear failure in the bottom track flanges was detected at the end of the loading cycles. For both specimens, however, the global response of the system was adequately captured by the numerical models.

The cumulative dissipated energy is the total area under the lateral load-displacement curve up to a given time in the test procedure and was also used to compare the experimental and numerical responses (Macillo *et al.*, 2018). The cumulative energy graphs for specimens 26A-C and 32A-C are displayed in Fig. 2.14a and Fig. 2.14b, respectively. The average difference between the experimental and the numerical values was 18% for specimen 26A-C and 17% for specimen 32A-C, which confirms the adequacy of the FE models adopted in this study.

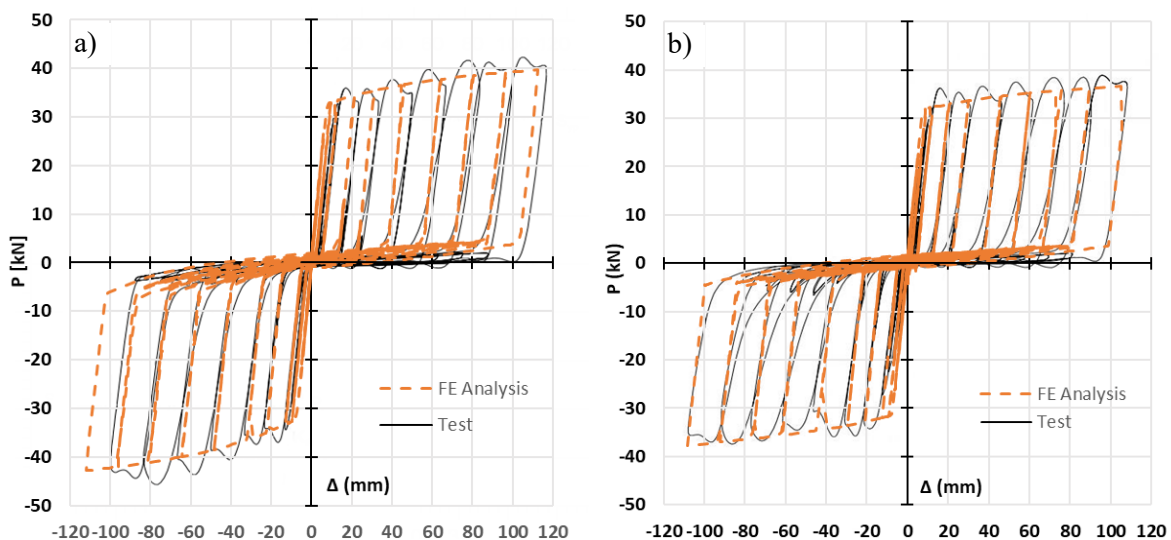


Fig. 2.13 Lateral load-displacement curves of a) 26A-C, and b) 32A-C test specimens and corresponding FE analysis results

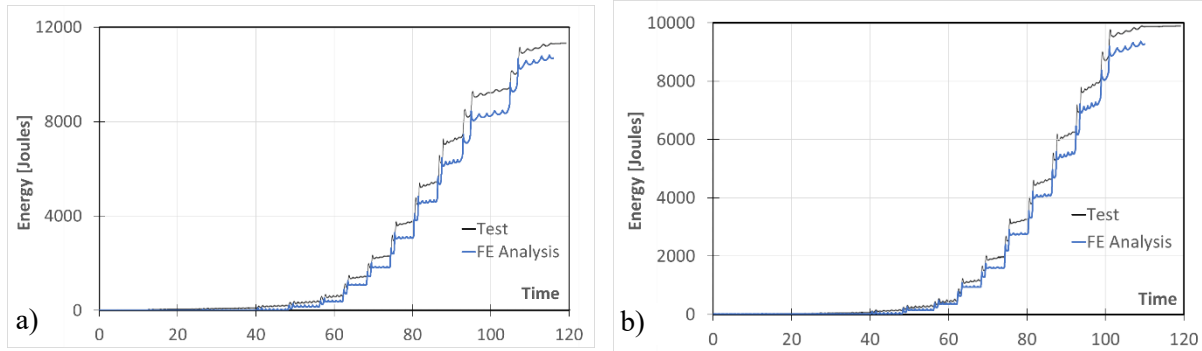


Fig. 2.14 Cumulative energy-time curves of a) 26A-C, and b) 32A-C test specimens and corresponding FE analysis results

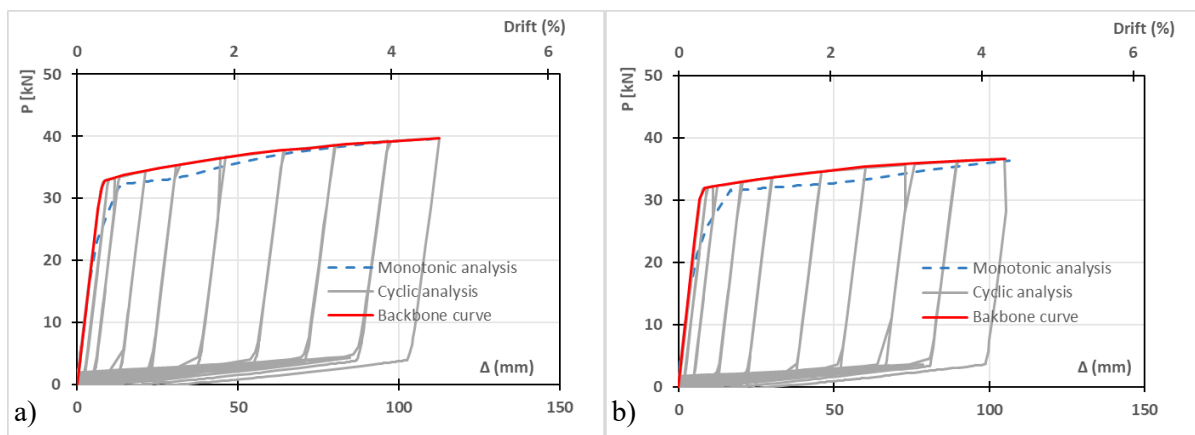


Fig. 2.15 Comparison of a) 26A-C backbone curve with 25A-M-1 monotonic curve and b) 32A-C backbone curve with 31A-M-1 monotonic curve

Fig. 2.15a and Fig. 2.15b compare the cyclic backbone curves of specimens 26A-C and 32A-C with the corresponding monotonic results. The comparison shows that the monotonic responses match the cyclic backbone curve results reasonably well, especially in terms of the initial stiffness, maximum capacity, and ultimate displacement.

To calculate performance parameters such as the energy dissipation capacity and the ductility, it is common practice to convert the load-displacement curves into equivalent bi-linear curves, in accordance with the FEMA 356 (FEMA 356, 2000) recommendations. The secant stiffness of the line intersecting the curve at 60% of the effective yield strength is thereby defined as the effective stiffness. The slope of a second line segment, starting at the yield point and passing through the original curve at the ultimate displacement, is then determined in such a way that the enclosed areas under the equivalent and the actual curves are equal. The ultimate displacement, by definition, corresponds either to failure of the wall or a 20% drop in load from the peak strength (whichever happens first). Fig. 2.15a and Fig. 2.15b show that the monotonic response and the backbone curve will lead to almost similar energy dissipation and ductility results.

Based on the above arguments and observations, the monotonic analyses were considered to be sufficient to evaluate the structural performance of the studied CFS walls under lateral loading, offering the advantage of dramatically reducing the amount of computational time, while still accurately predicting the overall response of the wall systems.

2.6 Evaluation of the non-linear performance of strap-braced walls

A series of parametric analyses were conducted to investigate the effect of key design parameters, i.e. (1) the number of vertical studs, (2) the thickness of the structural elements, (3) the diagonal strap material, and (4) different levels of vertical load. Their influence on the following performance parameters was studied:

- The lateral load capacity.
- The deformation capacity, expressed as the ultimate displacement (Δ_u), corresponding to failure of the wall (i.e. rupture of the straps or buckling of the chord stud) or a 20% drop relative to the maximum lateral load capacity.
- The ductility, which is the ability of a structure to undergo large plastic deformations without significant reduction in ultimate strength (Gioncu, 2000). It is here defined as the ratio Δ_u/Δ_y , where Δ_y and Δ_u respectively stand for the yield and ultimate displacements measured at the top of the wall.
- The energy dissipation capacity, defined as the area under the equivalent bi-linear load-displacement curve up to the ultimate displacement (Δ_u).

It should be noted that this study did not consider the depth of the stud/chord sections (equivalent to the width of the track sections) as design parameters, as the chosen values are considered typical for practical applications.

The validated numerical model of the 25A-M-1 specimen was used as the reference model in the parametric analyses.

It should be noted that in the actual design of strap-braced walls in multi-storey buildings some of the parameters under investigation are not independent, but become linked. For example, in accordance with the capacity design rules in Eurocode 8 (CEN, 2004) the design compressive force in the chord studs is related to the tensile force in the straps at first yielding. In practical design applications all members should be checked to ensure that they satisfy those requirements.

2.6.1 Effect of vertical load

While several experiments have been conducted to investigate the lateral response of stud wall systems, as previously mentioned, very limited information is available in the literature on the performance of these systems under the simultaneous effects of vertical and lateral loading. In practical applications, nevertheless, stud wall systems are invariably subject to dead and live gravity loads, as well as vertical loading due to overturning moments, which considerably affects their lateral response during an earthquake event. The first part of this parametric study therefore investigated the seismic performance under different levels of gravity loading.

In the analyses the vertical load was applied in the form of a surface load at the top plate, and expressed as a fraction of the total axial load capacity of the wall, P_w . Five cases were considered, with vertical loads equal to 7%, 15%, 22%, 30%, 35%, 44% and 50% of the total axial load capacity P_w . To obtain P_w the individual stud and chord stud capacities were calculated according to EC 3 (CEN, 2003, 2010). The buckling coefficients used in this process depend on the boundary conditions, i.e. the degree of restraint provided by the tracks to the stud ends and by the bridging at mid-height. In the present study, it was assumed that $K_x=1$ for out-of-plane buckling and $K_y=K_t=0.5$ for in-plane and torsional buckling. For the intermediate studs, these coefficients were applied to the full stud length, while for the chord studs they were applied to the distance between the hold-downs.

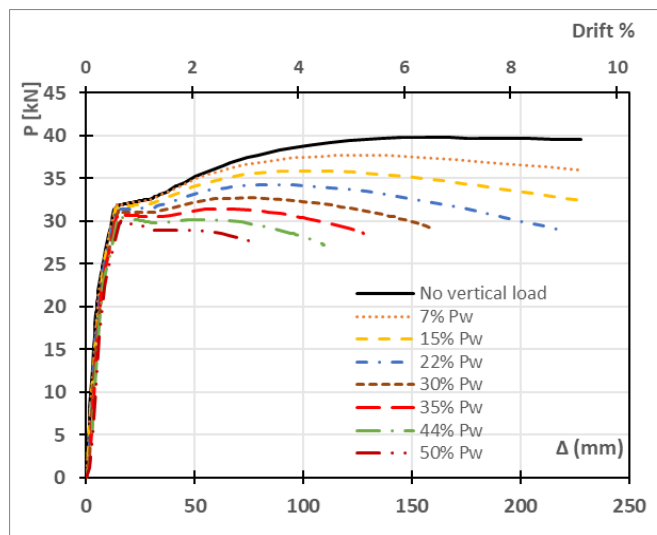


Fig. 2.16 Lateral load-displacement curves in the presence of vertical loading

The results of this study indicated that the presence of vertical loading has a significant effect on the lateral performance of the walls. It is seen from Fig. 2.16 that the lateral load capacity gradually decreased as the vertical load increased. Compared to the initial situation without vertical loading, the wall exhibited a significant 24% drop in lateral load capacity under vertical loading equal to 50% P_w .

Fig. 2.16 also shows that under low levels of vertical loading ($< 15\text{-}20\%$ of P_w) the ultimate lateral displacement of the wall remained largely unaffected. However, under a vertical load of 35% to 50% of P_w the ultimate displacements amounted to only 56% and 33% , respectively, of that of the original wall without vertical loading. The corresponding reductions in the ductility of the system were 47% and 70% , while the corresponding energy dissipation capacity of the wall dropped by 56% and 77% . These observations can be explained by noting that the lateral load capacity of the wall depends on both the tensile capacity of the straps and the compressive capacity of the chord studs. The chord studs are subjected to the vertical load applied to the model, in addition to carrying the vertical component of the tensile force in the strap. Moreover, the lateral displacements will introduce additional bending moments and compressive forces into the chord studs due to $P\text{-}\Delta$ effects, which become more substantial at higher vertical load levels. Up to a value of 15% P_w , the wall reached a maximum displacement determined by the straps reaching their ultimate strain. For vertical loads in excess of 22% P_w , however, the compressive chord stud reached its maximum capacity in distortional buckling before failure of the straps (Fig. 2.17). This implies that the straps did not reach their maximum strain, and hence, the wall failed prematurely. It should also be taken into account that, provided the intermediate studs have end conditions which can be approximated as hinges, the studs carry pure compressive forces oriented along their axis. As the lateral displacement increases, the straps are required also to resist the horizontal components of these stud forces, which remain axial yet are inclined. Less capacity is therefore available at higher vertical load levels to resist lateral forces.

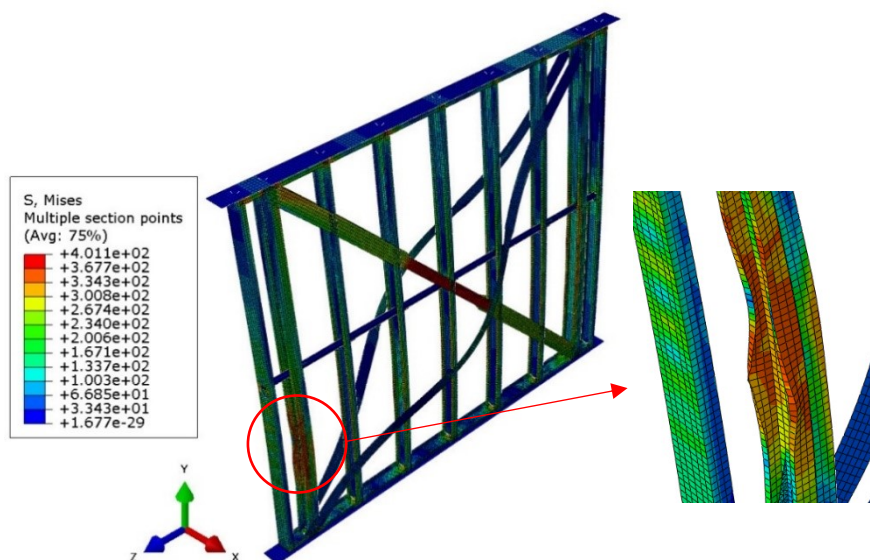


Fig. 2.17 Failure mode under vertical loading equal to 35% P_w

2.6.2 Number of studs

The original wall model featured seven studs: five intermediate ones and two outer chord studs. As part of the parametric analyses, the number of intermediate studs was reduced to four and three. As expected, reducing the number of studs did not affect the lateral load capacity of the wall. The ductility and energy dissipation also remained unaffected. Failure was still governed by the straps reaching their ultimate strain.

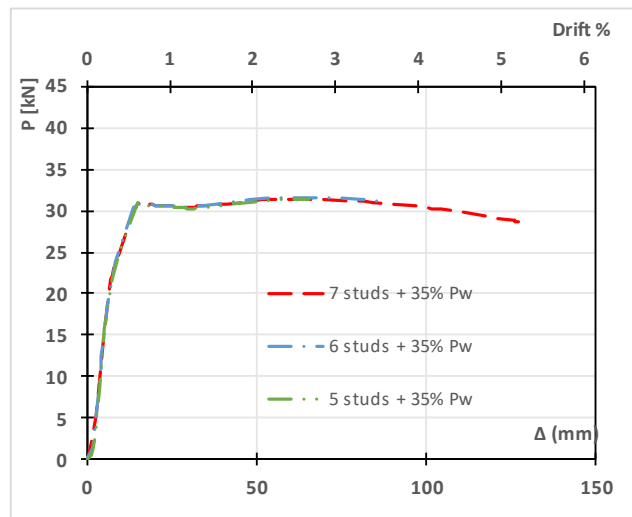


Fig. 2.18 Lateral load-displacement curves, varying the number of studs with 35% P_w vertical load

The responses of these wall panels featuring a different number of stud elements were compared in the presence of vertical loads. A vertical load equal to 35% P_w was applied to all wall panels, where P_w is the capacity of the original wall. Fig. 2.18 illustrates the responses of the three cases. It is seen that the lateral load capacity of the walls was virtually unaffected compared to the original wall panel with the same vertical load. The reason is that the increase in the strap force resulting from the P - Δ effect is the same in both cases, irrespective of the number of studs. Indeed, the sum of the horizontal components of the stud forces equals $P \times \Delta / H$, where (P) is the vertical load, (Δ) is the lateral displacement and (H) is the height of the wall. However, the ultimate lateral displacement reduced by 32% and 49% for the wall panels with 6 and 5 studs, respectively, compared to the original wall. The energy dissipation capacities of the wall panels followed the same trend. This can be explained by the fact that the chord studs were required to take a larger portion of the total axial load when the stud spacing increased, alongside a higher secondary moment, promoting their failure.

2.6.3 Thickness of the studs

Additional analyses were carried out where the thickness of all studs was increased to 2.32 mm and 3.48 mm. The results indicated that the stud thickness did not have any notable effect on the lateral response of the wall. The lateral load capacity remained constant in these analyses, whereas the ultimate displacement and the ductility slightly decreased (by 5%) for the case of the 3.48 mm stud thickness. This change was deemed negligible.

2.6.4 Thickness of the diagonal straps

The deformations of the diagonal straps constitute the primary seismic energy dissipation mechanism of the system. To study the effect of the strap thickness, three wall configurations were analysed and compared, employing strap thicknesses of 1.11 mm, 2.22 mm and 3.33 mm. Fig. 2.19 depicts the corresponding load-displacement curves. Increasing the diagonal strap thickness to 2.22 and 3.33 mm caused 86% and 140% increases in the lateral load capacity, respectively, compared to the original wall.

On the contrary, there was a significant decrease in the ultimate displacement of the wall, which dropped by 30% and 80% for the wall panels with 2.22 and 3.33 mm strap thicknesses, respectively. As a result, the ductility also fell by 39% and 82% in those respective cases. As expected, using an increased cross-sectional area for the straps led to higher compressive forces in the chord studs for the same deformation. Consequently, the reduction of the ultimate displacement in the walls with thicker straps is due to failure of the compression chord stud under the combination of a higher axial load and associated secondary moments due to P- Δ effects. These results imply that increasing the thickness of the straps without considering its implications may eventually lead to very low ductility levels and a brittle type of failure, which is obviously not acceptable in seismic applications.

Analysis of the data presented in Fig. 2.19 leads to the conclusion that the energy dissipation capacity of the walls increased by 28% when the strap thickness increased to 2.22 mm. However, the energy dissipation capacity dropped considerably (by 57%) compared to the original system when 3.33 mm thick straps were used. This illustrates the point previously conveyed.

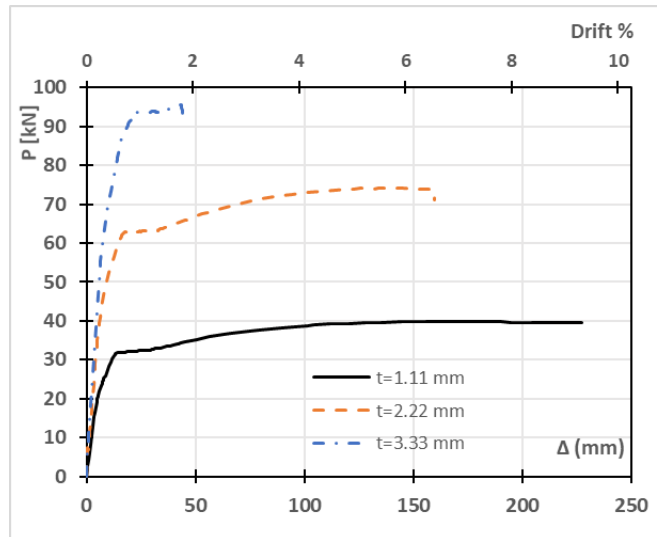


Fig. 2.19 Lateral load-displacement curves for walls with different diagonal strap thicknesses

2.6.5 Thickness of the wall frame elements

Parametric analyses were conducted in which the thicknesses of the wall elements in the bare frame (i.e. all CFS elements, including the top and bottom tracks, the studs, the chord studs and the bridging element, but excluding the straps) were increased to two and three times the original values shown in Table 2.1. Fig. 2.20a depicts the lateral response of the three frames. With the original thicknesses, the ultimate capacity of the bare frame reached 4.0 kN, which constituted approximately 10% of the total wall capacity of 39.8 kN. The capacity of the bare frame was increased to 8.5 kN and 11.9 kN when the thicknesses of the elements were increased by factors of two and three, respectively. It should be noted that the lateral resistance of the bare frame can almost solely be attributed to the hold-downs providing a degree of fixity at the ends of the chord studs, which led to the local development of a yield line mechanism in the advanced stages of loading (see Fig. 2.21). The intermediate studs, on the other hand, had virtually pinned connections at both ends and provided negligible lateral resistance.

Fig. 2.20b shows the lateral load-displacement curves of the bare frames studied in Fig. 2.20a, with the addition of strap elements with the original thickness of 1.11 mm. The figure demonstrates that the lateral capacity increased by 17% and 30% when doubling and trebling the frame element thicknesses, whereas the ultimate displacement remained practically unaffected. The ductility also remained virtually unchanged, while the wall dissipated around 11% and 19% more energy in the cases with double and triple wall thicknesses, respectively.

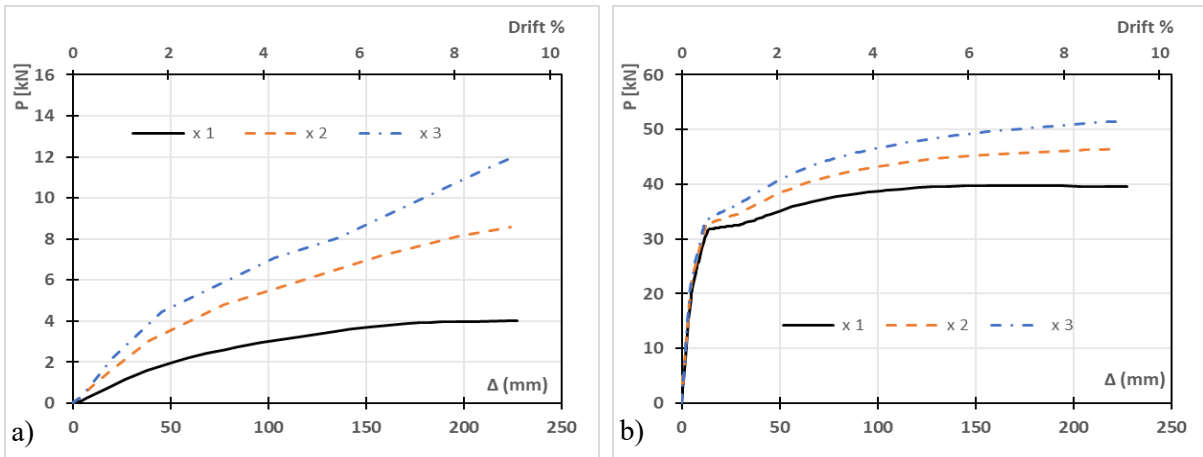


Fig. 2.20 Lateral load-displacement curves for frames with different thicknesses a) bare frame, b) frame with diagonal straps

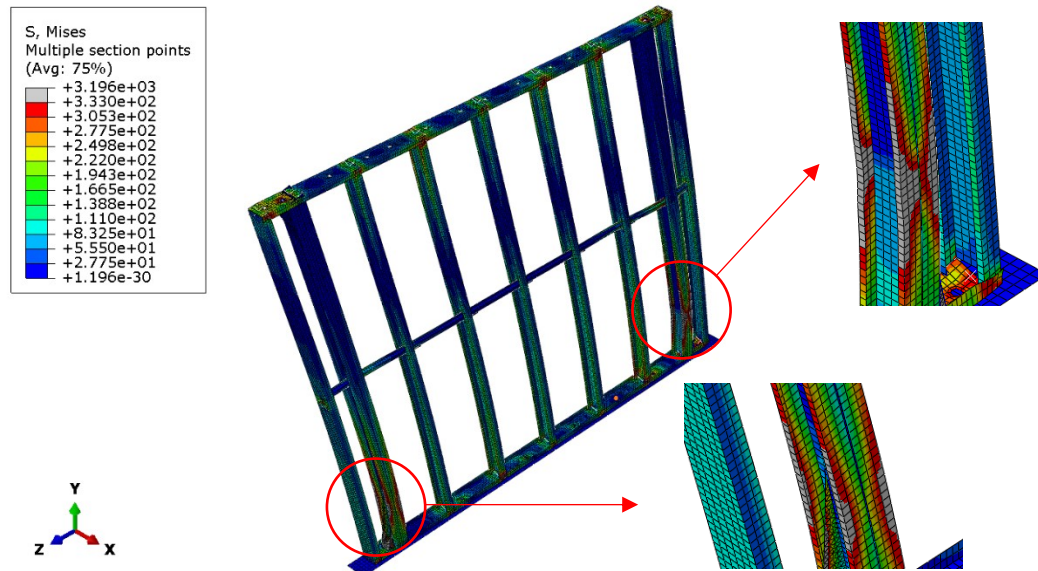


Fig. 2.21 Yielding of the chord studs in a bare frame with twice the original thickness

2.6.6 Thickness of the chord studs and the tracks

As illustrated in Fig. 2.22a, increasing the thickness of the chord studs to 2.32 mm and 3.48 mm (twice and three times the original thickness, respectively) yielded increases in lateral capacity of 5.6% and 8.5%, respectively. Negligible differences of less than 2% were also observed in the ultimate displacement, ductility and dissipated energy of the walls. This indicates that, in the absence of vertical loads, the effect of the chord stud thickness on the structural performance of the wall under lateral loads is small. However, this conclusion is only valid as long as the thickness of the chord elements is above

a minimum threshold, so that the straps can reach their ultimate strain before failure of the chord studs occurs.

The effect of the track thickness was also studied. For this purpose, two additional track thicknesses of 2.22 mm and 3.33 mm were investigated. Fig. 2.22b shows the lateral response of the system for each case. The lateral capacity increased slightly by 2.5% and 6.2%, respectively, compared to the original thickness of 1.11 mm. Meanwhile, the deformation capacity and ductility of the wall system remained unaffected. The energy dissipation capacity of the walls increased marginally by 2.4% and 4.7%, respectively. It can be concluded that, in general, the effect of the track thickness on the structural performance of the wall system is negligible.

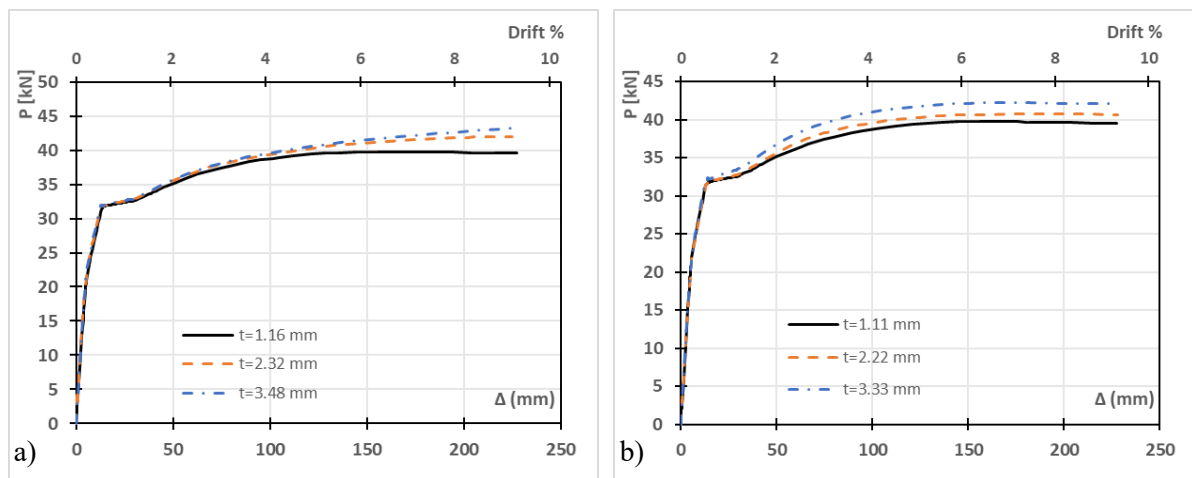


Fig. 2.22 Lateral load-displacement curves for wall panels with different thickness of a) the chord studs and b) the tracks

2.6.7 Steel grade of the diagonal straps

The structural behaviour of the wall panels was compared when using three different steel grades (S280, S460 and S690) for the diagonal straps. The steel initially used in the validation study and the experiment had a yield stress $f_y=295$ MPa and an ultimate tensile strength $f_u=366$ MPa, thus classifying as S280 according to Eurocode 3 (CEN, 2003). For the S460 and S690 grade materials, the stress-strain relationships from the experimental work by Versailles (Versailles, 2017) were adopted. The S460 grade steel had a yield stress $f_y=487$ MPa, an ultimate stress $f_u=634$ MPa and a modulus of elasticity $E=205$ GPa. The corresponding mechanical properties of the S690 grade steel were $f_y=800$ MPa, $f_u=860$ MPa and $E=202$ GPa. The stress-strain curves for the three steel grades are depicted in Fig. 2.23. The corresponding true stress-strain curves up to the ultimate stress (f_u) were inputted into ABAQUS.

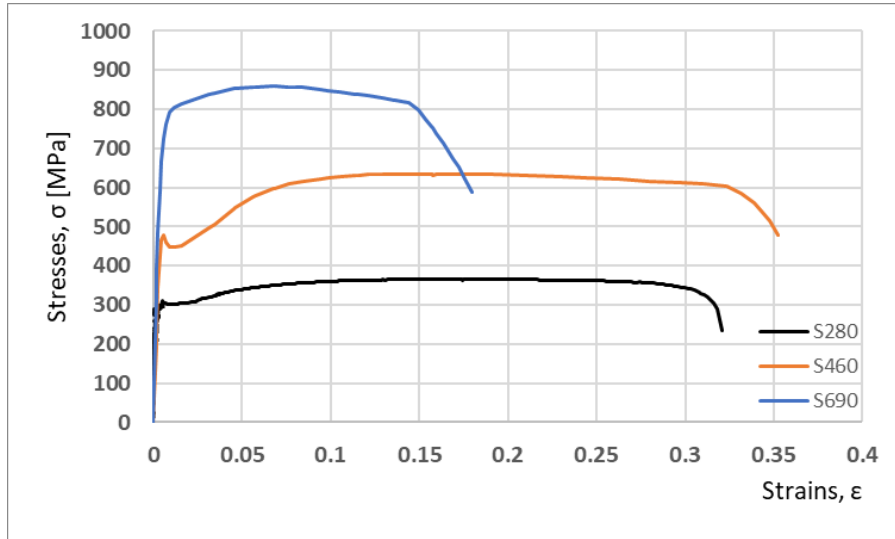


Fig. 2.23 Stress-strain curves for steel grades S280, S460 and S690

As Fig. 2.24 shows, the lateral capacity of the wall was considerably affected and increased by 61% for grade S460 and 116% for grade S690, compared to the the original design. The walls with the higher grade steel straps arrived at their ultimate displacement before the straps reached their ultimate strain. This was due to buckling failure of the compressive chord studs as a result of the higher strap force. The ultimate displacement corresponding to the S460 grade straps was 32% lower than for S280, while in the case of the S690 grade straps, it reduced by 60%. The ductility of the wall decreased by 51% in the case of the S460 grade steel and by 81% for the S690 grade steel. Additionally, the energy dissipation capacity remained unaffected for grade S460 and decreased by 21% for S690. These results generally indicate that using higher grade steel for the straps significantly increases the lateral load capacity but may reduce the ductility and energy dissipation capacity.

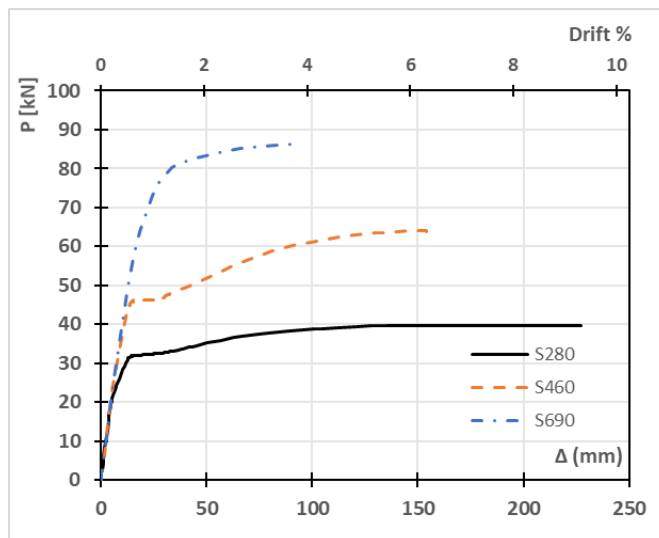


Fig. 2.24 Lateral load-displacement curves for various steel grades of the diagonal straps

2.7 Efficiency assessment of the design solutions

One of the objectives of the present study was to identify which design solutions were most efficient, combining maximum performance with optimal material use. To this end, an “Efficiency Index” (R_{ef}) was defined to evaluate the efficiency of the system with respect to different performance parameters. This index relates the effect that changing a design parameter has on the performance of the system to the corresponding change in material use, according to Eq. (1). “P” stands for the value of the considered performance parameter, while “W” stands for the total weight of the wall. The indices “i” and “v” denote the initial test configuration and the new configuration, respectively.

$$Efficiency\ Index\ (R_{ef}) = \frac{\frac{P_v}{P_i}}{\frac{W_v}{W_i}} \quad (1)$$

($R_{ef}=1$) means that the performance of the new design solution relative to its material use is equivalent to that of the original wall. ($R_{ef}>1$) indicates a better performance-to-weight efficiency, with a higher value indicating a more optimal design solution. On the other hand, ($R_{ef}<1$) implies an efficiency reduction, with a lower value indicating a less efficient design. The Efficiency Index can be used to rate various design options.

Fig. 2.25 depicts the Efficiency Index (R_{ef}) for all parametric studies completed in this work (see section 5), considering the following performance parameters: a) the lateral load capacity, b) the deformation capacity, c) the ductility, and d) the energy dissipation. Regarding the lateral load capacity, Fig. 2.25a shows that increasing the strap thickness yielded a more efficient solution, with $R_{ef}=1.83$ for the case of a 3.33 mm strap thickness. Choosing S690 steel for the straps led to an even more improved solution, with $R_{ef}=2.17$. On the other hand, the least efficient result with the lowest $R_{ef}=0.48$ was obtained when the wall frame thicknesses (excluding the straps) were increased to three times the original thicknesses. The other design solutions did not significantly affect the efficiency linked to the lateral load capacity.

The Efficiency Indices (R_{ef}) for deformation capacity (i.e. ultimate displacement) and ductility are shown in Fig. 2.25b and Fig. 2.25c, respectively. In both cases, increasing the thickness of the wall elements and using a higher steel grade for the straps led to lower R_{ef} values, with the maximum value of $R_{ef}=1$ corresponding to the original configuration. The largest strap thickness proved to have the most adverse effect since it reduced both the deformation capacity and ductility by 80% and increased the steel weight by 31%, leading to an $R_{ef}=0.13$.

Regarding the energy dissipation (Fig. 2.25d), the most efficient design solution corresponded to doubling the strap thickness, leading to a maximum R_{ef} value of 1.11. On the other hand, the least

efficient solution in terms of energy dissipation occurred for the largest strap thickness of 3.33 mm. Both facts can be explained by the fact that the energy dissipation capacity is equal to the area under the load-displacement curve up to the ultimate point, and when increasing the thickness of the straps, the lateral load capacity increases, while the deformation capacity may decrease.

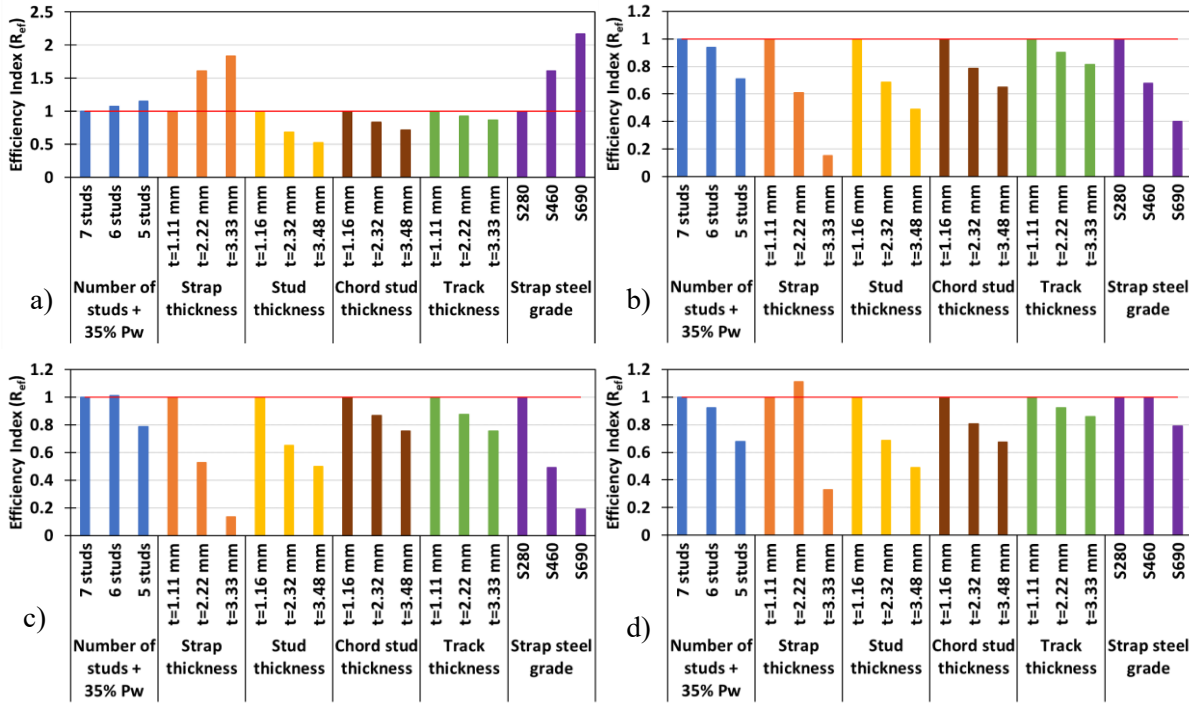


Fig. 2.25 Efficiency Index (R_{eff}) for a) lateral capacity, b) deformation capacity, c) ductility, and d) energy dissipation

2.8 Summary and conclusions

The work presented in this paper aimed to develop a better understanding of the lateral behaviour of CFS strap-braced stud walls and study the effect of key design parameters, such as the presence of vertical load, the number of studs, the thickness of the structural CFS elements and the steel grade of the straps, on the seismic performance of these systems. To achieve this, a detailed FE model was developed in ABAQUS, accounting for the nonlinear material behaviour of the structural components, initial geometric imperfections, secondary moments due to P- Δ effects and nonlinear behaviour of the connections. The model was validated against previously reported experimental results and shown to be capable of accurately predicting the response of the test specimens regarding stiffness, yield and ultimate displacements, and failure modes. The FE models were further used to conduct parametric studies, investigating the effect of the design parameters on critical performance criteria, such as the lateral load-bearing capacity, deformation capacity, ductility and energy dissipation. An Efficiency Index (R_{eff}) was proposed, which relates the impact of the variation of each design parameter on the strength, deformation

capacity, ductility or energy dissipation of the system to the corresponding change in material use, and allows design solutions to be rated. The research work led to the following main conclusions pertaining to CFS strap-braced walls:

- Additional vertical loading has a significant adverse effect on all key performance parameters. In the studied configuration a vertical load level of 50% P_w caused a 25 % drop in the lateral load capacity. Both the deformation capacity and the ductility decreased by almost 70%, while the system dissipated 76% less energy.
- The bare CFS frame (without straps) has a small but non-negligible resistance against lateral loads, resulting from the clamping effect provided by the hold-down devices and the resulting bending developing in the chord studs. However, a study of the efficiency indices R_{ef} indicates that increasing the thickness of the chord studs is an inefficient way to increase the lateral load capacity.
- The lateral load-bearing capacity is most significantly affected by the strap thickness and the steel grade of the diagonal straps. As expected, thicker straps and higher grade steel lead to a higher capacity, provided that the chord studs can withstand the increased vertical compressive component of the strap force.
- Increasing the strap thickness and the strap steel grade can also dramatically improve the efficiency of the design, as measured by the Efficiency Index for the lateral load capacity.
- The chord studs need to be designed for the additional compressive force and moment resulting from the $P-\Delta$ effects present at the time when the straps reach their required level of strain, corresponding to the target performance levels of ductility and energy dissipation. The increase in the strap force due to strain hardening of the strap material also needs to be accounted for when designing the chord stud.
- The deformation capacity and ductility of the wall can be adversely affected by choosing a larger strap thickness or a higher grade strap if the above point is ignored.
- The energy dissipation capacity strongly depends on the strap thickness since this is the crucial parameter affecting both the ultimate capacity and the deformation capacity. The analyses showed that there exists an optimum strap thickness, beyond which there is a significant drop in energy dissipation capacity due to low deformation capacity caused by chord stud buckling failure.

2.9 Acknowledgements

The authors would like to thank Prof. C.A. Rogers at the Department of Civil Engineering and Applied Mechanics, McGill University, for making previous experimental data available, which facilitated the

development of the numerical models, and Dr F.J. Ortiz, previously at the Department of Civil and Structural Engineering, The University of Sheffield, for sharing the experimental results of the shear lap tests.

2.10 Author contribution

- Ioannis Papargyriou:

Conceptualisation, Methodology, Formal Analysis, Investigation, Writing- Original draft, Writing- Reviewing and Editing, Visualisation

- Dr. Iman Hajirasouliha:

Conceptualisation, Methodology, Validation, Writing- Reviewing and Editing, Supervision

- Dr. Jurgen Becque:

Conceptualisation, Methodology, Validation, Writing- Reviewing and Editing, Supervision

- Prof. Kypros Pilakoutas:

Methodology, Writing- Reviewing and Editing, Supervision

CHAPTER 3

More efficient design of CFS strap-braced frames under vertical and seismic loading

This chapter is based on the published paper titled: “Papargyriou I., Hajirasouliha I., More efficient design of CFS strap-braced frames under vertical and seismic loading”, Journal of Constructional Steel Research, 185 (2021) 106886.

3.1 Abstract

Strap-braced stud walls are the primary lateral-force resisting system for conventional cold-formed steel (CFS) buildings. While CFS wall-panels in general exhibit a satisfactory seismic performance, previous studies showed that they may experience a premature brittle failure in the presence of vertical loading. However, current design codes do not make any provisions for calculating the lateral load capacity and ductility of strap-braced stud wall frames under vertical loading. This study aims to develop, for the first time, a practical design methodology for seismic design of CFS strap-braced stud wall frames under such conditions. To this end, a comprehensive parametric study was carried out using experimentally validated detailed numerical models in ABAQUS, accounting for material nonlinearities, initial geometric imperfections, and secondary moments due to P- Δ effects. Parameters of the investigations were the strap thickness and the intensity of the vertical loading. Design formulae were derived, and a preliminary design methodology was proposed for predicting the lateral load capacity and ductility of single strap-braced stud walls under a range of vertical loading ratios. The efficiency of the proposed method compared to Eurocode 8 design was then demonstrated for a 6-storey CFS multi-storey frame, which highlighted the importance of considering the effects of vertical loads in the seismic design of these systems. It was demonstrated that ignoring those factors can lead to a brittle lateral response even

if all other code requirements are satisfied, while the proposed design methodology was shown to be efficient to reach the target lateral load and ductility capacities.

3.2 Introduction

Over recent years, the construction industry has adopted cold-formed steel (CFS) systems for various structural applications. Apart from forming secondary members such as floor or cladding systems (Dubina *et al.*, 2012; Kyvelou *et al.*, 2017), they are already extensively used as the primary force-resisting system of multi-storey buildings to withstand vertical and lateral forces due to wind or earthquake (Dubina *et al.*, 2012). The vertical loads are typically transferred through stud elements, whereas the lateral resistance is mainly provided by X-shaped strap-braced stud walls.

The lateral resistance of strap-braced walls (Fig. 3.1) is delivered through a truss-mechanism formed by the tensile diagonal straps and the compressive chord stud. The straps under compression have negligible contribution since they buckle at an early stage because of their high slenderness (Mirzaei *et al.*, 2015). The lateral response of single strap-braced stud walls has been studied experimentally (Miller and Pekoz, 1993; Velchev, 2008b; Iuorio *et al.*, 2014; Fiorino, Terracciano, *et al.*, 2016; Lu and Rogers, 2018) and, to a lesser extent, numerically (Zeynalian and Ronagh, 2012; Gerami *et al.*, 2015; Kasaeian *et al.*, 2020). The favoured type of connections between the constituent parts is through self-drilling screws (Tomà and Stark, 1978; Pekoz, 1990; Casafont *et al.*, 2006b, 2007a; Serrette and Peyton, 2009; Yan and Young, 2012), which facilitate fabrication and erection. Alternatively, weld-connected walls also demonstrated a ductile response by maintaining their yield capacity (Comeau, 2008; Velchev *et al.*, 2010).

Monotonic and cyclic experimental tests have proven that yielding of the diagonal straps leads to the most ductile failure mechanism in strap-braced stud wall systems. Capacity design rules ensure that the seismic energy will be dissipated through plastic deformation of the net strap cross-sections, away from their connections with the chord studs (Al-Kharat and Rogers, 2008; Kasaeian *et al.*, 2020). Moreover, reducing the strap width over a length, forming a “dog-bone” shape, forces failure to develop in this “fuse” part, offering better damage control. Otherwise, undesirable non-ductile modes of failure occur, which decrease the lateral performance of the walls as previous studies have shown (Al-Kharat and Rogers, 2007). While in practical applications stud walls are sheathed with a wide range of materials, e.g. gypsum panels (Fiorino *et al.*, 2018), OSB (Buonopane *et al.*, 2015; Henriques *et al.*, 2017), steel sheets (Niari *et al.*, 2012; Attari *et al.*, 2016) and glass panes (Van Lancker *et al.*, 2015), the provisions of current design codes (e.g. Eurocode 3, Part 1-3 (CEN, 2003)) do not generally take into account the participation of the sheathing in the load-bearing mechanism, through composite action with the studs. This was supported by the results of previous studies, e.g. (Moghimi and Ronagh, 2009), where the gypsum sheathing proved to be unreliable in transferring lateral forces. The walls’ dimensions

significantly affect their lateral performance, with the optimal width to height ratio being 1:1 to 1:2. Higher ratios were deemed unacceptable to seismic applications, leading to premature failure due to high compression and bending of the chord studs and minimal yielding of the straps (Comeau, 2008; Velchev *et al.*, 2010; Mirzaei *et al.*, 2015).

Current seismic design codes provide relationships mainly for the calculation of the lateral load capacity of strap-braced stud wall systems under zero vertical loading without providing any means to predict their deformation capacity and ductility of the system. However, previous studies by Papargyriou *et al.* (Papargyriou *et al.*, 2021) demonstrated that the presence of the vertical loads could considerably affect the seismic performance of these systems, leading to a brittle type of failure as a result of secondary moments due to P- Δ effects.

In order to bridge the above knowledge gap, this study aims to develop a practical design methodology to predict the lateral load and ductility capacity of strap-braced stud wall systems under vertical loading by taking into account the material nonlinearity, geometric imperfections and P- Δ effects. An extensive parametric study was carried out to determine the effect of the strap thickness alongside additional vertical loading on the lateral load capacity and ductility of a single CFS strap-braced stud wall, with the aid of an experimentally validated detailed FE model in ABAQUS (Dassault Systèmes Simulia, 2014). The results were then used to derive appropriate design formulations, to predict the lateral load and ductility capacities of a strap-braced wall for a variation of strap and chord stud thicknesses under a range of vertical loading ratios. Subsequently, a practical design methodology was proposed, and its efficiency was demonstrated to design a 6-storey CFS frame system compared to a similar frame designed in accordance with the provisions of Eurocode 8. It was indicated that despite fulfilling the code requirements, the ductility capacity of the code-base design system was still inadequate at some storey levels due to the presence of vertical loads and secondary moments due to P- Δ effects, which can lead to poor seismic performance under strong earthquake events. However, the proposed design methodology could efficiently provide the target lateral load and ductility capacities. The results of this study highlighted the importance of considering the ductility reductions under vertical loads and secondary moments in the seismic design of CFS strap-braced stud wall systems.

3.3 Description of the numerical model in ABAQUS

The numerical model used in this study was developed in ABAQUS (Dassault Systèmes Simulia, 2014) software, because of its proven reliability in modelling and predicting the behaviour of thin-walled elements and systems, as previous studies have demonstrated (Jun Ye *et al.*, 2016; Kyvelou *et al.*, 2018; Mojtabaei *et al.*, 2018; Ye, Mojtabaei, Hajirasouliha, *et al.*, 2018, 2019). Papargyriou *et al.* (Papargyriou *et al.*, 2021) developed a detailed numerical model in ABAQUS and validated it against experimental

test results. This model was adopted and modified in this study, with the main features summarised below, while a comprehensive modelling description can be found in (Papargyriou *et al.*, 2021).

3.3.1 Geometry – FE type and mesh size

The wall considered as a reference, had a 1:1 ratio with the width and height measuring 2.44 m × 2.44 m. The configuration of the wall alongside the main structural elements and their dimensions are shown in Fig. 3.1.

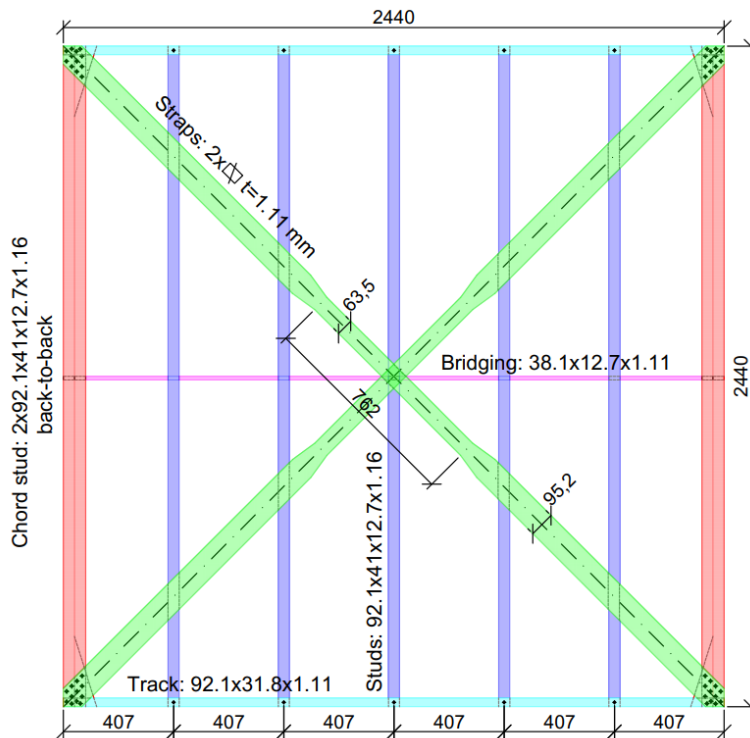


Fig. 3.1 Wall geometry and cross-sectional dimensions

In the present work, the “S4R” shell element of ABAQUS was selected, since it has been widely used to simulate the axial and bending non-linear response of CFS members, yielding accurate results (Jun Ye *et al.*, 2016; Ye, Mojtabaei, Hajirasouliha, *et al.*, 2018; Mojtabaei *et al.*, 2020). Fig. 3.2 illustrates the meshed structure along with modelling details. A mesh sensitivity analysis suggested a FE mesh size of 15 mm × 15 mm for all components, apart from the top and bottom rigid plates, for which a size of 20 mm × 20 mm was selected. This mesh size provided a balanced solution between the accuracy of the predictions and the computational efficiency.

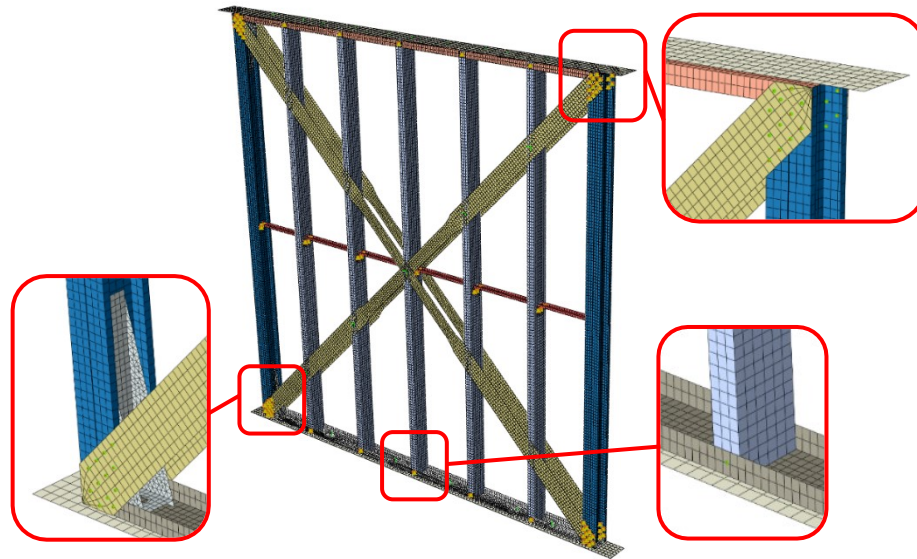


Fig. 3.2 Numerical model in ABAQUS

3.3.2 Material properties

The engineering values of yield (f_y) and ultimate (f_u) stresses of steel used for each structural element are given in Table 3.1. In the ABAQUS models, the engineering strains and stresses were converted to logarithmic plastic strains and true stresses. The modulus of elasticity (E) was equal to 203 GPa, the Poisson's ratio (ν) had a value of 0.3, and the isotropic hardening rule was followed.

Table 3.1 Material properties

Element	Yield stress f_y (MPa)	Ultimate stress f_u (MPa)
Straps / Tracks	296	366
Studs / Chord studs	325	382

3.3.3 Connections and member interactions

The screwed connections were modelled using discrete fasteners, a feature of ABAQUS to couple multiple surfaces. The fasteners were assigned connector properties to describe the relative motion of the connected components. The strength and stiffness properties of the connectors were specified by adopting Pham and Moen's proposed equations (Pham and Moen, 2015), which are modified

expressions of AISI S100-12 (AISI, 2012), based on the results and observations of their experimental study on shear-lap joints.

The vertical load was applied on the top rigid plate as a uniformly distributed surface load, whereas the lateral load displacements were applied at the shear anchor points and the top end-nodes of the anchor rods. To enable the transfer of the vertical load from the top plate to the ground and avoid any member overclosures, surface-to-surface contact interactions were defined. “Hard” contact properties were applied in the normal direction, whereas “frictionless” contact characterised the transverse direction.

3.3.4 Verification of the FE model

To verify the accuracy of the developed FE numerical model, the test specimens 25A-M-1 and 31A-M-1 adopted from the experimental work of Velchev (Velchev, 2008b), were simulated. Alongside material nonlinearities and the secondary moments due to P- Δ effects, the effect of initial geometric imperfections was also investigated. However, it was found that the overall response and the lateral load capacity of the strap-braced stud wall frame systems were insensitive to the applied geometric imperfections. Fig. 3.3 summarises the comparison between the 25A-M-1 and 31A-M-1 test specimens and the corresponding numerical analyses results under monotonic loading. It is shown that the predicted responses by the numerical model matched perfectly the reported test results, and the difference in the lateral load capacity was less than 2.5%. More information on the validation of the developed FE models against cyclic tests can be found in (Papargyriou *et al.*, 2021). However, previous studies by Velchev (Velchev, 2008b) and Papargyriou *et al.* (Papargyriou *et al.*, 2021) demonstrated that, in general, the monotonic response of the strap-braced stud walls can accurately represent the envelope of their cyclic response. Therefore, in this study, the response parameters of the walls are obtained from monotonic analyses to improve computational efficiency.

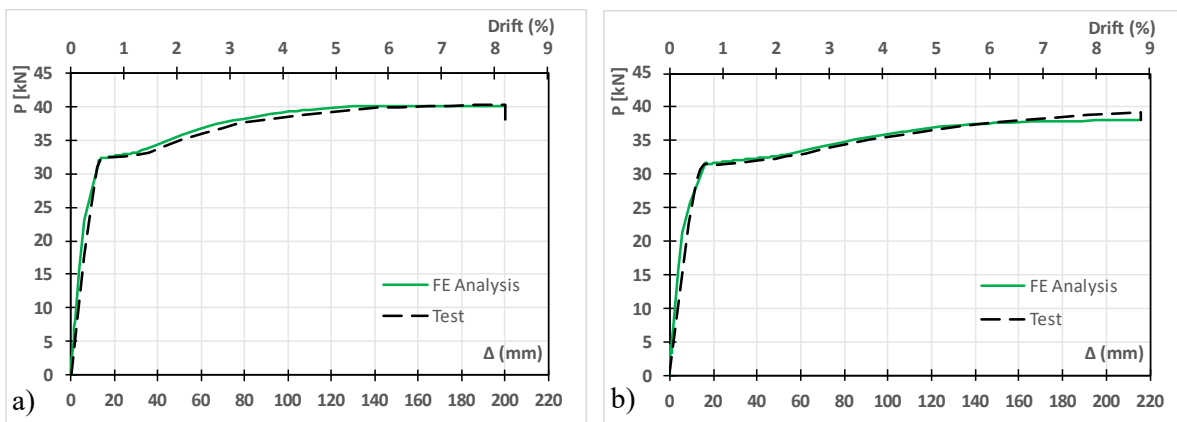


Fig. 3.3 a) Comparison of the lateral load-displacement curves of a) 25A-M-1 and b) 31A-M-1 test specimens and corresponding FE analyses.

3.4 Non-linear structural performance of single strap-braced walls

A previous preliminary study by Papargyriou et al. (Papargyriou *et al.*, 2021) indicated that the strap thickness and the vertical loading ratio are the key design parameters affecting the lateral response of strap-braced stud walls. In this section, the verified FE model in ABAQUS (see section 3.3) was adopted to comprehensively study the effect of different strap thicknesses and vertical loading ratios (i.e. the ratio of the vertical load against the axial load capacity of the wall) on lateral load capacity, ultimate displacement (Δ_u) and ductility capacity (μ) of the strap-braced walls.

Fig. 3.5 illustrates the lateral load-displacement curves for different strap thicknesses and vertical loading ratios. Whilst the discussion of the results in this section focuses on the trend in the change of the affected performance parameters, section 3.5 presents the relationships between the studied design parameters and the performance of the system through analytical expressions.

3.4.1 Effect of the diagonal strap thickness

The range of considered strap thicknesses was 0.56, 1.11, 1.67, 2.22, 2.78 and 3.33 mm (i.e. being 0.5, 1.0, 1.5, 2.0, 2.5 and 3.0 times the original thickness of 1.11 mm in the reference wall), while the thickness of the studs, the chord studs, the tracks and the bridging element remained fixed. As expected, Fig. 3.5 shows that increasing the diagonal strap thickness resulted in a considerably higher lateral load capacity of the wall almost proportionally. For the situation without any vertical loading, the walls with strap thicknesses of 1.67, 2.22, 2.78, and 3.33 mm reached 45%, 90%, 125% and 134% higher capacities, respectively, compared to the wall with the initial strap thickness of 1.11 mm. It would be anticipated that the lateral wall capacity should increase almost proportionally to the strap thickness, since the lateral capacity due to the frame action (i.e. the capacity of the wall without straps) is generally less than 20% of the total capacity of the system (Papargyriou *et al.*, 2021). However, in the case of the walls with thick straps, the compressive component of the strap force in the chord stud, combined with a secondary moment due to P- Δ effects, exceeded the capacity of the chord stud, yielding its premature failure.

As an example, Fig. 3.4 displays the von Mises stresses and the failure modes for the walls with 1.11 mm and 2.78 mm thick straps. It is shown in Fig. 3.4a that the straps reached their ultimate strain, so the failure mode was associated with net cross-section fracture of the straps. Subsequently, the chord stud exhibited distortional buckling mode at the cross-section above the top of the hold-down. Fig. 3.4b indicates that the straps did not reach their ultimate strain because the failure happened prematurely due to local buckling at the chord studs.

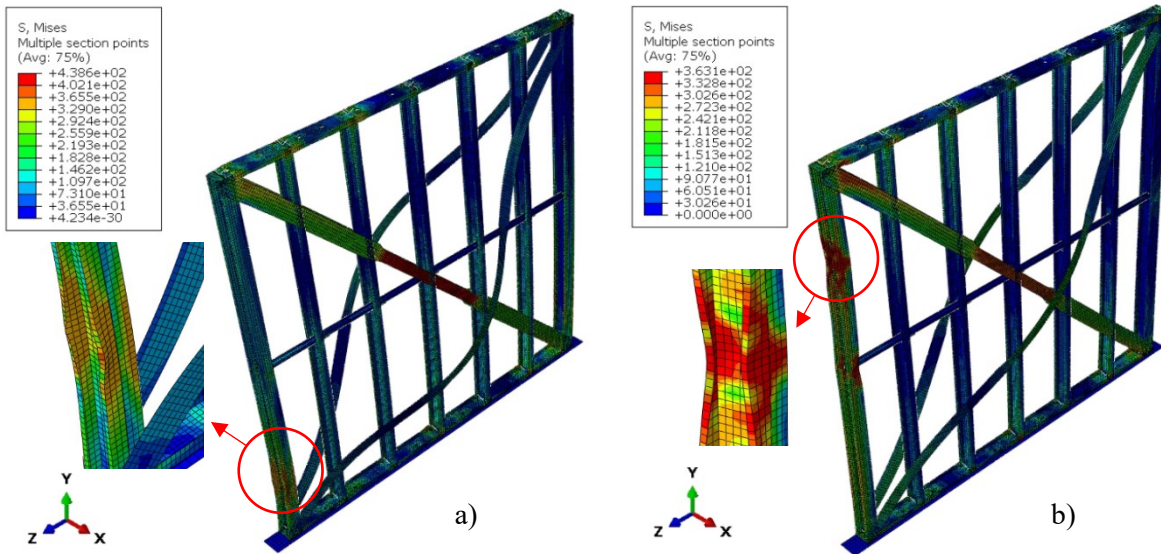


Fig. 3.4 Distribution of von Mises stresses and failure modes for walls with a) 1.11 mm straps and b) 2.78 mm straps, under no vertical loading

Under no vertical loading, the results presented in Fig. 3.5 indicate that the walls employing strap thicknesses of 2.22, 2.78, and 3.33 mm reached 15%, 61% and 90% lower values of ultimate displacement and hence ductility compared to the original wall with 1.11 mm thick straps. A further observation from Fig. 3.5 was that the walls with strap thicknesses of 0.56 mm and 1.11 mm reached the same ultimate displacements, whereas from strap thicknesses 1.67 mm and above, the ultimate displacement was decreasing. This means that a strap thickness exists, for which failure at the straps happens simultaneously with failure in the compressive chord stud. This threshold value of the strap thickness, for which the failure mode switches from the straps to the chord stud, was used in the design equations presented in the next section. On the other hand, while the ductility of the original frame was calculated to be 22.63, for the extreme case of a strap thickness of 3.33 mm, the wall ductility was reduced to 2.6, which is not generally acceptable for seismic applications. This will be discussed in more detail in the following section.

3.4.2 Effect of the vertical load

The vertical loading, applied as a surface load at the top plate, measured 7%, 14%, 22%, 29%, 36%, 43%, 51% and 58% of the total vertical load capacity of the wall (P_w), derived by adding the individual compressive capacities of the studs and the chord studs calculated per EN 1993 (CEN, 2003, 2010). The results indicated that the ultimate displacement and ductility of the walls were dramatically affected by the presence of vertical loading. This observation can be justified since the additional vertical load increases the axial force in the chord stud, which, when combined with the developed secondary moment due to the $P-\Delta$ effects, leads to the premature failure of chord studs before straps reach their ultimate

strain limit (Papargyriou *et al.*, 2021). The contribution of the secondary moment increases at higher vertical loading levels. It could be observed from Fig. 3.5 that for the walls with strap thicknesses less than or equal to 1.11 mm, vertical loading ratios of up to 22% did not reduce the ultimate displacement and ductility of the walls, whereas beyond this level, the effects of vertical loading were evident. For these elements, the maximum vertical loading ratio of 58% reduced the ultimate displacement and ductility values by more than 70%. For the walls with strap thicknesses greater than 1.11 mm and up to 2.22 mm, this reduction started at lower values of vertical load (due to an already higher compressive force on the chord stud), reaching a maximum reduction of more than 85% in the ultimate displacement and ductility under vertical loading ratio of 51%. It should be noted that the walls with strap thicknesses of 2.78 mm, under vertical loading ratios greater than 22%, alongside those with 3.33 mm straps under all vertical loading levels, reached ductility values below 2.5, which is generally considered unacceptable for seismic applications. This highlights the importance of considering the effects of vertical loads in the seismic performance assessment of strap-braced stud wall frames.

The lateral load capacity of strap-braced walls is mainly attributed to the tensile capacity of the straps. However, to accommodate the full capacity of the wall, the chord studs have to also resist the externally applied vertical load and the vertical compressive component of the tensile strap force. Due to the P- Δ effects, this vertical load yields a horizontal reaction in the opposite direction as the horizontal reaction of the strap, reducing the lateral capacity of the wall. On the other hand, as discussed above, the chord studs may fail before the straps reach their ultimate strength due to the secondary moments resulting from the P- Δ effects, which is more evident for high vertical loading ratios. This indicates that the simultaneous action of vertical and lateral loading can have an adverse effect on the lateral load capacity of the wall systems. As depicted in Fig. 3.5, for the wall with a strap thickness of 0.56 mm, the vertical loading ratio of 29% reduced the lateral load capacity by 26%, whereas the loading ratio of 58% resulted in a reduction of 31%. For the walls with strap thicknesses greater than 1.11 mm, the vertical loading ratios of 29% and 58% yielded a lateral load capacity reduction of about 17% and 58%, respectively.

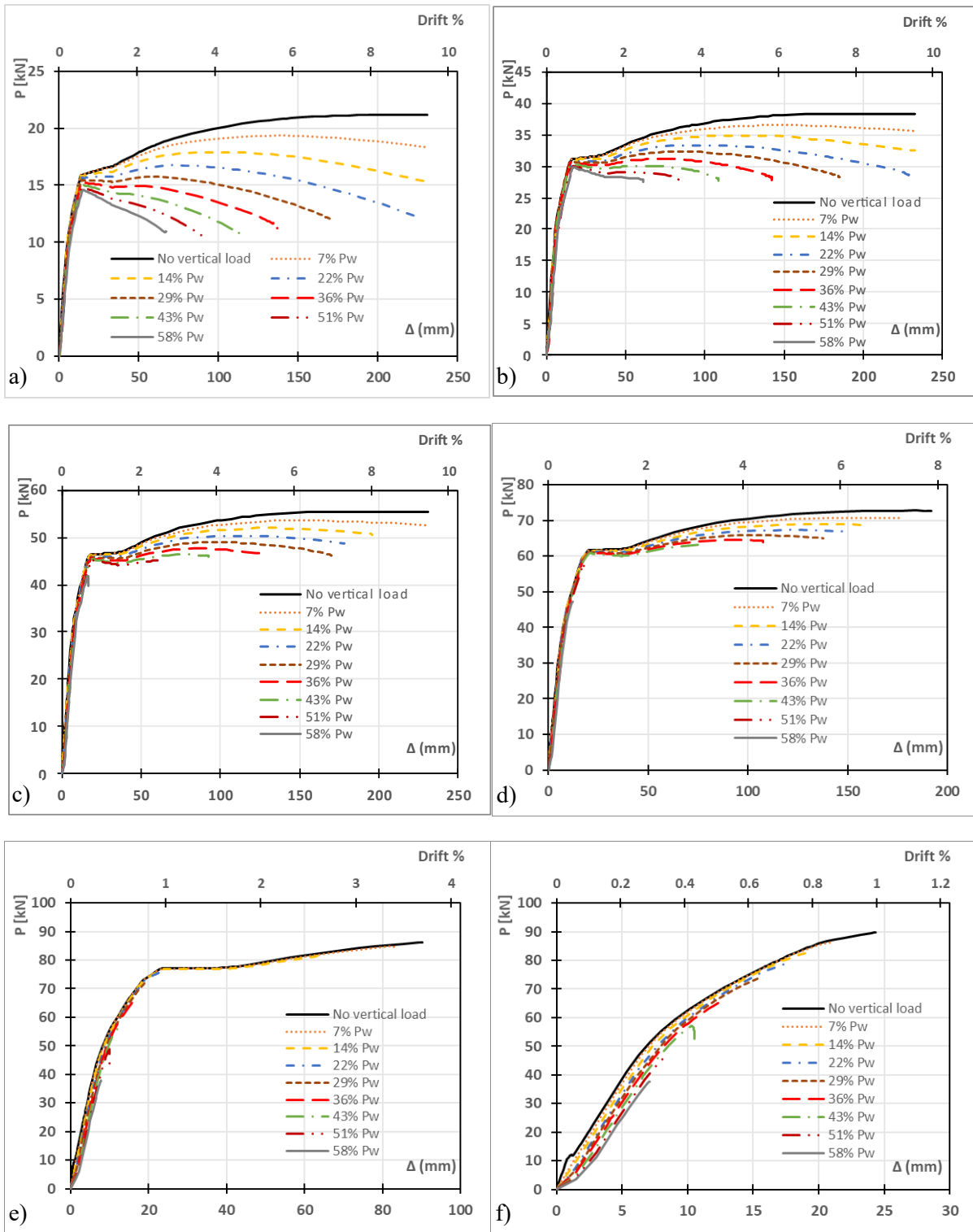


Fig. 3.5 Lateral load-displacement curves for walls with diagonal strap thickness a) $t_s=0.56$ mm, b) $t_s=1.11$ mm, c) $t_s=1.67$ mm, d) $t_s=2.22$ mm, e) $t_s=2.78$ mm and f) $t_s=3.33$ mm under various levels of vertical loading

3.5 Design of CFS strap-braced frames under simultaneous vertical and seismic loading

3.5.1 General design concept

In the design of framed structures employing strap-braced walls as the primary lateral force resisting system, it is favourable to distribute them along the height in such a way as to combine maximum capacity and ductility with minimum structural weight. This process would require to estimate the lateral response of the wall of the preferred configuration and topology, but for different strap, stud and chord stud thicknesses, under the applied vertical load at each storey, to obtain the most efficient solution. Current design codes, as the European Eurocode 3 (CEN, 2003, 2010) and Eurocode 8 (CEN, 2004), or the American S213-07 (AISI S213, 2012), do not provide specifications to calculate the lateral load capacity or the ductility of CFS strap-braced systems subjected to concurrent vertical loading. Moreover, as it will later be demonstrated, a CFS frame that satisfies the requirements of Eurocode 3 and 8 does not necessarily provide sufficient ductility capacity for high seismic regions.

The present work aims to introduce a practical methodology to predict the lateral load and ductility capacities of a strap-braced wall, for a variation of strap, stud and chord stud thicknesses, under a range of vertical loading ratios. Both performance parameters will be associated with the known lateral response (derived from a test or detailed numerical analysis) of a “reference” wall under zero vertical loading. The “reference” wall, named for brevity as number 1, has the same configuration, topology and material properties as the wall with the requested response, named as number 2. The lateral responses of walls 1 and 2, respectively, will be related with the aid of simple design formulations derived from the response curves. This can help to provide a practical framework to obtain the most efficient design solution that satisfies the required lateral load capacity and ductility using minimum element sizes, while the effects of vertical loads, leading to secondary moments due to P- Δ effects, and non-linear behaviour of the wall are included.

In a generalised form, the proposed formulations to express the lateral capacity and ductility of wall 2 were obtained based on the corresponding response of reference wall 1, using modification factors describing the effects of a) the thickness of the straps and chord studs and b) the vertical loading ratio. As a first step, under the condition of zero vertical loading, Eq. (2) was used to define the lateral load capacity of wall 2 ($F_{u,2}$) based on the lateral load capacity of reference wall 1 ($F_{u,1}$). The dimensionless parameters $t_{s,2}/t_{s,1}$ and $t_{ch,2}/t_{ch,1}$ were the ratios of the strap thicknesses ($t_{s,2}$) and ($t_{s,1}$) and the chord stud thicknesses ($t_{ch,2}$) and ($t_{ch,1}$) of walls 2 and 1, respectively. Similarly, the ductility of wall 2 was defined by Eq. (3). In this equation, ($t_{so,2}$) introduced in section 3.4.1 was defined as the strap thickness for which the wall under zero vertical loading would exhibit simultaneous failure of the straps in tension and the

chord stud in compression. In other words, it was an upper bound of the strap thickness for which the wall reached its maximum ductility. Hence, it provided a very effective means to relate the ductility of a wall with any strap and chord stud thickness to the ductility of its ($t_{so,2}$) thickness counterpart. The wall with a strap thickness of ($t_{so,2}$) had the same ductility as reference wall 1, thus ($\mu_{tso,2}=\mu_1$), under the condition that the failure mode of wall 1 was net cross-section fracture of the straps (this condition can be easily satisfied by using an appropriate reference wall).

$$\text{Lateral load capacity } F_{u,2} = F_{u,1} \cdot f1 \left(\frac{t_{s,2}}{t_{s,1}}, \frac{t_{ch,2}}{t_{ch,1}} \right) \quad (2)$$

$$\text{Ductility } \mu_2 = \mu_{tso,2} \cdot f2 \left(\frac{t_{s,2}}{t_{so,2}} \right) \quad (3)$$

The next step was to estimate the lateral response of wall 2 under the presence of vertical loading. For this purpose, Eqs. (4) and (5) were used, which provided relationships to calculate the lateral load capacity ($F_{u,P,2}$) and ductility ($\mu_{P,2}$), respectively, by incorporating the effect of the vertical loading ratio ($P/P_{w,2}$).

$$\text{Lateral load capacity } F_{u,P,2} = F_{u,2} \cdot f3 \left(\frac{P}{P_{w,2}} \right) \quad (4)$$

$$\text{Ductility } \mu_{P,2} = \mu_2 \cdot f4 \left(\frac{P}{P_{w,2}} \right) \quad (5)$$

Fig. 3.6 provides a schematic summary of the proposed design methodology, with the known response of the reference wall 1, shown on the left, and the requested response of wall 2, on the right, respectively.

Based on the results of a comprehensive parametric study, the functions $f1$, $f2$, $f3$, and $f4$ were obtained in the following sections, using the wall configuration described in Section 3.3 as the reference wall 1.

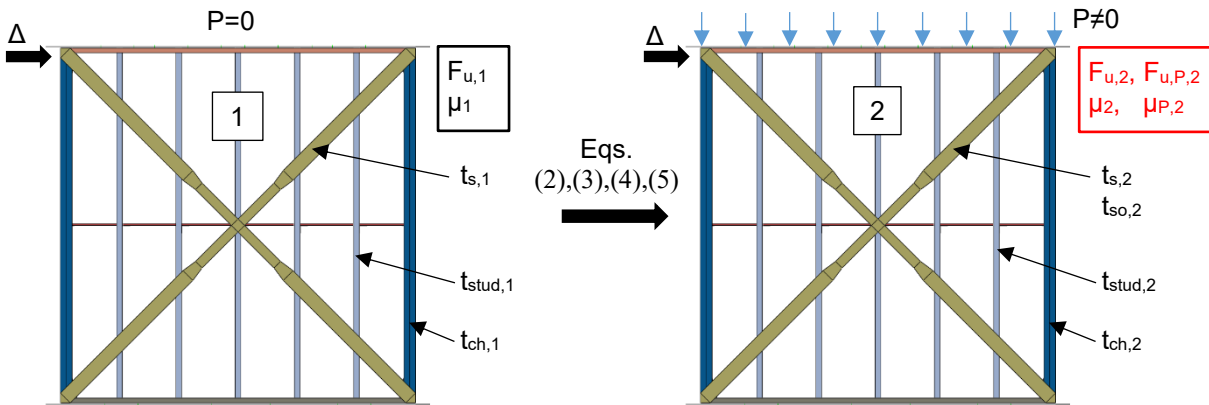


Fig. 3.6 Schematic of the proposed design concept

3.5.2 Proposed design equations

3.5.2.1 Lateral load capacity under zero vertical loading

The lateral load capacity of a wall under zero vertical loading was related to the capacity of the reference wall 1 through the strap and chord stud thickness ratios. Lateral analyses performed to the bare steel frame of a wall, without any diagonal straps, showed that the frame contributed 10% to 20% of the total lateral capacity, depending on the element thicknesses (Papargyriou *et al.*, 2021). Taking the proportion of truss action attributed to the straps as 85%, and of frame action attributed to the chord studs as 15%, led to Eq. (6), where ($F_{u,2}$) and ($F_{u,1}$) are the lateral load capacity, ($t_{ch,2}$) and ($t_{ch,1}$) are the chord stud thickness, and ($t_{s,2}$) and ($t_{s,1}$) represent the strap thickness of wall 2 and reference wall 1, respectively.

$$f1 = \frac{F_{u,2}}{F_{u,1}} = 0.85 \left(\frac{t_{s,2}}{t_{s,1}} \right) + 0.15 \left(\frac{t_{ch,2}}{t_{ch,1}} \right) \quad (6)$$

In Fig. 3.7, plotting a curve for different values of ($F_{u,2}/F_{u,1}$) ratio against various values of ($t_{s,2}/t_{s,1}$) ratio showed a linear trend, matching very well the predicted results of Eq. (6).

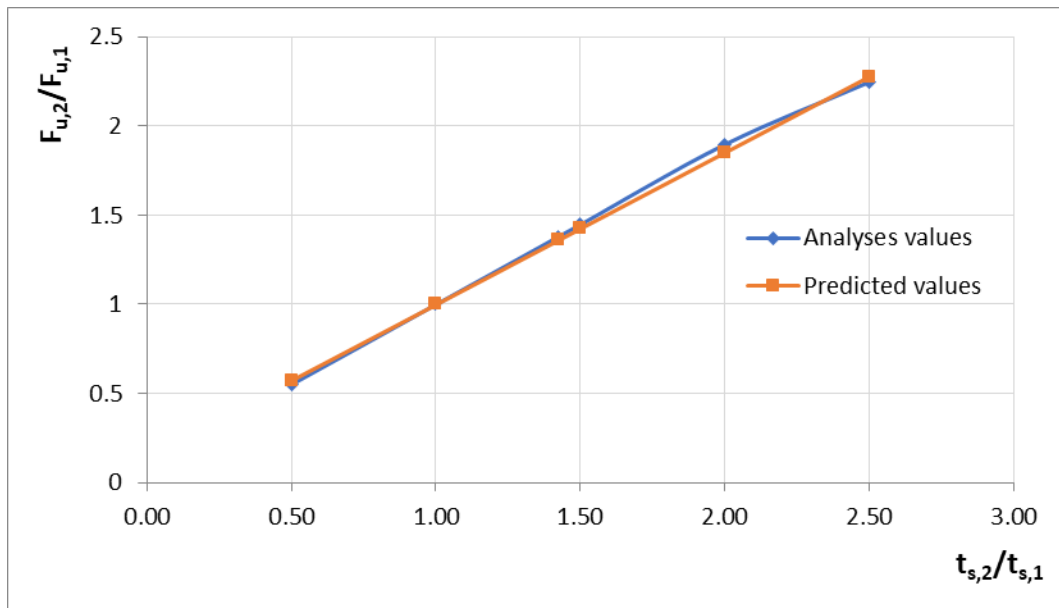


Fig. 3.7 Effect of strap and chord stud thickness ratio on the lateral load capacity ratio

3.5.2.2 Ductility under zero vertical loading

The ductility capacity of the wall is expressed as the ($\mu = \Delta_u/\Delta_y$) ratio, where (Δ_y) is the lateral displacement at yield, and (Δ_u) is the ultimate displacement at failure. In this study, Δ_u is defined as the displacement corresponding to the rupture of the diagonal straps or buckling of the chord stud or to a 20% drop of the maximum lateral load capacity (whichever occurs first). To obtain (Δ_y) and (Δ_u), the actual lateral load-displacement curves were approximated by idealised bilinear curves, as prescribed in FEMA 356 (FEMA 356, 2000).

The ductility ratio (μ_2) of wall 2 having a strap thickness ($t_{s,2}$) over the ductility ($\mu_{t_{so,2}}$) of the same wall having a strap thickness of ($t_{so,2}$) was plotted against various strap thickness ($t_{s,2}/t_{so,2}$) ratios. An initial plateau region was observed up to $(t_{s,2}/t_{so,2}) = 1$, while increasing the $(t_{s,2}/t_{so,2})$ ratio beyond this limit resulted in a steep decline of the $(\mu_2/\mu_{t_{so,2}})$ ratio. For the declined part of the curve, regression analysis yielded a second-order polynomial, expressed by Eq. (7), and plotted in Fig. 3.8.

$$\begin{cases} f2 = \frac{\mu_2}{\mu_{t_{so,2}}} = 1, & t_{s,2} \leq t_{so,2} \\ f2 = \frac{\mu_2}{\mu_{t_{so,2}}} = -0.09 + 2.16 \left(\frac{t_{s,2}}{t_{so,2}} \right) - 1.07 \left(\frac{t_{s,2}}{t_{so,2}} \right)^2 & t_{s,2} > t_{so,2} \end{cases} \quad (7)$$

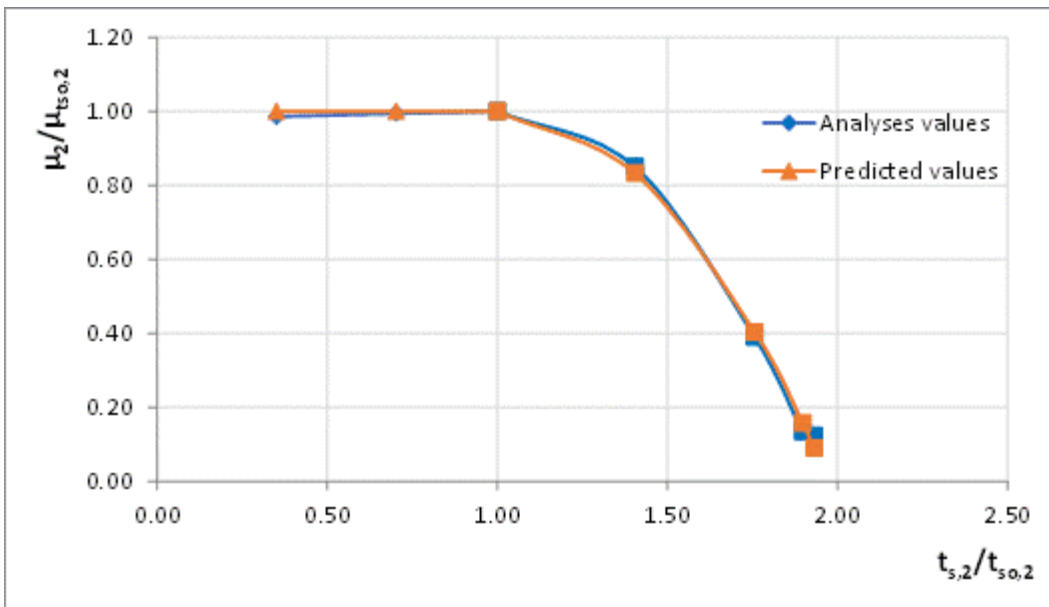


Fig. 3.8 Effect of strap ratio on the ductility ratio

In Fig. 3.8, the failure mode of the wall up to the inflexion point ($\mu_2/\mu_{tso,2}=1$) was fracture of the straps, meaning that the straps reached their ultimate strain. For ($\mu_2/\mu_{tso,2}>1$) the failure mode switched to buckling failure of the compressive chord stud. In this case, the wall fails before the straps can exploit their full capacity.

As it can be seen in Fig. 3.9, for a wall with external dimensions (L) and (H), the vertical compressive component of the strap force (F), acting on the chord stud, is equal to $F_c=F \cdot \cos(\alpha)$. Under lateral deflection (Δ), the force (F_c) produces a horizontal component $V=F_c \cdot \Delta/H$. This force yields a secondary moment just above the top of the hold-down of height (h_d), which is $M=V \cdot h_d$. The thickness ($t_{s0,2}$) is the strap thickness corresponding to a force (V) and a moment (M) that satisfy the interaction capacity formula $F_c/N_{c,Rd}+M/M_{c,Rd}=1$, where ($N_{c,Rd}$) and ($M_{c,Rd}$) are the compressive and bending moment capacities of the chord stud, respectively, calculated in accordance with EN 1993 (CEN, 2003, 2010).

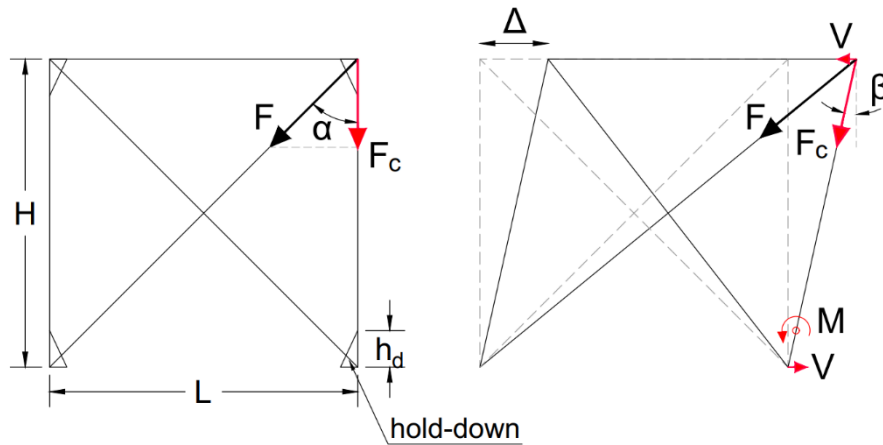


Fig. 3.9 Secondary force and moment for the calculation of (t_{s0}) strap thickness

3.5.2.3 Lateral load capacity under a vertical loading ratio

The effect of the vertical load ratio on the lateral load capacity of the walls for various strap thickness ratios ($t_{s,2}/t_{s0,2}$) is illustrated in Fig. 3.10. For each of those cases, the ratio of the lateral capacity of wall 2 ($F_{u,P,2}$) subjected to the vertical load, over the lateral capacity of the same wall ($F_{u,2}$) under zero vertical load, was plotted against the variation of the vertical load ratios ($P/P_{w,2}$) used in the parametric analysis. (P) stands for the applied vertical load, while ($P_{w,2}$) represents the total axial load capacity of wall 2. It can be seen that all the curves followed the same trend. Therefore, the average values of the lateral capacity ratios were considered, leading to Eq. (8), represented by a second-order polynomial and shown in Fig. 3.10.

$$f_3 = \frac{F_{u,P,2}}{F_{u,2}} = 1 - 0.60 \left(\frac{P}{P_{w,2}} \right) + 0.30 \left(\frac{P}{P_{w,2}} \right)^2 \quad (8)$$

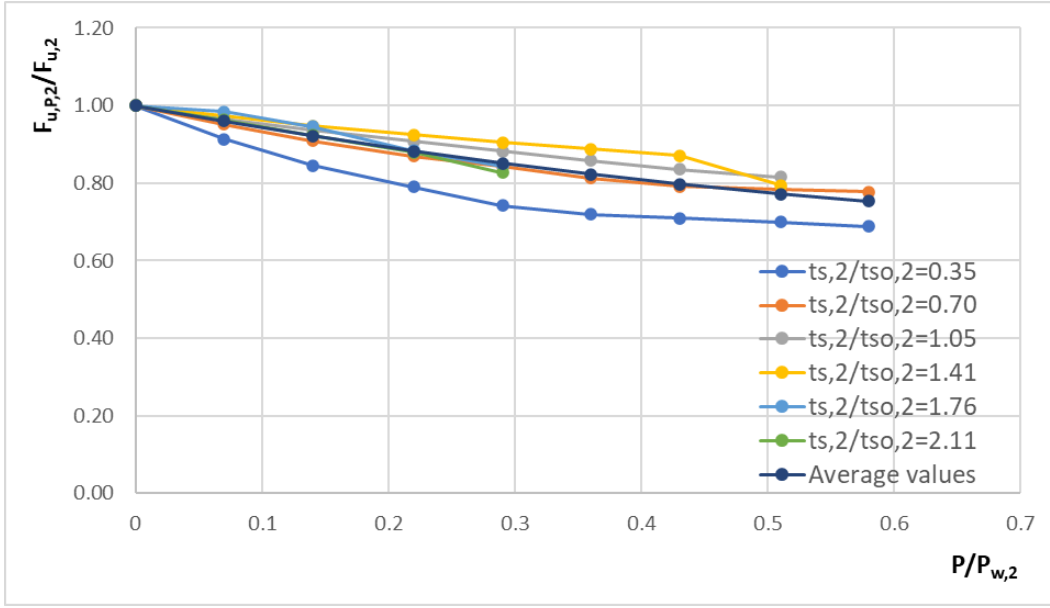


Fig. 3.10 Effect of vertical load ratio on the lateral load capacity

3.5.2.4 Ductility under a vertical loading ratio

To derive the equation for the ductility ($\mu_{P,2}$) of wall 2 subjected to vertical loading, the ratio ($\mu_{P,2}/\mu_2$) for each case of ($t_{s,2}/t_{so,2}$) was plotted against the range of ($P/P_{w,2}$) used in the parametric analysis (see Fig. 3.11). In this case, the average was not representative of the trend, and it was found that a third-degree polynomial best represented each curve in Fig. 3.11a. Plotting the coefficient A, B, and C (D was always 1) values against the ($t_{s,2}/t_{so,2}$) ratios yielded the best-fit curves, represented by the polynomials in Eqs. (10)-(12). The final equation for the ductility of the wall ($\mu_{P,2}$) under a vertical loading ratio ($P/P_{w,2}$) was given by Eq. (9), and the predicted values are plotted in Fig. 3.11b. The results showed a very good agreement between the two sets of data.

$$f_4 = \frac{\mu_{P,2}}{\mu_2} = A \left(\frac{P}{P_{w,2}} \right)^3 + B \left(\frac{P}{P_{w,2}} \right)^2 + C \frac{P}{P_{w,2}} + 1 \quad (9)$$

where,

$$A = 10.47 \left(\frac{t_{s,2}}{t_{so,2}} \right)^3 - 44.19 \left(\frac{t_{s,2}}{t_{so,2}} \right)^2 + 30.69 \left(\frac{t_{s,2}}{t_{so,2}} \right) + 4.85 \quad (10)$$

$$B = -8.55 \left(\frac{t_{s,2}}{t_{so,2}} \right)^3 + 31.65 \left(\frac{t_{s,2}}{t_{so,2}} \right)^2 - 18.64 \left(\frac{t_{s,2}}{t_{so,2}} \right) - 7.47 \quad (11)$$

$$C = -1.75 \left(\frac{t_{s,2}}{t_{so,2}} \right)^3 - 5.95 \left(\frac{t_{s,2}}{t_{so,2}} \right)^2 + 3.05 \left(\frac{t_{s,2}}{t_{so,2}} \right) + 0.81 \quad (12)$$

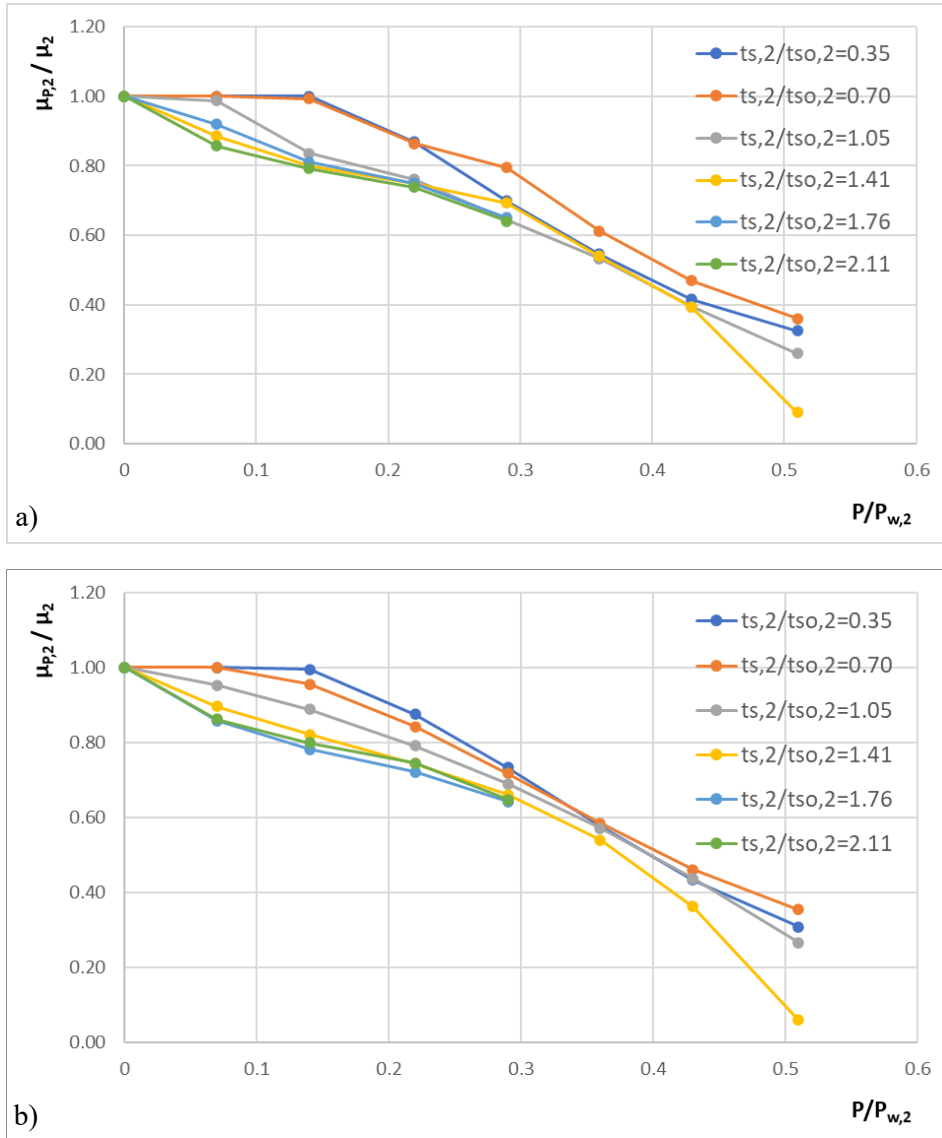


Fig. 3.11 Effect of vertical load ratio on the lateral load capacity, a) results of analyses, and b) predicted values using Eq. (9)

While the equations developed above are based on the models and design assumptions considered in this study, they can show the general response of the CFS strap-braced stud wall frames and hence should be useful for preliminary design purposes as discussed in the following section.

3.5.3 Practical design procedure for the preliminary design of multi-storey stud wall frames

The response prediction equations derived in this study can be directly implemented to design a multi-storey CFS strap-braced frame system, following the procedure summarised in the flowchart of Fig. 3.12. The proposed design process starts with the design for gravity loading, followed by design against seismic loading. It involves a) verifying the axial resistances of the straps and the chord studs calculated in accordance with Eurocode 3 (CEN, 2003, 2010), and b) calculating the lateral load and ductility capacities of the wall panels under the presence of vertical loading using the equations developed in section 3.5.2, and comparing them with the design storey shear forces obtained from Eurocode 8 (CEN, 2004) and the selected target ductility. It has to be noted that only the axial resistance of the chord studs needs to be checked because the effect of the $P-\Delta$ secondary moments is already included in the equations.

The proposed design methodology can take into account the effects of vertical loading on the lateral load capacity and ductility of strap-braced stud walls, while it can significantly simplify the design of non-linear multi-storey systems as there is no need to model the wall panels with different strap and chord thicknesses and vertical load ratios. As discussed before, all such data will be easily estimated based on the response of a single reference wall with the same topology and material properties under zero vertical loading, obtained from FE model analyses (as described in section 3.3) or available experimental data.

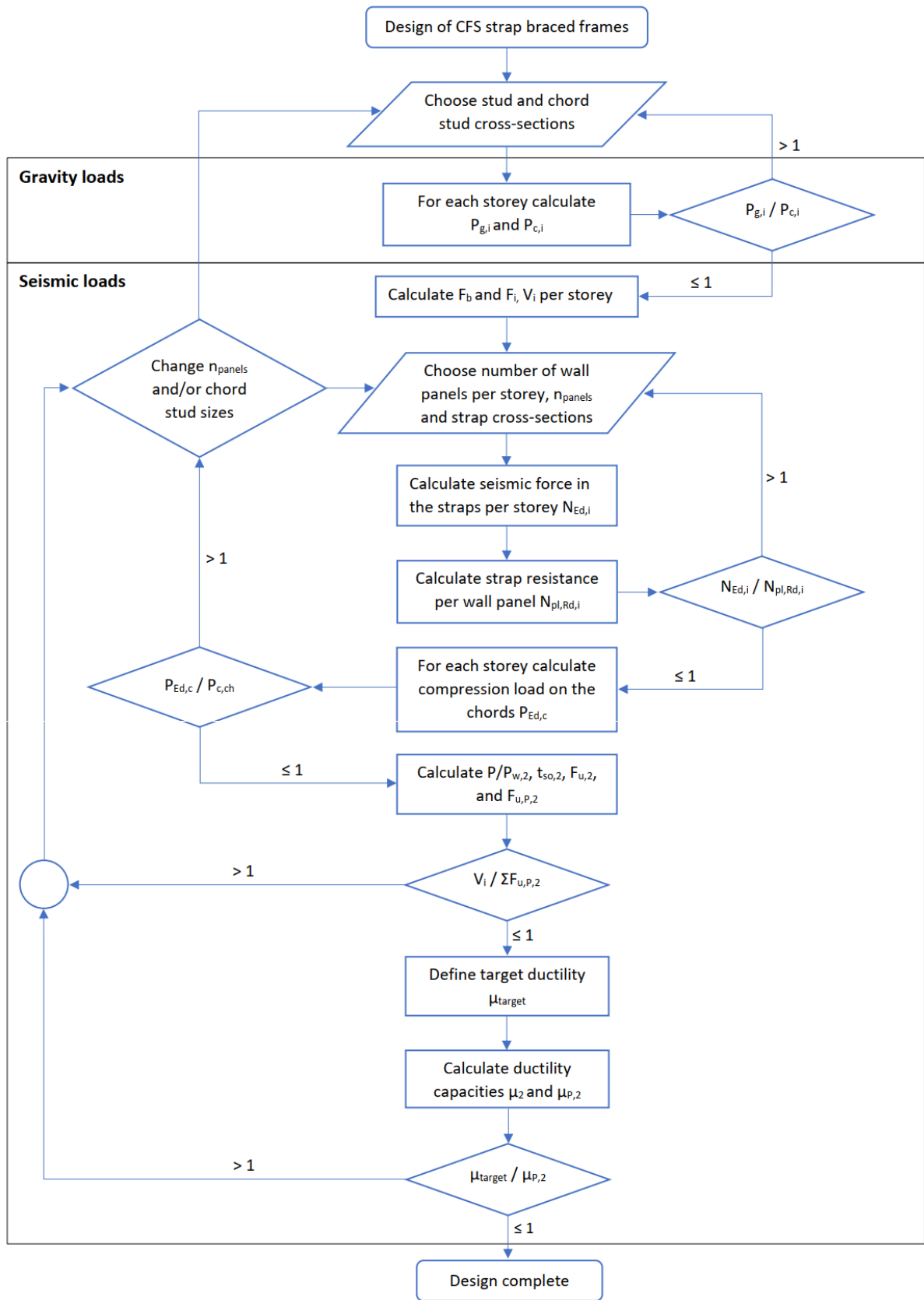


Fig. 3.12 Proposed design procedure of CFS strap-braced frames under simultaneous vertical and seismic loading

3.6 Design of a case study frame

The efficiency of the proposed design methodology, described in the previous section, was demonstrated through the preliminary design of a 6-storey CFS strap-braced frame, shown in Fig. 3.13, subjected to gravity and seismic loading. The gravity load capacities and verifications were done per EN 1993 (CEN, 2003, 2010), whereas the seismic loads and verifications followed the provisions of EN 1998-1 (CEN, 2004). However, the proposed methodology is general, and other design regulations can be easily adopted. The lateral load and ductility capacities of the walls at each storey, under the presence of vertical loading, were calculated with the proposed design formulation introduced in section 3.5. In this study, the target ductility (μ_{target}) was assumed to be equal to 4, representing a medium to high ductility class system.

The frame comprised three bays, each having a length of ($L_{\text{bay}}=2.44$ m) and a total length of 7.32 m. In the absence of any height limitations for these systems in EN 1998-1 (CEN, 2004), the maximum limit of 19.5 m (= 65 ft), imposed by S213-07 (AISI S213, 2012), was taken into account in this study, with the total frame height being 16.44 m. The storey height (H_i) was 2.74 m, with 2.44 m being the clear height and 0.3 m the floor depth. A tributary width (b_{eff}) of area loads equal to 5 m was adopted for the gravity loading and mass calculations.

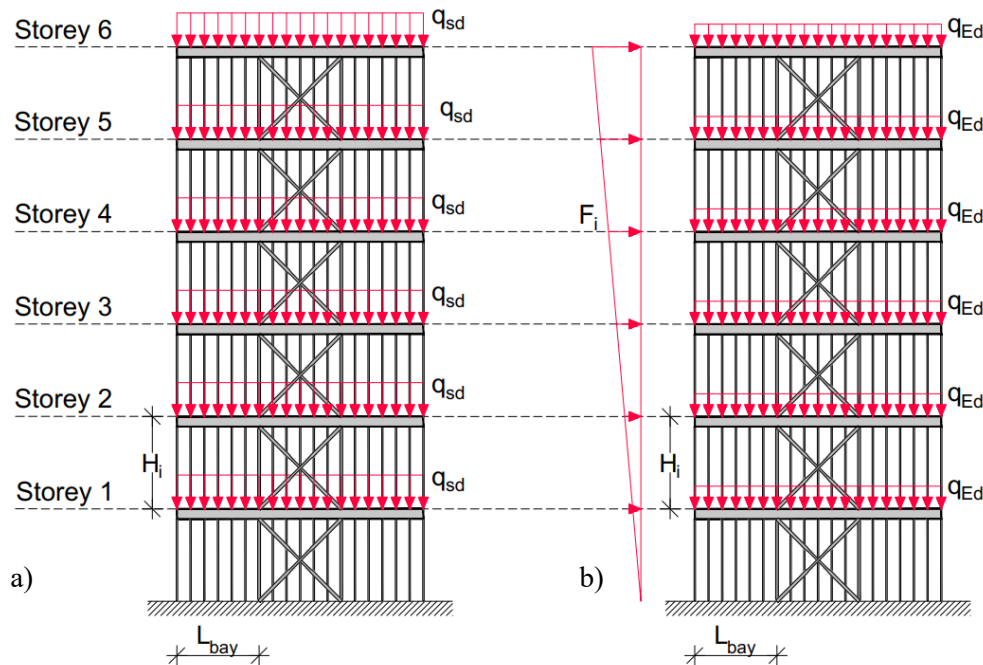


Fig. 3.13 Case study frame under a) non-seismic and b) seismic actions

Two design solutions were considered in this section. The first solution (Eurocode Design) was a conventional design that satisfied the capacity checks of the Eurocode. However, as discussed before,

the adverse effects of gravity load on the ductility of CFS strap-braced walls are not taken into account in the current design regulations, which resulted in low ductility capacity at some storey levels. The second solution (Proposed Design) was based on the proposed design procedure discussed in section 3.5.3 (see Fig. 3.12) to satisfy the selected target ductility throughout the structure. Finally, the adequacy of the two design solutions was assessed by using the results of detailed FE models in ABAQUS (Dassault Systèmes Simulia, 2014).

In this study, the studs were single lipped channel-sections, while the chord studs were composed of two back-to-back connected stud cross-sections. The dimensions of the studs and chord studs for the two solutions are shown in Table 3.2. In this table, (h) represents the depth, (b) the width, (c) the lip and (t) the thickness of the sections. The cross-sections were obtained based on the design checks for gravity and seismic loading performed in the following sections.

Table 3.2 Cross-sections of wall elements for Eurocode and Proposed Design solutions

Storey No	Eurocode Design		Proposed Design	
	Stud and chord stud cross-section h×b×c, t (mm)	Diagonal strap thickness t _s (mm)	Stud and chord stud cross-section h×b×c, t (mm)	Diagonal strap thickness t _s (mm)
1	92.1×41×12.7, 2.0	4.0	92.1×41×12.7, 2.0	4.0
2	92.1×41×12.7, 1.5	4.0	92.1×41×12.7, 2.0	4.0
3	92.1×41×12.7, 1.5	4.0	92.1×41×12.7, 2.0	4.0
4	92.1×41×12.7, 1.16	3.0	92.1×41×12.7, 1.5	3.0
5	92.1×41×12.7, 1.16	3.0	92.1×41×12.7, 1.5	3.0
6	92.1×41×12.7, 1.16	1.5	92.1×41×12.7, 1.16	1.5

3.6.1 Design for gravity loading

The frame was assumed to be part of a building of domestic and residential activities (category A), per EN1991-1 (CEN, 2002b). The total permanent load applied on each storey was taken as $g=1.5 \text{ kN/m}^2$, and the live load was $q=2 \text{ kN/m}^2$. The partial factors for the dead and the live loads per EN1990 (CEN, 2002a) were $\gamma_G=1.35$ and $\gamma_Q=1.50$, respectively. The capacity checks against gravity loading for the Eurocode design and the proposed design are summarised in Table 3.3.

Table 3.3 Design for gravity loading

Storey No	$P_{g,i}$ (kN)	Eurocode Design		Proposed Design	
		$P_{c,i}$ (kN)	$\frac{P_{g,i}}{P_{c,i}}$	$P_{c,i}$ (kN)	$\frac{P_{g,i}}{P_{c,i}}$
1	1103.5	1619.0	0.68	1619.0	0.68
2	919.6	1200.0	0.77	1619.0	0.57
3	735.7	1200.0	0.61	1619.0	0.45
4	551.8	895.3	0.62	1200.0	0.46
5	367.8	895.3	0.41	1200.0	0.31
6	183.9	895.3	0.21	895.3	0.21

In Table 3.3, ($P_{g,i}$) stands for the total vertical design load on i^{th} -storey, ($P_{c,i}$) is the total vertical load capacity of all vertical elements in the i^{th} -storey, calculated per Eurocode 3 (CEN, 2003, 2010), and ($P_{g,i}/P_{c,i}$) represents the gravity loading adequacy ratio. Both the Eurocode and the proposed design solutions satisfied the gravity load check, yielding a maximum adequacy ratio of 0.68.

3.6.2 Design for seismic loading

EN 1998-1 (CEN, 2004) does not include explicit rules for the design of CFS frames (unlike S213-07 (AISI S213, 2012)), and hence the generic rules for steel frames with concentric diagonal bracings were applied. These rules are added to the rules given in EN 1993 (CEN, 2003, 2010) and aim to ensure that the structure will dissipate the seismic energy in a ductile manner. This is achieved by allowing specific dissipative members to undergo large inelastic deformations while preventing non-desirable, brittle modes of failure through capacity design rules (CEN, 2004; PEER, 2010).

The ability of a structure to dissipate energy is expressed through the behaviour factor (q), which reduces the design seismic forces obtained based on the elastic behaviour (Pauley and Priestley, 1992; CEN, 2004). The level of this reduction directly depends on the expected ductility demand of the structure and subsequently affects the rules that will govern the design and detailing. EN 1998-1 (CEN, 2004) accounts for three ductility classes, low (DCL), medium (DCM) and high (DCH). The first class practically refers to non-dissipative structures, which are not suitable for seismic regions. For concentrically braced frames with diagonal bracings, the behaviour factor (q) corresponding to (DCM) and (DCH) classes is 4.

The seismic energy-dissipative elements in a CFS frame, employing strap-braced walls as the primary lateral force-resisting system, are the diagonal straps. Only the straps under tension are effective (the straps under compression have no contribution due to their high slenderness), and they have to resist the

force ($N_{Ed,i}$) as shown in Fig. 3.14, where (V_i) stands for the shear force at the i^{th} -storey, (α_i) is the angle of the braces and (n_{panels}) represents the number of the storey wall panels at each storey level.

$$N_{Ed,i} = \frac{V_i}{n_{\text{panels}} \cdot \cos(\alpha_i)} \quad (13)$$

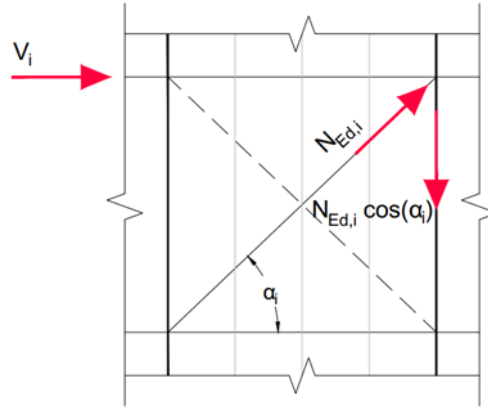


Fig. 3.14 Lateral force distribution on a wall panel

The chord-studs are considered as non-dissipative members. These elements are subjected to the axial compressive force due to gravity loads, alongside the vertical component of the diagonal tensile seismic force ($N_{Ed,i} \times \sin(\alpha_i)$), magnified by an overstrength factor using Eq. (14):

$$P_{Ed,c} = P_{Ed,G} + 1.1 \cdot \gamma_{ov} \cdot \Omega \cdot N_{Ed,i} \cdot \cos(\alpha_i) \quad (14)$$

where ($P_{Ed,G}$) is the design compression force of the chord studs due to the non-seismic gravity loads for the seismic design situation, (γ_{ov}) is the overstrength factor considered to be 1.25, and (Ω) is the minimum value of $\Omega_i = N_{pl,Rd,i} / N_{Ed,i}$ of all diagonals, in which ($N_{pl,Rd,i}$) is their design plastic capacity and ($N_{Ed,i}$) is their design axial force in the seismic design situation.

In this study, the seismic loading was calculated following the lateral force method in EN 1998-1 (CEN, 2004), as the structure was assumed to be regular in plan and elevation. The parameter values describing the Type 1 design response spectrum corresponded to ground type B and importance class II. The building site was assumed to be situated in a high-seismicity zone; thus, a value of reference peak ground acceleration $\alpha_{gR} = 0.35 \text{ g}$ was adopted. The combination of the seismic action per EN 1990 (CEN, 2002a) was used to calculate the mass: $G_k + \psi_{E,i} \cdot Q_k$, where (G_k) and (Q_k) represent the permanent (dead) and variable (live) loads, respectively, and ($\psi_{E,i}$) is the coefficient for variable actions, taken as 0.3. Finally, the behaviour factor $q=4$ was considered, as prescribed for this structural type for medium (DCM) and high (DCH) ductility classes.

3.6.2.1 Reference wall properties

The strap-braced walls used in the case study example had the same topology and material properties as the selected reference wall in section 3.3 (see Fig. 3.1). However, the strap-braced walls used in the multi-storey system (named as wall 2) have different section sizes and are subjected to different vertical load ratios, and therefore their lateral load capacity and ductility will be different compared to the reference wall (named as wall 1). Using the strap thickness $t_{s,1}=1.11$ mm for the reference wall 1, resulted in a load capacity $F_{u,1}=38.4$ kN and ductility $\mu_1=22.61$ under zero vertical loading condition, directly obtained from the validated FE model shown in Fig. 3.2. The material properties were given in Table 3.1, and the hold-down height (h_d) for the calculation of $t_{s,2}$ (see Fig. 3.9) was equal to 0.35 m. This information was then used to estimate the lateral load capacity and ductility of all the strap-braced walls during the proposed design process, as will be explained in the following sections.

3.6.2.2 Design of straps and chord studs

The axial capacity of the straps and the chord studs of both solutions for the seismic design situation were checked in accordance with section 3.6.2, and the results are summarised in Table 3.4. For the design of the straps, ($N_{pl,Rd,i}$) is the strap design plastic capacity, ($N_{Ed,i}$) is the design tensile force in the seismic design situation, ($N_{Ed,i}/N_{pl,Rd,i}$) is the adequacy ratio, and (i) represents the storey number. For the design of the chord studs, ($P_{Ed,c}$) is the chord stud design compressive force per Eq. (14), ($P_{c,ch}$) is the design compressive capacity, and ($P_{Ed,c}/P_{c,ch}$) is the adequacy ratio. It can be seen that the straps and chord studs of both the Eurocode and Proposed designs satisfied the code requirements at all storey levels (maximum adequacy ratio of 0.97).

Table 3.4 Strap and chord stud axial capacity

Storey No	Eurocode Design				Proposed Design			
	Straps		Chord studs		Straps		Chord studs	
	$N_{Ed,i}$ (kN)	$\frac{N_{Ed,i}}{N_{pl,Rd,i}}$	$P_{Ed,c}$ (kN)	$\frac{P_{Ed,c}}{P_{c,ch}}$	$N_{Ed,i}$ (kN)	$\frac{N_{Ed,i}}{N_{pl,Rd,i}}$	$P_{Ed,c}$ (kN)	$\frac{P_{Ed,c}}{P_{c,ch}}$
1	145.5	0.97	188.5	0.86	145.5	0.97	188.5	0.86
2	138.6	0.92	172.5	1.04	138.6	0.92	172.1	0.80
3	124.7	0.83	153.8	0.93	124.7	0.83	153.4	0.70
4	104.0	0.92	125.6	1.03	103.9	0.92	125.7	0.76
5	76.2	0.68	90.7	0.74	76.2	0.68	90.8	0.55
6	41.6	0.74	48.8	0.40	41.6	0.74	48.8	0.40

3.6.2.3 Lateral load capacity of the wall panels

The lateral load capacity of the wall panels at each storey was calculated with the aid of the proposed formulation, expressed by Eq. (6) for the zero vertical loading condition ($F_{u,2}$) and Eq. (8) for the case vertical loading is applied ($F_{u,P,2}$). The equation parameters alongside the lateral load capacities and the ($V_i/F_{u,P,2}$) adequacy ratios for the Eurocode and the proposed design solutions are given in Table 3.5. ($t_{s,2}$) and ($t_{s,1}$) are the diagonal strap thicknesses, whereas ($t_{ch,2}$) and ($t_{ch,1}$) are the chord stud thicknesses of the storey wall and the reference wall, respectively. ($P/P_{w,2}$) is the vertical loading ratio, and (V_i) is the shear force at storey (i). The results indicate that both the Eurocode and the proposed designs can provide the required lateral load capacity at all storey levels (maximum adequacy ratio of 0.9).

Table 3.5 Lateral load capacities and adequacy ratios of storey wall panels

Storey No	Eurocode Design						Proposed Design					
	$\frac{t_{s,2}}{t_{s,1}}$	$\frac{t_{ch,2}}{t_{ch,1}}$	$F_{u,2}$ (kN)	$\frac{P}{P_{w,2}}$	$F_{u,P,2}$ (kN)	$\frac{V_i}{F_{u,P,2}}$	$\frac{t_{s,2}}{t_{s,1}}$	$\frac{t_{ch,2}}{t_{ch,1}}$	$F_{u,2}$ (kN)	$\frac{P}{P_{w,2}}$	$F_{u,P,2}$ (kN)	$\frac{V_i}{F_{u,P,2}}$
1	3.60	1.72	127.6	0.20	114.0	0.90	3.60	1.72	127.6	0.20	114.0	0.90
2	3.60	1.29	125.1	0.22	110.5	0.89	3.60	1.72	127.6	0.16	116.0	0.84
3	3.60	1.29	125.1	0.17	113.1	0.78	3.60	1.72	127.6	0.13	118.2	0.75
4	2.70	1.00	94.0	0.18	84.9	0.87	2.70	1.29	95.7	0.13	88.6	0.83
5	2.70	1.00	94.0	0.12	87.7	0.61	2.70	1.29	95.7	0.09	90.9	0.59
6	1.35	1.00	49.9	0.06	48.2	0.61	1.35	1.00	49.9	0.06	48.2	0.61

3.6.2.4 Ductility of the wall panels

The storey wall panel ductility under zero vertical load (μ_2) and under vertical loading ($\mu_{P,2}$) was calculated using Eq. (7) and Eq. (9), respectively, for both design solutions. As mentioned before, the multi-storey CFS strap-braced frame was required to reach a target ductility (μ_{target}) equal to 4, which is representative of a medium to high ductility class system and consistent with the applied behaviour factor. It was observed that despite meeting all the Eurocode capacity requirements, the ductility capacity of storeys 2 to 5 was unacceptably low for seismic design, with values well below the target ductility. While the capacity design rules in the Eurocode aim to provide a minimum level of overstrength to the chord studs, the presented results clearly indicate that the adverse effects of the secondary moments due to P- Δ cannot be compensated. The proposed design method, however, led to high ductility levels at all storeys by preventing premature failure modes in the chord studs.

Table 3.6 Storey wall ductility values

Storey No	Eurocode Design					Proposed Design				
	$\frac{t_{s,2}}{t_{so,2}}$	μ^2	$\frac{P}{P_{w,2}}$	$\mu_{P,2}$	$\frac{\mu_{target}}{\mu_{P,2}}$	$\frac{t_{s,2}}{t_{so,2}}$	μ^2	$\frac{P}{P_{w,2}}$	$\mu_{P,2}$	$\frac{\mu_{target}}{\mu_{P,2}}$
	1	1.44	18.4	0.20	14.1	0.28	1.44	18.4	0.20	14.0
2	1.93	2.3	0.22	1.6	2.44	1.44	18.4	0.16	14.6	0.27
3	1.93	2.3	0.17	1.7	2.34	1.44	18.4	0.13	15.2	0.26
4	1.90	3.8	0.18	2.8	1.41	1.45	18.2	0.13	14.9	0.27
5	1.90	3.8	0.12	3.0	1.33	1.45	18.2	0.09	15.8	0.25
6	0.95	22.6	0.06	22.1	0.18	0.95	22.6	0.06	22.1	0.18

3.6.2.5 Verification of the predicted values

The predicted lateral load capacity and ductility for the wall panels of the Eurocode and Proposed designs were verified, comparing the results with corresponding detailed FE model analyses in ABAQUS. The experimentally validated numerical model presented in section 3.3 was adopted, accounting for the member thicknesses and vertical loading ratios of the design solutions. A very good agreement was achieved between the corresponding values predicted by the formulas and ABAQUS analyses. For the Eurocode Design solution, the average errors in the estimation of lateral load capacity and ductility were 4.0% and 12.4%, respectively. For the proposed design solution, the average error in the estimation of the lateral load capacity and ductility was around 4.0%. It should be mentioned that for the Eurocode Design solution, the ductility error was slightly higher since the walls reached unacceptably low ductility levels, for which the proposed formula was slightly less accurate. However, the proposed method could efficiently identify the storey levels that exhibited low ductility levels with acceptable accuracy for practical applications.

Table 3.7 Verification of the predicted values

Storey No	Eurocode Design				Proposed Design			
	$F_{u,P,2}$	F_{ABAQUS}	$\mu_{P,2}$	μ_{ABAQUS}	$F_{u,P,2}$	F_{ABAQUS}	$\mu_{P,2}$	μ_{ABAQUS}
	(kN)	(kN)			(kN)	(kN)		
1	114.0	120.4	14.1	14.8	114.0	120.3	14.0	14.8
2	110.5	105.2	1.6	1.9	116.1	121.7	14.6	15.5
3	113.1	108.8	1.7	2.1	118.2	123.1	15.2	15.9
4	85.0	80.7	2.8	2.4	88.6	93.0	14.9	15.3
5	87.7	85.5	3.0	2.6	90.9	94.4	15.8	16.3
6	48.2	49.1	22.1	21.3	48.2	49.1	22.1	21.3
Average Error	4 %		12.4 %		4 %		4.1 %	

3.7 Summary and concluding remarks

The work presented in this paper aimed to investigate the seismic performance of strap-braced stud walls under simultaneous vertical and seismic loading and develop a preliminary design methodology for such systems. To this end, an experimentally validated detailed FE model in ABAQUS was employed, accounting for material nonlinearities and secondary moments due to P- Δ effects. Through a comprehensive parametric study, the effect of strap thickness and vertical loading ratio on the lateral capacity and ductility of single CFS strap-braced stud walls was investigated. The results were used to develop practical equations to predict the structural response of the single stud walls, leading to a design framework for non-linear multi-storey CFS strap-braced frame systems in accordance with Eurocode 8. The research work led to the following conclusions:

- As expected, increasing the strap thickness increased the lateral load-bearing capacity of the wall almost proportionally. However, if the strap thickness exceeded a limit value, the compressive chord stud failed prematurely due to buckling, as a result of being subjected to a higher compressive force transferred from the straps, and hence secondary bending moment from P- Δ effects. Consequently, the straps could not reach their ultimate strain, and the ultimate displacement and ductility of the wall significantly dropped (up to 90%), leading to unacceptable seismic performance.
- Increasing the vertical load applied on a strap-braced stud wall always caused a reduction in the lateral load-bearing capacity of the wall, especially for the load ratios above 22%. In such cases, the increased compressive force in the chord stud, combined with the secondary moment due to P- Δ effects, led to the premature buckling failure of the chord stud before the full capacity of the straps was exploited.
- It was shown that the developed secondary moments due to P- Δ effects adversely affected the shear resistance, deformation capacity and ductility of strap-braced stud walls, something that is not directly accounted for in current design guidelines such as those in the Eurocode. This observation indicates that the compressive chord stud, designed as an axially loaded member per capacity design rules, may experience premature failure, leading to unacceptably low ductility capacity of the wall system for seismic applications.
- A framework was developed for seismic design of non-linear multi-storey strap-braced wall frames under simultaneous vertical and seismic loading, using the results of numerical analysis on a single “reference” wall under zero vertical loading. The efficiency of the proposed method was demonstrated through the preliminary design of a 6-storey strap-braced wall frame. While both the Eurocode and the proposed design solutions could provide the required lateral load capacity, it was shown that the code based design exhibited a very low ductility at some storey

levels leading to brittle failure modes and unacceptable seismic performance. The proposed design method, however, led to high ductility levels at all storeys by preventing premature failure modes in the chord studs.

- The proposed design formulation predicted the lateral load capacity and ductility with an accuracy of around 4%, compared to the results of detailed ABAQUS analyses. While these equations are based on the models and design assumptions considered in this study, they can show the general response trends, and therefore, should prove suitable for the preliminary design of multi-storey CFS strap-braced frames.

3.8 Acknowledgements

The authors would like to express their gratitude to Prof. C.A. Rogers, at the Department of Civil Engineering and Applied Mechanics, McGill University, for providing experimental material data used for the development of the numerical models.

3.9 Author contribution

- Ioannis Papargyriou:

Conceptualisation, Methodology, Formal Analysis, Investigation, Writing- Original draft, Writing- Reviewing and Editing, Visualisation

- Dr. Iman Hajirasouliha:

Conceptualisation, Methodology, Validation, Writing- Reviewing and Editing, Supervision

CHAPTER 4

Performance-Based Seismic Design and Assessment of Multi-Storey CFS Strap-Braced Frames

This chapter is based on the paper titled: “I. Papargyriou, I. Hajirasouliha, Performance-based seismic design and assessment of multi-storey CFS strap-braced frames”. Submitted to: Engineering Structures, Date submitted: 8/9/2021, under review.

4.1 Abstract

Cold-formed steel (CFS) structures typically rely on diagonally braced stud walls to withstand lateral forces. While the response of CFS single-wall panels has been extensively investigated, limited studies focused on the seismic performance of multi-storey CFS strap-braced frames. Previous research highlighted that the presence of vertical loading can significantly reduce the lateral load and ductility capacity of strap-braced walls by amplifying the secondary moments due to P- Δ effects. While this effect is generally ignored in current design practice, it may lead to premature failures and poor seismic performance. This study aims to investigate the efficiency of a new design methodology to take into account the vertical load effects on the performance of multi-storey CFS strap-braced frames. Detailed experimentally validated FE models of CFS panels were developed in ABAQUS and used to obtain equivalent hysteretic models in OpenSees. The seismic performance of 6-storey strap-braced frames designed based on the Eurocode 8 and the proposed design methodology were then investigated under a set of artificial spectrum-compatible records. While the code-base design did not satisfy the ASCE/SEI 41-17 Life Safety (LS) and Collapse Prevention (CP) ductility limits, all performance targets were met using the proposed design methodology. The results of Incremental Dynamic Analyses (IDA) also indicated that meeting the code capacity requirements could not prevent extensive global damage in the strap-braced frames, due to soft-storey failure modes associated with the premature buckling of chord

studs. Finally, the efficiency of the proposed design compared to its code-compliant counterpart was demonstrated under a set of 20 real spectrum compatible records, showing higher ductility capacity and considerably lower damage levels.

4.2 Introduction

Cold-Formed Steel (CFS) structural systems are increasingly used in modern construction practices due to their unique advantages, such as lightweight, flexibility in cross-sectional shapes, and ease of handling and transportation compared to conventional hot-rolled steel structures. In conventional multi-storey CFS buildings, strap-braced stud walls are widely used as the primary force-resisting system against lateral wind and earthquake loads. The lateral resistance is generally provided by diagonal X-shaped bracing members (Velchev, 2008b), while knee-braced (Zeynalian and Ronagh, 2012), K-braced (Zeynalian *et al.*, 2012; Pourabdollah *et al.*, 2017; Usefi *et al.*, 2020), or a combination of K- and X-shaped braces (Gerami and Lotfi, 2014) have also been utilised. Previous studies indicated that the structural response of the strap-braced stud walls can be considerably affected by the wall's aspect ratio (Comeau, 2008; Velchev *et al.*, 2010; Mirzaei *et al.*, 2015). It was shown that ratios greater than 1:2 might lead to a less ductile behaviour due to the premature failure of the chord studs. Studies on the performance of walls employing welded joints (Comeau, 2008; Velchev *et al.*, 2010) suggested a ductile response, provided a careful design and fabrication are implemented. In common practice, CFS strap-braced walls are sheathed with a wide range of materials like gypsum, OSB or plywood boards. Although they can increase the lateral load capacity through their stiffness (Lu and Rogers, 2018), a composite action with the diagonal braces is not accounted for in the current design codes as a result of their brittle nature (Moghimi and Ronagh, 2009).

Under seismic load actions, diagonally strap braced systems dissipate energy mainly by the plastic deformation of the tensile straps, as the straps in compression buckle at a very early loading stage due to their high width-to-thickness ratio (or high slenderness). Although the straps usually have a uniform cross-section over their total length, it has proven beneficial to reduce the width over a length in the middle, acting as a seismic fuse and protecting the susceptible elements such as the connections of the straps with the chord studs (Velchev, 2008b). Currently, the primary approach to avoid brittle modes of failure in CFS stud wall systems is achieved by implementing capacity design rules. The aim is to provide non-dissipative members with a desirable level of over-strength, to sustain the maximum forces anticipated in the plastic regions. This eventually allows the system to develop ductility (i.e. the ability to experience large plastic deformations while maintaining their yield capacity) through yielding at controlled locations (Al-Kharat and Rogers, 2008; Kasaeian *et al.*, 2020). The highest ductility capacity

can be attained if premature failure modes in the cord studs are prevented before the diagonal straps reach their ultimate strain (Papargyriou *et al.*, 2021).

There are limited experimental research studies on the seismic response of CFS multi-storey systems employing diagonal braces. Aiming to study the non-linear dynamic behaviour of CFS structural systems, Kim *et al.* (Kim *et al.*, 2006) performed full-scale shaking table tests on two-storey one-bay strap-braced frames with box-shaped chord studs and welded connections. A maximum drift ratio of 3% at the first storey was reported, and no obvious damage was observed, confirming the suitability of the system for seismic applications. In a similar study, Fiorino *et al.* (Fiorino *et al.*, 2019) tested three-storey two-bay CFS strap-braced wall frames designed per Eurocode 8 as non-dissipative systems. The system exhibited satisfactory performance and achieved a maximum drift ratio of over 2%, without significant damage.

In their numerical study at the structural level, Lee and Foutch (Lee and Foutch, 2010) performed a modified incremental dynamic analysis of two-, four- and six-storey strap-braced wall frames, employing twenty accelerograms. They concluded that the R factor of 4 was adequate for this system, while the per FEMA 355F (FEMA, 2000b) estimated collapse drift capacities were too conservative. Velchev (Velchev, 2008b) and Comeau *et al.* (Comeau *et al.*, 2010) assessed the AISI S213 Canadian and FEMA P695 seismic force modification factors, alongside the building height limits for multi-storey concentrically strap-braced systems. Their studies, in general, confirmed the code suggested values for limited ductility (LD) and conventional construction (CC) systems. In another relevant study, Fiorino *et al.* (Fiorino *et al.*, 2017) conducted a numerical study following FEMA P695 (ATC, 2009) specifications to assess the behaviour factor for CFS strap-braced stud wall systems. They investigated the seismic performance of a set of fourteen archetypes using CFS strap-braced stud walls featuring screwed connections with gusset plates. The results indicated the suitability of the system for seismic applications; however, the studied structures exhibited a relatively low behaviour factor (q) around 2.5. Davani *et al.* (Davani *et al.*, 2016) also evaluated the performance of nine full-scale wall specimens based on the experimental work of Moghimi and Ronagh (Moghimi and Ronagh, 2009), subjected to 14 ground motions. Their study showed that the contribution of cladding and corner brackets can increase the lateral strength and stiffness and reduce the occurrence of damage in strap-braced wall systems.

Experimental test studies on the monotonic and cyclic response of single-wall panels were generally conducted without accounting for any additional vertical loads. Additional vertical loads have been applied only in a few experimental studies focusing on sheathed walls without employing diagonal straps (Lange and Naujoks, 2007; Accorti *et al.*, 2016; Jihong Ye *et al.*, 2016). However, due to their inherently different mechanism, the results do not apply to strap-braced systems. It should be noted that Eurocode 8 (CEN, 2004) does not contain explicit design rules for CFS stud wall systems, and the ones intended

for conventional hot-rolled steel structures are generally used. Following these, the lateral load capacity of strap-braced walls is based on the tensile strength of the straps alone, under zero vertical loading. Therefore, the secondary bending moments due to P- Δ effects are not currently accounted for in the seismic design of CFS strap-braced stud wall systems. However, research conducted by Papargyriou *et al.* (Papargyriou *et al.*, 2021) suggested that the lateral load and ductility capacities of strap-braced wall systems were adversely affected by vertical loads leading to premature failure modes in chord studs due to the P- Δ effects.

In a recent study by Papargyriou and Hajirasouliha (Papargyriou and Hajirasouliha, 2021), a new methodology was developed for designing CFS strap-braced wall frames, proposing preliminary design formulae to predict the lateral load and ductility capacity of strap-braced stud walls, considering different cross-sectional thicknesses and vertical load levels. The efficiency of the proposed method was demonstrated by designing a CFS 6-storey frame following Eurocodes' guidelines. It was shown that although the member capacity checks were satisfied, the ductility of the system was well below the target ductility at some storey levels, yielding a brittle response and an unacceptable seismic performance. By applying their proposed methodology, however, the design solution could satisfy both the Eurocode capacity checks and the target ductility demands at different earthquake intensity levels.

The present work aims to assess the efficiency of the design methodology proposed by Papargyriou and Hajirasouliha (Papargyriou and Hajirasouliha, 2021), for the first time, at the structural level and provide a better understanding of the seismic performance of CFS strap-braced multi-storey systems by quantifying their global damage and failure mechanism at different earthquake intensity levels. Detailed non-linear FE models of CFS panels are developed in ABAQUS (Dassault Systèmes Simulia, 2014), and their accuracy is demonstrated against experimental results in the literature. To increase the computational efficiency, the validated models are then used to obtain equivalent hysteretic models in OpenSees (Mazzoni *et al.*, 2007). The seismic performance of 6-storey strap-braced frames designed based on the Eurocode-8 and the proposed design methodology is then investigated under a set of artificial spectrum-compatible records under increasing intensity (i.e. incremental dynamic analyses) as well as twenty real earthquake ground motion records representing the selected design spectrum. Finally, the efficiency and reliability of the design solutions are assessed based on ASCE/SEI 41-17 ductility limits for different performance levels, wall ductility capacities obtained from the validated FE models in ABAQUS, and a global cumulative damage index. The results indicated that the Eurocode design solution, ignoring the effect of vertical loads in the ductility capacity, did not fulfil the Life Safety (LS) and Collapse Prevention (CP) performance levels and sustained extensive damage even at low earthquake intensity levels. However, the proposed methodology yielded improved seismic performance with higher ductility capacity and significantly lower damage levels.

4.3 Proposed design methodology

In a previous study by Papargyriou et al. (Papargyriou *et al.*, 2021), it was found that additional vertical loads imposed to a CFS strap-braced stud wall led to increased secondary moments in the compressive chord stud due to P-Δ effects. The interaction of the axial loads and the secondary moments can result in the premature buckling failure of chord studs before straps reach their ultimate strain and subsequently reduce the lateral load-bearing capacity and ductility of the system. To address this issue, Papargyriou and Hajirasouliha [Paper 2] proposed a design methodology to estimate the lateral load-bearing and ductility capacity of CFS strap-braced stud walls under the presence of vertical loads. Their proposed procedure can be summarised as follows:

- Step 1: The lateral response of a reference CFS strap-braced stud wall (wall 1) under monotonic loading is obtained using a detailed FE model or experimental test results. No vertical load is applied at this stage, and therefore the failure mode is expected to be due to gross cross-section rupture of the straps.
- Step 2: The results of the previous step are used to estimate the structural performance of a selected CFS strap-braced stud wall (wall 2) with the same configuration and material properties as wall 1, but different element sizes. To achieve this, Eqs. (15) and (16) are used to calculate the lateral capacity ($F_{u,2}$) and ductility (μ_2) of wall 2, under zero vertical load, as functions of the diagonal strap thicknesses ($t_{s,1}$) and ($t_{s,2}$) and chord stud thicknesses ($t_{ch,1}$) and ($t_{ch,2}$) of walls 1 and wall 2, respectively.

$$F_{u,2} = F_{u,1} \cdot f1 \left(\frac{t_{s,2}}{t_{s,1}}, \frac{t_{ch,2}}{t_{ch,1}} \right) \quad (15)$$

$$\mu_2 = \mu_{t_{so,2}} \cdot f2 \left(\frac{t_{s,2}}{t_{so,2}} \right) \quad (16)$$

In the above equations, ($F_{u,1}$) is the lateral capacity of wall 1, while ($\mu_{t_{so,2}}$) is the ductility of wall 2, corresponding to a diagonal strap thickness ($t_{so,2}$) which leads to the simultaneous failure of the strap and the chord stud. A simple design process is proposed to obtain ($t_{so,2}$) using the axial-bending moment interaction relationship $F_c/N_{c,Rd} + M/M_{c,Rd} = 1$, where (F_c) is the compressive component of the strap force transferred on the chord stud, ($N_{c,Rd}$) and ($M_{c,Rd}$) are the compressive and bending moment capacities of the chord stud, respectively, calculated in accordance with EN 1993 (CEN, 2003, 2010), and (M) is the secondary bending moment due to P-Δ effects.

- Step 3: At this stage, Eqs. (17) and (18) are used to predict the lateral load capacity ($F_{u,p,2}$) and ductility ($\mu_{p,2}$) of wall 2, under the presence of a vertical load (P), expressed as a ratio against

the total vertical load capacity of the wall ($P_{w,2}$), obtained by adding the axial load capacities of the intermediate and chord studs calculated per Eurocode 3 (CEN, 2003, 2010).

$$F_{u,P,2} = F_{u,2} \cdot f3 \left(\frac{P}{P_{w,2}} \right) \quad (17)$$

$$\mu_{P,2} = \mu_2 \cdot f4 \left(\frac{P}{P_{w,2}} \right) \quad (18)$$

The functions $f1$, $f2$, $f3$ and $f4$ were obtained based on the results of a comprehensive parametric study conducted by Papargyriou and Hajirasouliha (Papargyriou and Hajirasouliha, 2021) on a wide range of CFS strap-braced stud walls. Table 4.1 lists the adopted functions for the wall configuration used in this study (see Fig. 4.1). It should be noted that while the proposed design methodology is general, these functions may slightly change if a very different bracing system is utilised.

Table 4.1 Functions $f1$, $f2$, $f3$ and $f4$ used to obtain lateral load capacity and ductility per Eqs. (15), (16), (17) and (18)

$f1 = \frac{F_{u,2}}{F_{u,1}} = 0.85 \left(\frac{t_{s,2}}{t_{s,1}} \right) + 0.15 \left(\frac{t_{ch,2}}{t_{ch,1}} \right)$	
$\begin{cases} f2 = \frac{\mu_2}{\mu_{tso,2}} = 1, & t_{s,2} \leq t_{so,2} \\ f2 = \frac{\mu_2}{\mu_{tso,2}} = -0.09 + 2.16 \left(\frac{t_{s,2}}{t_{so,2}} \right) - 1.07 \left(\frac{t_{s,2}}{t_{so,2}} \right)^2 & t_{s,2} > t_{so,2} \end{cases}$	
$f3 = \frac{F_{u,P,2}}{F_{u,2}} = 1 - 0.60 \left(\frac{P}{P_{w,2}} \right) + 0.30 \left(\frac{P}{P_{w,2}} \right)^2$	
$f4 = \frac{\mu_{P,2}}{\mu_2} = A \left(\frac{P}{P_{w,2}} \right)^3 + B \left(\frac{P}{P_{w,2}} \right)^2 + C \frac{P}{P_{w,2}} + 1$	
$A = 10.47 \left(\frac{t_{s,2}}{t_{so,2}} \right)^3 - 44.19 \left(\frac{t_{s,2}}{t_{so,2}} \right)^2 + 30.69 \left(\frac{t_{s,2}}{t_{so,2}} \right) + 4.85$	
$B = -8.55 \left(\frac{t_{s,2}}{t_{so,2}} \right)^3 + 31.65 \left(\frac{t_{s,2}}{t_{so,2}} \right)^2 - 18.64 \left(\frac{t_{s,2}}{t_{so,2}} \right) - 7.47$	
$C = -1.75 \left(\frac{t_{s,2}}{t_{so,2}} \right)^3 - 5.95 \left(\frac{t_{s,2}}{t_{so,2}} \right)^2 + 3.05 \left(\frac{t_{s,2}}{t_{so,2}} \right) + 0.81$	

4.3.1 Design solutions of a case study frame

To demonstrate the efficiency of the proposed methodology, a case study multi-storey CFS frame was designed following Eurocodes' specifications. The frame had six storeys above ground level, each having a height of 2.74 m, and three 2.44 m span bays. The middle span at each level was configured as the strap-braced wall panel, providing the lateral bearing resistance (see Fig. 4.1). The cross-sectional dimensions of the walls' elements, including the studs, the top and bottom tracks, the bridging element, and the diagonal straps, are shown in Fig. 4.1. The chord studs consisted of two back-to-back single lipped-channel sections, while the diagonal straps had a "dogbone" shape, having a reduced depth over a length of 762 mm in the middle. The thicknesses of the studs and the diagonal straps varied along the frame height. A tributary width of 5.0 m was assumed for the calculation of the gravity loads and the storey masses.

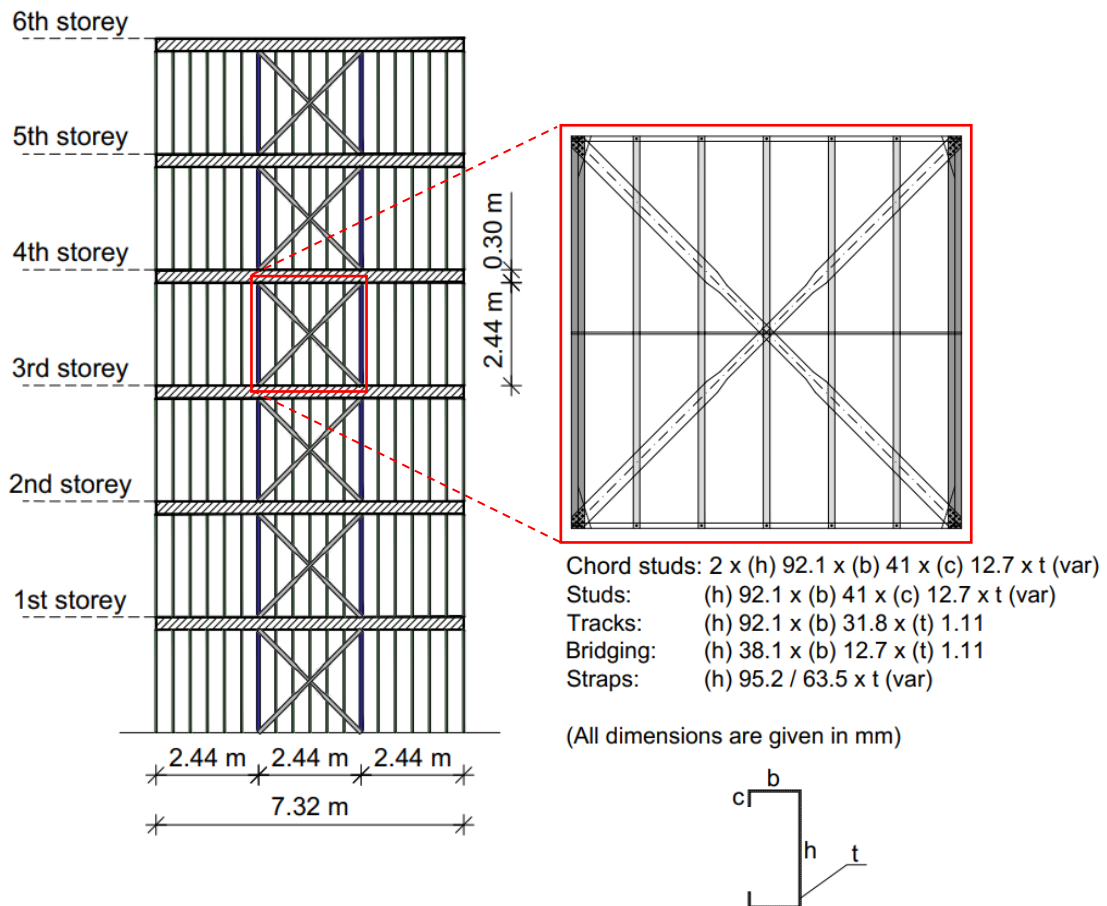


Fig. 4.1 Geometry of the case-study strap-braced wall frame

4.3.2 Design specifications

The frame was assumed to be part of a residential-use building, of importance class II, designed for a permanent load $g = 1.5 \text{ kN/m}^2$ and a live load $q = 2 \text{ kN/m}^2$, while the partial safety factors per EN 1990 (CEN, 2002a) were $\gamma_G=1.35$ and $\gamma_Q=1.50$, respectively. The storeys all had equal masses, calculated from the combination of the seismic action in accordance with EN 1990 (CEN, 2002a): $G_k + \psi_{E,i} \cdot Q_k$, where (G_k) and (Q_k) represent the permanent and variable (live) loads, respectively, and ($\psi_{E,i}$) is the coefficient for variable actions taken as 0.3. The site was assumed to be in a high seismicity area, with a reference peak ground acceleration $\alpha_{gR}=0.35 \text{ g}$ and a ground type B (i.e. deposits of very dense sand, gravel, or very stiff clay). The building was assumed to be regular in plan and elevation, and the base shear force was calculated and distributed along the height following the lateral force method per Eurocode 8 (CEN, 2004).

4.3.3 Conventional and proposed design solutions

For the conventional design solution, the frame members were designed in accordance with Eurocode 3 (CEN, 2003, 2010) and the capacity design rules of Eurocode 8 (CEN, 2004). However, as discussed before, the effects of vertical loads on the lateral load capacity and ductility of the strap-braced wall frames are not taken into account in the Eurocode design process. To address and further study this issue, the same frame was designed following the proposed methodology, explained in section 4.3 (proposed design solution). The thicknesses of the studs (t_{ch}) and the diagonal straps (t_s) of the Eurocode and the proposed design solutions are listed in Table 4.2, while the general dimensions of the sections are shown in Fig. 4.1.

Table 4.2 The plate thickness of the members in the Eurocode and the proposed design solutions (sizes are shown in Fig. 4.1)

Storey No	Eurocode design		Proposed design	
	Stud thickness t_{ch} (mm)	Diagonal strap thickness t_s (mm)	Stud thickness t_{ch} (mm)	Diagonal strap thickness t_s (mm)
1	2.0	4.0	2.0	4.0
2	1.5	4.0	2.0	4.0
3	1.5	4.0	2.0	4.0
4	1.16	3.0	1.5	3.0
5	1.16	3.0	1.5	3.0
6	1.16	1.5	1.16	1.5

4.4 Development of non-linear numerical models

Numerical modelling has been widely used as a cost-effective and efficient means to predict the response of CFS elements and structural systems under different loading conditions (Usefi *et al.*, 2019, 2020). In this study, ABAQUS software (Dassault Systèmes Simulia, 2014) was utilised to simulate the non-linear behaviour of CFS strap-braced wall panels, as previous studies showed that it can provide accurate results for thin-walled CFS elements and connections (Jun Ye *et al.*, 2016; Mojtabaei *et al.*, 2018, 2020; Ye, Mojtabaei, Hajirasouliha, *et al.*, 2018). The developed models were validated against available experimental data and were then used to: a) derive the load-displacement curves for the wall panels of the Eurocode and the proposed design solutions, as discussed in section 4.3, and b) obtain equivalent non-linear hysteretic models in OpenSees software (Mazzoni *et al.*, 2007) to simulate the non-linear seismic behaviour of multi-storey CFS strap-braced frames under different earthquake intensity levels. Using this approach can significantly reduce the computational costs of non-linear dynamic analyses of such complex systems. However, it should be noted that, in general, the wall panels have a different lateral response at each storey, depending on their cross-sectional dimensions and the amount of vertical loading, and therefore equivalent models should be obtained for them individually.

4.4.1 Detailed non-linear numerical model in ABAQUS

As shown in Fig. 4.2, the detailed wall models in ABAQUS comprised the chord and intermediate studs, the top and bottom tracks, and the bridging element at the mid-height of the wall. Two pairs of diagonal dogbone-shaped straps were used as bracing elements. The element dimensions are shown in Fig. 4.2. The model accounted for material non-linearity and P- Δ effects. The initial geometric imperfections were omitted in this work since previous studies (Papargyriou *et al.*, 2021) showed that they had a negligible effect on the lateral response of the system. Table 4.3 summarises the engineering values of yield (f_y) and ultimate (f_u) stresses for the structural elements. The modulus of elasticity (E) and the Poisson's ratio (ν) had values of 203 GPa and 0.3, respectively.

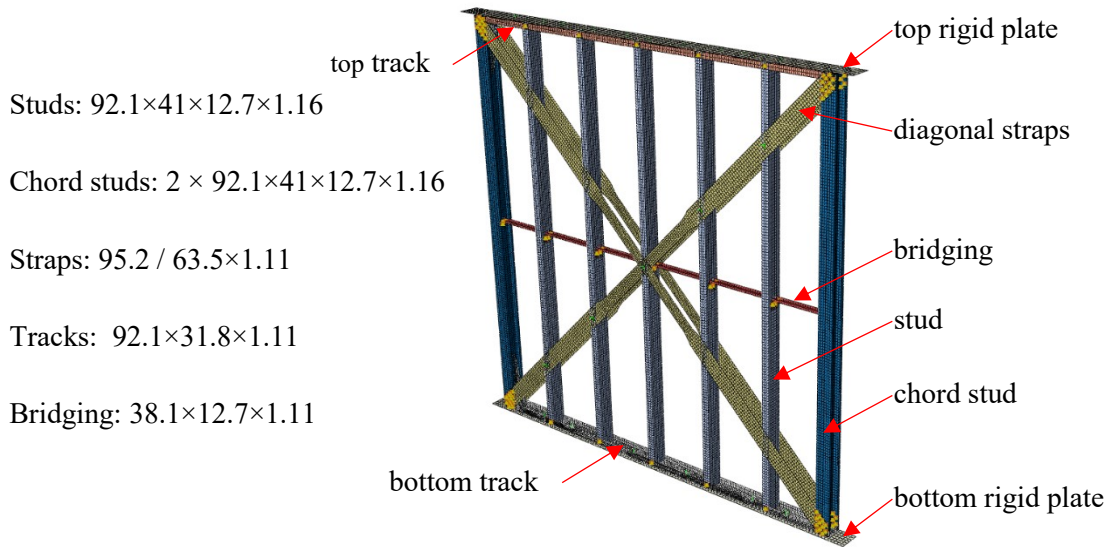


Fig. 4.2 Detailed ABAQUS numerical model

Table 4.3 Material properties of ABAQUS model

Element	Yield stress f_y (MPa)	Ultimate stress f_u (MPa)
Straps	296	366
Studs / Chord studs	325	382
Tracks	296	366

In the following section, the key features of the developed FE model are presented. For a more thorough description and discussion, the reader can refer to (Papargyriou *et al.*, 2021).

4.4.1.1 Summary of model features

Similar to the reference experimental test set-up, the developed models featured the hold-down devices and anchor rods at the chord stud top and bottom ends alongside the connections of the tracks through shear anchors. Over the top and below the bottom track, rigid plates were used to transfer the vertical loads uniformly to the chord studs, the intermediate studs and the foundation. The bridging element, intended to reduce the effective length of the vertical elements, was attached to them through L-shaped brackets.

The ABAQUS “S4R” shell element (four-node element with three translational and three rotational degrees of freedom per node) was used to discretise the wall’s elements as it was proven accurate in

predicting the behaviour of CFS systems in the previous studies (Jun Ye *et al.*, 2016; Ye, Mojtabaei, Hajirasouliha, *et al.*, 2018; Mojtabaei *et al.*, 2020).

Following a mesh sensitivity analysis, the lateral load capacity value converged at a mesh size of 15 mm × 15 mm, yielding a difference of less than 0.5% compared to a coarser mesh of 20 mm × 20 mm.

The straps were connected to the chord studs and the top and bottom tracks through 12 No 10 (Ø10 mm) self-drilling screws, while the intermediate studs were connected to the top and bottom tracks through 1 No 8 (Ø8 mm) self-drilling screw per side, at each end. The screwed connections were modelled using discrete fasteners, which were assigned connector properties, defining the relative motion between the connected surfaces. The proposed equations in Pham and Moen’s work (Pham and Moen, 2015), derived based on their experimental work on steel screw-fastened connections, were adopted to describe the strength and stiffness of the connectors.

The vertical load was applied in the first analysis step as a uniformly distributed surface load on the rigid top plate, and the lateral displacements were imposed in the second step. A maximum displacement value of 300 mm was applied for monotonic analysis, whereas cyclic loading followed the reversed cyclic protocol suggested by ASTM E2126 (ASTM, 2019) , as shown in Fig. 4.3.

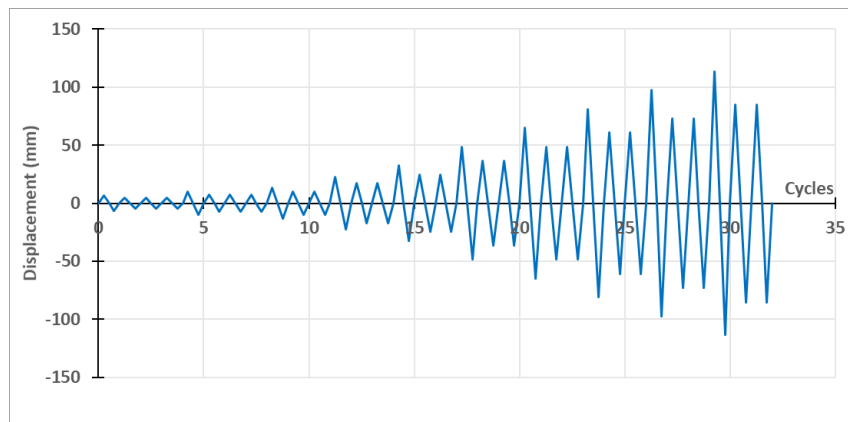


Fig. 4.3 Reversed cyclic protocol per ASTM E2126 (ASTM, 2019)

In order to transfer the vertical load and account for the correct interaction between the structural elements, surface-to-surface interactions were described, using a “hard” contact definition in the normal direction and a “frictionless” contact in the transverse direction.

4.4.1.2 Model validation

The developed FE model was verified under cyclic loading against the results of test specimens 26A-C and 32A-C included in the experimental work of Velchev (Velchev, 2008b). The lateral load-displacement responses of the test and the FE analyses are compared in Fig. 4.4. The results, in general,

demonstrate the efficiency of the adopted FE models to simulate the hysteretic response of the tested CFS strap-braced walls. The average error in the estimated cumulative energy dissipation (i.e. the area enclosed by the load-displacement curves) of the walls was 18% and 17% for the test specimens 26A-C and 32A-C, respectively. A more comprehensive comparison can be found in (Papargyriou *et al.*, 2021).

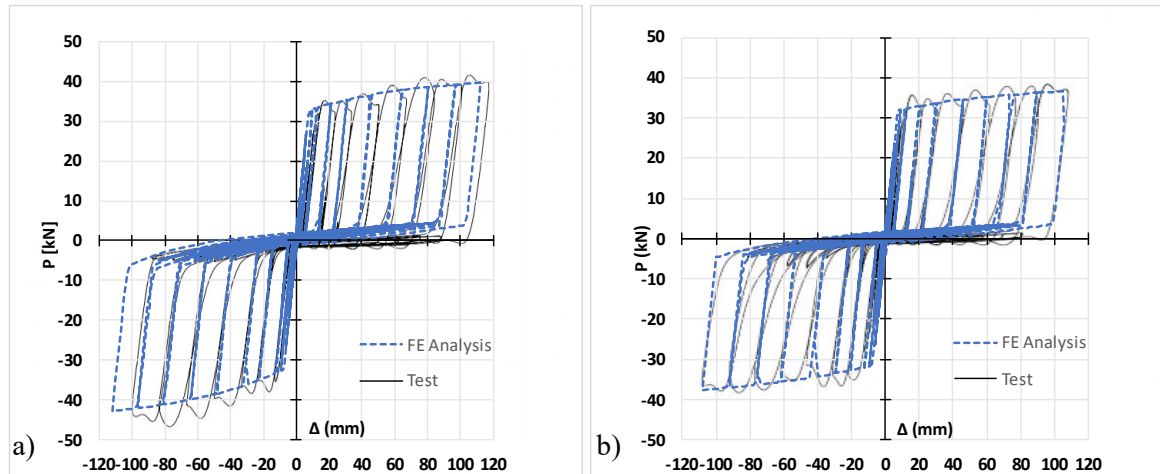


Fig. 4.4 Comparison of the experimental and FE analysis predicted cyclic responses of specimens a) 26A-C, and b) 32A-C

To assess the efficiency of the Eurocode and the proposed design methodology in terms of the lateral load capacity and ductility of the wall panels, the validated FE models were adopted to obtain the load-displacement curves for all the wall panels of the Eurocode and the proposed design solutions by taking into account their cross-sectional dimensions and the amount of vertical loading. The results were then used to calculate the ultimate load capacity (F_u) and ductility (μ) for each wall panel. Ductility was expressed as a ratio of the ultimate displacement (Δ_u) over the displacement at yield (Δ_y) (i.e. $\mu = \Delta_u/\Delta_y$). The ultimate displacement was taken as the minimum of the displacement corresponding to the failure of the wall (due to strap rupture or buckling of the compressive chord stud) or the displacement corresponding to a 20% drop of the ultimate load capacity. To obtain the values of (Δ_u) and (Δ_y), idealised bilinear curves of the actual responses, based on the FEMA 356 (FEMA 356, 2000), were used.

The ultimate lateral load (F_u) and ductility (μ) capacities of the walls at each storey level are summarised in Table 4.4 for the Eurocode and the proposed design solutions. It can be noted that, despite satisfying the code's load capacity checks, the Eurocode design solution exhibits relatively low ductility capacity at storeys 2 to 5, well below the target ductility of 4 expected for ductility class medium (DCM) structures. As discussed before, this is mainly attributed to the premature buckling of the chord studs caused by the interaction of the compressive force and secondary moment due to P- Δ effects, amplified

by the presence of vertical loads. By contrast, the proposed design solution reached high ductility values at all storeys.

Table 4.4 Lateral load and ductility capacities of the Eurocode and the proposed design solutions

Storey No	Eurocode design		Proposed design	
	F_u (kN)	μ	F_u (kN)	μ
1	120.4	14.8	120.3	14.8
2	105.2	1.9	121.7	15.5
3	108.8	2.1	123.1	15.9
4	80.7	2.4	93.0	15.3
5	85.5	2.6	94.4	16.3
6	49.1	21.3	49.1	21.3

4.4.2 Non-linear numerical models in OpenSees

In this study, OpenSees software (Mazzoni *et al.*, 2007) is used to assess the seismic performance of multi-storey CFS strap-braced frames. Fig. 4.5 shows the OpenSees numerical model of a single wall panel. It comprised the intermediate and chord studs, the top track and one diagonal element that represents the overall hysteretic behaviour of the X-shaped braces. The studs and chord studs were modelled with “truss” elements and assigned elastic “uniaxialMaterial” properties. The top track was modelled using the “elasticBeamColumn” element, which supports uniformly distributed loading and incorporates elastic material properties. The non-linear lateral behaviour of the wall was simulated by using the diagonal element with the non-linear “Pinching4” material, derived from the corresponding monotonic analysis of detailed ABAQUS numerical models for each wall panel. In practical terms, this single diagonal element controls the non-linear lateral performance of the wall, while the effects of local buckling and failure of all the elements on the overall response of the system are indirectly included. This is explained in more detail in the next section.

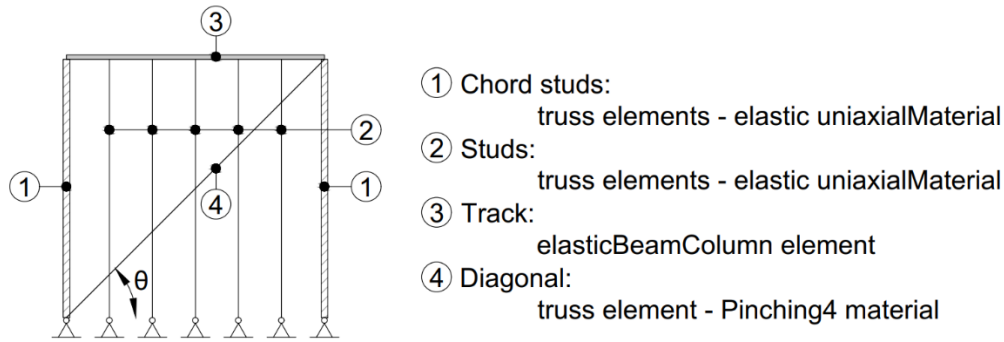


Fig. 4.5 Single strap-braced wall model in OpenSees

4.4.3 Hysteretic response

In general, strap-braced stud walls subjected to cyclic loading exhibit a pinching behaviour, which results from only the tensile straps being active in every excursion (Kim *et al.*, 2006). Therefore, in this study, the hysteretic response of the wall was defined by assigning the hysteretic “Pinching4” material (see Fig. 4.6) of OpenSees (Mazzoni *et al.*, 2007) to the diagonal element which in previous studies (Shamim and Rogers, 2015; Fiorino *et al.*, 2017) was proven accurate in capturing this behaviour.

The “Pinching4” material definition comprises 39 parameters, including the backbone curve points of the cyclic response for both positive and negative loading directions, the pinching, and finally, the strength and stiffness degradation parameters. Since neither strength nor stiffness degradation was observed in the studied walls, their corresponding parameters were set equal to zero.

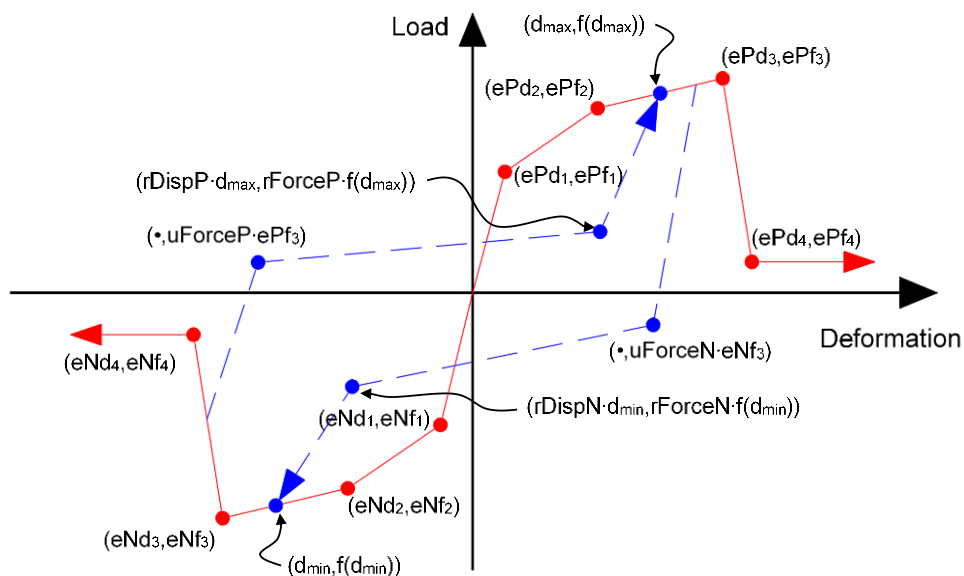


Fig. 4.6 Definition of OpenSees (Mazzoni *et al.*, 2007) “Pinching4” hysteretic model

The point pairs (ePd₁, ePf₁), (ePd₂, ePf₂), (ePd₃, ePf₃) and (ePd₄, ePf₄), defining the positive loading direction backbone envelope, were selected from the bi-linearised, per FEMA 356 (FEMA 356, 2000), monotonic lateral load-displacement relationship of the corresponding ABAQUS numerical models, whilst the pairs (eNd₁, ePf₁), (eNd₂, ePf₂), (eNd₃, ePf₃) and (eNd₄, ePf₄), representing the negative-loading backbone curve were set equal to their negative symmetrical ones. It should be noted that since these points were assigned as material properties of the diagonal element, they needed to be transformed into equivalent stresses ($\sigma = P / (A \times \cos\theta)$) and strains ($\varepsilon = \Delta \times \cos \theta / L$). In the above equations (P) is the lateral force, (A) the area of one pair of straps, (Δ) the lateral displacement, (L) the initial diagonal length and (θ) the angle of the diagonal (see Fig. 4.5).

The pinching controlling parameters (rDispP, rForceP, uForceP, rDispN, rForceN, and uForceN) were obtained through a calibration process. Their values were iteratively modified, aiming to reach the best agreement between the OpenSees analysis and the actual cyclic response from ABAQUS models and to minimise the difference in the cumulative dissipated energies. The results indicated that, in general, these parameters are not very sensitive to the imposed vertical load level. Following the calibration process, the pinching parameter values of (rDispP=0.9, rForceP=0.03, uForceP=0, rDispN=0.9, rForceN=0.03, and uForceN=0) were found to be suitable for all cases, and therefore, these values were used in the analyses henceforth.

The accuracy of the equivalent OpenSees model was investigated for two cased study examples. Wall SW1 had no additional vertical load and failed because the straps reached their ultimate strain. Wall SW2 had an additional vertical load equal to 29% of its axial load capacity (P_w), and its failure mode was the premature buckling of the compressive chord stud before the straps reached their ultimate strain. Fig. 4.7 compares the monotonic lateral load-displacement responses of these wall specimens.

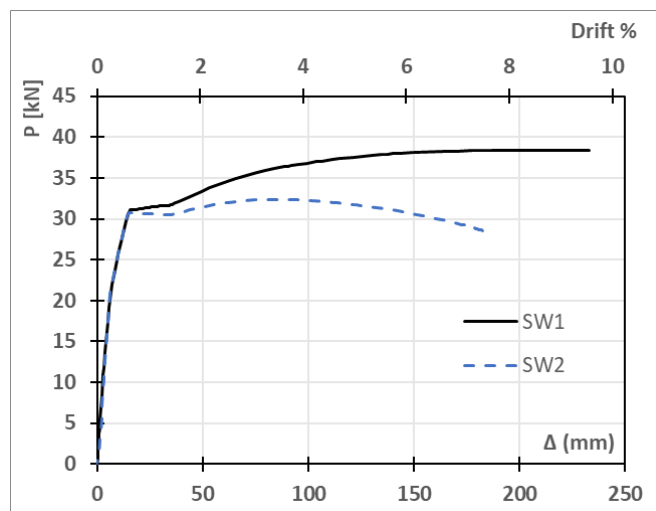


Fig. 4.7 Lateral load-displacement relationships for walls SW1 and SW2

In Fig. 4.8, the accuracy of the “Pinching4” model is verified by comparing the hysteretic response of the SW1 and SW2 models in ABAQUS and OpenSees, in terms of lateral-load displacement curves and the cumulative dissipated energy. It can be observed from Fig. 4.8a and Fig. 4.8b that for both cases, there was a good agreement between the hysteretic lateral load-displacement curves with respect to the initial stiffness and the maximum capacity (P_u). Regarding the cumulative dissipated energy, the average error was 8.6% for wall SW1 and 4.5% for wall SW2 (see Fig. 4.8c and Fig. 4.8d).

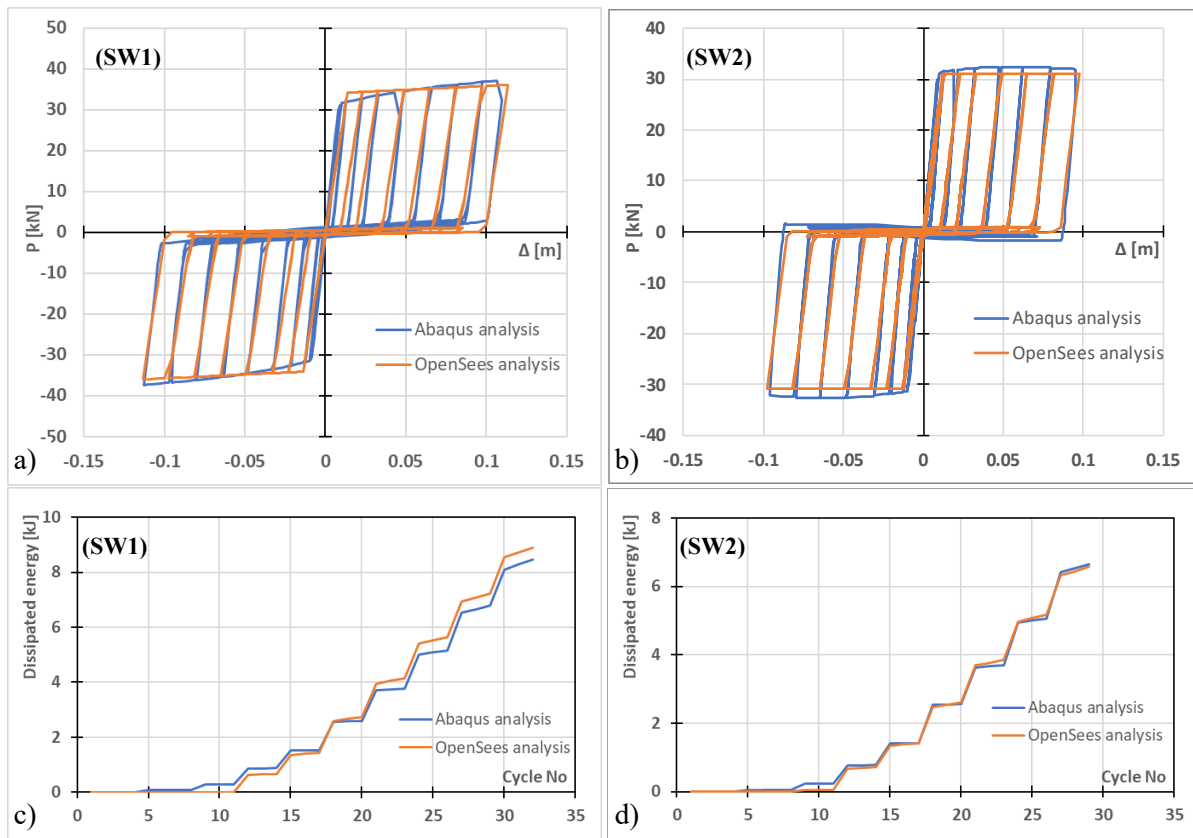


Fig. 4.8 ABAQUS and OpenSees hysteretic response and cumulative energy of (a & c): SW1 wall and (b & d): SW2 wall

4.4.4 Multi-storey frame system

The previously verified non-linear OpenSees models of the single strap-braced wall panels were employed to develop the multi-storey frame models, as depicted in Fig. 4.9. The chord studs and the intermediate studs were modelled as elastic truss elements, not transferring any moments. Assuming that the flooring system provided a rigid diaphragm action, the top and bottom tracks were modelled as elastic beam-column elements of very high stiffness, connected at their endpoints with “bar”-type rigid links. At each storey level, the hysteretic behaviour for the walls was characterised by “Pinching4” material properties assigned to each diagonal element through the backbone curve parameters obtained from the corresponding ABAQUS monotonic results (see Section 4.4.3). In order to account for second-

order effects, a P- Δ frame was attached to the main CFS frame (Shamim and Rogers, 2015; Fiorino *et al.*, 2017). It comprised a leaning column on each level (Geschwindner, 2002), modelled as an elastic beam-column element with a high axial and low flexural stiffness. The leaning columns were connected to the main frame through rigid beams, modelled by rigid truss elements, using zero-length hinge elements at both ends (see Fig. 4.9). The horizontal movement of the leaning column end nodes was constrained relative to their adjacent nodes of the main frame at each level.

The vertical loads and the storey masses, calculated in Section 4.3.2, were applied as uniformly distributed on the track elements at the top of each floor level, while a concentrated vertical force equal to the total gravity load of each storey was applied at the joints of the P- Δ frame. Following gravity analysis, a modal analysis was performed. For the dynamic analyses, a Rayleigh damping value of 2% was considered as suggested by (Shamim and Rogers, 2015; Fiorino *et al.*, 2017).

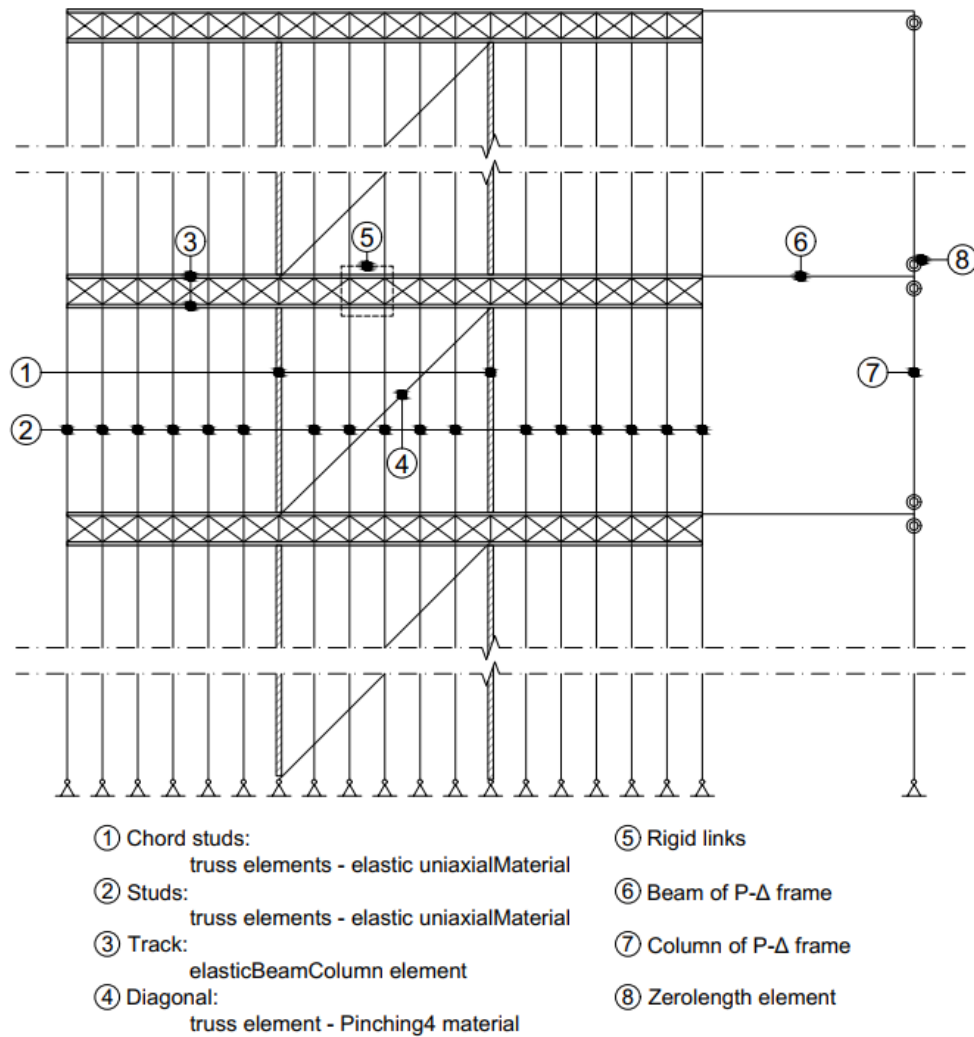


Fig. 4.9 The strap-braced wall frame model in OpenSees

4.5 Non-linear time-history analysis

To evaluate the performance of CFS strap-braced wall frame systems and assess the efficiency of the proposed design methodology under seismic excitations, the Eurocode and the proposed design solutions were subjected to non-linear time-history analyses by selecting appropriate artificial and real ground motion records. The ductility demand and capacity of the systems were compared, and their expected overall structural damage, expressed by a global damage index, was calculated.

4.5.1 Artificial spectrum-compatible ground motion records

The elastic response spectrum per Eurocode 8 (CEN, 2004) was produced for a ground acceleration value of 0.35 g, soil category B, and importance class II. This response spectrum was used for the seismic design of the frames, as discussed in Section 2.2. Seven compatible artificial records (Syn1-Syn7) were then generated with SeismoArtif software (Seismosoft, 2018) to match the design spectrum. In this study, artificial records were initially utilised to assess the seismic performance of the design solutions as representatives of the selected design spectrum (Hajirasouliha and Pilakoutas, 2012; Nabid *et al.*, 2020; Moghaddam *et al.*, 2021). Fig. 4.10 demonstrates the good agreement between the response spectra of the artificial records and the Eurocode 8 design response spectrum.

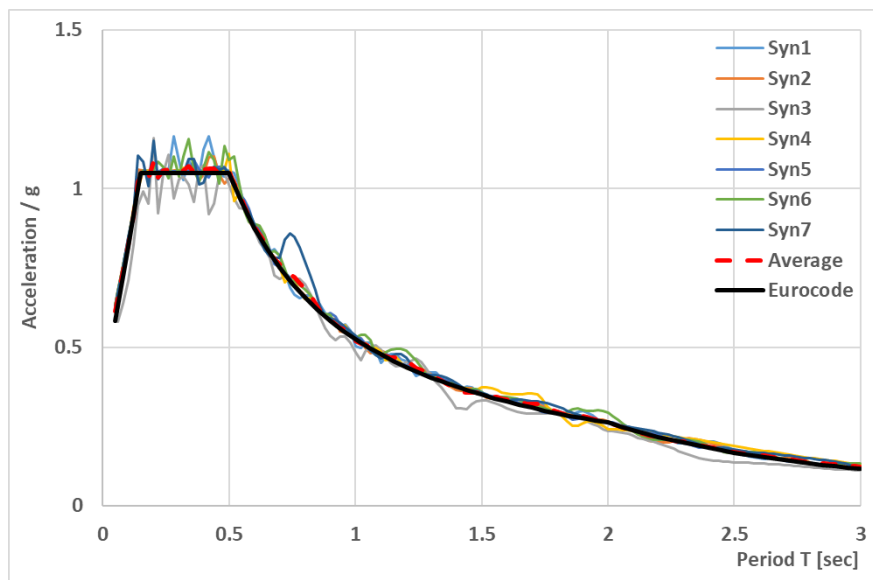


Fig. 4.10 Comparison between elastic response spectra of artificial records and the selected Eurocode 8 design spectrum

4.5.2 Performance Assessment Parameters

For performance-based design and assessment of structures, ASCE/SEI 41-17 (ASCE, 2017) specifies three seismic performance objectives: Immediate Occupancy (IO), Life Safety (LS) and Collapse Prevention (CP). Each performance objective is represented based on acceptance criteria corresponding to a specific ground motion intensity level. In this study, the Design-Basis Earthquake (DBE), corresponding to (LS) performance target, had a PGA = 0.35 g consistent with the adopted design response spectrum. The Maximum Considered Earthquake (MCE), associated with (CP) level, had a PGA = 0.5 g (1.5 times the DBE level as recommended by ASCE 7-05 (ASCE, 2005)). The PGA of the Frequent Earthquake (FE), corresponding to (IO) performance level, was set to 0.1 g. It should be noted that for practical applications, these earthquake intensity values should be obtained based on the results of the seismic hazard assessment of the selected site.

In general, the seismic performance of structures is measured based on Engineering Demand Parameters (EDP), such as inter-storey drift, roof displacement, plastic hinge rotation, and peak storey ductility (Vamvatsikos and Cornell, 2002; D'Ayala *et al.*, 2015). ASCE/SEI 41-17 (ASCE, 2017) prescribes limits for the storey ductility demand ($\mu_i = \Delta_{inelastic,i} / \Delta_{y,i}$) corresponding to (IO), (LS) and (CP) performance levels. ($\Delta_{inelastic,i}$) and ($\Delta_{y,i}$) stand for the drift demand and wall drift at yield at storey (i). In this study, ($\Delta_{y,i}$) was calculated based on the idealised bilinear load-displacement curves, as prescribed in ASCE/SEI 41-17 (ASCE, 2017), using the results of ABAQUS models. The ductility limits for wall systems employing dogbone-shaped diagonal straps were set at 3.2, 7.3 and 10.1, for performance levels (IO), (LS) and (CP), respectively (ASCE, 2017).

The ductility capacity of the walls at each storey level were calculated in accordance with the dominant failure mode (i.e. failure of the straps reaching their ultimate strain, or buckling of the compressive chord stud). To calculate the ductility capacity ($\mu_{c,i} = \Delta_{u,i} / \Delta_{y,i}$), the ultimate wall drift ($\Delta_{u,i}$) was considered as the drift corresponding either to the respective failure mode or a 20% drop in the maximum lateral load, whichever occurs first.

The efficiency and reliability of the design solutions were also assessed based on the cumulative global damage model proposed by Krawinkler (Krawinkler and Zohrei, 1983) and Powell and Allahabadi (Powell and Allahabadi, 1988), measuring the change in the dissipated energy relative to the displacement demands. In this work, the damage index (DI_i) of each storey (i) was selected to be a function of the inter-storey drift demands (Hajirasouliha and Pilakoutas, 2012; Nabid *et al.*, 2020):

$$DI_i = \sum_{j=1}^N \left(\frac{\Delta\delta_{pj}}{\Delta y_{,i}} \right)^c \quad (19)$$

where $(\Delta\delta_{pj})$ is the inelastic inter-storey drift at the j -th excursion, (N) the total number of the inelastic excursions, $(\Delta y_{,i})$ the inter-storey drift at yield, and (c) is a constant parameter accounting for the stability of the hysteretic behaviour taken equal 1.5 (Nabid *et al.*, 2020).

To quantify the overall damage at the frame-level, the global damage index (DI_g) (Hajirasouliha and Pilakoutas, 2012; Nabid *et al.*, 2020) was used as a weighted average of the damage indices (DI_i) at each storey:

$$DI_g = \frac{\sum_{i=1}^n DI_i \cdot W_{pi}}{\sum_{i=1}^n W_{pi}} \quad (20)$$

where (DI_i) is the damage index of each storey (i) , (W_{pi}) is the dissipated energy of each storey (i) , and (n) is the number of storeys. The global damage index estimates the overall condition of the structure after an earthquake event and takes values between 0 (no damage) and 1 (complete damage or failure).

4.6 Performance evaluation of CFS strap-braced wall multi-storey frames

4.6.1 Seismic Performance Assessment

The seismic performance of the design solutions was assessed in terms of the maximum inter-storey drifts and storey ductility demands by scaling the seven artificial records (Syn1 to Syn7) to 0.1 g, 0.35 g and 0.5 g, corresponding to (IO), (LS) and (CP) performance levels (see Section 4.2). As per Eurocode 8 (CEN, 2004), since the results of at least seven time-history analyses are obtained, their average response can be used for design purposes. Therefore, for each of the three performance levels, the inter-storey drift distributions for both design solutions were obtained under the seven spectrum compatible artificial records. Fig. 4.11 illustrates the average and average plus standard deviation of the results. In general, the results indicate that the inter-storey drift distributions were more uniform in the proposed design solution compared to its code-compliant counterpart, especially under higher earthquake intensity levels. The proposed design method could also reduce the maximum inter-storey drifts, on average, by around 10% and 20% under (LS) and (CP) earthquake intensity levels, respectively.

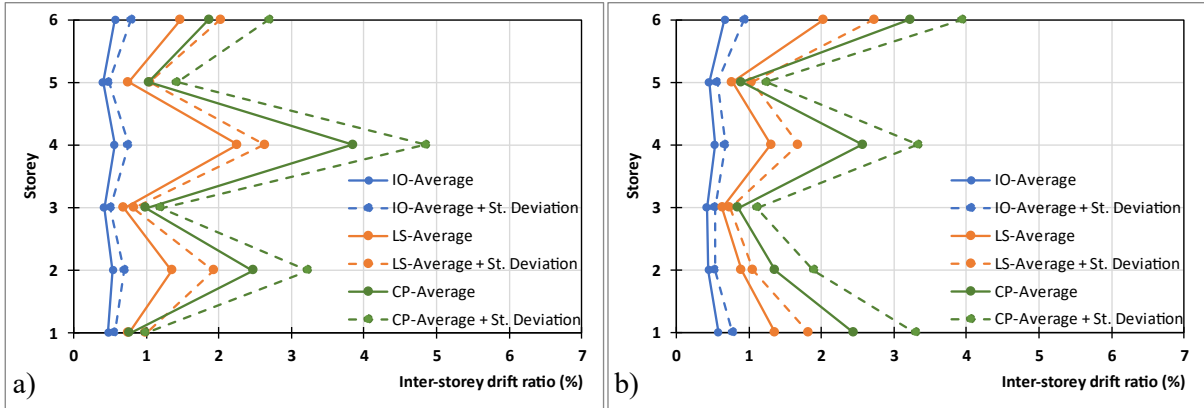


Fig. 4.11 Inter-storey drift distribution of a) Eurocode design and b) Proposed design under seven artificial spectrum compatible records

Fig. 4.12 to Fig. 4.14 display the average and the average plus standard deviation distribution of the storey ductility demands of the Eurocode and the proposed design solutions for (IO), (LS) and (CP) performance levels, respectively. The code ductility limits and the ductility capacity of each storey are also plotted for comparison purposes (see Section 4.5.2). It is shown in Fig. 4.12 that both frames could satisfy the code ductility limit of 3.2 for the (IO) performance level. The storey ductility capacity values (obtained from ABAQUS models) were also above the demand values for both cases. However, the proposed design solution provided a considerably higher safety margin in this case. The results presented in Fig. 4.13 indicate that, on average, both frames satisfied the code ductility limit of 7.3 for the (LS) performance level. However, the average plus standard deviation ductility marginally exceeded this limit at the 4th storey of the Eurocode design solution. Moreover, it is shown that the average storey ductility demands at the 2nd and 4th storey of the Eurocode design were considerably higher than their corresponding capacity values. This indicates that the Eurocode frame exhibited a soft-storey mode of failure at these storey levels due to the premature buckling of the compressive chord studs, not allowing the diagonal straps to reach their ultimate capacity. This confirms that satisfying the code suggested ductility demands by ignoring the effects of vertical loads may lead to unsafe design solutions. It can be seen that this issue was addressed by using the proposed design method, as the storey ductility capacities were always considerably higher than the demand values. For the (CP) performance level, Fig. 4.14 shows that the code ductility limit of 10.1 was exceeded, by 13% at the 4th storey of the code design solution, while it was fully satisfied in the proposed design solution. The storey ductility demands at the 2nd, 3rd, 4th and 5th storey levels of the Eurocode design frame were also exceeded their capacity values, indicating a premature failure mechanism under this earthquake intensity level. Similar to the previous case, by adopting the proposed design method, the capacity values were always considerably above the storey ductility demands at all storey levels.

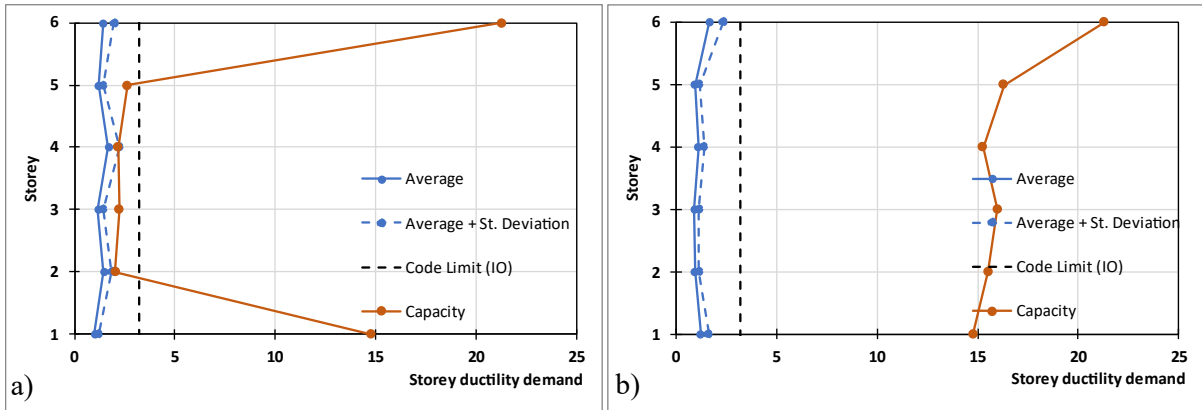


Fig. 4.12 Storey ductility demand and capacity distribution of a) Eurocode design and b) proposed design under seven artificial spectrum compatible records, IO performance limit

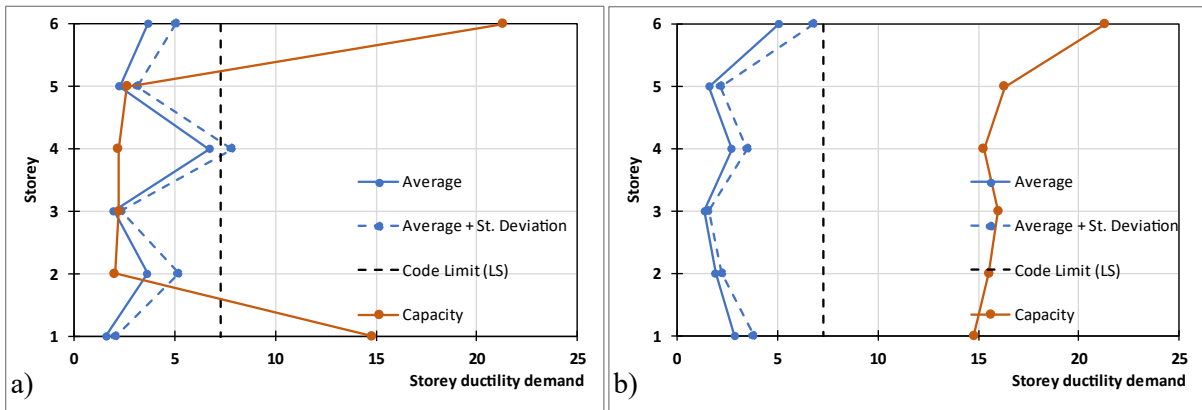


Fig. 4.13 Storey ductility demand and capacity distribution of a) Eurocode design and b) proposed design under seven artificial spectrum compatible records, LS performance limit

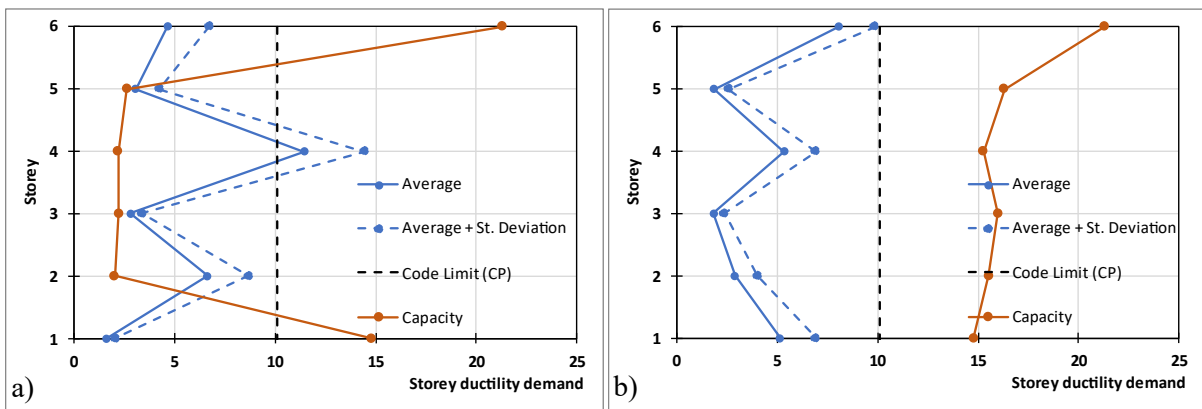


Fig. 4.14 Storey ductility demand and capacity distribution of a) Eurocode design and b) proposed design under seven artificial spectrum compatible records, CP performance limit

4.6.2 Non-linear Incremental Dynamic Analysis (IDA)

Incremental Dynamic Analysis (IDA) is a numerical method to assess the performance and vulnerability of structures under seismic loads (Vamvatsikos and Cornell, 2002; Mohsenian *et al.*, 2020). The studied structure is subjected to ground motion records scaled to a progressively increased intensity, and its structural performance is evaluated using a response parameter such as maximum roof displacement or global damage index. In this study, IDA was performed on the Eurocode and the proposed design solutions subjected to the seven artificial spectrum-compatible ground motion records, as was described in Section 4.5.1. The PGA of the input earthquakes was considered as the intensity parameter to be consistent with the limits used for the ASCE/SEI 41-17 (ASCE, 2017) performance targets (see Section 4.5.2).

The average and average plus standard deviation of the global damage index (DI_g) values for the Eurocode and the proposed design solutions subjected to the artificial spectrum-compatible records at different intensity levels are shown in Fig. 4.15. Due to the low ductility capacity of some storey levels, the Eurocode design frame exhibited a high level of damage even under low intensity records. It is shown that the global damage index for the Eurocode design solution was around 40% at PGA= 0.10 g (IO performance level), while the frame was completely damaged under the PGA levels above 0.20 g. This clearly indicates that the frame did not comply with the performance targets of the seismic design codes. As discussed before, this is mainly attributed to the buckling of the compressive studs due to the negligence of the P- Δ secondary moment effects during the code-base design process.

The improved proposed design frame, on the other hand, experienced considerably lower damage compared to its code-compliant counterpart at all earthquake intensity levels. By adopting the proposed design method, the frame exhibited a global damage index of 4%, 26% and 58% at PGA levels of 0.10 g (IO performance level), 0.35 g (LS performance level) and 0.5 g (CP performance level), respectively. The full damage ($DI_g=100\%$) in this case was reached only at PGA levels above 0.65 g. In general, these results confirm that the proposed design solution fulfils the expected performance targets for typical building structures.

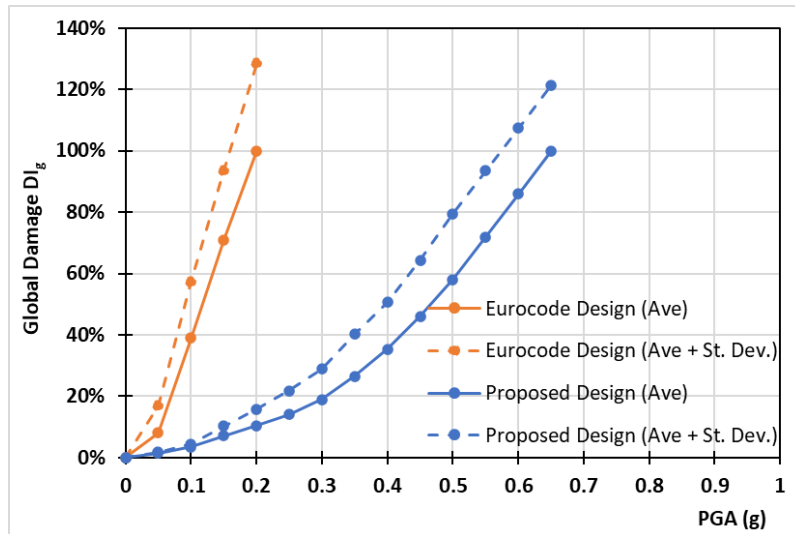


Fig. 4.15 Global damage index (DI_g) for the Eurocode and proposed design solution frames subjected to artificial spectrum-compatible ground motion records

4.6.3 Seismic performance under real ground motion records

In this section, the seismic performance of the Eurocode and the proposed design solutions are assessed under compatible real ground motion records. A set of twenty earthquakes from the Pacific Earthquake Engineering Research Centre (PEER) ground motion database (*PEER ground motion database*, <https://ngawest2.berkeley.edu/>. Accessed Dec, 2020) were selected to be compatible with the selected elastic design response spectrum of Eurocode 8 (CEN, 2004). All the accelerograms were obtained for a combination of near and far-field earthquakes with magnitudes between 6.8 and 7.6 (i.e. medium to strong earthquake records). The characteristics of the selected records are summarised in Table 4.5, and their respective response spectra are compared with the Eurocode design spectrum in Fig. 4.16. In Table 4, (R_{rup}) is the site distance from the epicentre, and (V_{s30}) is the average shear wave velocity, with the search range set between 360-800 m/sec, to match ground type B, per Eurocode 8 (CEN, 2004). It is shown in Fig. 4.16 that the average of the earthquake response spectra of the selected records compares very well with the Eurocode design spectrum used in the design process of the frames (see Section 2.1). Therefore, these records were used without scaling.

Table 4.5 Real ground motion records

Record name	Earthquake Name	Year	Magnitude	R _{rup} (km)	V _{s30} (m/sec)
E1	"Loma Prieta"	1989	6.93	10.72	476.54
E2	"Loma Prieta"	1989	6.93	3.85	462.24
E3	"Loma Prieta"	1989	6.93	8.5	380.89
E4	"Cape Mendocino"	1992	7.01	8.18	422.17
E5	"Kobe_ Japan"	1995	6.9	7.08	609
E6	"Chi-Chi_ Taiwan"	1999	7.62	5.8	624.85
E7	"Chi-Chi_ Taiwan"	1999	7.62	7.08	468.14
E8	"Chi-Chi_ Taiwan"	1999	7.62	2.74	614.98
E9	"Chi-Chi_ Taiwan"	1999	7.62	8.2	443.04
E10	"Chi-Chi_ Taiwan"	1999	7.62	10.97	363.99
E11	"Chi-Chi_ Taiwan"	1999	7.62	9	671.52
E12	"Chi-Chi_ Taiwan"	1999	7.62	45.18	446.63
E13	"Manjil_ Iran"	1990	7.37	12.55	723.95
E14	"Cape Mendocino"	1992	7.01	18.31	459.04
E15	"Cape Mendocino"	1992	7.01	19.32	387.95
E16	"Chuetsu-oki_ Japan"	2007	6.8	11.94	383.43
E17	"Chuetsu-oki_ Japan"	2007	6.8	16.86	561.59
E18	"Chuetsu-oki_ Japan"	2007	6.8	20.03	561.59
E19	"Chuetsu-oki_ Japan"	2007	6.8	20	561.59
E20	"Iwate_ Japan"	2008	6.9	12.85	512.26

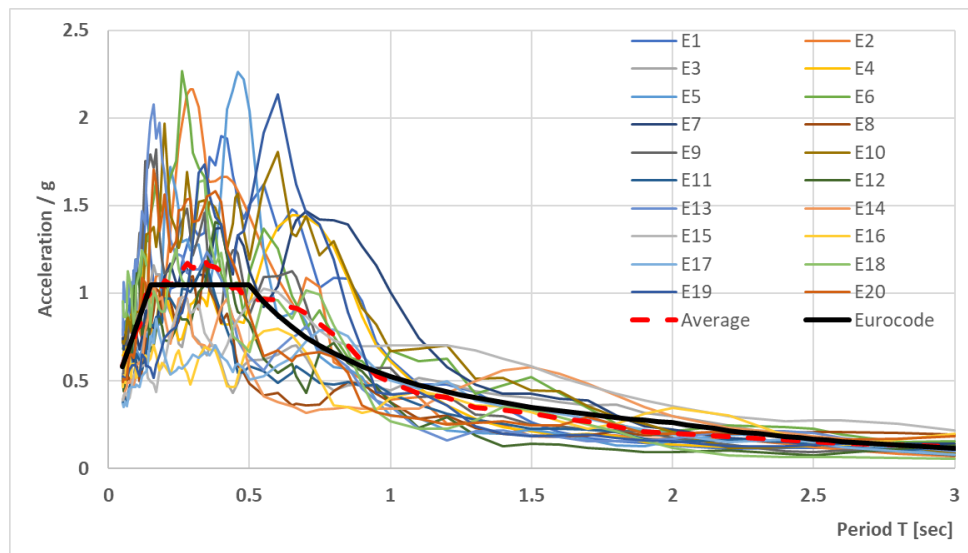


Fig. 4.16 Comparison between the response spectra of the real earthquakes and the elastic design response spectrum of Eurocode

The Eurocode and the proposed design frames were subjected to the set of the real earthquake records, and the average and the average plus standard deviation of inter-storey drift distributions were calculated as displayed in Fig. 4.17. It can be noted that the average inter-storey drift patterns were almost similar to those under artificial spectrum-compatible ground motions, which confirms the general agreement between the artificial and real records. The Eurocode design frame reached a maximum average inter-storey drift value of 2.4% (average plus standard variation of 3.6%), while the maximum average inter-storey drift value slightly increased to 2.7% (average plus standard variation of 3.6%) in the proposed design solution.

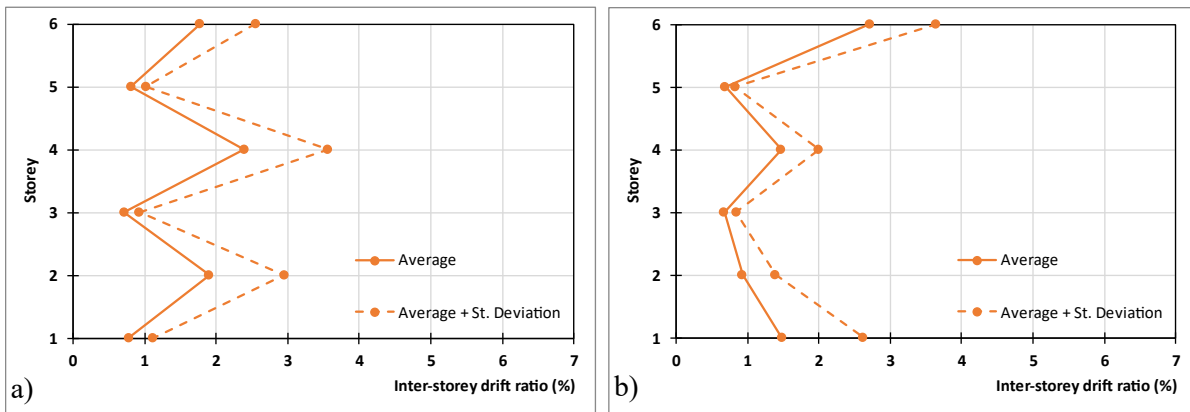


Fig. 4.17 Inter-storey average drift distribution for (LS) performance limit of a) the Eurocode design and b) the proposed design solutions subjected to real ground motion records

The average and the average plus standard deviation of storey ductility demands for the Eurocode and the proposed design solutions are shown in Fig. 4.18. The average storey ductility demands for the Eurocode design frame were always below the code limit of 7.3 for the (LS) performance level. However, at the 2nd and 4th storey levels, they exceeded the ductility capacity by 2.5 and 3.2 times, reaching values of 5.1 and 7.2, respectively. As discussed before, this can lead to extensive damage in the Eurocode design structure under strong earthquake events.

The average storey ductility demand for the proposed design solution reached a maximum value of 6.8, which means the frame satisfied the code (LS) performance level. Besides, the results indicate that in the proposed design frame, the average storey ductility demands were always well below the storey ductility capacity values. It is shown that the adopted design methodology could significantly increase

the ductility capacity of the storeys that initially suffered from the premature failure of the compressive chord studs. These results are consistent with those observed under artificial records in Section 4.6.1.

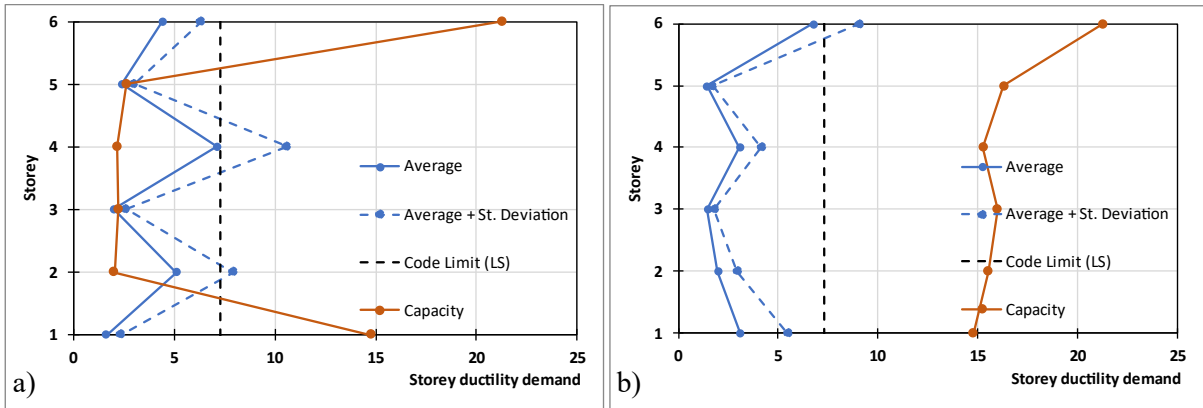


Fig. 4.18 Average storey ductility demand and capacity for (LS) performance limit of a) the Eurocode design and b) the proposed design solutions subjected to real ground motion records

The global damage indices (DI_g) for the Eurocode and the proposed design solutions were also calculated under the set of 20 real ground motion records (E1 to E20), as plotted in Fig. 4.19. For the Eurocode design frame, the global damage index was very high for all the selected records, indicating an unacceptable level of damage leading to complete collapse in most cases. The global damage index for the proposed design solution ranged between 10% and 63%, with an average value of 40%. This significant improvement in the seismic performance of the modified frame is attributed to the higher ductility capacity of the system achieved by taking into account the effects of vertical loads on the lateral load capacity and ductility of the wall panels in the design process. The results of this study, in general, highlight the efficiency of the proposed method, which should prove useful in the preliminary design of multi-storey CFS strap-braced frames in seismic regions.

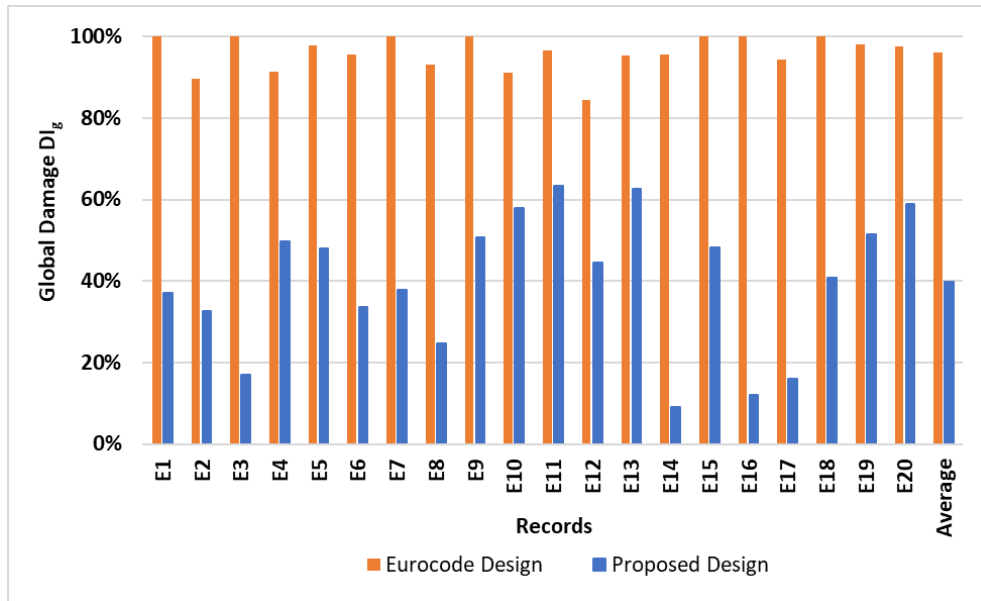


Fig. 4.19 Global damage index (DI_g) for the Eurocode and proposed design solution frames subjected to a set of real ground motion records

4.7 Summary and Conclusions

This study aimed to investigate the efficiency of the Eurocode and a newly developed methodology, which accounts for the secondary moments due to P- Δ effects, amplified by the presence of additional vertical loading, for the seismic design of multi-storey CFS strap-braced stud wall frames. Detailed non-linear FE models of single strap-braced wall panels were developed in ABAQUS and validated against available experimental data. The validated models were then adopted to develop equivalent hysteretic models in OpenSees for different cross-section sizes and vertical load levels. Subsequently, a case study 6-storey CFS frame was designed per Eurocode 8 and the proposed methodology. The seismic performance of the frames was assessed in terms of the maximum inter-storey drifts and storey ductility demands under a set of artificial spectrum-compatible records scaled to (IO), (LS) and (CP) performance earthquake intensity levels. For further comparison, an incremental dynamic analysis (IDA) was also conducted by using a global cumulative damage index to assess the overall performance of the frames. Finally, the efficiency of the two design methods was demonstrated under a set of 20 real spectrum-compatible records. The study led to the following main conclusions:

- The Eurocode 8 design solution could satisfy the ASCE/SEI 41-17 ductility demand limits for (IO) and (LS) performance levels, while the ductility limit for (CP) performance level was exceeded by 13%. The proposed design methodology yielded a more uniform inter-storey drift distribution compared to its Eurocode 8 counterpart, especially for the higher intensity levels, and met all the ductility requirements with a higher safety margin.

- It was shown that ignoring the effects of vertical loads may lead to unsafe design solutions. The Eurocode frame was completely damaged under the PGA levels above 0.20 g, due to the premature buckling of the compressive chord studs leading to unacceptable ductility capacities at some storeys. The proposed design experienced significantly lower damage at all earthquake intensity levels and exhibited a global damage index of 4%, 26% and 58% at PGA levels corresponding to IO, LS and CP performance levels, respectively.
- Both frames could satisfy the ASCE/SEI 41-17 (LS) ductility demand limits under a set of design compatible real ground motion records. While the Eurocode design frame completely collapsed in most cases, the global damage index for the proposed design solution ranged between 10% and 63%, with an average value of 40%.
- These results highlight the efficiency of the proposed methodology for the preliminary design of multi-storey CFS strap-braced frames in seismic regions.
- However, further studies are needed to investigate the efficiency of the methodology for other strap-braced wall configurations and topologies.

4.8 Author contribution

- Ioannis Papargyriou:

Conceptualisation, Methodology, Formal Analysis, Investigation, Writing- Original draft, Writing- Reviewing and Editing, Visualisation

- Dr. Iman Hajirasouliha:

Conceptualisation, Methodology, Validation, Writing- Reviewing and Editing, Supervision

CHAPTER 5

Cold-formed steel beam-to-column bolted connections for seismic applications

This chapter is based on the paper titled: “I. Papargyriou, S. Mojtabaei, I. Hajirasouliha, J. Becque, K. Pilakoutas”, Cold-formed steel beam-to-column bolted connections for seismic applications”. Submitted to: Thin Walled Structures, Date submitted: 22/8/2021, under review.

5.1 Abstract

Cold-formed steel (CFS) portal frames are gaining increased popularity around the world. The structural performance of these frames is to a large extent controlled by the CFS beam-to-column connections, which in most practical applications transfer the loads through the beam web using a gusset plate, while the flanges are left unconnected. This can lead to premature local buckling failure of either the CFS beam web in the connection zone or the gusset plate, leading to poor seismic performance. This paper aims to develop two new connection configurations capable of transferring the loads through both web and flanges, as well as present practical seismic design recommendations which provide a balance between load carrying capacity and seismic performance of the connections. The proposed moment-resisting CFS connections are suitable for modular construction while being fully demountable and hence offer advantages such as adaptive off-site construction and reusability. Detailed Finite Element models, taking into account material nonlinearity and initial geometric imperfections, are developed and validated against experimental data. The validated FE models are then used to conduct a comprehensive parametric study to investigate the effects of key design parameters, including the beam thickness and the gusset plate shape and thickness, on the moment-rotation behaviour of the connections. Based on the results, suitable connections with balanced performance are introduced for each connection configuration. Finally, the seismic performance of different connection configurations is compared in

terms of ductility, energy dissipation and damping coefficient, leading to some practical design recommendations commensurate with different seismic performance levels.

5.2 Introduction

The demand for cold-formed steel (CFS) systems has significantly increased over the past decade, and CFS portal frames have become a popular structural system, mainly for single-storey industrial buildings. The seismic performance of CFS frames is to a large extent controlled by the beam-to-column connections, which are implemented in a fundamentally different way compared to the traditional frames composed of hot-rolled sections. Consequently, the use of CFS moment-resisting frames in seismic regions is still very limited due to the challenges associated with developing resilient moment-resisting CFS connections that can prevent premature local buckling failure of the thin-walled elements. As a result, strap-braced load-bearing stud walls (Fülöp and Dubina, 2004; Velchev, 2008b; Leng *et al.*, 2013; Iuorio *et al.*, 2014; Zeynalian and Ronagh, 2015) are currently the dominant lateral force-resisting system used in multi-storey CFS structures, while moment-resisting systems are generally reserved for low-rise CFS portal frames.

The behaviour and design of CFS Web-Connected (W-C) bolted connections have been previously investigated experimentally and numerically in several research studies. Chung and Lau (Chung and Lau, 1999) and Wong and Chung (Wong and Chung, 2002) carried out a series of experiments on CFS bolted beam-column connections, using various forms of gusset plates. They demonstrated the practical feasibility of these connections, which achieved a moment resistance ranging between 42% and 84% of the beam bending moment capacity, and exhibited a semi-rigid response. Similar observations were reported by Lim and Nethercot (Lim and Nethercot, 2003), who tested apex and eaves joints of CFS portal frames to study their behaviour under monotonic bending. The joints failed by premature web buckling. The authors also identified an increased bolt-group length and an increased number of bolts as the main factors which can improve the rotational stiffness of the connections. Dubina *et al.* (Dubina *et al.*, 2009) tested eaves and apex joints of portal frames under monotonic and cyclic loading and observed initial bearing elongations of the bolt holes, as well as local buckling failure in the beam adjacent to the connection, which led to a low overall ductility. In the same study, full-scale testing of a pair of portal frames with bolted connections revealed that these systems lose their capacity rapidly once local buckling occurs in the connections. In another relevant study, Zhang *et al.* (Zhang *et al.*, 2016) carried out three full-scale tests of portal frames and concluded that the stiffness of the eaves and apex connections significantly depends on the bolt tightness and the bracket (i.e. gusset plate) dimensions. More recently, Sabbagh and Torabian (Sabbagh and Torabian, 2021) conducted a proof-of-concept study on a more efficient joist-stud framed design for semi-rigid floor-to-wall connections and proposed a method to estimate the rotational stiffness of such connections. Blum and Rasmussen (Blum and

Rasmussen, 2019) quantified the stiffness of portal frame connections based on the results of experiments, while Bučmys et al. (Bučmys *et al.*, 2018) used an approach based on the component method. In another study, Rinchen and Rasmussen (Rinchen and Rasmussen, 2019) established simplified nonlinear moment-rotation relations for eaves, apex and base connections.

Several studies have demonstrated that the capacity of W-C connections can be considerably affected by the bolt group length (Lim and Nethercot, 2003; Lim *et al.*, 2016; Rinchen *et al.*, 2019; Mojtabaei *et al.*, 2020, 2021b; Phan *et al.*, 2020). This effect was initially attributed by Lim et al. (Lim and Nethercot, 2003) to the presence of a bimoment in the connection, and different design approaches were presented using the Direct Strength Method (DSM) and the Direct Design Method (DDM) to account for this bimoment (Lim *et al.*, 2016; Rinchen *et al.*, 2019; Phan *et al.*, 2020). However, more recently, Mojtabaei et al. (Mojtabaei *et al.*, 2020, 2021b) argued that the effect of the bolt group length can mainly be attributed to a shear lag effect, and the researchers subsequently proposed design equations for the connection strength under various load combinations.

The cyclic behaviour of the CFS beam-to-column W-C connections was studied experimentally and numerically by Sabbagh et al. (Sabbagh *et al.*, 2012, 2013). It was reported that while the connections were categorised as Rigid based on their rotational stiffness per Eurocode 3 (CEN, 2005), the curved flanges of the beam and the welded-in beam stiffeners delayed local buckling failure and improved the bending moment capacity and ductility by 35% and 75%, respectively. A similar experimental study was conducted by Serror et al. (Serror *et al.*, 2016). However, in this case, the column consisted of a hot-rolled profile. It was reported that the presence of stiffeners improved the connection characteristics, while additional flange bends averted premature buckling of the flanges but could not prevent buckling of the web.

Shahini et al. (Shahini *et al.*, 2018) investigated the effect of different bolt arrangements on the instantaneous centre of rotation of connections and demonstrated that a circular arrangement with slotted holes in the gusset plate can delay premature local buckling failure in the CFS beam. Sabbagh et al. (Sabbagh *et al.*, 2013) adopted a more detailed approach by including slip-bearing action and geometric imperfections. Similarly, Ye (Ye, 2016) developed detailed Finite Element (FE) models of CFS moment-resisting connections while taking into account material nonlinearity and geometric imperfections and studied the effects of key design parameters such as the beam cross-sectional shape and the bolt arrangement on the cyclic performance. In a follow-up study conducted by Ye et al. (Ye, Mojtabaei and Hajirasouliha, 2019), the seismic characteristics of beam-to-column connections which mobilised a friction-slip fuse mechanism were assessed and compared with similar connections where bolt slippage is prevented. However, no experimental verification of the feasibility of prestressing CFS connections was provided.

Current CFS moment-resisting connections are mostly implemented as W-C connections. This has the implication that, unlike in moment resisting connections in hot-rolled steel structures, the beam and column flanges do not directly participate in the transferring of the applied loads. This considerably affects the stiffness, load bearing capacity and resilience of these connections, especially under extreme loading events such as earthquakes and blasts. The present work aims to address this important issue by developing two new configurations of beam-to-column bolted connections: Flange-Connected (F-C) and Web-and-Flange-Connected (WF-C) joints, which benefit from the load transfer contribution of the flanges. The efficiency of the newly proposed connections is compared to the conventional Web-Connected (W-C) connections. To achieve this, detailed ABAQUS (Dassault Systèmes Simulia, 2014) FE models were employed, which were first validated against experimental results. A parametric study further investigated the effect of key design parameters, such as the beam thickness, and the gusset plate shape and thickness, on the moment-rotation behaviour of each type of connection. The connections with the overall best performance were identified, selected and compared in terms of ductility, energy dissipation and damping coefficient, leading to practical seismic design considerations linked to different seismic performance levels.

5.3 Description of the ABAQUS numerical models

Sabbagh et al. (Sabbagh *et al.*, 2012) carried out a comprehensive experimental programme on W-C connections, where the webs of back-to-back channel beam and column sections were bolted to a gusset plate, and the panel zone was stiffened to prevent local failure in the column, in alignment with the common strong-column/weak-beam philosophy in earthquake engineering. More detailed information about these experiments can be found in (Sabbagh, 2011). In this section, the results of two of these tests, pertaining to specimens A1 and B1, which were tested under cyclic loading conditions, were selected to validate the numerical models. The models were developed using ABAQUS software (Dassault Systèmes Simulia, 2014) and accounted for material nonlinearity and initial geometric imperfections. Various previous studies have demonstrated that the adopted modelling approach can be used to simulate the nonlinear behaviour of CFS systems in an effective and reliable way (Sabbagh *et al.*, 2013; Mojtabaei *et al.*, 2018; Ye, Mojtabaei and Hajirasouliha, 2019; Ye, Mojtabaei, Hajirasouliha, *et al.*, 2019; Phan *et al.*, 2020).

5.3.1 Material properties

The nonlinear stress-strain relationships of the CFS beam and the gusset plate materials were established in ABAQUS (Dassault Systèmes Simulia, 2014) using the two-stage material model proposed by Heidarali and Nethercot (Haidarali and Nethercot, 2011), based on the results of coupon tests reported

by Sabbagh et al. (Sabbagh, 2011). In a the first stage, the stress-strain behaviour was defined up to the 0.2% proof stress ($\sigma_{0.2}$) using Eq. (21), initially proposed by Ramberg and Osgood (Ramberg and Osgood, 1943) and later modified by Hill (Hill, 1944). A straight line with a slope $E = \frac{E_o}{100}$ was used in the second stage, as expressed by Eq. (22). In Eqs. (21) and (22), $\varepsilon_{0.2}$ is the strain corresponding to the $\sigma_{0.2}$ proof stress, E_o stands for the elastic modulus (which was taken as 210 GPa), and n is a constant which was assumed equal to 10, as recommended by Rasmussen (Rasmussen, 2003).

$$\varepsilon = \frac{\sigma}{E_o} + 0.002 \left(\frac{\sigma}{\sigma_{0.2}} \right)^n, \quad \sigma \leq \sigma_{0.2} \quad (21)$$

$$\varepsilon = \varepsilon_{0.2} + \frac{\sigma - \sigma_{0.2}}{E}, \quad \sigma \geq \sigma_{0.2} \quad (22)$$

In a next step the engineering strains and stresses were converted to logarithmic plastic strains and stresses, while the linear kinematic hardening rule available in ABAQUS was adopted to simulate the hardening behaviour of the material. The (engineering) material properties of the connection components are summarised in Table 5.1 for reference tests A1 and B1.

Table 5.1 Material properties of the tests A1 and B1

Test	Element	$\sigma_{0.2}$ (MPa)	f_u (MPa)
A1	Beam	313	479
	Gusset Plate	353	516
B1	Beam	322	479
	Gusset Plate	308	474

5.3.2 Finite element type and mesh-size

The S4R general-purpose finite element available in ABAQUS was employed to model all connection components since it has previously been proven to be accurate in capturing the behavioural mechanics of CFS elements and connections (Mojtabaei *et al.*, 2018, 2020, 2021b; Ye, Mojtabaei and Hajirasouliha, 2018; Ye, Mojtabaei, Hajirasouliha, *et al.*, 2018). This four-noded shell element has six degrees of freedom per node. It can account for nonlinear material properties and finite membrane strains and features hourglass control and reduced integration. Following a mesh sensitivity analysis, a mesh size of 10×10 mm was selected to guarantee adequate numerical accuracy while keeping the computational time within acceptable limits.

5.3.3 Bolt modelling

The bolt behaviour was simulated by employing the Discrete Fastener feature of the ABAQUS software (Dassault Systèmes Simulia, 2014). This type of fastener creates attachment lines between the fastening points located on the connecting elements, as shown in Fig. 5.1(a-b). An influence radius was assigned to each fastening point, with the implication that the displacements of the fastening points are coupled to the average displacements of the nodes within this radius. An influence radius equal to 8 mm was used in the FE models, corresponding to half the bolt diameter, as recommended in (Mojtabaei *et al.*, 2018, 2020). In this study, rigid bearing behaviour was assumed for the bolts connecting the column to the gusset plate, while combined friction and bearing behaviour were modelled for the beam to gusset plate bolts. This was due to the fact that bolt hole elongation is more critical for the beam elements due to their lower thickness compared to the column and the gusset plate. In the A1 and B1 tests, preloading forces of $P_b=88$ kN and $P_b=70$ kN, respectively, were applied to the head of the bolt by using a torque wrench, which generated friction between the beam web and gusset plate. The relationship between the torque and preloading force can be expressed as (Juvinall and Marshek, 2006; Ye, Mojtabaei, Hajirasouliha, *et al.*, 2018):

$$T = KP_b d \quad (23)$$

where T is the applied tightening torque, K is the torque coefficient, which is approximately equal to 0.2 (Juvinall and Marshek, 2006), and d is the nominal bolt diameter. When friction is overcome, bearing action of the bolts is mobilised, which was modelled using the equation proposed by Fisher (Fisher, 1964):

$$R_B = R_{ult} [1 - e^{-\mu \left(\frac{\delta_{br}}{25.4} \right)}]^\lambda \quad (24)$$

$$R_{ult} = 2.1dtF_u \quad (25)$$

where R_B is the bearing force, R_{ult} is the ultimate bearing strength, δ_{br} is the bearing deformation, t is the plate thickness, d is the bolt diameter, F_u is the ultimate tensile strength of the plate material, and μ and λ are constants equal to 5 and 0.55, respectively, according to the recommendations by Uang *et al.* (Uang *et al.*, 2010). The load-displacement behaviour of the bolts obtained from the above-mentioned equations for tests A1 and B1 are shown in Fig. 5.2. It should be noted that in experiments A1 and B1 (Sabbagh, 2011), no bolt damage was observed, and the slip between the connecting elements was found to be insignificant.

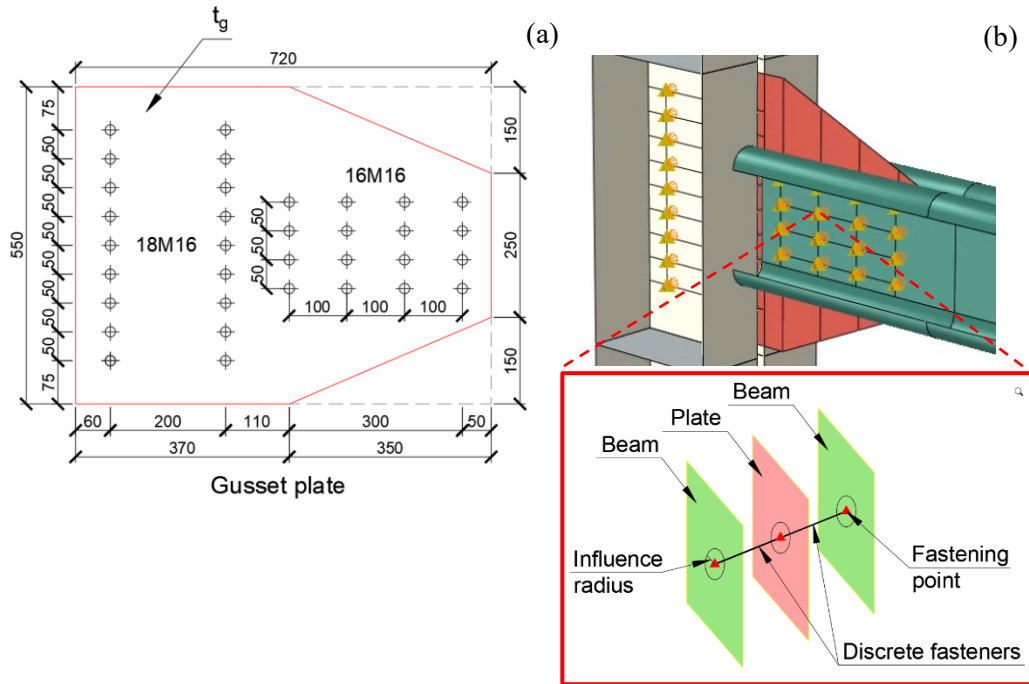


Fig. 5.1 FE modelling of the tested connections: a) bolt arrangement and b) discrete fastener

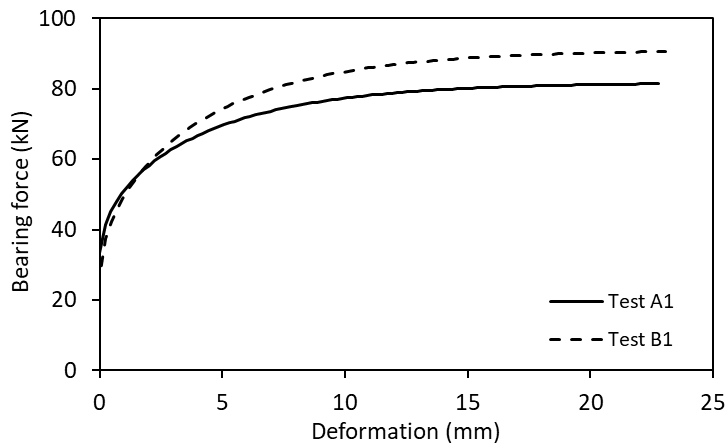


Fig. 5.2 Bearing behaviour of the beam to gusset plate bolts incorporated into the FE models of tests A1 and B1

5.3.4 Boundary conditions and interactions

The boundary conditions imposed onto the FE models of the W-C connection are shown in Fig. 5.3. All three translational degrees of freedom of the nodes at the bottom of the column were restrained ($U_x=U_y=U_z=0$), while the horizontal displacements of the top nodes were also restrained ($U_x=U_y=0$). To prevent out-of-plane deformations of the beam element, lateral restraints were modelled at the locations where the lateral bracing system was positioned in the experiments (see Fig. 5.3). The webs of the back-to-back channels were connected at three different locations using the “Tie” constraint to

simulate the bolts outside the connection zone. Similarly, tie constraints were used to connect the column stiffeners rigidly to the column web and flanges. The “Hard” contact feature was employed between the connecting faces of the beam webs and the gusset plate to avoid penetration of the surfaces into each other. All degrees of freedom of the beam end section, where the external load was applied, were coupled to a Reference Point (RP) located at mid-height of the webs.

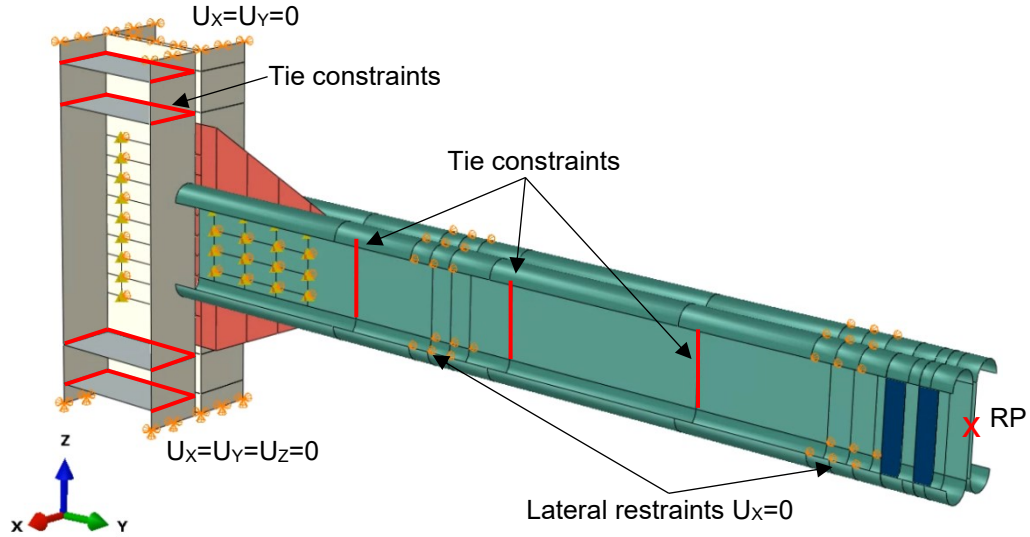


Fig. 5.3 Boundary conditions of the FE models

5.3.5 Initial geometric imperfections

The global buckling mode of the CFS beam was prevented due to the presence of the lateral bracing system in the experiments. Hence, either a local or a distortional imperfection (i.e. whichever mode had the lower critical buckling load) was included in the FE models. Imperfection magnitudes of $0.94t$ and $0.34t$ (where t is the plate thickness) were used for the distortional and local imperfections, respectively, as recommended by Schafer and Peköz (Schafer and Peköz, 1998). These are the 50% values of the cumulative distribution function of experimentally measured imperfections and represent ‘most probable’ values. Since these magnitudes are only applicable for $t \leq 3$ mm, Walker’s (Walker, 1975) equation was instead used for plate thicknesses larger than 3 mm:

$$w_d = 0.3t \lambda \quad (26)$$

where w_d is the imperfection magnitude and λ represents the cross-sectional slenderness, which is calculated as:

$$\lambda = \sqrt{\frac{M_y}{M_{cr}}} \quad (27)$$

In the above equation, M_y is the yield moment of the cross-section and M_{cr} is the elastic local/distortional buckling moment obtained using the CUFSM software (Li and Schafer, 2010). To generate the overall shape of the geometric imperfections, an elastic eigenvalue buckling analysis was first performed in ABAQUS. The shape of the critical buckling mode was then scaled by the appropriate imperfection magnitude.

5.3.6 Loading

The FE models of the connections were loaded in a displacement controlled manner under both monotonic and cyclic conditions. While a maximum displacement of 200 mm was applied for monotonic loading, in the cyclic analyses, the loading protocol of AISC 341-16 (AISC, 2016), as used in the corresponding experiments, was adopted (Fig. 5.4).

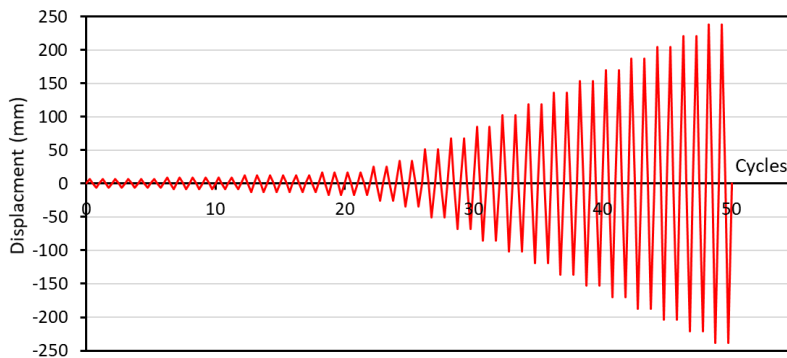


Fig. 5.4 Cyclic loading protocol adopted from AISC 341-16 (AISC, 2016)

5.3.7 Numerical model validation

‘Static General’ analyses were carried out using the High-Performance Computing (HPC) facilities at the University of Sheffield. Fig. 5.5 compares the moment-rotation relationships extracted from experiments A1 and B1 with the corresponding FE predictions for both cyclic and monotonic loading conditions. The moments were made dimensionless relative to the plastic moment of the CFS beam (M_p) and the rotation of the connection was determined as the ratio of the beam tip displacement to the length of the beam up to the gusset plate. Fig. 5.5 indicates that the FE models were able to simulate the behaviour of both tested connections with a good level of accuracy over the whole loading range. The initial stiffnesses of the tested connections were virtually identical to those obtained from the FE models,

while the experimental and predicted maximum flexural capacities compared as 54.3 kNm and 51.6 kNm for test A1, and 81.7 kN.m and 82.4 kN.m for test B1. A comparison between the FE cyclic and monotonic results generally indicates that the initial stiffness and the maximum strength values are coincident in both cases. However, the results of the monotonic analyses slightly underestimated the stiffness degradation rate. Regarding the failure mode, the results of the experiments indicated that local buckling of the beam web occurred close to the connection zone (see Fig. 5.5). Similarly, failure of the connections under both monotonic and cyclic loads was predicted by the FE analyses to be initiated by local buckling of the beam web, followed by buckling of the compression flange, as shown in Fig. 5.6. These observations confirm the adequacy of the adopted FE models in this study. It should be noted that these modelling techniques have also been verified against experiments reported by Lim and Nethercot (Lim and Nethercot, 2003) in two recent publications by the authors (Mojtabaei *et al.*, 2020, 2021a).

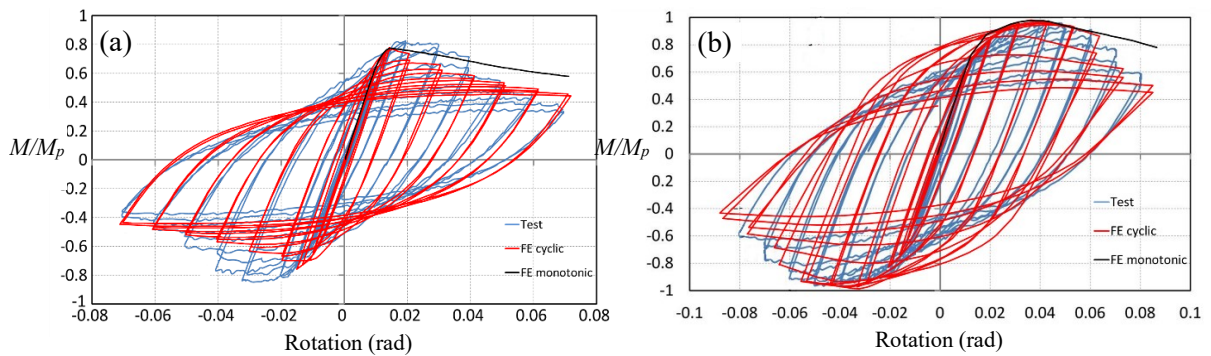
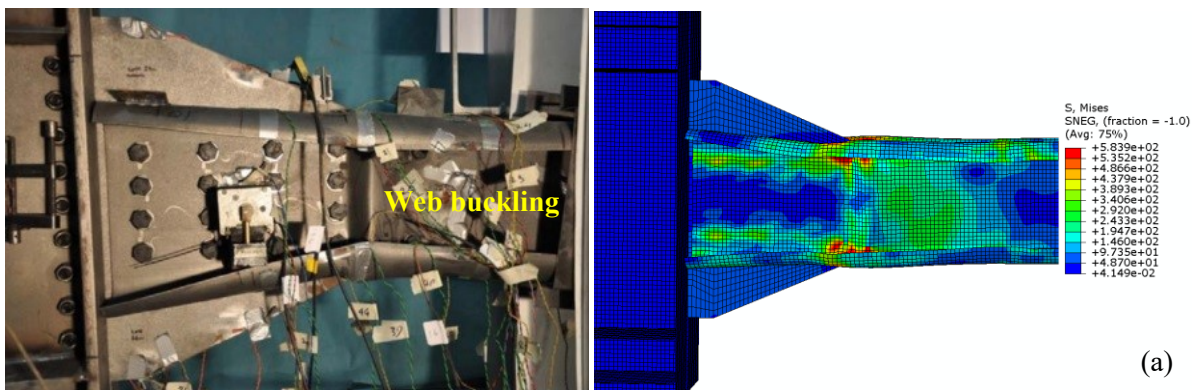


Fig. 5.5 Comparison between experimental moment-rotation behaviour (Sabbagh, 2011) and FE analysis results for: (a) A1 and (b) B1 specimens



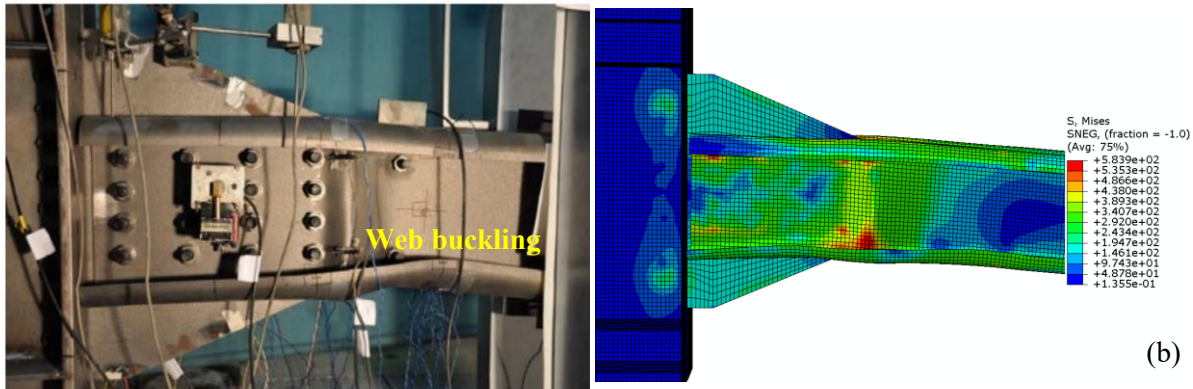


Fig. 5.6 Comparison between the experimental (Sabbagh, 2011) and predicted failure modes under cyclic loading for: (a) A1 and (b) B1 specimens

5.4 Flexural behaviour of various connection configurations

This section discusses the development of two new configurations of bolted CFS beam-to-column connections which are capable of transferring the applied loads through either the flanges only (F-C connection) or both the flanges and the webs (WF-C connection). The behaviour and failure mechanism of these connections, along with the W-C connections introduced in Section 5.3, were investigated under monotonic loading conditions while considering various beam thicknesses and gusset plate shapes and thicknesses. The obtained moment-rotation curves were compared in terms of their relevant performance criteria, including the bending moment capacity, the ultimate rotation and the rotational rigidity in relation to code-prescribed categories. As shown in the previous section, the monotonic loading results can be considered representative of both monotonic and cyclic loading when considering these parameters. Based on these results, the connection types having the best overall performance in terms of their bending moment capacity, ultimate rotation, rotational rigidity and seismic classification of the connections were identified for each connection configuration and further investigated under cyclic loading with the aim of developing practical design recommendations.

5.4.1 Connection configurations

Three different types of CFS beam-to-column bolted connections were investigated in this study: W-C, F-C, and WF-C connections. All proposed connections are easily demountable (i.e. no welding is used in the connection assembly), and therefore offer advantages such as adaptive off-site construction, fast assembly, and reusability, resulting in potential sustainability improvements in construction.

The W-C connection is assembled by bolting a gusset plate in between the webs of the beam and the webs of the column. The choice of the gusset plate shape is a rather challenging issue encountered in practice since it may cause either architectural limitations or reductions in structural performance.

Therefore, as shown in Table 5.2, three different gusset plate shapes were selected in this study, including a T-shaped plate with sharp corners (further referred to as the ‘T-shape’), a T-shaped plate with rounded corners (the ‘rounded T-shape’, having a radius of 350 mm) and the rectangular plate with chamfered corners which was employed in the experiment (see Section 2), and is simply referred to as ‘Chamfered shape’.

For the F-C connection configuration, either unstiffened or stiffened top and seat angles were used, bolted to the column and beam flanges, as shown in Table 5.2. The WF-C connections, on the other hand, were conceived as a combination of the other two configurations, where both a T-shaped gusset plate and unstiffened top and seat angles were used. The bolt group length (l_b) in the CFS beam was consistently taken equal to the beam depth (h), and a fixed number of bolts was used in each type of connections, as illustrated in Table 5.2. However, the thicknesses of the CFS beam and the gusset plate were varied to identify the slenderness limits where failure shifts from the gusset plate to the beam. The CFS beam was assigned thicknesses $t_b = 1, 2, 4$ and 6 mm, whereas the gusset plate thickness was taken as a multiple of the beam thickness. Table 5.2 summarises the selected thicknesses for each connection configuration. It is noted that for the chosen beam dimensions $t_b = 1, 2, 4$ and 6 mm correspond to Class 4, 3, 2 and 1 cross-sections according to EC3 (CEN, 2010), respectively.

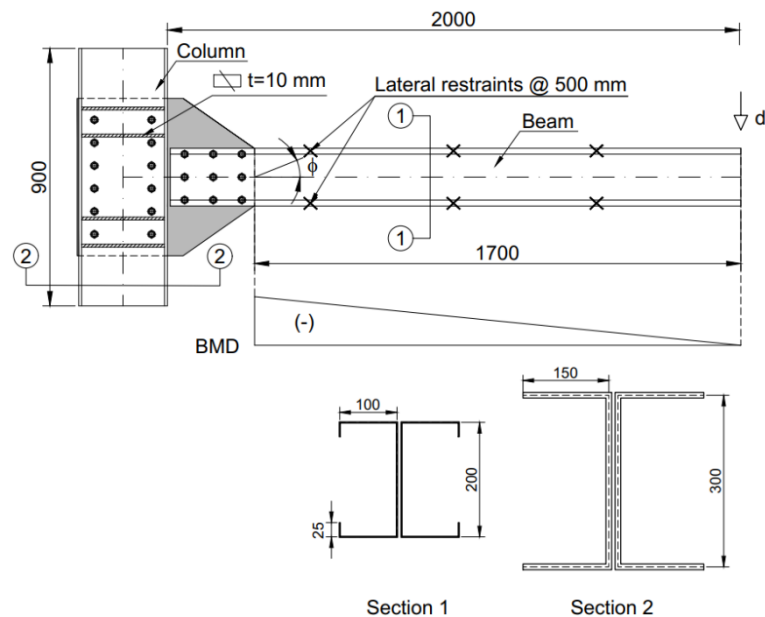
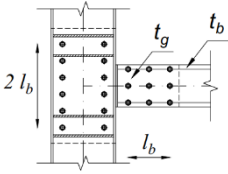
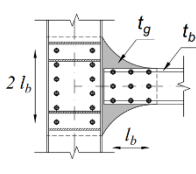
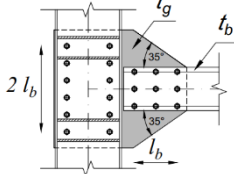
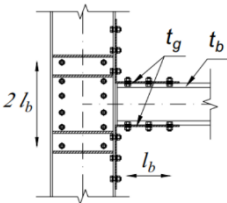
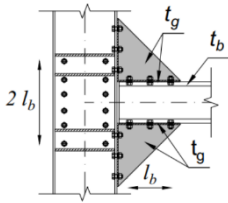
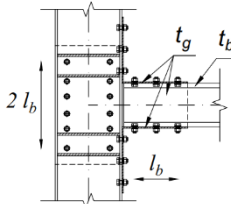


Fig. 5.7 Connection configuration

The other design parameters were kept constant across all connection models, including the material properties, the locations of the lateral bracing, the lengths of the members, the cross-sectional dimensions and the thickness of the column and its stiffeners, as shown in Fig. 5.7. The 2000 mm long beam and 900 mm long column elements used in the FE models consisted of back-to-back lipped channel and plain channel sections, respectively, with the dimensions (along the centrelines) (Fig. 5.7).

The modelled beam segment can be considered representative of the part of a beam in a moment-resisting frame between the point of contraflexure and the column. The material properties listed in Table 5.1 were used for all FE models. Lateral bracing was provided along the length of the beam at 500 mm spacing, consistent with the experiment.

Table 5.2 Connection configurations and selected design variables

Web-connected (W-C)			
$t_b=1$ mm $t_g = t_b, 1.5t_b, 2t_b, 3t_b$	$t_b=2$ mm $t_g = t_b, 1.5t_b, 2t_b, 3t_b$	$t_b=4$ mm $t_g = t_b, 1.5t_b, 2t_b, 3t_b$	$t_b=6$ mm $t_g = t_b, 1.5t_b, 2t_b, 3t_b$
T-shape	Rounded T-shape	Chamfered shape	
			
Flange-connected (F-C)			
$t_b=1$ mm $t_g = t_b, 2t_b, 3t_b, 4t_b, 5t_b, 6t_b$	$t_b=2$ mm $t_g = t_b, 2t_b, 3t_b, 4t_b, 5t_b, 6t_b$	$t_b=4$ mm $t_g = t_b, 2t_b, 3t_b$	$t_b=6$ mm $t_g = t_b, 2t_b, 3t_b$
Unstiffened top and seat angles	Stiffened top and seat angles		
			
Web and flange-connected (WF-C)			
$t_b=1$ mm $t_g = t_b, 1.5t_b, 2t_b, 3t_b$	$t_b=2$ mm $t_g = t_b, 1.5t_b, 2t_b, 3t_b$	$t_b=4$ mm $t_g = t_b, 1.5t_b, 2t_b, 3t_b$	$t_b=6$ mm $t_g = t_b, 1.5t_b, 2t_b, 3t_b$
T-shape and unstiffened top and seat angles			
			

5.4.2 Evaluation of connections under monotonic loading

5.4.2.1 Performance criteria

The rotational behaviour of the connections was quantified through various performance parameters related to their (i) rotational rigidity, and (ii) rotational capacity. The latter was assessed in two distinct ways, as detailed below.

To assess the rigidity of the connections, the provisions of EN 1993-1-8 (CEN, 2005) were followed, in which the moment-rotation relationship of the connection is derived by calculating the bending moment (M_j) at the face of the column and by taking the corresponding rotation (ϕ) as the difference between rotations (ϕ_1) and (ϕ_2), shown in Fig. 5.8(a). The initial stiffness ($S_{j,ini}$) is then defined as the secant slope of the moment-rotation curve (see Fig. 5.8(b)) at a value of $2/3 \times M_{j,R}$, where ($M_{j,R}$) is the moment resistance of the connection. Subsequently, the connection is categorised as either rigid, semi-rigid or pinned, by comparing the initial stiffness ($S_{j,ini}$) with the limits shown in Fig. 5.8(c). A Rigid (R) connection has an initial stiffness greater or equal to $k_b \times E \times I_b / L_b$, where $k_b=25$ for an unbraced system, (E) is the elastic modulus, (I_b) is the second moment of area of the beam and (L_b) is the beam span, measured between the centre lines of the columns. The connection is classified as Pinned (P) if the initial stiffness is smaller or equal to $0.5 \times E \times I_b / L_b$. For intermediate values, the connection is Semi-Rigid (S-R).

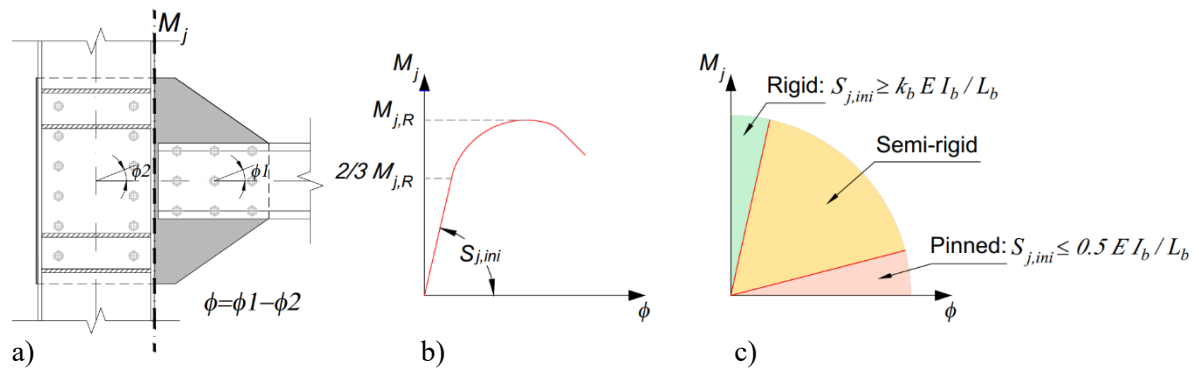


Fig. 5.8 Definition of a) moment-rotation relationship, b) initial stiffness ($S_{j,ini}$), and c) boundaries for the rotational stiffness classification of connections

The first performance parameter adopted to assess the rotational capacity of the connections was the ultimate rotation, taken equal to the minimum of the 0.06 rad and the rotation corresponding to a 20% drop in the moment from the peak point in the moment-rotation curve. This is based on the recommendations given by the American Seismic codes: AISC 341-16 (AISC, 2016) and FEMA-350 (FEMA, 2000a).

The second indicator of inelastic rotational capacity is provided by the American Seismic Provisions for Structural Steel Buildings (AISC 341-16), in which moment-resisting connections are classified into three categories: Ordinary Moment Frames (OMF), Intermediate Moment Frames (IMF) and Special Moment Frames (SMF). The connections of SMFs and IMFs should be able to accommodate minimum storey drift angles of 0.04 and 0.02 rad, respectively, while OMFs do not meet the 0.02 rad value. It should be noted that using OMFs in seismic regions is prohibited by most seismic design codes.

5.4.2.2 Moment-rotation results and discussions

5.4.2.2.1 W-C connections

Fig. 5.9 shows the moment-rotation curves obtained for the W-C connections with various beam thicknesses (t_b), gusset plate thicknesses (t_g) and gusset plate shapes (①: T-shape, ②: rounded T-shape and ③: chamfered shape) up to their ultimate rotations (which are listed in Table 5.2). Both the moment and the rotation in Fig. 5.9 were calculated based on the location of failure, which was idealised to coincide with the end of the gusset plate, i.e. at a distance of 1700 mm from the cantilever tip (Fig. 5.7). Failure occurred by either local/distortional buckling of the beam immediately adjacent to the connection, or local buckling of the gusset plate. Each curve corresponds to a certain gusset plate thickness (t_g), being multiples of the beam thicknesses (t_b).

It is seen that the connections with the chamfered gusset plate (i.e. ③) reached higher moment capacities than their ‘rounded T-shape’ counterparts (i.e. ②) for gusset plate thicknesses t_g with $t_b \leq t_g \leq 1.5t_b$, while both configurations reached the same moment capacities for gusset plate thicknesses of $2t_b \leq t_g \leq 3t_b$. The latter is due to gusset plate failure no longer being critical for those thicknesses. This makes the rounded T-shape a suitable alternative to the conventional chamfered gusset plates at those higher thicknesses. The T-shaped gusset plate connections exhibited the lowest moment capacity (M_{max}) among the three selected gusset plate shapes, which can be attributed to the abrupt change in depth and slenderness of the gusset plate at the column face, leading to stress concentrations and premature buckling at the corners of the T-shaped plate, especially for lower plate thicknesses.

Table 5.3 lists the dominant failure modes for all connections, which consisted of local/distortional buckling of either the CFS beam (B) or the gusset plate (GP). Fig. 5.10 shows examples of the typical failure modes of the connections with T-shaped, rounded T-shaped and chamfered gusset plates for $t_b=4$ mm and $t_g=1.5t_b$, where the yielding areas are highlighted in grey. It is seen that significant plasticity developed in the beam for the connection with the chamfered gusset plate, while the connections with T-shaped and rounded T-shaped gusset plates mainly experienced plasticity in the gusset plate rather than the beam.

According to EC3 (CEN, 2005) (see section 5.4.2.1), all connections with T-shaped gusset plates were classified as Semi-Rigid (S-R) (Table 5.3). All rounded T-shaped connections also performed as Semi-Rigid joints, with the exception of those with the thickest gusset plates connecting Class 3 or 4 beams, which were classified as Rigid (R). With the chamfered connections, however, mostly Rigid (R) connections were obtained in Class 2, 3 and 4 beams, with the exception of those with the thinnest gusset plates ($t_g = t_b$ for Class 2-4, and $t_g = 1.5t_b$ for Class 2).

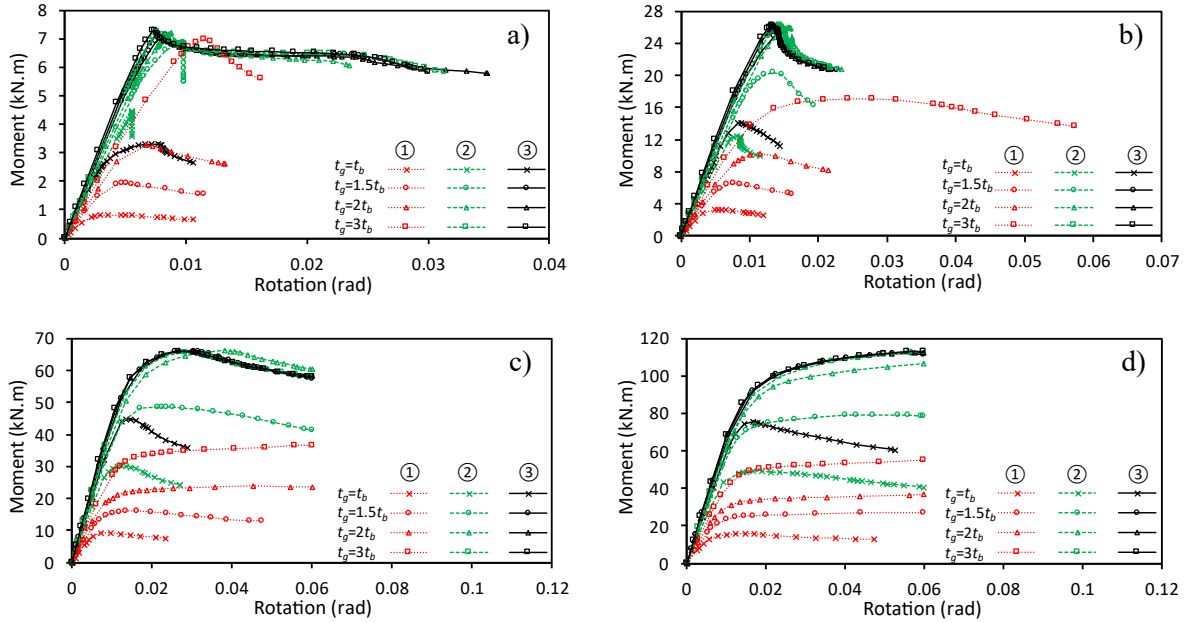


Fig. 5.9 Moment-rotation responses of W-C connections with various gusset plate thicknesses (t_g) and shapes (①: T-shape, ②: rounded T-shape and ③ chamfered shape), and beam thicknesses (t_b) of a) 1 mm, b) 2 mm, c) 4 mm and d) 6 mm

Table 5.3 Ultimate rotation (ϕ_{max}), flexural rigidity per EC3 (CEN, 2005), rotational category per AISC provisions (AISC, 2016) and failure modes of W-C connections

Beam thickness t_b	Gusset plate thickness t_g	T-shape				Rounded T-shape				Chamfered shape			
		Failure mode	EC3 rotational rigidity	ϕ_{max} (rad)	AISC category	Failure mode	EC3 rotational rigidity	ϕ_{max} (rad)	AISC category	Failure mode	EC3 rotational rigidity	ϕ_{max} (rad)	AISC category
1 mm	t_b	GP	S-R	0.01	OMF	GP	S-R	0.006	OMF	GP	S-R	0.01	OMF
	$1.5t_b$	GP	S-R	0.011	OMF	GP	S-R	0.01	OMF	B	R	0.025	IMF
	$2t_b$	GP	S-R	0.013	OMF	B	S-R	0.024	IMF	B	R	0.035	IMF
	$3t_b$	GP	S-R	0.017	OMF	B	R	0.032	IMF	B	R	0.03	IMF
2 mm	t_b	GP	S-R	0.013	OMF	GP	S-R	0.012	OMF	GP	S-R	0.014	OMF
	$1.5t_b$	GP	S-R	0.016	OMF	GP	S-R	0.02	OMF	B	R	0.023	IMF
	$2t_b$	GP	S-R	0.021	IMF	B	S-R	0.023	IMF	B	R	0.022	IMF
	$3t_b$	GP	S-R	0.059	SMF	B	R	0.022	IMF	B	R	0.022	IMF
4 mm	t_b	GP	S-R	0.025	IMF	GP	S-R	0.027	IMF	GP	S-R	0.028	IMF
	$1.5t_b$	GP	S-R	0.05	SMF	GP	S-R	0.06	SMF	B	S-R	0.06	SMF
	$2t_b$	GP	S-R	0.06	SMF	B	S-R	0.06	SMF	B	R	0.06	SMF
	$3t_b$	GP	S-R	0.056	SMF	B	S-R	0.06	SMF	B	R	0.06	SMF
6 mm	t_b	GP	S-R	0.048	SMF	GP	S-R	0.06	SMF	GP	S-R	0.052	SMF
	$1.5t_b$	GP	S-R	0.06	SMF	GP	S-R	0.06	SMF	GP	S-R	0.06	SMF
	$2t_b$	GP	S-R	0.056	SMF	GP	S-R	0.06	SMF	B	S-R	0.06	SMF
	$3t_b$	GP	S-R	0.06	SMF	B	S-R	0.06	SMF	B	S-R	0.06	SMF

(GP): Gusset plate failure, (B): Beam failure

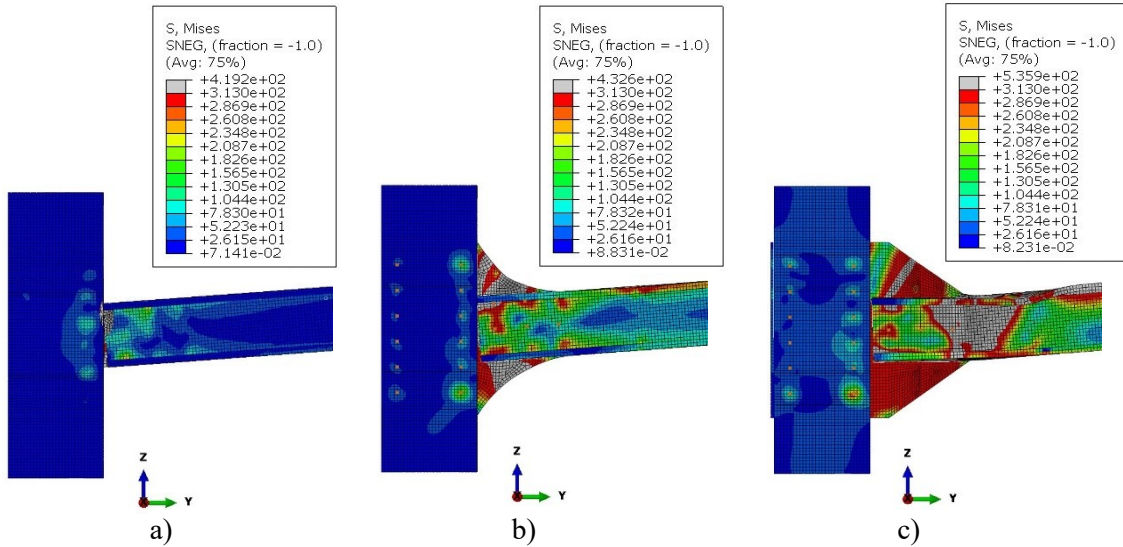


Fig. 5.10 Failure modes of W-C connections with: a) T shape, b) rounded T-shape and c) chamfered gusset plate, for $t_b=4$ mm and $t_g=1.5t_b$

5.4.2.2.2 F-C connections

The F-C connections considered in this study employed either stiffened or unstiffened angle sections, instead of a gusset plate, to transfer shear and bending moments to the column (see Table 5.2). The thicknesses of the angle sections were taken as multiples of the beam thickness, and ranged between t_b and $6t_b$ for the 1 mm and 2 mm thick beams, and between t_b and $3t_b$ for the 4 mm and 6 mm thick beams (as to not exceed a maximum value of 18 mm). In the case of stiffened seats, the thickness of the stiffening plate was taken equal to the thickness of the angles. Fig. 5.11 presents the moment-rotation relationships, up to the ultimate rotation, for beam thicknesses of 1, 2, 4 and 6 mm, where ① and ② stand for connections with unstiffened and stiffened angles, respectively. It is seen that, in general, using stiffened angles has the ability to significantly increase the flexural stiffness and capacity (on average 4 times) of the connections, compared to those with unstiffened angles. This is especially evident for the connections with Class 3 and 4 beam sections (i.e. 1 mm and 2 mm thickness). Table 5.4 presents the failure modes of the studied F-C connections. The unstiffened angles failed in bending, while the connections employing stiffened angles failed predominately due to angle bending and local buckling of the stiffening plates, indicated with (GP), or local/distortional buckling of the beam, indicated with (B), respectively. For low gusset plate thicknesses, the F-C connections with Class 2, 3 and 4 beam sections (i.e. 1, 2 and 4 mm thickness) practically acted as pin connections, and are hence unsuited for seismic use in unbraced moment-resisting frames. On the contrary, the studied connections with Class 1 beam sections (i.e. $t_b=6$ mm) were determined to all be Semi-Rigid. It should be noted that incorporating stiffened angles, as opposed to unstiffened angles, improved the rigidity of the connections from Pinned to Semi-Rigid in many cases, as shown in Table 5.4.

Due to the deformability of the unstiffened angles under combined tension/compression and bending, with a gap opening up between the beam and the column on the tension side, all connections with unstiffened angles reached an ultimate rotation of at least 0.06 rad without a significant drop in moment resistance and satisfied SMF requirements according to the AISC 341 (AISC, 2016) classification. These large rotations led to a failure in the angles, while the beam element remained unbuckled (see Fig. 5.12(a)). On the other hand, stiffening the top and seat angles with infill plates dramatically reduced their deformations, and as a result, failure shifted to the beam element instead (see Fig. 5.12(b)). This has the potential to reduce the rotational capacity to below 0.06 rad and alter the connection behaviour from a SMF to an IMF for the larger plate thicknesses and Class 3 and 4 beam sections (i.e. 1 and 2 mm thickness). These results indicate that for seismic applications, using thick stiffened angle sections to connect thin-walled beam sections may not be beneficial.

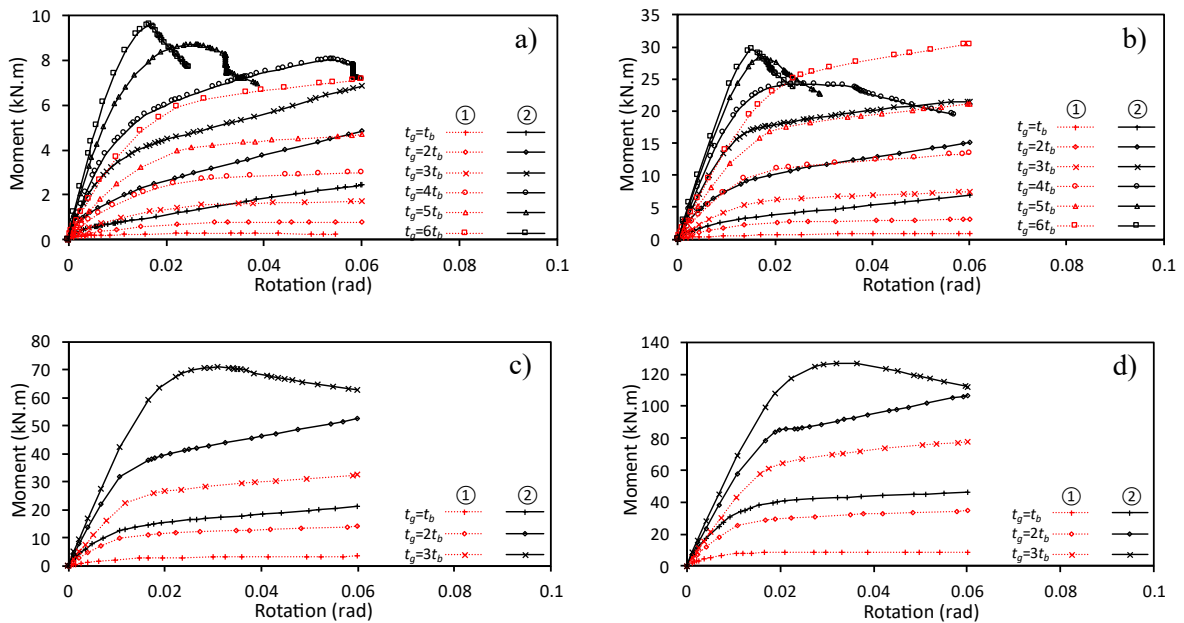


Fig. 5.11 Moment-rotation responses of F-C connections with various gusset plate thicknesses (t_g) and shapes (①: unstiffened angles and ②: stiffened angles), and beam thicknesses (t_b) of a) 1 mm, b) 2 mm, c) 4 mm and d) 6 mm

Table 5.4 Ultimate rotation (ϕ_{max}), flexural rigidity per EC3 (CEN, 2005), rotational category per AISC provisions (AISC, 2016) and failure modes of F-C connections

Beam thickness t_b	Gusset plate thickness t_g	Unstiffened top and seat angles				Stiffened top and seat angles			
		Failure mode	EC3 rotational rigidity	ϕ_{max} (rad)	AISC category	Failure mode	EC3 rotational rigidity	ϕ_{max} (rad)	AISC category
1 mm	t_b	GP	P	0.06	SMF	GP	P	0.06	SMF
	$2t_b$	GP	P	0.06	SMF	GP	P	0.06	SMF
	$3t_b$	GP	P	0.06	SMF	B	S-R	0.06	SMF
	$4t_b$	GP	P	0.06	SMF	B	S-R	0.06	SMF
	$5t_b$	GP	S-R	0.06	SMF	B	S-R	0.038	IMF
	$6t_b$	GP	S-R	0.06	SMF	B	S-R	0.025	IMF
2 mm	t_b	GP	P	0.06	SMF	GP	P	0.06	SMF
	$2t_b$	GP	P	0.06	SMF	GP	S-R	0.06	SMF
	$3t_b$	GP	P	0.06	SMF	B	S-R	0.06	SMF
	$4t_b$	GP	S-R	0.06	SMF	B	S-R	0.055	SMF
	$5t_b$	GP	S-R	0.06	SMF	B	S-R	0.029	IMF
	$6t_b$	GP	S-R	0.06	SMF	B	S-R	0.023	IMF
4 mm	t_b	GP	P	0.06	SMF	GP	P	0.06	SMF
	$2t_b$	GP	P	0.06	SMF	GP	S-R	0.06	SMF
	$3t_b$	GP	S-R	0.06	SMF	B	S-R	0.06	SMF
6 mm	t_b	GP	S-R	0.06	SMF	GP	S-R	0.06	SMF
	$2t_b$	GP	S-R	0.06	SMF	GP	S-R	0.06	SMF
	$3t_b$	GP	S-R	0.06	SMF	B	S-R	0.06	SMF

(GP): Gusset Plate failure, (B): Beam failure

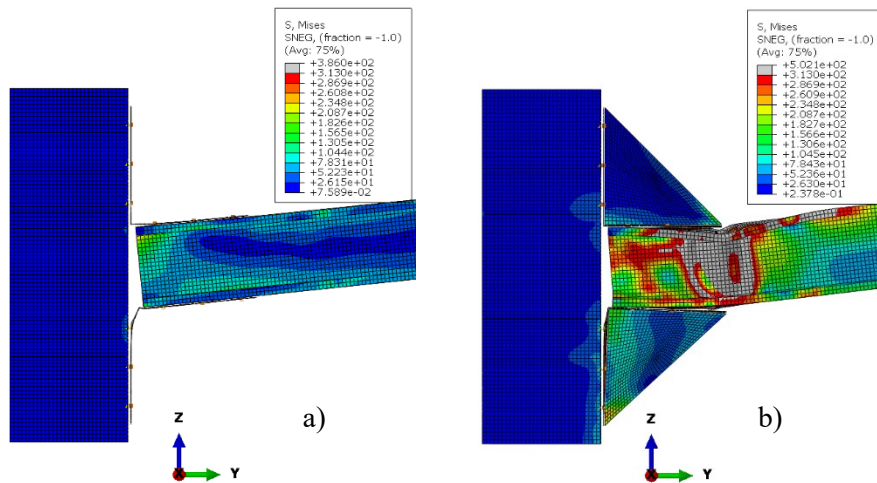


Fig. 5.12 Failure modes of connections with a) unstiffened angles and b) stiffened angles, when $t_b=2$ mm and $t_g=3t_b$

5.4.2.2.3 WF-C connections

The WF-C connections consisted of a T-shaped gusset plate in combination with unstiffened top and seat angles, connecting both the web and the flanges of the beam (see Table 5.2). The moment-rotation relationships of the studied WF-C connections, up to their ultimate rotations, are shown in Fig. 5.13 for different beam thicknesses (i.e. $t_b=1, 2, 4$ and 6 mm) and gusset plate thicknesses ($t_g=t_b, 1.5t_b, 2t_b,$ and $3t_b$). As expected, increasing the gusset plate thickness generally increased both the flexural capacity and the rotational stiffness of the WF-C connections. As illustrated in Fig. 5.14 (and listed in Table 5.5), the failure mode of WF-C connections was identified to be local/distortional buckling of the CFS beam element for the connections with the highest gusset plate thickness (i.e. $t_g=3t_b$), while in the other cases the failure mode was yielding of the gusset plate (i.e. T-shape plate and/or angles). This is reflected in the rotational capacities (ϕ_{max}) of the connections listed in Table 5.5: increasing the gusset plate thickness up to $t_g=2t_b$ enhances the rotational capacity, while for higher plate thicknesses increasing the gusset plate thickness decreases the rotational capacity due to local failure of the CFS beam.

Based on the AISC 341-16 (AISC, 2016) classification, all connections with Class 1 beam sections (i.e. 6 mm thickness) were categorised as SMF (i.e. they reached the ultimate rotation of 0.06 rad). Connections using Class 2 and 3 beams (i.e. $t_b=4$ mm and 2 mm) also satisfied the SMF requirement when the gusset plate thickness $t_g \leq 2t_b$. On the contrary, WF-C connections with Class 4 beam sections (i.e. $t_b=1$ mm) always belonged to IMFs or OMFs, which indicates they are not suitable for regions with high seismicity. In terms of rotational rigidity, all connections needed to be classified as Semi-Rigid according to EC3 (CEN, 2005).

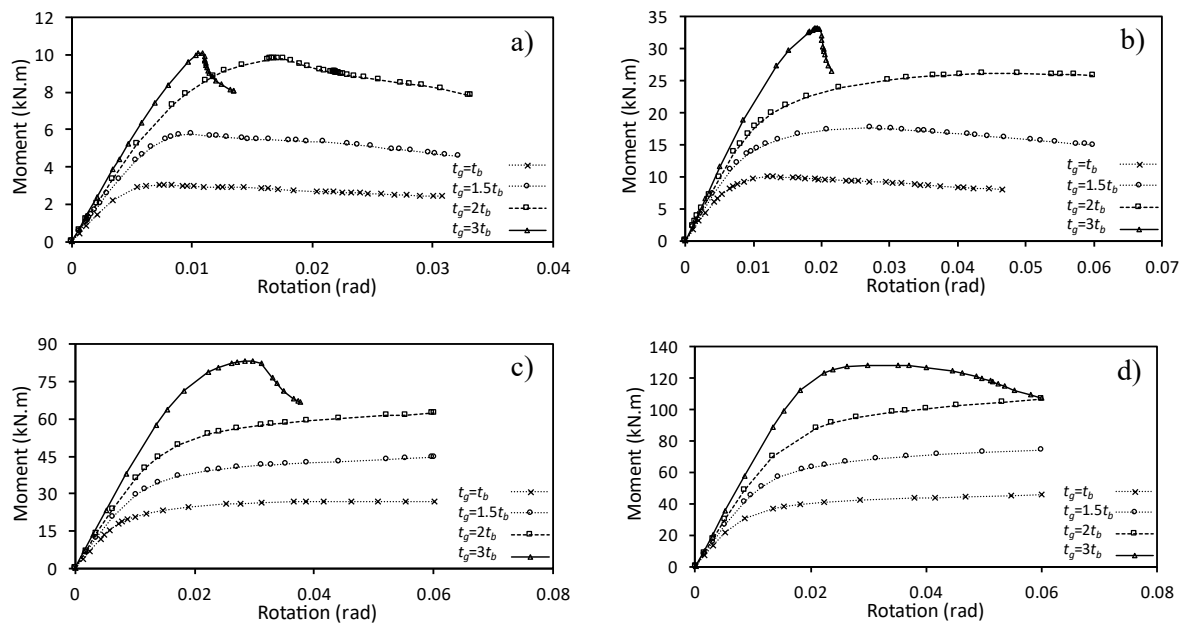


Fig. 5.13 Moment-rotation responses of WF-C connections with various gusset plate thicknesses (t_g), and beam thicknesses (t_b) of a) 1 mm, b) 2 mm, c) 4 mm and d) 6 mm

Table 5.5 Ultimate rotation (ϕ_{max}), flexural rigidity as per EC3 (CEN, 2005), rotational category as per AISC provisions (AISC, 2016) and failure modes for WF-C connections

Beam thickness t_b	Gusset plate thickness t_g	T-shape with unstiffened top and seat angles			
		Failure mode	EC3 rotational rigidity	ϕ_{max} (rad)	AISC category
1 mm	t_b	GP	S-R	0.031	IMF
	$1.5t_b$	GP	S-R	0.032	IMF
	$2t_b$	GP	S-R	0.033	IMF
	$3t_b$	B	S-R	0.013	OMF
2 mm	t_b	GP	S-R	0.048	SMF
	$1.5t_b$	GP	S-R	0.06	SMF
	$2t_b$	GP	S-R	0.06	SMF
	$3t_b$	B	S-R	0.0215	IMF
4 mm	t_b	GP	S-R	0.06	SMF
	$1.5t_b$	GP	S-R	0.06	SMF
	$2t_b$	GP	S-R	0.06	SMF
	$3t_b$	B	S-R	0.037	IMF
6 mm	t_b	GP	S-R	0.06	SMF
	$1.5t_b$	GP	S-R	0.06	SMF
	$2t_b$	GP	S-R	0.06	SMF
	$3t_b$	B	S-R	0.06	SMF

(GP): Gusset Plate failure, (B): Beam failure

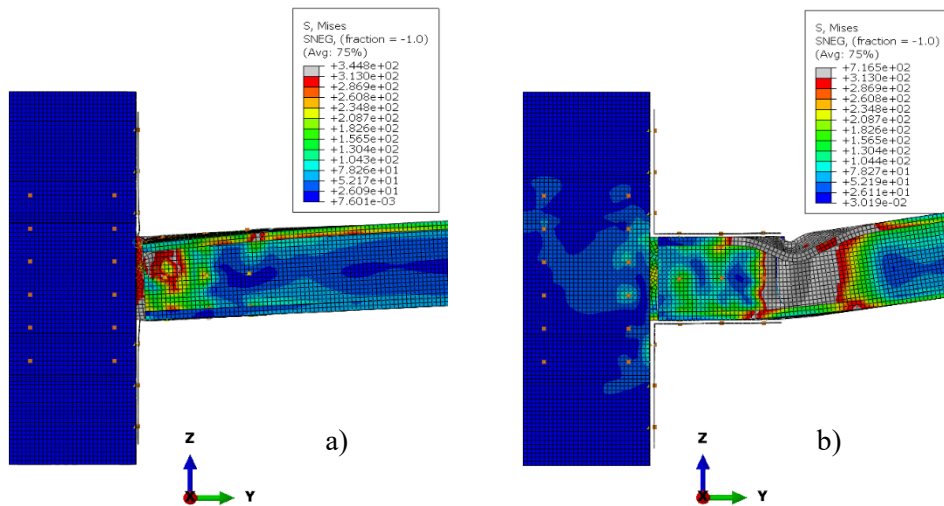


Fig. 5.14 Failure modes of WF-C connections for $t_b=1$ and a) $t_g=t_b$ and b) $t_g=3t_b$

5.4.3 Connection types with the best overall seismic performance

The results regarding the bending moment capacity, ultimate rotation, rotational rigidity and seismic classification of the connections obtained in the previous section were used to identify and select the connection types having the best overall performance for each connection configuration.

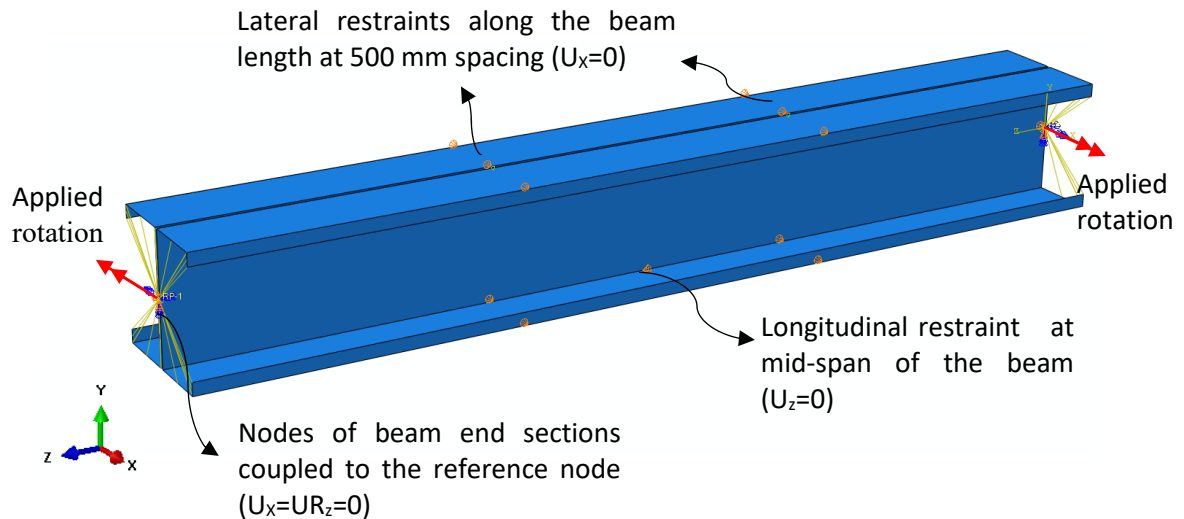


Fig. 5.15 FE model of CFS beam with back-to-back channel sections used to determine the cross-sectional flexural capacity ($M_{u,b}$)

For comparative purposes, the flexural capacity of each connection was normalised with respect to the cross-sectional bending capacity of the beam, obtained from the FE analysis of a beam segment subject to pure bending. This FE model is shown in Fig. 5.15. The beam remained laterally restrained at discrete locations (i.e. every 500 mm) to prevent global buckling. The length of the beam segment was taken as three times the distortional buckle half-wave length, calculated using the CUFSM (Li and Schafer, 2010) software, as suggested by Shifferaw and Schafer (Shifferaw and Schafer, 2012). The values of $M_{u,b}$ obtained for the studied cross-sections with thicknesses of 1, 2, 4 and 6 mm were calculated to be 10.6, 32.3, 79.3 and 121.6 kNm, respectively.

Fig. 5.16, Fig. 5.17 and Fig. 5.18 show the variation of $M_{max}/M_{u,b}$ (where M_{max} is the connection capacity) for various gusset plate and beam thicknesses for the W-C, F-C and WF-C connections, respectively. These figures, along with the results presented in Table 5.3, Table 5.4 and Table 5.5, were used to draw the following conclusions:

- Among the three gusset plate configurations considered for the W-C connections, the rounded T-shape and the chamfered shape are generally preferred over the plain T-shape, because of their higher flexural capacity, higher stiffness and more ductile behaviour, the latter evaluated based on the AISC code. There was no significant difference between the performance of the

connections with the rounded T-shape and the chamfered shape in terms of the rotational capacity, stiffness and strength for $t_g \geq 2t_b$. However, the rounded T-shape provides more flexibility for the installation of the flooring system. Therefore, a rounded T-shaped gusset plate with a minimum thickness of $t_g=2t_b$ was taken forward as the preferred W-C option.

- With regards to the F-C connections, the connections with stiffened angles were demonstrated to be more efficient for seismic applications than those with unstiffened angles, due to having higher flexural capacities (see Fig. 5.17) and stiffnesses (see Table 5.4). For the connections with Class 3 and 4 beam sections, the most efficient thickness of the angles and stiffeners was identified to be equal to $4t_b$. F-C connections with this thickness act as Semi-Rigid and satisfy SMF requirements while developing around 80% of the beam strength. For the F-C connections with Class 2 beam sections, a plate thickness of $2t_b$ was preferred for the stiffened angles, as this satisfied SMF requirements while providing virtually the same rotational capacity and rigidity as the connections with thicker angles. For the F-C connection with Class 1 beams, although using a plate thickness of $3t_b$ resulted in a bending capacity which was about 10% higher than for a thickness of $2t_b$, it may not be practical to use, for instance, 18 mm angles. Therefore, $t_g=2t_b$ was chosen for Class 1 beam sections.
- For WF-C connections, plate thicknesses $t_g=2t_b$ were chosen for the gusset plate and angles. These connections were able to develop more than 90% of the flexural capacity of the beam section while maintaining a high rotational capacity and ductile behaviour according to the AISC code (see Table 5.5).

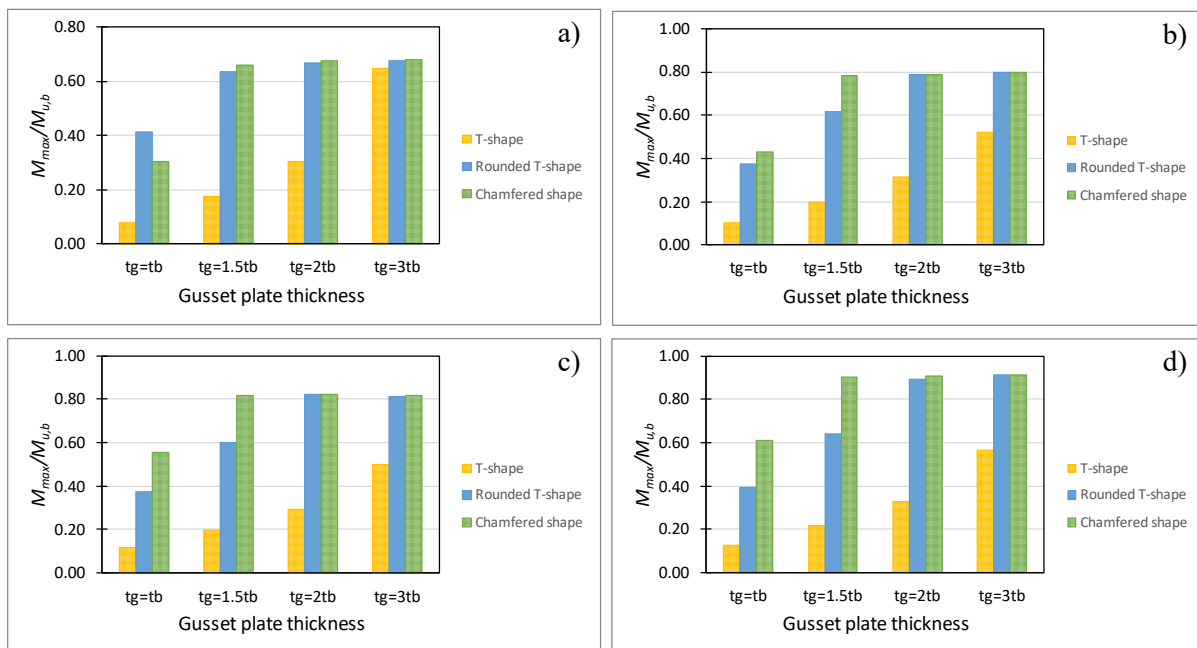


Fig. 5.16 $M_{max}/M_{u,b}$ ratios for W-C connections with beam thicknesses t_b of a) 1 mm, b) 2 mm, c) 4 mm and d) 6 mm

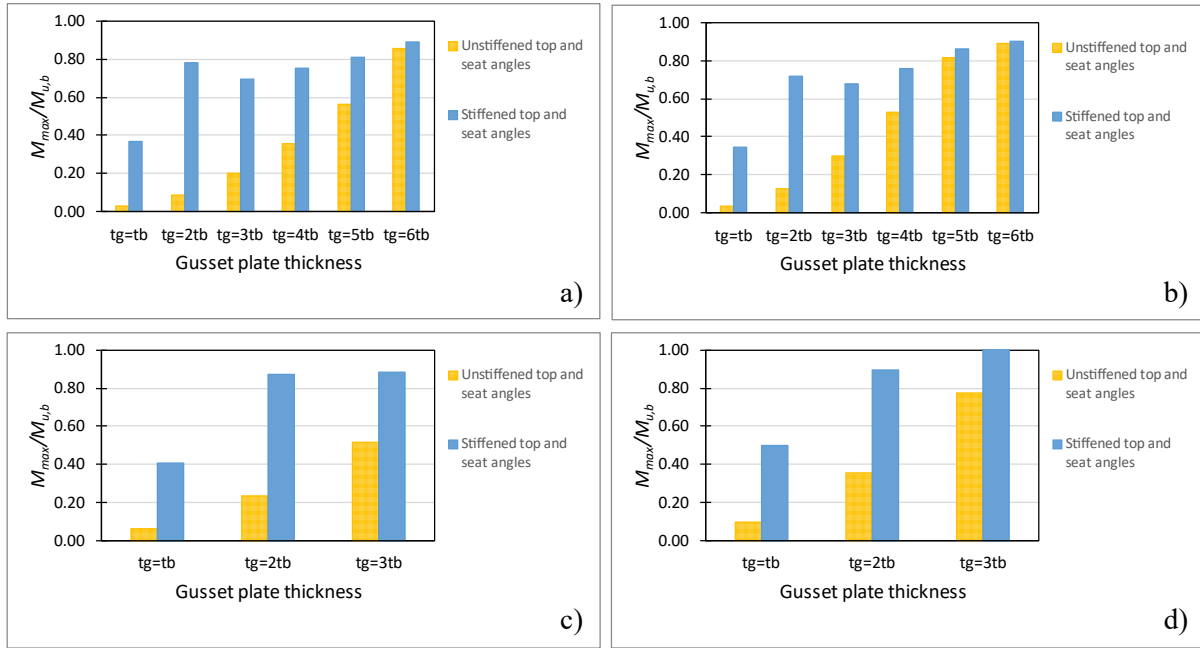


Fig. 5.17 $M_{max}/M_{u,b}$ ratios for F-C connections with beam thicknesses t_b of a) 1 mm, b) 2 mm, c) 4 mm and d) 6 mm

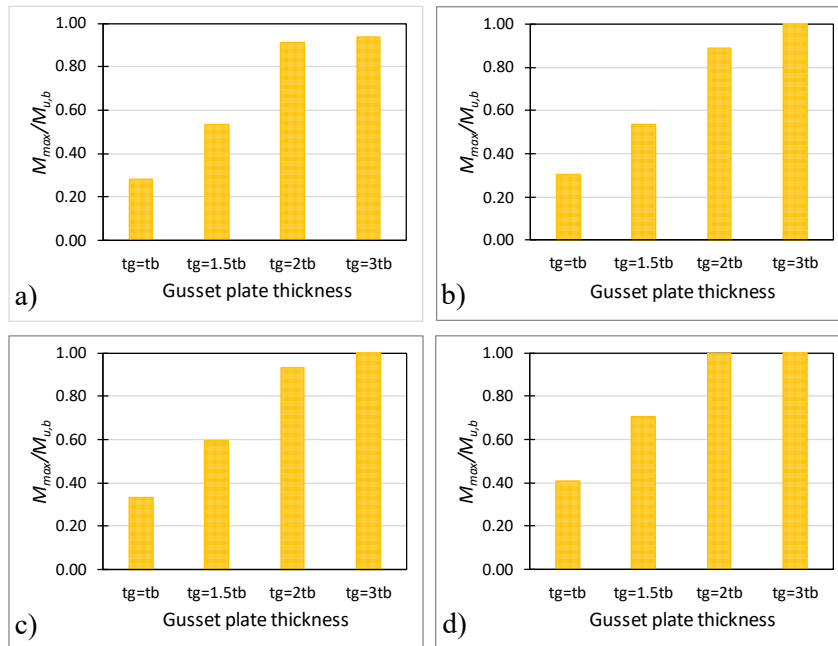


Fig. 5.18 $M_{max}/M_{u,b}$ ratios for WF-C connections with beam thicknesses t_b of a) 1 mm, b) 2 mm, c) 4 mm and d) 6 mm

Table 5.6 summarises the connections which were selected for their performance with respect to the criteria in section 5.4.2.1. It should be noted that the dominant failure mode for the W-C and F-C connections was generally local/distortional buckling in the beam, whereas the WC-F connections exhibited yielding in the gusset plates. While it is possible to prevent yielding of the gusset plate in WF-

C connections by increasing its thickness, this would reduce the ultimate rotation capacity and hence the ductility of this connection type.

Table 5.6 Connections with balanced performance

Connection type	EC3 beam class	Gusset plate thickness t_g	Failure mode	Gusset plate shape
W-C	1, 2, 3 and 4	$2t_b$	B	Rounded T-shape
F-C	3 and 4	$4t_b$	B	Stiffened top and seat angles
	2	$3t_b$	B	
	1	$2t_b$	GP	
WF-C	1, 2, 3 and 4	$2t_b$	GP	T-shape and unstiffened top and seat angles

5.5 Seismic efficiency of the selected connection types

Fig. 5.19, Fig. 5.20 and Fig. 5.21 present the hysteretic moment-rotation relationships of the W-C, F-C and WF-C connections with balanced performance listed in Table 5.6, including beams of all four cross-sectional classes (i.e. $t_b=1, 2, 4$ and 6 mm). The results were obtained by applying the cyclic loading protocol shown in Fig. 5.4 to the FE models. For comparative purposes, the cyclic moment-rotation backbone curve is also presented, which was obtained by plotting the locus of the peak moment points in the first cycle of each loading amplitude.

For the W-C connections with Class 3 and 4 beams, the hysteretic curves exhibited an abrupt strength degradation immediately after reaching the maximum bending moment. For beams with a larger thickness (i.e. Class 1 and 2 sections), on the other hand, the connections experienced a certain amount of plastic rotation before degradation commenced.

F-C connections with Class 2-4 beams comprised a softening branch in their hysteretic behaviour before reaching the ultimate rotation, which was again taken as the minimum of 0.06 rad and the rotation at which a 20% drop from the peak moment was recorded (see Fig. 5.20(a), (b) and (c)). However, no strength degradation was observed in the hysteretic behaviour of the F-C connection with a Class 1 beam before the ultimate rotation, as shown in Fig. 5.20(d). This is attributed to the considerably lower slenderness of both the beam and the stiffened angle elements in this case, reducing their susceptibility to local buckling.

The moment-rotation curves of the WF-C connections indicated that, in general, the connection responses were characterised by plastic strain hardening without any strength degradation. This was due to the opening and closing behaviour of the angles, which acted as a seismic fuse and increased the rotational capacity of the connection, postponing connection failure to larger rotations. However, an

exception can be seen for the connection with a Class 4 beam. This is attributed to the high slenderness of both the beam and the gusset plate, leading to premature local buckling.

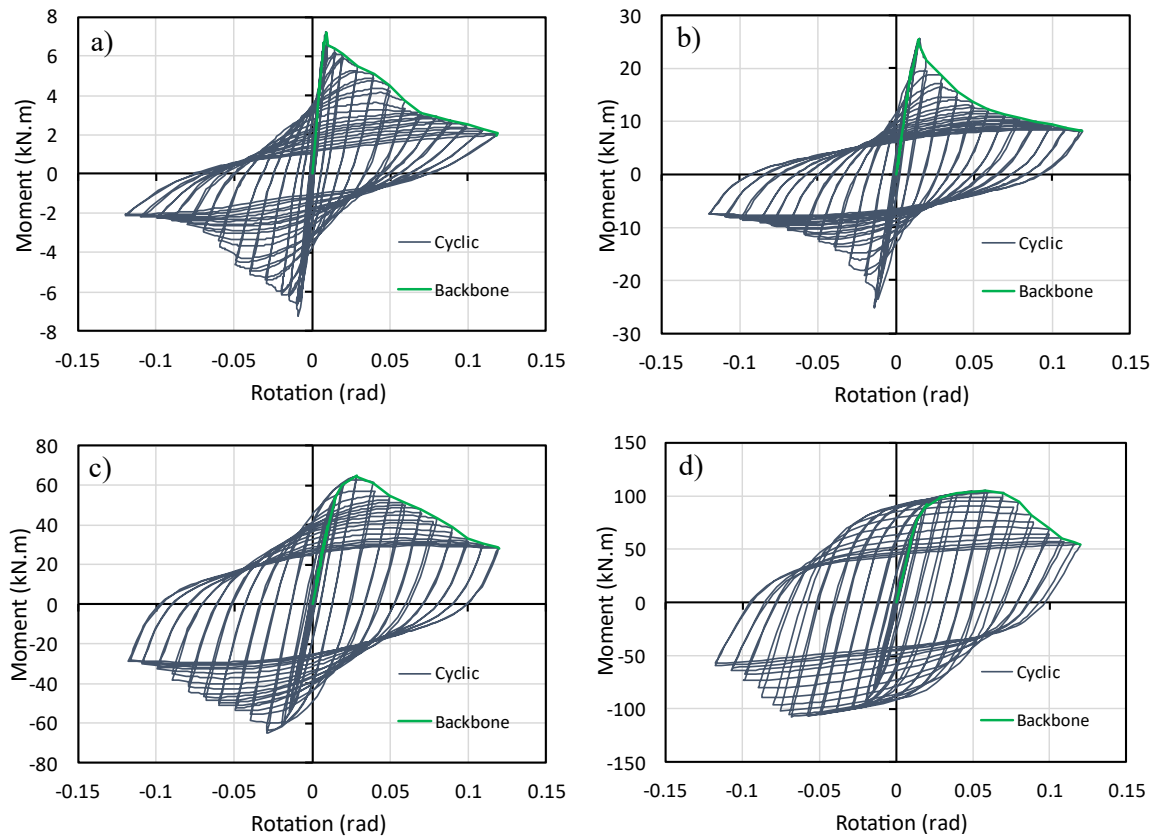


Fig. 5.19 Hysteretic moment-rotation curves for balanced W-C connections with gusset plate thickness $t_g=2t_b$ and beam thickness (t_b) of a) 1 mm, b) 2 mm, c) 4 mm and d) 6 mm

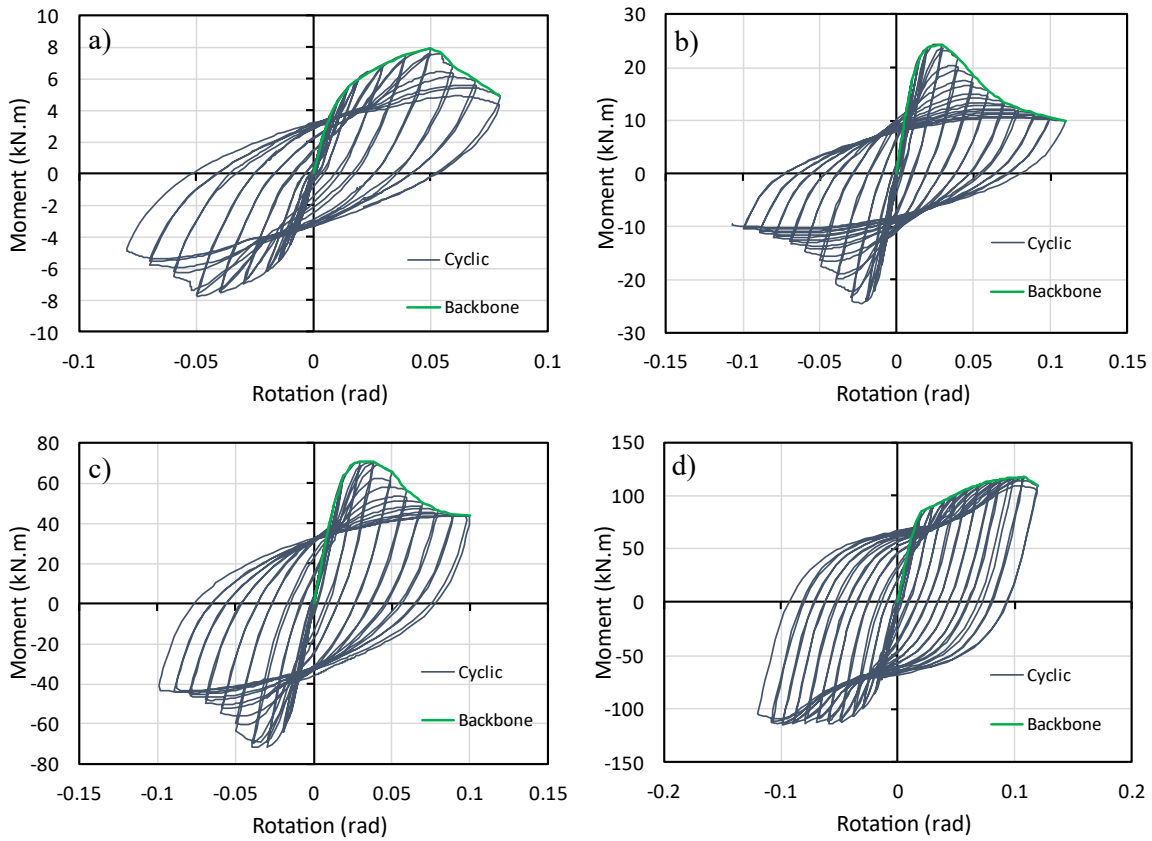


Fig. 5.20 Hysteretic moment-rotation curves for balanced F-C connections with beam and gusset plate thicknesses of a) $t_b=1$ mm, $t_g=4t_b$, b) $t_b=2$ mm, $t_g=4t_b$, c) $t_b=4$ mm, $t_g=3t_b$ and d) $t_b=6$ mm, $t_g=2t_b$

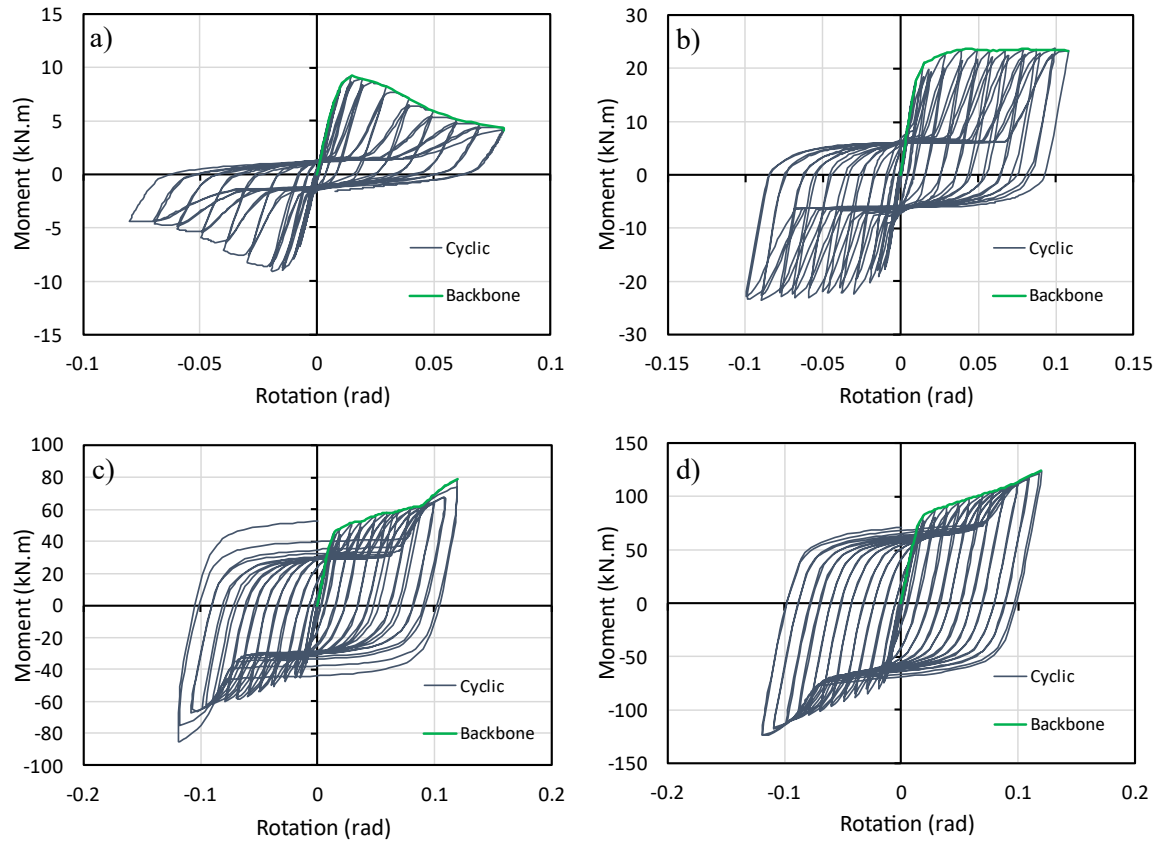


Fig. 5.21 Hysteretic moment-rotation curves for balanced WF-C connections with gusset plate thickness $t_g=2t_b$ and beam thickness (t_b) of a) 1 mm, b) 2 mm, c) 4 mm and d) 6 mm

5.5.1 Ductility

Ductility is an indicator of the ability to sustain plastic deformations without experiencing a significant drop in strength. The ductility of a structure (μ_ϕ) is commonly expressed as the ratio of ϕ_u/ϕ_y , where (ϕ_u) is the ultimate rotation and (ϕ_y) is the rotation at yield. In this study, the rotation at yield (ϕ_y) was calculated based on the equivalent energy elastic-plastic method (EEEP) recommended by ASTM E2126 (ASTM, 2019). An iterative procedure was carried out to define the equivalent bilinear elasto-plastic curve so that the net area enclosed between the equivalent and the backbone curve is zero (with the area below the backbone curve being taken as negative). As shown in Fig. 5.22, the rotation at yield (ϕ_y) corresponds to the rotation where a secant line intersecting the backbone curve at 40% of the peak moment (M_{max}) meets a horizontal line extending to the ultimate rotation. The ultimate rotation (ϕ_u) was previously defined in section 5.4.2.1.

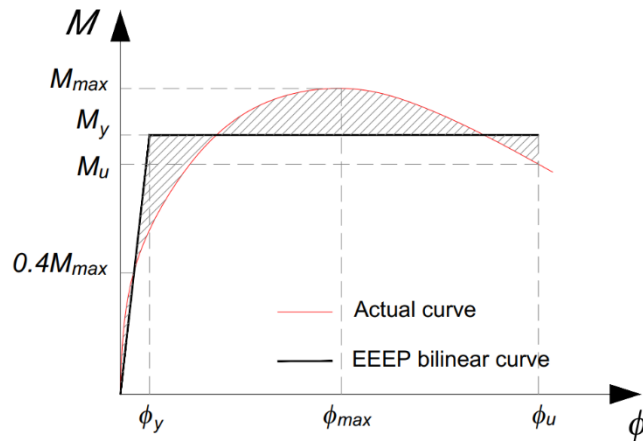


Fig. 5.22 Equivalent (EEEE) analysis model per ASTM E2126

Fig. 5.23 and Fig. 5.24 compare the ductility (μ_ϕ) and the yield rotation (ϕ_y) of different connection configurations selected for having the best overall performance, as discussed in section 5.4.2.1. The results demonstrate that using Class 1 and 2 beam sections generally led to similar ductility level across all connection configurations. However, ductility results varied significantly when Class 3 and 4 beam sections were used, with the F-C and WF-C connections providing significantly higher ductility (by up to 136%) compared to the W-C joints.

In general, the results presented in Fig. 5.24 indicate that the equivalent yield rotation depends more on the beam classification than on the connection type. While increasing the thickness of the beam section always led to a higher yield rotation of the connection (see Fig. 5.24), no such trend could be observed for the ductility.

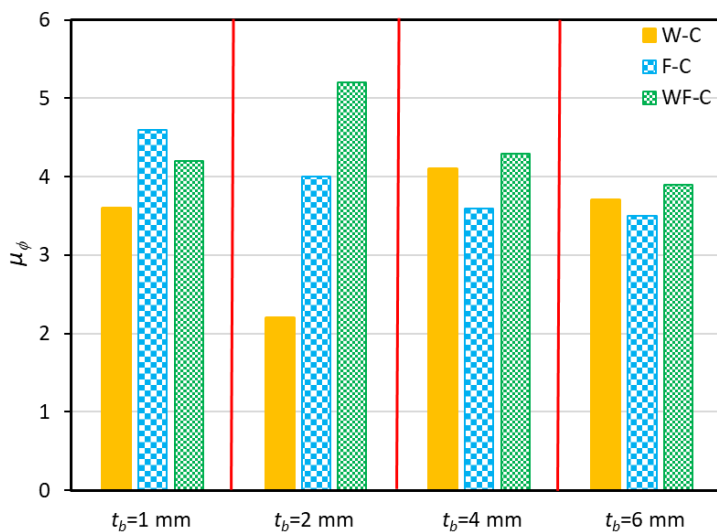


Fig. 5.23 Ductility (μ_ϕ) of different connection configurations with balanced performance

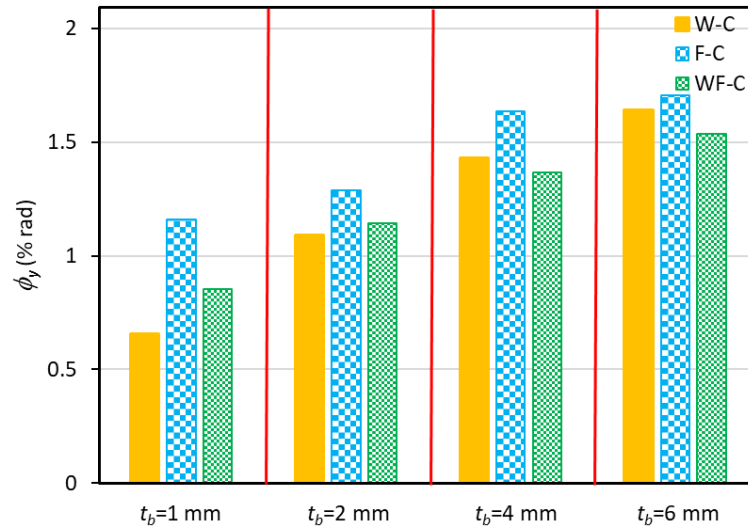


Fig. 5.24 Yield rotation (ϕ_y) of different connection configurations with balanced performance

5.5.2 Energy dissipation

In this study, the area below the idealised EEEP model up to the ultimate rotation (see Section 5.5.1) was used to calculate the energy dissipation capacity (E) of various connections conforming to Table 5.6, and the results are compared in Fig. 5.25. As expected, the connections with Class 1 and 2 beam sections dissipated significantly more energy than those with Class 3 or 4 beam sections, due to their higher moment capacity and ductility.

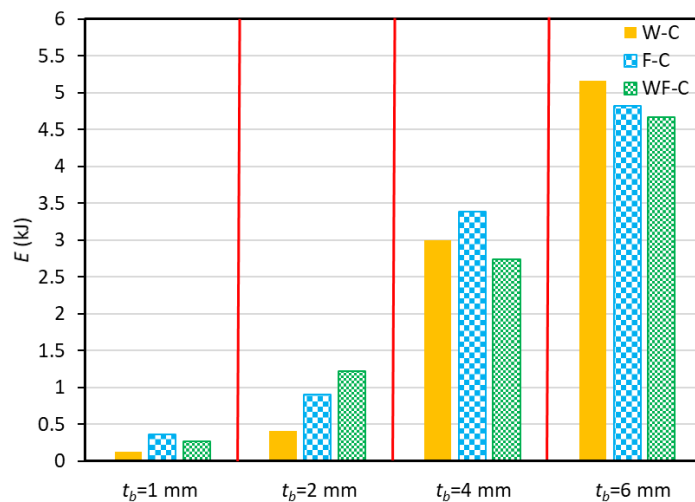


Fig. 5.25 Energy dissipation (E) of connections with balanced performance

All connection configurations using Class 1 beam sections performed similarly in terms of their energy dissipation capacity, as did those with Class 2 beams. On the other hand, F-C and WF-C connections

with Class 3 and 4 beam sections provided energy dissipation capacities which were up to 181% and 196% higher, respectively, than the corresponding W-C connections.

5.5.3 Damping coefficient

The equivalent viscous damping coefficient (ζ_{eq}) is another indicator of the energy dissipation capacity of the system, quantifying the energy loss per cycle. As shown in Fig. 5.26, ζ_{eq} is defined by relating the energy dissipated in the hysteresis loop (E_h) of a cycle to the fictitious energy ($E_{(OAB)}+E_{(OCD)}$) dissipated in viscous damping during the same cycle (Chopra, 2001), and is calculated using the following equation (Liu *et al.*, 2019; Ye, Mojtabaei, Hajirasouliha, *et al.*, 2019):

$$\zeta_{eq} = \frac{1}{2\pi} \cdot \frac{E_h}{E_{(OAB)} + E_{(OCD)}} \quad (28)$$

The points A and C in Fig. 5.26 correspond to the maximum positive and negative bending moments, respectively. The above quantity was calculated for two different cycles, corresponding to the maximum bending moment (M_{max}) and the bending moment at the ultimate rotation (i.e. $M_u = \min\{0.8M_{max}, M_{\phi=0.06}\}$).

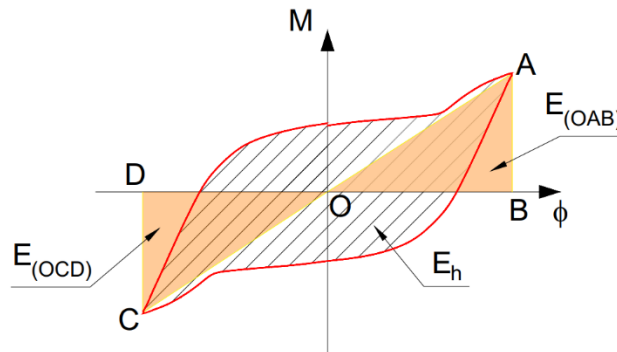


Fig. 5.26 Definition of equivalent viscous damping coefficient (ζ_{eq})

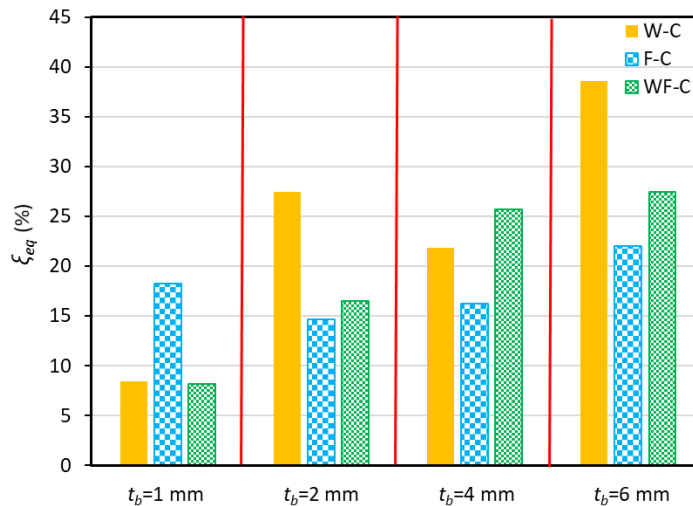


Fig. 5.27 Equivalent viscous damping coefficient (ζ_{eq}) at M_{max} for connections with balanced performance

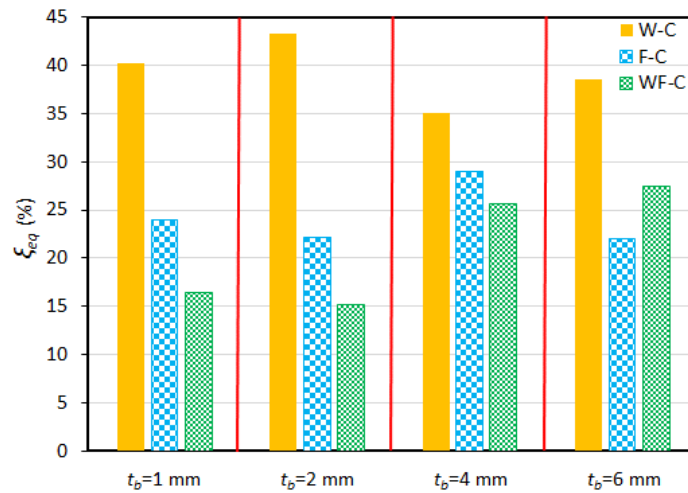


Fig. 5.28 Equivalent viscous damping coefficient (ζ_{eq}) at M_u for connections with balanced performance

In general, W-C connections were capable of more substantial damping compared to the other connection configurations at the ultimate rotation. This can be attributed to the fact that more material plasticity is developed in W-C connections compared to other types, which in turn increases the plumpness of the hysteresis loop and consequently the value of the damping coefficient.

By comparing the values of the damping coefficients in Fig. 5.27 and Fig. 5.28, it can be concluded that in the connections with Class 2, 3 and 4 beam sections the majority of the cyclic energy was dissipated after the connections reached their maximum bending moment. On the other hand, for the connections with Class 1 beam sections there was negligible difference between the values of ζ_{eq} at the peak moment and at the moment corresponding to the ultimate rotation, as plasticity was already significantly developed before the attainment of the maximum bending moment. It should also be noted that the WF-C connections with Class 1 and 2 beams reached their maximum bending moment at the point of the ultimate rotation ($\phi_u=0.06$ rad), and thus the damping coefficients for both cycles were identical.

5.6 Summary and Conclusions

This study aimed to develop novel CFS beam-to-column bolted connections for seismic applications and evaluate their performance based on a number of established seismic performance criteria.

Detailed FE models of a range of CFS beam-to-column joints were developed, which first were validated against previous experimental data and accounted for material nonlinearities and initial geometric

imperfections. The structural performance of different configurations of Web-Connected (W-C), Flange-Connected (F-C) and Web-and-Flange-Connected (WF-C) joints was assessed while parametrically varying the thicknesses of key components and the shape of gusset plates. Based on the overall performance in terms of flexural capacity, ultimate rotation and rotational rigidity of a wide range of connections, the most suitable connection configurations for seismic applications were identified. Subsequently, these connections were evaluated under cyclic loading against key seismic performance parameters, including ductility, energy dissipation capacity and damping coefficient. Based on the results of this study, the following conclusions can be drawn:

- Among the Web-Connected (W-C) joints, a rounded T-shaped gusset plate with a thickness larger than $2t_b$ was identified as the preferred option across all beam classes. This connection combined advantageous bending moment capacity, rotation capacity and stiffness, while the shape of the gusset plate creates a minimal obstruction when installing the floor system.
- Flange-Connected (F-C) joints employing stiffened top and seat angles exhibited a flexural capacity and rotational stiffness which was by average 4 times higher than their unstiffened counterparts. However, the results also indicated that using thick stiffened angle sections alongside thin-walled beam sections led to a lower rotation capacity. The preferred angle and stiffener thicknesses were $2t_b$ for Class 1 beams, $3t_b$ for Class 2 beams, and $4t_b$ for Class 3 and 4 beams.
- A study of Web-and-Flange-Connected (WF-C) joints, employing both unstiffened top and seat angles and a gusset plate, revealed that plate thicknesses larger than $2t_b$ offered the best combination of flexural capacity, rotational stiffness and rotation capacity across all beam classes.
- Cyclic analyses of the recommended W-C, F-C and WF-C connections indicated that they were all suitable for practical seismic applications, as they provided an acceptable level of ductility while developing more than 80% of the flexural capacity of the connected beam.
- Very similar ductility levels were encountered for Class 1 and 2 beam sections across all connection configurations. However, for Class 3 and 4 beam sections WF-C and F-C connections exhibited up to 136% more ductility than W-C joints.
- In terms of the dissipated energy, a similar performance was observed among all connections with Class 1 or 2 beams, whereas for Class 3 and 4 beams, the WF-C and F-C connections significantly outperformed the W-C connections by up to two orders of magnitude. However, W-C joints displayed higher equivalent viscous damping coefficients at the ultimate rotation, reflecting the more extensive development of material plasticity in their components compared to other types.

5.7 Author contribution

- Ioannis Papargyriou:

Conceptualisation, Methodology, Formal Analysis, Investigation, Writing- Original draft, Writing- Reviewing and Editing, Visualisation

- Dr. Mohammad Mojtabaei:

Conceptualisation, Methodology, Validation, Writing- Reviewing and Editing, Supervision

- Dr. Iman Hajirasouliha:

Conceptualisation, Methodology, Validation, Writing- Reviewing and Editing, Supervision

- Dr. Jurgen Becque:

Methodology, Writing- Reviewing and Editing, Supervision

- Prof. Kypros Pilakoutas:

Methodology, Writing- Reviewing and Editing, Supervision

CHAPTER 6

Conclusions and recommendations for future work

6.1 Summary and conclusions

This research aimed to provide a better understanding on the non-linear lateral response of CFS lateral force-resisting systems and propose design considerations to improve their efficiency and resilience for seismic applications. The focus was on strap-braced stud walls, as the most widely used system in CFS multi-storey buildings, and CFS beam-column moment connections, as the key elements in multi-storey frame systems. Experimentally validated FE models were developed, and the effect of key design parameters on critical performance parameters of strap-braced stud walls was investigated. The efficiency of each design solution was evaluated based on a derived efficiency index parameter, which led to recommendations to obtain the most efficient solution, offering maximum performance with minimum material use. The results indicated that the developed secondary moments due to P- Δ effects, amplified by additional vertical loading, had a significantly adverse impact on the lateral performance of the system. Current seismic design codes, such as Eurocode 8, lack specifications to predict the lateral load capacity and ductility of CFS strap-braced walls under those conditions. In order to bridge this gap, a novel seismic design framework was developed, and its efficiency was demonstrated through the preliminary design of a 6-storey strap-braced frame, considering a conventional solution following Eurocodes' specifications and one based on the proposed methodology. Subsequently, the Eurocode and the proposed design solutions were subjected to non-linear time-history analyses using artificial and real spectrum-compatible ground motions. The aim was to further assess the efficiency of the proposed design methodology at the structural level and better understand the behaviour of strap-braced wall frames under dynamic loading for different performance targets. Finally, new CFS beam-column moment connections were developed, engaging the elements' flanges, and their performance was compared to conventional joint configurations using gusset plates. To this end, detailed and

experimentally validated FE models were developed to investigate the non-linear monotonic and cyclic response of the joint configurations, which led to practical seismic design considerations for best performance in seismic applications. The following sections summarise the main findings and conclusions of each chapter.

6.1.1 Performance-based assessment of CFS Strap-braced stud walls under seismic loading

The aim of this chapter was to numerically study the lateral performance of CFS strap-braced stud walls, identify the key design parameters, investigate their effect on critical performance criteria and rate the design solutions relative to their ability to improve the efficiency of the system.

- The thickness and the steel grade of the diagonal straps had the most significant impact on the lateral load-bearing capacity of the wall. A higher thickness and steel grade increased the lateral resistance and led to more efficient design solutions, as the Efficiency Index (R_{ef}) indicated.
- Depending on the degree of clamping action provided by the hold-downs, the CFS bare frame (without the straps) has a small but non-negligible effect on the lateral load-bearing resistance.
- The additional compressive force and moment, resulting from the P- Δ effects when the straps reach their required level of strain and from the increased strap force due to strain hardening, should be accounted for in the design of the chord studs. Ignoring them would yield a reduced deformation capacity and ductility when choosing thicker straps or a higher strap steel grade. Nevertheless, according to the Efficiency Index, increasing the chord stud thickness further is an inefficient way to increase the lateral load-bearing capacity.
- Additional vertical loading adversely affected all critical performance criteria. In the studied wall configuration, a 50% P_w vertical load decreased the lateral load capacity by 25%, the deformation capacity and ductility by almost 70% and the energy dissipation capacity by 76%.
- The system's efficiency regarding the energy dissipation capacity was most considerably affected by the strap thickness. However, as analyses and the Efficiency Index indicated, there is an optimal strap thickness, beyond which the energy dissipation capacity drops significantly, caused by buckling failure of the chord stud.

6.1.2 More efficient design of CFS strap-braced frames under vertical and seismic loading

This chapter aimed to develop a practical methodology for the seismic design of CFS strap-braced stud wall frames under vertical loading and demonstrate its efficiency compared to the provisions of Eurocode 8.

- A comprehensive parametric study with varying design parameters being the strap thickness and the vertical loading ratio showed that increasing the strap thickness almost proportionally increased the lateral load-bearing capacity. Nonetheless, increasing the vertical load had the opposite effect, causing a drop in the lateral load capacity, especially for loading ratios over 22% P_w in the studied walls.
- The secondary moment due to P- Δ effects had a significantly adverse effect on the system's lateral load-bearing, deformation and ductility capacity, not directly accounted for in current design guidelines, like those in the Eurocode.
- The compressive chord stud, designed per capacity design rules as an axially loaded member, may experience premature failure due to the secondary moment developed by P- Δ effects, leading to unacceptably low ductility capacity of the wall system for seismic applications.
- The efficiency of the developed framework for the design of multi-storey, CFS, strap-braced wall frames under the simultaneous action of vertical and seismic loading was demonstrated through the preliminary design of a case study 6-storey frame. Both the Eurocode and proposed design solutions could provide the required lateral load-bearing capacity. However, some storeys in the Eurocode-based design exhibited a very low ductility, leading to unacceptable seismic performance. On the other hand, the proposed design achieved high ductility capacity by preventing the premature failure of the chord studs.
- Compared to detailed ABAQUS analyses, the proposed formulation predicted the lateral load-bearing capacity and ductility with an accuracy of 4%. Furthermore, based on the studied wall configuration results and assumptions, the equations can show the general response trends and, therefore, should prove suitable for the preliminary design of multi-storey CFS strap-braced frames.

6.1.3 Performance-based seismic design and assessment of multi-storey CFS strap-braced frames

This chapter aimed to assess the efficiency of the proposed design methodology developed and discussed in section 3.5, taking into account the secondary moment due to P- Δ effects under the presence of vertical loads. The performance of case-study CFS 6-storey frames, designed following the methodology and Eurocode 8 specifications, was investigated under a set of spectrum-compatible artificial and real ground motion records, and damage was quantified at the structural level.

- Despite satisfying the ASCE/SEI 41-17 ductility demand limits for (IO) and (LS) performance levels, the Eurocode 8 design solution did not meet the (CP) performance level, exceeding the limit by 13%. By contrast, the frame designed per the proposed methodology exhibited a more uniform inter-storey drift distribution, which was more evident for the higher intensity levels.

At the same time, the ductility demand remained lower than the code limits with a higher safety margin.

- The Eurocode 8 frame was totally damaged under PGA levels over 0.20 g, due to premature buckling of the compressive chord studs, yielding unacceptably low ductility capacities at some storeys. This showed that not accounting for vertical loads might lead to unsafe design solutions. The proposed design solution performed significantly better, at all ground motion intensity levels, with the global damage index being 4%, 26% and 58% at PGA levels corresponding to IO, LS and CP performance levels, respectively.
- Under the set of real ground motion records, both solutions met the ASCE/SEI 41-17 (LS) ductility demand limits. However, the Eurocode 8 design frame was completely damaged in most cases, while the global damage index for the proposed design solution ranged between 10% and 63%, with an average value of 40%.
- The above results indicate that the proposed methodology is efficient for the preliminary design of CFS multi-storey strap-braced frames in seismic regions.

6.1.4 Cold-formed steel beam-to-column bolted connections for seismic applications

5. This chapter focused on the development of novel, demountable, bolted types of CFS beam-column moment-resisting connections capable of transferring the loads through the beam and column flanges or a combination of flanges and webs and propose practical seismic design considerations for the beam-to-column bolted connections to reach the best performance and satisfy different seismic performance levels.

- This study also investigated the efficiency of different shapes of web-connected joints. The rounded T-shape configuration with a gusset plate thickness over $2t_b$ had the most desirable performance, combining a high bending moment and rotation capacity, high stiffness and a shape facilitating the installation of the flooring system.
- Among the flange-connected joints, those using stiffened top and seat angles reached the highest bending moment capacity, rotation capacity and stiffness for gusset plate thicknesses of $2t_b$ for beam Class 1, $3t_b$ for beam Class 2, and $4t_b$ for beam Classes 3 and 4. However, combining thick, stiffened angle sections with thin beam sections led to a lower rotation capacity.
- The best performance among the web and flange-connected joints resulted from the configuration employing unstiffened top and seat angles, with a plate thickness greater than $2t_b$.
- All selected connection types demonstrated their applicability for seismic applications, reaching high ductility and a flexural capacity being at least 80% of the beam's capacity.

- All selected joint configurations with beam classes 1 and 2, per EC3, reached approximately the same level of ductility. However, for flange connected and web-flange connected joints with beam classes 3 and 4, 136% higher ductility was achieved than for web-connected joints.
- It was shown that all connection types reached a similar level of energy dissipation capacity for beam classes 1 and 2, while the flange-connected and the web-flange connected joints for classes 3 and 4 outperformed the web-connected joints by up two orders of magnitude. Nevertheless, the web-connected joints exhibited a higher equivalent damping coefficient at the ultimate point, as more extensive material plasticity developed in their elements compared to the other connection types.

6.2 Recommendations for future work

Extensive numerical analyses in ABAQUS and OpenSees based on experimentally validated, FE models indicated the impact of additional vertical loading and the secondary moments due to P- Δ effects on critical performance parameters and especially ductility, which led to the development of a practical seismic design methodology. The proposed equations were proven efficient and accurate for the preliminary design of strap-braced wall configurations similar to those adopted in this study. However, more research work is needed to enable their generic use for a greater variety of wall configurations and topologies. Furthermore, the performance and efficiency of CFS strap-braced frames could be improved through the optimisation of the cross-sections. To this end, the following topics are suggested for future studies in this area:

- Experimentally investigate the effect of additional vertical loading in strap-braced wall systems using different vertical load levels.
- Extend the proposed methodology to different strap-braced wall configurations, e.g. employing gusset plates or sheathed wall systems.
- Optimise the wall's cross-sections to make more efficient use of the materials and achieve improved seismic performance with a more uniform drift, ductility and damage distribution along the height of multi-storey CFS strap-braced frames.
- Develop a methodology to automatically derive the parameters defining “Pinching4” hysteretic material model for simulations of different strap-braced wall configurations in OpenSees, enabling global analyses of these systems without the need to calibrate it through detailed FE analyses using artificial intelligence (AI).

The present study indicated the suitability of the new beam-column joint configurations and provided design considerations to reach high flexural capacity, deformability, ductility and rotational stiffness. However, experimentally validated design equations are required to calculate the connections' strength,

rotational capacity and stiffness for practical design purposes. Moreover, research work on the seismic performance of CFS multi-storey frames at the structural level is essential to understand their response and evaluate their limits. Finally, previous studies demonstrated that optimising the cross-sections can improve the connections' and the frames' overall performance, providing higher energy dissipation capacity and lower damage under seismic events. In this respect, the present research work could be complemented by studies aiming to:

- Experimentally study the behaviour of the proposed connection types by evaluating their structural performance under cyclic loading.
- Derive flexural and ductility capacity design equations for the newly-developed flange-connected and web-flange connected joints.
- Investigate the response and performance of CFS multi-storey moment-resisting frames, employing the connection configurations of the present study, under non-linear dynamic analyses.
- Optimise the beam and plate thickness of the proposed connections in this study to achieve the best seismic performance in terms of load-bearing capacity and ductility.

References

- Accorti, M., Baldassino, N., Zandonini, R., Scavazza, F. and Rogers, C. A. (2016) 'Response of CFS Sheathed Shear Walls', *Structures*, 7, pp. 100–112. doi: 10.1016/j.istruc.2016.06.009.
- AISC (2016) 'Seismic Provisions for Structural Steel Buildings, ANSI/AISC 341-16'.
- AISI (2012) *AISI S100-12, North American Specification for the Design of Cold-Formed Steel Structural Members*.
- AISI S213 (2012) *S213-07/S1-09. North American Standard for Cold-Formed Steel Framing - Lateral Design, 2007 Edition with Supplement No.1, American Iron and Steel Institute*. Washington DC: American Iron and Steel Institute.
- AISI S400 (2015) *North American Standard for Seismic Design of Cold-Formed Steel Structural Systems*. Washington DC: American Iron and Steel Institute.
- Al-Kharat, M. and Rogers, C. A. (2007) 'Inelastic performance of cold-formed steel strap braced walls', *Journal of Constructional Steel Research*, 63(4), pp. 460–474. doi: 10.1016/j.jcsr.2006.06.040.
- Al-Kharat, M. and Rogers, C. A. (2008) 'Inelastic performance of screw-connected cold- formed steel strap-braced walls', *Canadian Journal of Civil Engineering*, 35(1), pp. 11–26. doi: 10.1139/L07-081.
- ASCE (2005) 'ASCE 7-05 Minimum design loads for buildings and other structures', *ASCE standard*, p. 608. doi: 10.1061/9780784412916.
- ASCE (2017) *ASCE/SEI 41-17 Seismic Evaluation and Retrofit of Existing Buildings, Seismic Evaluation and Retrofit of Existing Buildings*. doi: <https://doi.org/10.1061/9780784414859>.
- ASTM (2019) 'ASTM E2126-19. Standard Test Methods for Cyclic (Reversed) Load Test for Shear Resistance of Vertical Elements of the Lateral Force Resisting Systems for Buildings', *ASTM International*. Available at: www.astm.org.
- ATC (2009) *Quantification of building seismic performance factors, Fema P695*.
- Attari, N. K. A., Alizadeh, S. and Hadidi, S. (2016) 'Investigation of CFS shear walls with one and two-sided steel sheeting', *Journal of Constructional Steel Research*, 122, pp. 292–307. doi: 10.1016/j.jcsr.2016.03.025.
- Blum, H. B. and Rasmussen, K. J. R. (2019) 'Experimental and numerical study of connection effects in long-span cold-formed steel double channel portal frames', *Journal of Constructional Steel Research*, 155, pp. 480–491. doi: 10.1016/j.jcsr.2018.11.013.
- Bučmys, Ž., Daniūnas, A., Jaspert, J. P. and Demonceau, J. F. (2018) 'A component method for cold-formed steel beam-to-column bolted gusset plate joints', *Thin-Walled Structures*, 123(October 2016), pp. 520–527. doi: 10.1016/j.tws.2016.10.022.
- Buonopane, S. G., Bian, G., Tun, T. H. and Schafer, B. W. (2015) 'Computationally efficient fastener-based models of cold-formed steel shear walls with wood sheathing', *Journal of Constructional Steel Research*, 110, pp. 137–148. doi: 10.1016/j.jcsr.2015.03.008.
- Carr, A. J. (2007) 'User Manual for the 2-Dimensional Version Ruaumoko2D', *Computer Program Library*, 1(May 2015), p. 87. doi: 10.13140/RG.2.1.1872.2728.
- Casafont, M., Arnedo, A., Roure, F. and Rodríguez-Ferran, A. (2006a) 'Experimental testing of joints for seismic design of lightweight structures. Part 1. Screwed joints in straps', *Thin-Walled Structures*,

44(2), pp. 197–210. doi: 10.1016/j.tws.2006.01.002.

Casafont, M., Arnedo, A., Roure, F. and Rodríguez-Ferran, A. (2006b) ‘Experimental testing of joints for seismic design of lightweight structures. Part 2: Bolted joints in straps’, *Thin-Walled Structures*, 44(6), pp. 677–691. doi: 10.1016/j.tws.2006.04.006.

Casafont, M., Arnedo, A., Roure, F. and Rodríguez-Ferran, A. (2007a) ‘Experimental testing of joints for seismic design of lightweight structures. Part 3: Gussets, corner joints, x-braced frames’, *Thin-Walled Structures*, 45(7–8), pp. 637–659. doi: 10.1016/j.tws.2007.05.008.

Casafont, M., Arnedo, A., Roure, F. and Rodríguez-Ferran, A. (2007b) ‘Experimental testing of joints for seismic design of lightweight structures. Part 3: Gussets, corner joints, x-braced frames’, *Thin-Walled Structures*, 45(7–8), pp. 637–659. doi: 10.1016/j.tws.2007.05.008.

CEN (2002a) *Eurocode-Basis of structural design*.

CEN (2002b) *Eurocode 1: Actions on structures - Part 1-1: General actions — Densities, self-weight, imposed loads for buildings*.

CEN (2003) *Eurocode 3 : Design of steel structures - Part 1-3: General rules - Supplementary rules for cold-formed members and sheeting*. European Committee for Standardization.

CEN (2004) *Eurocode 8 : Design of structures for earthquake resistance - Part 1: General rules, seismic actions and rules for buildings*. European Committee for Standardization.

CEN (2005) *Eurocode 3: Design of steel structures - Part 1-8: Design of joints*. European Committee for Standardization.

CEN (2010) *Eurocode 3: Design of steel structures - Part 1-1: General rules and rules for buildings*. European Committee for Standardization.

Chopra, A. (2001) *Dynamics of structures: Theory and applications to earthquake engineering, 2nd edition*. Prentice Hall.

Chung, K. . and Lau, L. (1999) ‘Experimental investigation on bolted moment connections among cold formed steel members’, *Engineering Structures*, 21(10), pp. 898–911. doi: 10.1016/S0141-0296(98)00043-1.

Comeau, G. (2008) *Inelastic Performance of Welded CFS Strap Braced Walls Research Report RP08-4*. Available at: <https://scholarsmine.mst.edu/cfss-aisi-spec/87>.

Comeau, G., Velchev, K. and Rogers, C. A. (2010) ‘Development of seismic force modification factors for cold-formed steel strap braced walls’, *Canadian Journal of Civil Engineering*, 37(2), pp. 236–249. doi: 10.1139/L09-153.

D’Ayala, D. et al. (2015) *Guidelines for Analytical Vulnerability Assessment - Low/Mid-Rise Buildings, Vulnerability Global Component Project*. doi: 10.13117/GEM.VULN-MOD.TR2014.12.

Dassault Systèmes Simulia (2014) *Abaqus 6.14 CAE User Guide*.

Davani, M. R., Hatami, S. and Zare, A. (2016) ‘Performance-based evaluation of strap-braced cold-formed steel frames using incremental dynamic analysis’, *Steel and Composite Structures*, 21(6), pp. 1369–1388. doi: <http://dx.doi.org/10.12989/scs.2016.21.6.1369>.

Deierlein, G. G. (2004) ‘Overview of a comprehensive framework for earthquake performance assessment’, *PEER report 2004/05*, 23(8), pp. 15–26.

Ding, X. and Foutch, D. A. (2004) *A note on the application of Incremental Dynamic Analysis for determining collapse drift of structures, Internal Working, Department of Civil and Environmental Engineering, University of Illinois at Urbana-Champaign, Urbana, IL*.

- Dubina, D., Stratan, A. and Nagy, Z. (2009) 'Full - Scale tests on cold-formed steel pitched-roof portal frames with bolted joints', *Advanced Steel Construction*, 5(2), pp. 175–194.
- Dubina, D., Ungureanu, V. and Landolfo, R. (2012) *Design of cold-formed steel structures*. 1st edn. Edited by E. & Sohn. ECCS.
- Fajfar, P. and Krawinkler, H. (2004) *Performance-based seismic design concepts and implementation*, PEER report 2004/05.
- FEMA (2000a) 'FEMA-350 Recommended Seismic Design Criteria for New Steel Moment-Frame Buildings', in Intergovernmental Panel on Climate Change (ed.). Cambridge: Cambridge University Press. Available at: https://www.cambridge.org/core/product/identifier/CBO9781107415324A009/type/book_part.
- FEMA (2000b) 'FEMA 355F - State of the Art Report on Performance Prediction and Evaluation of Steel Moment-Frame Buildings', *Fema-355F*, 1, pp. 1–367.
- FEMA (2000c) 'Prestandard and Commentary for the Seismic Rehabilitation of Buildings', *Rehabilitation Requirements*, (1), pp. 1–518.
- FEMA (2012) 'Seismic Performance Assessment of Buildings - methodology', *Fema P-58-1*, 1(September), p. 278.
- FEMA 356 (2000) *Prestandard and Commentary for the Seismic Rehabilitation of Building*, ASCE. Washington, D.C.
- Fiorino, L., Iuorio, O., *et al.* (2016) 'Seismic Design Method for CFS Diagonal Strap-Braced Stud Walls: Experimental Validation', *Journal of Structural Engineering*, 142(3), p. 04015154. doi: 10.1061/(ASCE)ST.1943-541X.0001408.
- Fiorino, L., Bucciero, B. and Landolfo, R. (2019) 'Shake table tests of three storey cold-formed steel structures with strap-braced walls', *Bulletin of Earthquake Engineering*, 17(7), pp. 4217–4245. doi: 10.1007/s10518-019-00642-z.
- Fiorino, L., Shakeel, S., Macillo, V. and Landolfo, R. (2017) 'Behaviour factor (q) evaluation the CFS braced structures according to FEMA P695', *Journal of Constructional Steel Research*, 138, pp. 324–339. doi: 10.1016/j.jcsr.2017.07.014.
- Fiorino, L., Shakeel, S., Macillo, V. and Landolfo, R. (2018) 'Seismic response of CFS shear walls sheathed with nailed gypsum panels: Numerical modelling', *Thin-Walled Structures*, 122(September 2017), pp. 359–370. doi: 10.1016/j.tws.2017.10.028.
- Fiorino, L., Terracciano, M. T. and Landolfo, R. (2016) 'Experimental investigation of seismic behaviour of low dissipative CFS strap-braced stud walls', *Journal of Constructional Steel Research*, 127, pp. 92–107. doi: 10.1016/j.jcsr.2016.07.027.
- Fisher, J. W. (1964) *On the behavior of fasteners and plates with holes*. Bethlehem, Pennsylvania: Lehigh University.
- Fülöp, L. A. and Dubina, D. (2004) 'Performance of wall-stud cold-formed shear panels under monotonic and cyclic loading Part II: Numerical modelling and performance analysis', *Thin-Walled Structures*, 42(2), pp. 321–338. doi: 10.1016/S0263-8231(03)00063-6.
- Gerami, M. and Lotfi, M. (2014) 'Analytical Analysis of Seismic Behavior of Cold-Formed Steel Frames with Strap Brace and Sheathings Plates', 2014.
- Gerami, M., Lotfi, M. and Nejat, R. (2015) 'Inelastic behavior of cold-formed braced walls under monotonic and cyclic loading', *International Journal of Advanced Structural Engineering*, 7(2), pp. 181–209. doi: 10.1007/s40091-015-0091-8.

- Geschwindner, L. F. (2002) 'A practical look at frame analysis, stability and leaning columns', *Engineering Journal*, 39(4), pp. 167–181.
- Gioncu, V. (2000) 'Framed structures. Ductility and seismic response: General Report', *Journal of Constructional Steel Research*, 55(1–3), pp. 125–154. doi: 10.1016/S0143-974X(99)00081-4.
- Grant, N. S. F., Schafer, B. W., Buonopane, S. G. and Madsen, R. L. (2011) 'CFS-NEES : Advancing Cold-Formed Steel Earthquake Engineering'.
- Haidarali, M. R. and Nethercot, D. A. (2011) 'Finite element modelling of cold-formed steel beams under local buckling or combined local/distortional buckling', *Thin-Walled Structures*, 49(12), pp. 1554–1562. doi: 10.1016/j.tws.2011.08.003.
- Hajirasouliha, I. and Pilakoutas, K. (2012) 'General seismic load distribution for optimum performance-based design of shear-buildings', *Journal of Earthquake Engineering*, 16(4), pp. 443–462. doi: 10.1080/13632469.2012.654897.
- Hamburger, R. (2004) 'Development of next-generation performance based seismic design guidelines', *PEER report 2004/05*, 23(8), pp. 89–100.
- Henriques, J., Rosa, N., Gervasio, H., Santos, P. and da Silva, L. S. (2017) 'Structural performance of light steel framing panels using screw connections subjected to lateral loading', *Thin-Walled Structures*, 121(September), pp. 67–88. doi: 10.1016/j.tws.2017.09.024.
- Hill, N. (1944) 'Determination of stress-strain relations from the offset yield strength values. Technical Note No. 927'. Washington.
- Iuorio, O. *et al.* (2014) 'Seismic response of Cfs strap-braced stud walls: Experimental investigation', *Thin-Walled Structures*, 85, pp. 466–480. doi: 10.1016/j.tws.2014.09.008.
- Juvinall, R. C. and Marshek, K. M. (2006) *Fundamentals of machine component design*. New York: John Wiley & Sons.
- Kasaeian, S., Usefi, N., Ronagh, H. and Dareshiry, S. (2020) 'Seismic performance of CFS strap-braced walls using capacity-based design approach', *Journal of Constructional Steel Research*, 174. doi: 10.1016/j.jcsr.2020.106317.
- Kim, T. W., Wilcoski, J., Foutch, D. A. and Lee, M. S. (2006) 'Shaketable tests of a cold-formed steel shear panel', *Engineering Structures*, 28(10), pp. 1462–1470. doi: 10.1016/j.engstruct.2006.01.014.
- Krawinkler, H. and Zohrei, M. (1983) 'Cumulative damage in steel structures subjected to earthquake ground motions', *Computers and Structures*, 16(1–4), pp. 531–541. doi: 10.1016/0045-7949(83)90193-1.
- Kyvelou, P., Gardner, L. and Nethercot, D. A. (2017) 'Testing and Analysis of Composite Cold-Formed Steel and Wood-Based Flooring Systems', *Journal of Structural Engineering*, 143(11), p. 04017146. doi: 10.1061/(ASCE)ST.1943-541X.0001885.
- Kyvelou, P., Gardner, L. and Nethercot, D. A. (2018) 'Finite element modelling of composite cold-formed steel flooring systems', *Engineering Structures*, 158(May 2017), pp. 28–42. doi: 10.1016/j.engstruct.2017.12.024.
- Van Lancker, B., Sonck, D., De Corte, W. and Belis, J. (2015) 'Lateral stiffness of cold-formed steel shear wall panels braced with glass panes : A numerical study', in *Proceedings of the Annual Stability Conference Structural Stability Research Council (SSRC2015)*, pp. 1–14. Available at: <http://hdl.handle.net/1854/LU-5931744>.
- Lange, J. and Naujoks, B. (2007) 'Behaviour of cold-formed steel shear walls under horizontal and vertical loads', *Thin-Walled Structures*, 44(12), pp. 1214–1222. doi: 10.1016/j.tws.2007.01.007.

Lee, M. S. and Foutch, D. A. (2010) 'Performance evaluation of cold-formed steel braced frames designed under current U.S. seismic design code', *International Journal of Steel Structures*, 10(3), pp. 305–316. doi: 10.1007/BF03215839.

Leng, J. ., Schafer, B. W. . and Buonopane, S. G. . (2013) 'Modeling the seismic response of cold-formed steel framed buildings: Model development for the CFS-NEES building', *Structural Stability Research Council Annual Stability Conference 2013, SSRC 2013*, pp. 426–442. Available at: <http://www.scopus.com/inward/record.url?eid=2-s2.0-84883374860&partnerID=40&md5=035e26ef0181ae5611c16d94776dd18b>.

Li, Z. and Schafer, B. W. (2010) 'Buckling analysis of cold-formed steel members with general boundary conditions using CUFSM: Conventional and constrained finite strip methods', *Proceedings Twentieth International Speciality Conference on Cold-Formed Steel Structures*, pp. 17–31. doi: 10.1016/j.tws.2006.03.013.

Lim, J. B. P., Hancock, G. J., Charles Clifton, G., Pham, C. H. and Das, R. (2016) 'DSM for ultimate strength of bolted moment-connections between cold-formed steel channel members', *Journal of Constructional Steel Research*, 117, pp. 196–203. doi: 10.1016/j.jcsr.2015.10.005.

Lim, J. B. P. and Nethercot, D. A. (2003) 'Ultimate strength of bolted moment-connections between cold-formed steel members', *Thin-Walled Structures*, 41(11), pp. 1019–1039. doi: 10.1016/S0263-8231(03)00045-4.

Liu, Y., Guo, Z., Liu, X., Chicchi, R. and Shahrooz, B. (2019) 'An innovative resilient rocking column with replaceable steel slit dampers: Experimental program on seismic performance', *Engineering Structures*, 183(July), pp. 830–840. doi: 10.1016/j.engstruct.2019.01.059.

Lu, S. and Rogers, C. A. (2018) 'Influence of gypsum panels on the response of cold-formed steel framed strap-braced walls', in *CCFSS Proceedings of International Specialty Conference on Cold-Formed Steel Structures*, pp. 925–939. Available at: <https://scholarsmine.mst.edu/isccss/24icfss/session12/7>.

Macillo, V., Shakeel, S., Fiorino, L. and Landolfo, R. (2018) 'Development and calibration of a hysteretic model for cfs strap braced stud walls', *Advanced Steel Construction*, 14(3), pp. 337–360. doi: 10.18057/IJASC.2018.14.3.2.

Madsen, R. L., Castle, T. A. and Schafer, B. W. (2016) 'NEHRP Seismic Design Technical Brief No. 12 Seismic Design of Cold-Formed Steel Lateral Load-Resisting Systems A Guide for Practicing Engineers'. doi: 10.6028/NIST.GCR.16-917-38.

Maio, R. and Tsionis, G. (2015) *Seismic fragility curves for the European building stock: review and evaluation of analytical fragility curves. EUR 27635 EN*. doi: 10.2788/586263.

Mazzoni, S., McKenna, F., Scott, M. H. and Fenves, G. L. (2007) 'OpenSees command language manual', *Pacific Earthquake Engineering Research (PEER) Center*, p. 451. Available at: <http://opensees.berkeley.edu/OpenSees/manuals/usermanual/OpenSeesCommandLanguageManual.pdf>.

Meza, F. and Becque, J. (2017) 'Experimental and numerical investigation of cold-formed steel built-up stub columns', in *Eurosteel 2017*. Copenhagen. Available at: <https://doi.org/10.1002/cepa.205>.

Meza, F. J. (2018) *The Behaviour of Cold-Formed Steel Built-up Structural Members*. PhD Thesis, The University of Sheffield.

Miller, T. H. and Pekoz, T. (1993) 'Behavior of cold-formed steel wall stud assemblies', 119(2), pp. 641–651.

Mirzaei, A. *et al.* (2015) 'Seismic capacity-based design of narrow strap-braced cold-formed steel walls', *Journal of Constructional Steel Research*, 115, pp. 81–91. doi: 10.1016/j.jcsr.2015.08.023.

Moghaddam, H., Hajirasouliha, I. and Hosseini Gelekolai, S. M. (2021) 'Performance-based seismic

- design of moment resisting steel frames: Adaptive optimisation framework and optimum design load pattern’, *Structures*, 33(May), pp. 1690–1704. doi: 10.1016/j.istruc.2021.05.014.
- Moghim, H. and Ronagh, H. R. (2009) ‘Performance of light-gauge cold-formed steel strap-braced stud walls subjected to cyclic loading’, *Engineering Structures*, 31(1), pp. 69–83. doi: 10.1016/j.engstruct.2008.07.016.
- Mohsenian, V., Filizadeh, R., Ozdemir, Z. and Hajirasouliha, I. (2020) ‘Seismic performance evaluation of deficient steel moment-resisting frames retrofitted by vertical link elements’, *Structures*, 26(April), pp. 724–736. doi: 10.1016/j.istruc.2020.04.043.
- Mojtabaei, S. M., Becque, J. and Hajirasouliha, I. (2020) ‘Local Buckling in Cold-Formed Steel Moment-Resisting Bolted Connections: Behavior, Capacity, and Design’, *Journal of Structural Engineering*, 146(9), p. 04020167. doi: 10.1061/(asce)st.1943-541x.0002730.
- Mojtabaei, S. M., Becque, J. and Hajirasouliha, I. (2021a) ‘Behavior and Design of Cold-Formed Steel Bolted Connections Subjected to Combined Actions’, *Journal of Structural Engineering*, 147(4), p. 04021013. doi: 10.1061/(ASCE)ST.1943-541X.0002966.
- Mojtabaei, S. M., Becque, J. and Hajirasouliha, I. (2021b) ‘Behaviour and design of cold-formed steel bolted connections under combined actions’, *Journal of Structural Engineering (ASCE)*, in press.
- Mojtabaei, S. M., Kabir, M. Z., Hajirasouliha, I. and Kargar, M. (2018) ‘Analytical and experimental study on the seismic performance of cold-formed steel frames’, *Journal of Constructional Steel Research*, 143, pp. 18–31. doi: <https://doi.org/10.1016/j.jcsr.2017.12.013>.
- Nabid, N., Hajirasouliha, I., Escolano Margarit, D. and Petkovski, M. (2020) ‘Optimum energy based seismic design of friction dampers in RC structures’, *Structures*, 27(August), pp. 2550–2562. doi: 10.1016/j.istruc.2020.08.052.
- Niari, S. E., Rafezy, B. and Abedi, K. (2012) ‘Numerical Modeling and Finite Element Analysis of Steel Sheathed Cold-Formed Steel Shear Walls’, *15th World Conference on Earthquake Engineering, Lisbon Portugal*.
- Papargyriou, I. and Hajirasouliha, I. (2021) ‘More efficient design of CFS strap-braced frames under vertical and seismic loading’, *Journal of Constructional Steel Research*, 185, p. 106886. doi: 10.1016/j.jcsr.2021.106886.
- Papargyriou, I., Hajirasouliha, I., Becque, J. and Pilakoutas, K. (2021) ‘Performance-based assessment of CFS strap-braced stud walls under seismic loading’, *Journal of Constructional Steel Research*, 183, p. 106731. doi: 10.1016/j.jcsr.2021.106731.
- Pauley, T. and Priestley, M. J. N. (1992) *Seismic Design of Reinforced Concrete and Masonry Buildings*. John Wiley & Sons Inc.
- PEER (2010) *Guidelines for Performance Based Seismic Design of Tall Buildings, Report No 2010/05*. Berkeley.
- PEER ground motion database, <https://ngawest2.berkeley.edu/>. Accessed Dec (2020).
- Pekoz, T. (1990) ‘Design of Cold-Formed Steel Screw Connections’, in *Tenth International Speciality Conference on Cold-Formed Steel Structures*, pp. 575–588. Available at: <https://scholarsmine.mst.edu/isccss/10iccfss/10iccfss-session6/1>.
- Pham, H. S. and Moen, C. D. (2015) *Stiffness and strength of single shear cold-formed steel screw-fastened connections, Report No. CE/VPI-ST-15-07*. VirginiaTech.
- Phan, D. T., Mojtabaei, S. M., Hajirasouliha, I., Lau, T. L. and Lim, J. B. P. (2020) ‘Design and Optimization of Cold-Formed Steel Sections in Bolted Moment Connections Considering Bimoment’, *Journal of Structural Engineering*, 146(8), p. 04020153. doi: 10.1061/(asce)st.1943-541x.0002715.

- Pourabdollah, O., Farahbod, F. and Rofooei, F. R. (2017) 'The seismic performance of K-braced cold-formed steel shear panels with improved connections', *Journal of Constructional Steel Research*, 135(April), pp. 56–68. doi: 10.1016/j.jcsr.2017.04.008.
- Powell, G. H. and Allahabadi, R. (1988) 'Seismic damage prediction by deterministic methods: Concepts and procedures', *Earthquake Engineering & Structural Dynamics*, 16(5), pp. 719–734. doi: <https://doi.org/10.1002/eqe.4290160507>.
- Prakash, V., Powell, G. and Campbell, S. (1993) *DRAIN- 2DX base program description and user guide-version 1.10, Report No. UCB/SEMM-93/17 and 93/18, Structural Engineering Mechanics and Materials, Structural Engineering Mechanics and Materials, Berkeley, CA.*
- Ramberg, W. and Osgood, W. (1943) *Description of stress-strain curves by three parameters - Technical Note No. 902.* Washington, D.C., USA: National Advisory Committee for Aeronautics.
- Rasmussen, K. J. R. (2003) 'Full-range stress–strain curves for stainless steel alloys', *Journal of Constructional Steel Research*, 59(2003), pp. 47–61.
- Rinchen and Rasmussen, K. J. R. (2019) 'Behaviour and modelling of connections in cold-formed steel single C-section portal frames', *Thin-Walled Structures*, 143(June), p. 106233. doi: 10.1016/j.tws.2019.106233.
- Rinchen, Rasmussen, K. J. R. and Zhang, H. (2019) 'Design of cold-formed steel single C-section portal frames', *Journal of Constructional Steel Research*, 162, p. 105722. doi: 10.1016/j.jcsr.2019.105722.
- Rogers, C. A. (2018) *Personal communication through e-mail.*
- Sabbagh, A. B. (2011) *Cold - Formed Steel Elements for Earthquake Resistant Moment Frame Buildings, PhD Thesis.* The University of Sheffield.
- Sabbagh, A. B., Mirghaderi, R., Petkovski, M. and Pilakoutas, K. (2010) 'An integrated thin-walled steel skeleton structure (two full scale tests)', *Journal of Constructional Steel Research*, 66(3), pp. 470–479. doi: 10.1016/j.jcsr.2009.10.007.
- Sabbagh, A. B., Petkovski, M., Pilakoutas, K. and Mirghaderi, R. (2012) 'Experimental work on cold-formed steel elements for earthquake resilient moment frame buildings', *Engineering Structures*, 42, pp. 371–386. doi: 10.1016/j.engstruct.2012.04.025.
- Sabbagh, A. B., Petkovski, M., Pilakoutas, K. and Mirghaderi, R. (2013) 'Cyclic behaviour of bolted cold-formed steel moment connections: FE modelling including slip', *Journal of Constructional Steel Research*, 80, pp. 100–108. doi: 10.1016/j.jcsr.2012.09.010.
- Sabbagh, A. B. and Torabian, S. (2021) 'Semi-rigid floor-to-wall connections using side-framed lightweight steel structures: Concept development', *Thin-Walled Structures*, 160(December 2020), p. 107345. doi: 10.1016/j.tws.2020.107345.
- Schafer, B. . and Peköz, T. (1998) 'Computational modeling of cold-formed steel: characterizing geometric imperfections and residual stresses', *Journal of Constructional Steel Research*, 47(3), pp. 193–210. doi: 10.1016/S0143-974X(98)00007-8.
- Schafer, B. W. *et al.* (2016) 'Seismic Response and Engineering of Cold-formed Steel Framed Buildings', *Structures*, 8, pp. 197–212. doi: 10.1016/j.istruc.2016.05.009.
- Seismosoft (2018) 'SeismoArtif - A computer program for generation of artificial accelerograms'. Available at: <http://www.seismosoft.com>.
- Serrette, R. and Peyton, D. (2009) 'Strength of Screw Connections in Cold-Formed Steel Construction', *Journal of Structural Engineering*, 135(August), pp. 951–958. doi: 10.1061/(ASCE)0733-9445(2009)135:8(951).

- Serror, M. H., Hassan, E. M. and Mourad, S. A. (2016) 'Experimental study on the rotation capacity of cold-formed steel beams', *Journal of Constructional Steel Research*, 121, pp. 216–228. doi: 10.1016/j.jcsr.2016.02.005.
- Shahini, M., Sabbagh, A. B., Davidson, P. and Mirghaderi, R. (2018) 'Cold-formed steel bolted moment-resisting connections with friction-slip mechanism for seismic areas', *Wei-Wen Yu International Specialty Conference on Cold-Formed Steel Structures 2018 - Recent Research and Developments in Cold-Formed Steel Design and Construction*, pp. 389–395.
- Shamim, I. and Rogers, C. A. (2015) 'Numerical evaluation: AISI S400 steel-sheathed CFS framed shear wall seismic design method', *Thin-Walled Structures*, 95, pp. 48–59. doi: 10.1016/j.tws.2015.06.011.
- Sharafi, P. *et al.* (2018) 'Lateral force resisting systems in lightweight steel frames: Recent research advances', *Thin-Walled Structures*, 130(March), pp. 231–253. doi: 10.1016/j.tws.2018.04.019.
- Shifferaw, Y. and Schafer, B. W. (2012) 'Inelastic bending capacity of cold-formed steel members', *Journal of Structural Engineering*, 138(4), pp. 468–480. doi: 10.1061/(ASCE)ST.1943-541X.0000469.
- Tian, Y. S., Wang, J. and Lu, T. J. (2004) 'Racking strength and stiffness of cold-formed steel wall frames', *Journal of Constructional Steel Research*, 60(7), pp. 1069–1093. doi: 10.1016/j.jcsr.2003.10.002.
- Tomà, A. W. and Stark, J. W. B. (1978) 'Connections in Cold-formed Sections and Steel', in (1978) - *4th International Specialty Conference on Cold-Formed Steel Structures*, pp. 951–987. Available at: <https://scholarsmine.mst.edu/isccss/4iccfss/4iccfss-session4/5>.
- Uang, C., Sato, A., Hong, J. and Wood, K. (2010) 'Cyclic testing and modeling of cold-formed steel special bolted moment frame connections', *Journal of Structural Engineering*, 136(8), pp. 953–960. doi: 10.1061/(ASCE)ST.1943-541X.0000190.
- Usefi, N., Ronagh, H. and Sharafi, P. (2020) 'Numerical modelling and design of hybrid cold-formed steel wall panels', *Thin-Walled Structures*, 157(September), p. 107084. doi: 10.1016/j.tws.2020.107084.
- Usefi, N., Sharafi, P. and Ronagh, H. (2019) 'Numerical models for lateral behaviour analysis of cold-formed steel framed walls: State of the art, evaluation and challenges', *Thin-Walled Structures*, 138(January), pp. 252–285. doi: 10.1016/j.tws.2019.02.019.
- Vamvatsikos, D. and Cornell, A. C. (2002) 'Incremental dynamic analysis', *Earthquake Engineering and Structural Dynamics*, 31(3), pp. 491–514. doi: 10.1002/eqe.141.
- Velchev, K. (2008a) 'Inelastic Performance and Design of Cfs Walls Braced with Straps Having Reduced Width Fuses'.
- Velchev, K. (2008b) *Inelastic Performance of Screw Connected CFS Strap Braced Walls Research Report RP08-5*. Available at: <https://scholarsmine.mst.edu/ccfss-aisi-spec/88>.
- Velchev, K., Comeau, G., Balh, N. and Rogers, C. A. (2010) 'Evaluation of the AISI S213 seismic design procedures through testing of strap braced cold-formed steel walls', *Thin-Walled Structures*, 48(10–11), pp. 846–856. doi: 10.1016/j.tws.2010.01.003.
- Versailot, P. (2017) *Effects Of Cyclic Loading On The Mechanical Properties Of Steel*. Universitatea Politehnica Timisoara, Romania.
- Walker, A. C. (1975) *Design and Analysis of Cold-formed Sections*. Halsted Press.
- Wong, M. F. and Chung, K. F. (2002) 'Structural behaviour of bolted moment connections in cold-formed steel beam-column', 58, pp. 253–274. doi: 10.1016/S0143-974X(01)00044-X.
- Yan, S. and Young, B. (2012) 'Screwed connections of thin sheet steels at elevated temperatures - Part

- II: Transient state tests', *Engineering Structures*, 35, pp. 228–233. doi: 10.1016/j.engstruct.2011.10.027.
- Ye, J. (2016) *More efficient cold-formed steel elements and bolted connections*. PhD Thesis, The University of Sheffield.
- Ye, Jihong, Feng, R., Chen, W. and Liu, W. (2016) 'Behavior of cold-formed steel wall stud with sheathing subjected to compression', *Journal of Constructional Steel Research*, 116, pp. 79–91. doi: 10.1016/j.jcsr.2015.08.028.
- Ye, Jun, Hajirasouliha, I., Becque, J. and Eslami, A. (2016) 'Optimum design of cold-formed steel beams using Particle Swarm Optimisation method', *Journal of Constructional Steel Research*, 122, pp. 80–93. doi: 10.1016/j.jcsr.2016.02.014.
- Ye, J., Mojtabaei, S. M. and Hajirasouliha, I. (2018) 'Local-flexural interactive buckling of standard and optimised cold-formed steel columns', *Journal of Constructional Steel Research*, 144, pp. 106–118. doi: 10.1016/j.jcsr.2018.01.012.
- Ye, J., Mojtabaei, S. M. and Hajirasouliha, I. (2019) 'Seismic performance of cold-formed steel bolted moment connections with bolting friction-slip mechanism', *Journal of Constructional Steel Research*, 156, pp. 122–136. doi: 10.1016/j.jcsr.2019.01.013.
- Ye, J., Mojtabaei, S. M., Hajirasouliha, I. and Pilakoutas, K. (2019) 'Efficient design of cold-formed steel bolted-moment connections for earthquake resistant frames', *Thin-Walled Structures*, (October), pp. 0–1. doi: 10.1016/j.tws.2018.12.015.
- Ye, J., Mojtabaei, S. M., Hajirasouliha, I., Shepherd, P. and Pilakoutas, K. (2018) 'Strength and deflection behaviour of cold-formed steel back-to-back channels', *Engineering Structures*, 177(July), pp. 641–654. doi: 10.1016/j.engstruct.2018.09.064.
- Yun, X. and Gardner, L. (2017) 'Stress-strain curves for hot-rolled steels', *Journal of Constructional Steel Research*, 133, pp. 36–46. doi: 10.1016/j.jcsr.2017.01.024.
- Zeynalian, M. and Ronagh, H. R. (2012) 'A numerical study on seismic performance of strap-braced cold-formed steel shear walls', *Thin-Walled Structures*, 60, pp. 229–238. doi: 10.1016/j.tws.2012.05.012.
- Zeynalian, M. and Ronagh, H. R. (2015) 'Seismic performance of cold formed steel walls sheathed by fibre-cement board panels', *Journal of Constructional Steel Research*, 107, pp. 1–11. doi: 10.1016/j.jcsr.2015.01.003.
- Zeynalian, M., Ronagh, H. R. and Hatami, S. (2012) 'Seismic characteristics of K-braced cold-formed steel shear walls', *Journal of Constructional Steel Research*, 77, pp. 23–31. doi: 10.1016/j.jcsr.2012.04.009.
- Zhang, X., Rasmussen, K. J. R. and Zhang, H. (2016) 'Experimental investigation of locally and distortionally buckled portal frames', *Journal of Constructional Steel Research*, 122, pp. 571–583. doi: 10.1016/j.jcsr.2016.04.017.